Zebrafish Bipolar Cells: Exploiting Ancestral Cone-Type Diversity to Build Complex Spatiochromatic Encoding

A thesis presented for the degree of
Doctor of Philosophy

Simen Bruøygard

School of Life Sciences
University of Sussex

September 2025

Declaration

This thesis has not previously been submitted to this or any other university for a degree, nor will it be in the future. The work here is my own and has been carried out independently under the supervision of Prof. Tom Baden.

Abstract

BCs integrate spatial and chromatic information to shape all downstream visual processing, yet how this integration occurs in spectrally complex systems remains poorly understood. Using the larval zebrafish as an evolutionarily conserved vertebrate model, I investigated the spatiochromatic integration properties of bipolar cells. I developed experimental protocols for *in vivo* receptive field identification, utilised a receptive field mapping technique adapted for calcium imaging, and created analysis pipelines to characterise the spatial and chromatic response properties of bipolar cells.

Key findings include: i) Receptive fields were reliably measured and spectrally decomposed, revealing predominantly centre-dominant organization with weak surround structure across all chromatic conditions. ii) Spatial offsets between spectral components were common in colour opponent terminals, whereas On and Off cells typically showed overlapping spectral channels. Thus, this may constitute a functional organisation principle. iii) Blocking glycinergic and GABAergic signalling reduced chromatic integration diversity, altered spatiotemporal RF profiles, and greatly reduced the incidence of spatial offsets in opponent bipolar cells. iv) Preliminary experiments suggest spatial offsets between chromatic components of receptive fields mediate orientation selectivity at the level of bipolar cells, indicating a functional role of non-concentric spatial antagonism.

These findings demonstrate that zebrafish bipolar cells establish diverse feature detection channels through selective spectral integration and systematic spatial organization. Lateral inhibition via amacrine cells further diversifies these channels by modulating chromatic responses and spatial integration profiles. This retinal complexity exceeds that of terrestrial mammals, indicating tetrachromatic systems enable more sophisticated early visual processing through enhanced spectral information. Together, these results suggest that inner plexiform layer circuits establish complex spectral feature detection, enable early orientation selectivity via chromatic offsets, and serve to orchestrate downstream visual processing streams.

Acknowledgements

I would like to express my deepest gratitude to my supervisor, Prof. Tom Baden for his invaluable guidance, support, and patience throughout these past years. His expertise and insights have been instrumental in shaping this work, and his encouragement kept me afloat amongst doubts and challenges. I would also like to thank my co-supervisor, Dr. Takeshi Yoshimatsu, who taught me a great deal about zebrafish, two-photon imaging, and experimental design.

I also thank all funding bodies that have supported my PhD, including the University of Sussex, the Leverhulme Trust, and the European Research Council.

I am grateful to my colleagues in the Baden lab, both past and present, for their support, engaging discussions, and stimulating working environment. I feel we have fostered a collaborative and scientifically inspiring atmosphere that has greatly contributed to my growth as a researcher.

I would also like to thank the support of my friends and family, both domestically and abroad. Especially my parents, who have always believed in me and encouraged me to pursue my interests.

Finally, I want to thank my partner, Alicja, for her unwavering support, understanding, and love throughout this journey. She has encouraged me to persevere through adversity and has been a constant source of strength throughout the years. This achievement would not have been possible without her.

Contents

List of Figures

List of Tables

Abbreviations

α-BTX α-bungarotoxin.

AC amacrine cell.

BC bipolar cell.

CaM calmodulin.

CCA calcium-correlated average.

CNQX 6-cyano-7-nitroquinoxaline-2,3-dione.

dpf days post-fertilisation.

FOV field of view.

GFP green fluorescent protein.

HC horizontal cell.

INL inner nuclear layer.

IPL inner plexiform layer.

LcR Lightcrafter.

LWS long-wavelength sensitive.

nAChRs nicotinic acetylcholine receptors.

OPL outer plexiform layer.

OS orientation selectivity.

PTU phenylthiourea.

RF receptive field.

RGC retinal ganglion cell.

RO reverse osmosis.

ROI region of interest.

STA spike-triggered average.

STRF spatiotemporal receptive field.

TPMPA (1,2,5,6-Tetrahydropyridin-4-yl) methylphosphinic acid.

trb2 thyroid hormone receptor β2.

1 | Introduction

1.1 Overview

Upon hatching, zebrafish emerge in their larval form into an unfamiliar aquatic environment in which they must survive independently. Originating in rivers and rice paddies of the Indian subcontinent, the larvae inhabit both clear and murky waters, preferring river banks or other waterways where cover is plentiful. Despite its simplistic appearance and small size, zebrafish larva must already from a few days after hatching use vision to hunt prey, escape predators, and navigate its surroundings.

In this thesis I explore bipolar cells (BCs) of the larval zebrafish eye. Zebrafish are tetrachromats, with four cone photoreceptors sensitive to wavelengths from orange-red well into the ultraviolet range. On one hand, this enables a richer and more information dense representation of the visual world. On the other, it presents challenges in building neural circuits to represent, segregate, integrate, and transmit this information in a manner with utility for the downstream portions of its nervous system. This may provide insights into fundamental circuit principles for encoding such information. For this reason, it is imperative that we understand the information processing within each step of the visual processing hierarchy. Here, I focus on how the larval zebrafish represents space, time, and colour at the level of BCs.

Despite the ubiquity of this model organism in neuroscience research, and decades of effort on the anatomy and physiology of their eyes, surprisingly little is understood about the signal processing throughout their retina. Zebrafish bipolar cells have been described in terms of their morphology and connectivity (Connaughton 2011; Li, Tsujimura, et al. 2012). Moreover, spatial RFs have been mapped in larval zebrafish (Johnston, Ding, et al. 2014), and functional diversity has been probed (Antinucci, Suleyman, et al. 2016; Johnston, Seibel, et al. 2019; Zimmermann et al. 2018; Bartel, Yoshimatsu, et al. 2021). However, there are no direct investigations of the BCs's spatiochromatic receptive field (RF) in larval zebrafish. This therefore presents for the first time *in vivo* spectral RF mapping within the outer retina of an aquatic vertebrate species.

There has recently been a rapid proliferation of genetically manipulated mutants expressing fluorescent proteins along with advances in two-photon imaging (Abu-Siniyeh and Al-Zyoud 2020; Antinucci and Hindges 2016; Bollmann 2019; Janiak et al. 2022). This allows direct

access to the neuronal dynamics involved in visual processing and enable opportunities to investigate the unknown properties of spatial vision in zebrafish larvae. Accordingly, the overarching aim of this thesis is to elucidate the mechanisms underlying spatial vision in zebrafish larvae. The bipolar cell was chosen as the primary focus because it is the only cell type in the vertebrate retina to integrate spatial information from photoreceptors and transmit it to the inner retina. Although the zebrafish retina has been extensively studied, the functional properties of its BCs remain poorly understood.

Evidence here presented shows that zebrafish BCs play a multifaceted role in combining colour and space, serving to set up systematic colour channels by integrating chromatic inputs in spatially variable ways. The overarching results can be summarised as follows:

1. RFs within the early visual system of the zebrafish can be reliably found and mapped *in vivo* using 2-photon imaging and tetrachromatic spatial stimulation. Sequential chromatic noise stimuli and calcium-correlated average can be used to calculate per-channel RFs. This decomposes the spectral content that makes up each cell's RF, allowing analysis of the chromatic spatial integration of each bipolar cell output.

2. Centre-surround antagonism is surprisingly weak, often to the extent that they are undetectable. Those that could be detected, are typically spatially diffuse with a broad spatial extent, and possibly constrained to certain bipolar cell types. No obvious concentric spatial antagonism nor outer boundary of the spatial antagonism was identifiable. The vast majority of BCs were found to be centre-only encoding, irrespective of chromatic content.

3. However, chromatic channels regularly had spatial offsets to one another, and stimulation with broad-spectrum white light highlighted a population of cells with strong asymmetric spatial antagonism. Together, this suggests that spatially constrained local contrast encoding, such as that typically associated with concentric antagonism, may be implemented via a non-classical mechanism in the zebrafish outer retina.

4. Amacrine cells (ACs) mediated spatial antagonism, both in the form of subtle surrounds and in non-classical ways. Pharmacological blockade of ACs caused a dilation of the RF centre, and a loss of weak spatial antagonism, confirming that ACs play a role in shaping the spatial integration of BCs despite surrounds being weak. Moreover, the spatially offset spectral antagonism in a subset of colour opponent BCs was abolished after AC blockade. Therefore, lateral inhibition is likely involved in generating this non-concentric form of spatial antagonism.

1.2 Background

1.2.1 The emergence of centre-surround theory

The ability to encode the spatial distribution of light within a visual scene represents one of the most fundamental and evolutionarily conserved functions of vertebrate visual systems.

Spatial vision provides immense behavioural utility, as evidenced by its early emergence in vertebrate evolution and persistence across virtually all members of the phylum. The present work focuses specifically on the sensory mechanisms underlying spatial vision: the transduction of electromagnetic energy into electrochemical signals by photoreceptors, the subsequent processing of spatial information through local retinal circuits, and the transmission of spatially organised visual data to higher brain centres. This mechanistic approach to vision provides the foundation for understanding how retinal circuits construct the spatial representations that guide behaviour.

Decoding the signals involved in vertebrate vision is approaching a century's worth of effort (Adrian and Matthews 1927). In 1938, inspired by recent advances in electrophysiology, Hartline conducted a series of single-cell extracellular recordings from delaminated nerve fibres from the eye of the arthropod *Limulus*. He measured how they were affected by changes in light intensity and spatial location within its RF. Hartline 1938 noted discharge impulses were stronger when light was presented to the centre of the RF, and weaker when light was presented close to its margins. In addition, a handful of these cells would invert their responses if stimulated in the margins. While this was deemed aberrant at the time, Hartline had unknowingly identified spatial antagonism.

After a series of technical improvements including intraocular electrophysiological recording techniques (Hartline 1938; Gernandt and Granit 1947; Granit 1948) and the invention of a multibeam opthamalscope for targeted retinal stimulation (Talbot and Kuffler 1952), Kuffler 1953 described an antagonistic "centre-surround relationship" observed in cat retinal ganglion cells. Stimuli of a given polarity (increment, decrement) in the centre would elicit depolarisation whereas the same stimuli in the surround resulted in hyperpolarisation. Concurrently, Barlow 1953 described that an "inhibitory effect is elicited by light falling on that part of the retina which immediately surrounds the RF [. . .]". Together the phraseology of centre-surround antagonism emerged.

Early lines of research resulted in a simple and elegant way of modelling RFs: classical Gaussian centre-surround antagonism (Enroth-Cugell and Robson 1966; Rodieck 1965). In short, stimuli that hit the centre of the
glsrf lead to stronger depolarisation compared to distal stimuli flanking either side. Past this region the polarity flips, according to the centre-surround principle, resulting in overall hyperpolarisation (Figure 1.1). This architecture generates graded responses that decrease with distance from the RF centre, with polarity reversals at the centre-surround boundary. Through these seminal observations a schema was forming: concentric, antagonistic RF interactions of a given polarity were crucial for spatial integration in the retina.

1.2.2 Spatial integration in the retina

Evidently, spatially constrained information is collected by and processed within the retina, driven by RFs tiling each eye to represent the visual scene. Each neuron in the eye has systematic spectral and spatial conditions under which it will respond, and others which may inhibit it. When grouped into types rooted in their morphology and physiology, patterns

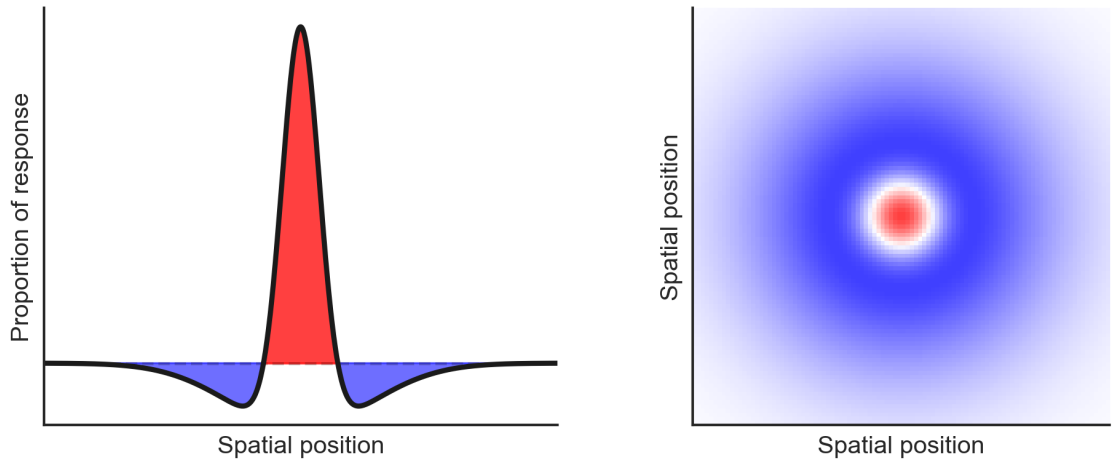

Figure 1.1: Classical Gaussian centre-surround RF organization. The left panel shows the response profile as a function of spatial position, with centre excitation flanked by antagonistic surround inhibition. The right panel illustrates the spatial organization of this field, with darker regions representing stronger responses. The centre-surround antagonism generates spatial filtering properties fundamental to retinal processing.

emerge that describe how different layers of the retina process information.

In the outer retina photoreceptors transduce light into graded electrochemical signals, which are then passed onto BC dendrites in the outer plexiform layer (OPL). These cells pool and integrate photoreceptor signals, creating a first stage of spatial integration and chromatic processing. Importantly, BCs retain the graded signalling of photoreceptors, resulting in analog encoding of stimulus strength. The BCs then transmit this information to retinal ganglion cells (RGCs) in the inner plexiform layer, where further spatial and chromatic processing occurs through lateral interactions with ACs and horizontal cells (HCs) (Baden and Osorio 2019; Thoreson and Dacey 2019). As a result, each layer builds upon the previous one to extract and integrate increasingly complex features from the visual input.

The visual system must be capable of resolving and encoding a vast range of spatial scales, and be able to do so at different levels of granularity across the visual field. Subsequently, spatial vision is largely posited to be driven by RFs which tile the retina at various levels of granularity (Field et al. 2010; Turner, Schwartz, and Rieke 2018). These then sum onto cells in the next layer where RFs again tile the retina at a broader scale (Freed, Smith, and Sterling 1992; Balasubramanian and Sterling 2009). Antagonistic centre-surround organisation within these layers of processing has been implicated in contrast detection, edge detection (Marr, Hildreth, and Brenner 1980; Zhang, Kim, et al. 2012), orientation selectivity (Baden, Berens, Franke, et al. 2016), motion processing (Vlasits et al. 2016; Kerschensteiner 2022), and even colour processing (Kaneko and Tachibana 1981; Shimbo et al. 2000). This theoretical framework has been developed primarily from terrestrial vertebrate studies, raising questions about whether the same organizational principles apply universally across different visual environments and evolutionary pressures.

1.2.3 Environmental demands and circuit adaptations in aquatic vision

Aquatic visual environments differ fundamentally from terrestrial habitats in ways that should shape retinal circuit organization. From the zebrafish perspective (Figure 1.2), the aquatic world presents systematic relationships between spectral content, distance, and illumination that are distinct from terrestrial vision. Underwater, green-blue hues dominate the horizon, the lower visual field reflects red-orange wavelengths from river substrates, and the upper visual field against the sky additonally contains blue-UV wavelengths (Nevala and Baden 2019; Zimmermann et al. 2018). Crucially, chromatic content attenuates with distance in water unlike in air, providing systematic distance cues that terrestrial systems cannot exploit (Baden 2024b).

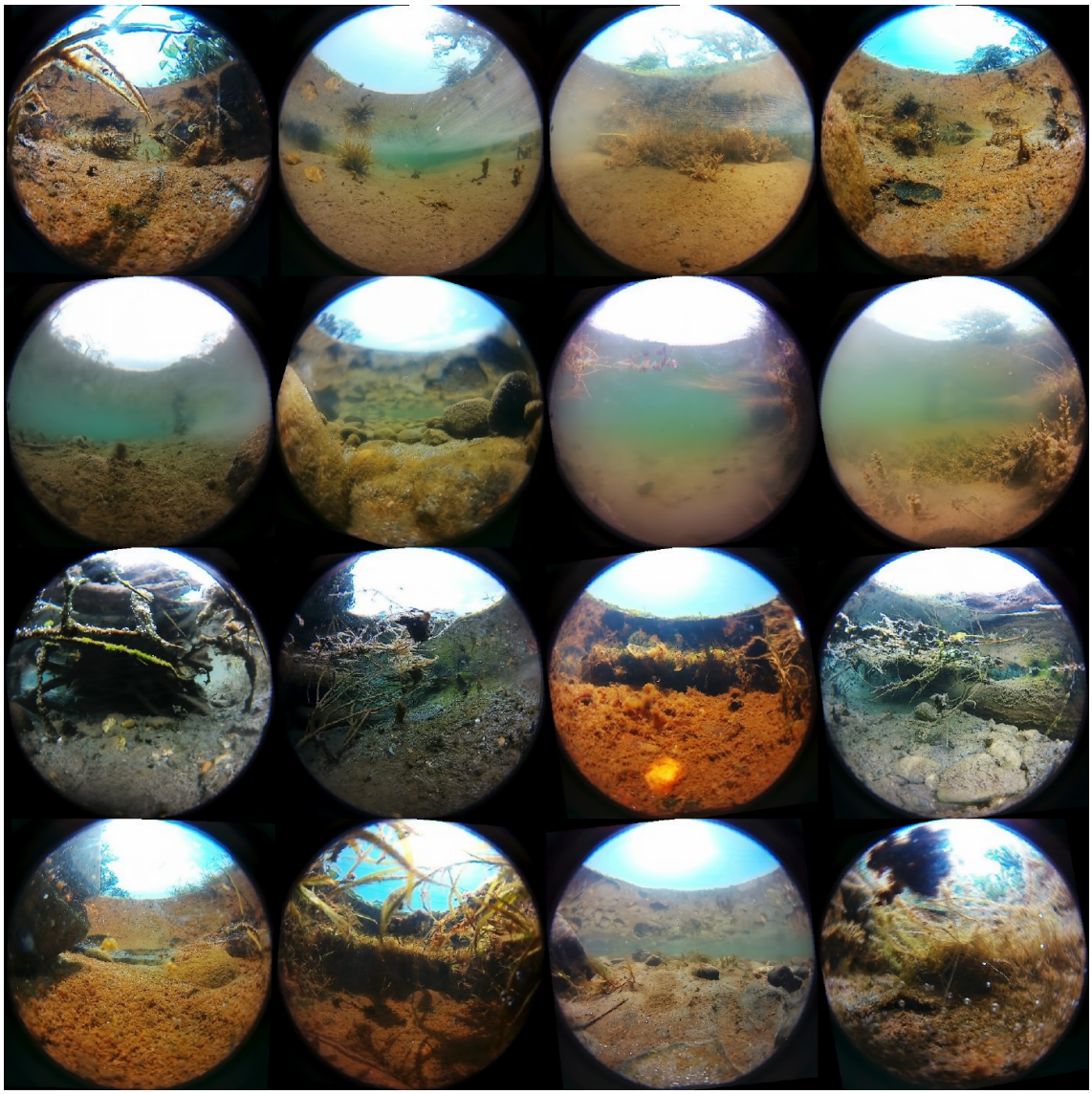

Figure 1.2: Collage of visual scenes approximating the zebrafish larva's perspective, illustrating the systematic spatial and spectral patterns of aquatic environments. Note the predictable relationships between spatial location and spectral content that differ markedly from terrestrial visual statistics. From Nevala and Baden 2019; Zimmermann et al. 2018.

These environmental differences have been quantified systematically, revealing distinct

visual statistics that predict alternative circuit implementations. Cai et al. 2023 compared natural scenes from zebrafish habitats to terrestrial environments, finding aquatic scenes contained approximately 70% lower visual contrast and proportionally fewer fine spatial details, whilst exhibiting greater spatial predictability but higher temporal variability. These environmental statistics suggest that aquatic visual systems should be optimised for different computational strategies than their terrestrial counterparts.

Zebrafish visual capabilities indeed reflect these environmental adaptations. Adult zebrafish show optimal spatial frequency preferences of 0.116 ± 0.01 cycles/degree (cpd), with processing optimised for speed rather than fine spatial discrimination (Hollbach et al. 2015). This matches the high temporal frequency content of their environment due to conspecifics, particulates, and flowing vegetation (Cai et al. 2023). Importantly, larval zebrafish exhibit even stronger biases toward low spatial frequencies (0.03-0.05 cpd optimal responses), posited to be driven by immature retinal circuits resulting in processing limitations rather than optical constraints (Haug et al. 2010; Dehmelt et al. 2021).

These neural processing characteristics are further shaped by developmental constraints. First, their eye is smaller, thereby limiting the number of photoreceptors, typically estimated at around 10000 (Zimmermann et al. 2018). This constrains resolution because physiologically the photoreceptor density is limited (Yoshimatsu, Schröder, et al. 2020; Dehmelt et al. 2021; Haug et al. 2010). Additionally, rod-bipolar pathways remain functionally immature until approximately 15 dpf, making retinal signalling cone-dominated throughout the 5-9 dpf period when critical visual behaviours emerge (Perkins, Fadool, and Dowling 2004; Bilotta and Saszik 2001).

Larvae compensate through regional specializations, showing strong attentional preferences for specific visual field locations (Dehmelt et al. 2021). For example, attention towards UV signals coincides with a fovea-like region of the retina used for high-acuity prey capture via increased photoreceptor density (Yoshimatsu, Schröder, et al. 2020). It has been shown that RGCs are also tuned to match the spectral characteristics of the visual field (Zimmermann et al. 2018; Zhou et al. 2020). Taken together, this suggests larval zebrafish exploit spatially and chromatically dependent feature channels for behaviours.

1.2.4 Zebrafish larvae as a model for aquatic circuit integration

Understanding how retinal circuits implement spatial integration strategies requires direct measurement of neural processing at the circuit level. Aquatic visual systems may employ fundamentally different strategies compared to terrestrial vertebrate retinae. The environmental and developmental constraints described above therefore raise fundamental questions about how zebrafish process spatial information and whether these circuits conform to established principles derived from terrestrial species.

Zebrafish larvae provide exceptional experimental access to address these circuit-level questions. The gross morphology of the zebrafish retina is largely complete by 3 dpf, coinciding with hatching, yet larvae must achieve functional vision for critical behaviours by

5 dpf when their yolk sac is depleted (Schmitt and Dowling 1999; Fleisch and Neuhauss 2006). Already from this early developmental stage the larvae must rely on their vision to engage in essential behaviours such as prey capture and predator avoidance. Moreover, the genetic and optical tractability of zebrafish larvae enables direct investigation of these circuit mechanisms. Transparent mutant lines eliminate pigmentation that would otherwise impede optical access (White et al. 2008), whilst well-characterized genetics enable genetically encoded indicators in specific cell types (Muto et al. 2011; Choe et al. 2021). This combination allows for 2-photon imaging of retinal circuits *in vivo* (Janiak et al. 2022). As such, behaviourally relevant visual circuits can be investigated in a live vertebrate model.

To understand how aquatic environments might shape spatial integration strategies, we focused on bipolar cells as the first site where multiple photoreceptor inputs converge and spatial computations begin. Unlike downstream ganglion cells, which integrate dozens of inputs through complex lateral circuits, bipolar cells provide a tractable entry point for dissecting fundamental integration mechanisms. Bipolar cell responses offer a relatively unfiltered view of how spatial information is first processed before being passed to the inner retina.

1.2.5 Measuring bipolar cell activity

Transgenic lines expressing jGCaMP8m in bipolar cell synapses via the *ribeyeA* promoter (Wan, Almers, and Chen 2005; Zhang, Rózsa, et al. 2023) enable direct measurement of spatially-evoked neural activity at this stage of vision. As the flux in membrane potential propagate down the axon and arrive at the synaptic terminal, voltage-gated calcium channels open leading to transient influx of extracellular calcium, required to start exocytosis of neurotransmitter (Südhof 2012). Briefly, calcium influx is sensed by synaptotagmin, which displaces complexin protein and triggers vesicle fusion with the presynaptic membrane. SNARE proteins (syntaxin, SNAP-25, and synaptobrevin) form trans-SNARE complexes that fuse together, providing the mechanical force necessary for membrane fusion by bringing vesicle and plasma membranes into proximity. This fusion opens a pore that enables neurotransmitter release into the synaptic cleft (Morgans 2000; Morgans et al. 1996). Synaptophysin is strongly expressed on synaptic vesicles and facilitates vesicle fusion via interactions with the SNARE proteins (Cousin 2021; Valtorta et al. 2004). The synaptophysin-bound GCaMP (*RibbeyeA:SyGCaMP8m*) leverages this interaction to provide a reliable readout of calcium dynamics at the bipolar cell's ribbon synapse (Dreosti, Odermatt, et al. 2009; Magupalli et al. 2008; Wan, Almers, and Chen 2005), providing rapid and robust estimates of bipolar cell activity.

As the sole interface between outer and inner retina, bipolar cells must integrate the systematic spatial and spectral patterns of aquatic environments into functionally relevant feature channels whilst operating under the developmental constraints described above. Whether these circuits employ classical centre-surround organisation as in terrestrial systems, or have evolved alternative integration mechanisms suited to aquatic visual statistics,

remains unknown. Resolving this question is crucial for understanding how environmental pressures shape fundamental visual processing strategies across vertebrate evolution.

1.3 Bipolar cells: feature channels at the second synapse of vision

1.3.1 The role of bipolar cells in the retina

BCs are interneurons that integrate signals from photoreceptors and pass them onto RGCs. Their name comes from their morphology, with cell bodies sitting in the inner nuclear layer (INL), extending two processes. A single dendritic tree ramifies into the OPL where they contact photoreceptors and HCs forming a triadic synapse complex (Li, Tsujimura, et al. 2012). On the other end, a single axonal process extends into the inner plexiform layer (IPL), where they branch out to form synapses with RGCs and ACs (Masland 2012a). They interact with HCs at their dendrites and with ACs at their axon terminals, forming a complex network of connections that enables the processing of visual information.

BCs are the only type of neuron in the vertebrate retina to form synapses with all other neuron types. Their primary role is to integrate signals from photoreceptors and transmit them to RGCs, serving as the sole interface between the outer retina and inner retina. As such, they are crucial for the feed forward vertical pathway, relaying information from the outer to the inner retina (See Figure 1.3). Together with HCs and ACs, they form the local lateral circuits that process visual information before it reaches the RGCs (See Figure 1.3c). BCs utilise their morphology, physiology, and circuit wiring to selectively process photoreceptor outputs through specific connectivity patterns.

Unlike simple relay neurons, BCs actively integrate, filter, and diversify the visual input they receive from photoreceptors. This intermediate processing role represents what Euler, Haverkamp, et al. 2014 describe as an extra layer of processing that is not typically found in other sensory organs, allowing for signal transformation before information reaches the ganglion cell output stage. While photoreceptors provide a raw sampling of the environment, BCs process this information through systematic integration patterns (Masland 2012a).

1.3.2 The On and Off systems

Perhaps the most fundamental feature encoded by BCs is the contrast between light increments and decrements. Due to their transduction cascade, photoreceptors hyperpolarise in the presence of light and consequently reduce their tonic release of glutamate onto BCs. In order to encode both increments and decrements of light, BCs express two classes of glutamate receptors: Metabotropic glutamate receptors (mGluRs) postsynaptically invert the sign at the photoreceptor synapse by depolarising the BCs in response to light increments and hyperpolarising in response to light decrements (Euler, Haverkamp, et al. 2014;

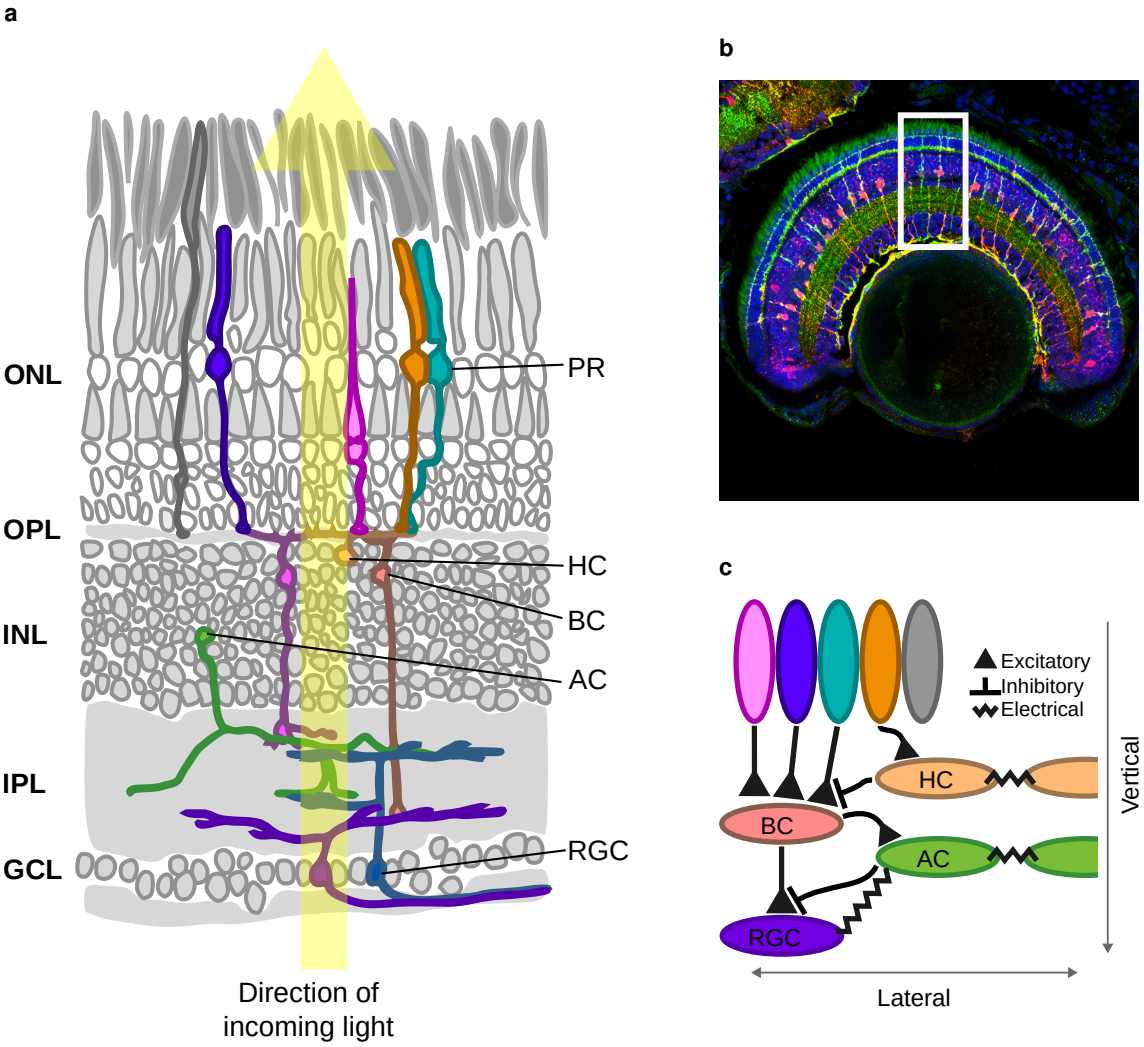

Figure 1.3: Retinal structure and neural connectivity. To help explain how visual systems handle this demand, we can split neuronal signalling within the vertebrate retina along two axes: vertical and lateral (Werblin and Dowling 1969; Euler, Haverkamp, et al. 2014; Roska and Werblin 2001). **(a)** Schematic showing the layered organization of retinal cell types with direction of incoming light. ONL: Outer Nuclear Layer, OPL: Outer Plexiform Layer, INL: Inner Nuclear Layer, IPL: Inner Plexiform Layer, GCL: Ganglion Cell Layer. **(b)** Cross-sectional microscopy image showing retinal layers with various immunostaining. Taken from Macpherson 2020. White box denotes approximate cross-section as shown in a. **(c)** Simplified circuit diagram illustrating connections. Key: horizontal cells (HCs), bipolar cells (BCs), amacrine cells (ACs), and retinal ganglion cells (RGCs).

Masland 2012a). On the other hand, ionotropic glutamate receptors (iGluRs) preserve the sign of the photoreceptor input, hyperpolarising BCs in response to light increments and depolarising them in response to light decrements (Euler, Haverkamp, et al. 2014; Masland 2012a). This determines the cell's encoding polarity. Thus, BCs expressing mGluRs are classified as *On* types, while those expressing iGluRs are classified as *Off* types, respectively.

This functional dichotomy is also reflected in the morphology and physiology of BCs. The dendrites of On BCs invaginate into the cone pedicle, forming triadic synapses together with horizontal cell processes, while Off BCs make flat, basal contacts at the base of the pedicle (Nemitz, Dedek, and Janssen-Bienhold 2021; Haverkamp, Grünert, and Wässle 2000; Wässle 0000; Suzuki et al. 2013). The morphological placement of BC synapses within the OPL is therefore indicative of their functional identity.

On and Off BCs also occupy distinct sublaminae within the IPL, with On BCs stratifying in the inner sublaminae and Off BCs in the outer sublaminae (Connaughton 2011; Li, Tsujimura, et al. 2012). This stratification pattern reflects a fundamental organisational principle where morphological positioning directly correlates with functional identity. Accordingly, monostratifying On and Off RGCs, and bistratifying On-Off RGC dendrites ramify in the corresponding sublaminae of the IPL to receive input from their respective BCs (Masland 2012a; Baden, Euler, and Berens 2020). This spatial organisation facilitates parallel processing of visual information, with distinct pathways for On and Off signals.

1.3.3 Setting up spatiochromatic channels

BCs generate spectral and spatial channels by integrating signals from multiple photoreceptors through systematic connectivity patterns. In the vertical pathway, photoreceptors exhibit both convergence and divergence onto BCs, creating the foundation for spatiochromatic processing. Convergence refers to the pooling of signals from multiple photoreceptors onto a single BC, while divergence refers to the distribution of a single photoreceptor's signal across multiple BCs (Euler, Haverkamp, et al. 2014; Li, Tsujimura, et al. 2012). These connectivity patterns enable both diverse spectral encoding and parallel processing of visual information.

Because zebrafish are tetrachromats, up to four different types of cone photoreceptors can provide input to a single BC, generating diverse chromatic and achromatic channels. Importantly, this lays the basis for both colour selective, colour opponent, and achromatic pathways (Wong and Dowling 2005; Bartel, Yoshimatsu, et al. 2021). For example, Li, Tsujimura, et al. 2012 found the following types of BCs in adult zebrafish: G, RGB, GBUV, RG, and RGBUV, in addition to four mixed rod- and cone-contacting types. The broadband RGBUV cells are thought of as achromatic, since they do not exhibit colour selectivity. Cone convergence therefore sets up essential chromatic and achromatic channels for downstream processing.

In addition to spectral integration, the spatial extent of convergence determines RF proper-

ties. Thus, spatial extents and chromatic convergence varies between BCs types, hinting at distinct functional roles. For instance, Li, Tsujimura, et al. 2012 found that adult RGB BCs integrate inputs from an average of 7 red, 11 green, and 3 blue cones, deviating from the cone mosaic ratio (R:G:B:UV = 2:2:1:1). On the other hand, GBUV cells connected to 8 green, 4 blue, and 5 UV cones, showing a more balanced integration between long and short wavelengths. The spatial extent of the dendritic field varies substantially between BCs types (Li, Tsujimura, et al. 2012; Connaughton 2011), although this BC integration and spatial extent analysis has not been explored in larval zebrafish. Nevertheless, the cone convergence patterns of BCs are not random, but rather systematic and likely reflect functional demands of the visual system.

Conversely, divergence enables parallel processing by distributing single cone signals across multiple functional pathways for colour, contrast, and motion processing (Euler, Haverkamp, et al. 2014). Each cone photoreceptor must contact multiple bipolar cell types to support this parallel processing architecture. While the exact divergence ratios are not quantified in zebrafish, the diversity of bipolar cell connectivity subtypes suggests extensive divergence from individual cones. For instance, a single red cone likely contacts at least five different bipolar cell types: R-only cells (though rare, representing <1% of the population), RG cells (9% of bipolar cells), RGB cells (6%), RGBUV cells (11%), and mixed RGRod cells (24%) (Li, Tsujimura, et al. 2012). Similarly, green cones must diverge to G-only cells (5%), RG, RGB, GBUV (9%), and RGBUV types, plus several mixed rod-cone types (Li, Tsujimura, et al. 2012). This divergence pattern ensures that signals from each cone type are simultaneously processed through multiple parallel channels with distinct downstream targets.

Thus, convergence and divergence act in concert to create a rich set of feature channels that can be processed in parallel. A single BC may pool information from multiple photoreceptor types, according to systematic rules that depend on the BC-type and its presynaptic connections (Euler, Haverkamp, et al. 2014; Li, Tsujimura, et al. 2012). Conversely, a single photoreceptor is also contacted by multiple BCs, diverging the same input into multiple micro circuits. This convergence-divergence architecture establishes the spatiochromatic channels that provide the foundation for downstream spatial encoding.

1.3.4 Lateral interactions

While convergence and divergence establish the basic spatiochromatic channels through vertical pathway connections, lateral interactions modulate the signals within these channels through horizontal information flow within the retina. Lateral interactions refer to the pooling and contrasting of signals between neighbouring cells at the same retinal layer, fundamentally distinct from the feed-forward transmission of the vertical pathway.

Two classes of inhibitory interneurons mediate lateral interactions: HCs in the outer retina and ACs in the inner retina. HCs are specialised inhibitory interneurons that connect photoreceptors through electrical and chemical synapses, operating at relatively wide spatial scales through their electrically coupled networks (Chapot, Euler, and Schubert

2017; Chaya et al. 2017). ACs are interneurons that laterally connect BCs at multiple spatial scales, with wide-field GABAergic amacrine cells mediating long-range interactions and narrow-field glycinergic amacrine cells providing localised inhibition (Eggers and Lukasiewicz 2011). Blocking these pathways subsequently disrupts spatial and chromatic processing (Thoreson and Mangel 2012; Masland 2012b; Wang et al. 2023). HCs and ACs both shape visual processing through inhibitory modulation via GABAergic and glycinergic signalling.

Lateral interactions also include electrical coupling via gap junctions, allowing current to pass between cells. HCs networks prominently exhibit coupling in the OPL (Chapot, Euler, and Schubert 2017), but homotypic electrical coupling can be found at every layer of the retina (Völgyi et al. 2013; Trenholm and Awatramani 1995; Cook and Becker 1995). Although the functional significance of electrical coupling is not fully understood, it is thought to play a role in synchronising activity across neighbouring cells and enhancing spatial integration (Völgyi et al. 2013).

Classical theories of vertebrate spatial integration predict that lateral inhibitory circuits are essential for generating antagonistic RF structures (Marr, Hildreth, and Brenner 1980; Kuffler 1953). This is because lateral inhibition enhances contrast sensitivity, edge detection, and spatial resolution by creating antagonistic centre-surround RFs (Cook and McReynolds 1998). Additionally, they have been implicated in decorrelating redundant visual signals, enhancing the efficiency of information transmission (Franke, Berens, et al. 2017). Therefore, lateral interactions are thought to play a crucial role in shaping the spatial structure of RFs and enhancing the visual system's ability to extract relevant features from the visual field.

1.3.5 Feature encoding at vision's second synapse

The integration of On/Off polarity, spatiochromatic convergence patterns, and lateral interactions creates a diverse feature encoding system already at the second synapse of vision. Unlike simple relays, BCs actively synthesise multiple information streams through systematic mechanisms: they inherit spectral selectivity through specific convergence patterns, acquire spatial and spectral antagonism through lateral inhibitory circuits, and maintain temporal kinetics through graded responses.

17 morphologically distinct BC types have been identified in the zebrafish retina, each exhibiting unique dendritic field sizes, axonal stratification patterns, and photoreceptor connectivity profiles (Connaughton 2011). This is likely an undercount because it does not account for physiological properties such as glutamate receptor expression, synaptic kinetics, or lateral connectivity patterns. In fact, transcriptomics suggests 23 BC types exist, 21 of which are cone-BC (Hellevik et al. 2024). Their stratification patterns reveal important aspects of functional diversity, with chromatic and achromatic channels organised in distinct IPL sublaminae according to their feature encoding (Zimmermann et al. 2018). Via their morphological and functional properties, each BC type likely represents a specialised feature detection channel optimised for specific computational tasks.

Through spatiochromatic convergence, they generate diverse spectral channels including colour opponency, spectral selectivity, and broadband luminance pathways essential for tetrachromatic processing. Then lateral interactions mediated by GABA and glycine signalling implement contrast enhancement, edge detection, and decorrelation of redundant visual signals (Franke, Berens, et al. 2017). Individual BCs encode local contrast through centre-surround antagonistic configurations, detect edges and motion across multiple spatial scales (Vlasits et al. 2016), and represent chromatic opponencies through systematic spectral integration patterns (Bartel, Yoshimatsu, et al. 2021; Zhou et al. 2020). Thus, vertical and lateral processing in both the OPL and IPL act in concert to encode spatiochromatic features. This feature encoding at the second synapse of vision demonstrates that significant visual processing occurs within the retina itself, well before information reaches the brain.

1.4 Evolution

1.4.1 The evolution of the vertebrate eye

Spatial vision is virtually ubiquitous amongst animals, with only few exceptions. In fact, this is the functional purpose of the vertebrate eye cup, which evolved to enable image-forming vision about 500-600 million years ago (Lamb, Collin, and Pugh 2007). By placing photoreceptors inside a spherical cavity and collecting their outputs with spatially integrative horizontal cells, the retinae of early vertebrate ancestors were able to detect the direction of incoming light (Lamb 2013). Initially, resolution was undoubtedly poor, but lens evolution was completed by approximately 500 million years ago as evidenced by the camera-style eyes with functional lenses found in modern lampreys, whose lineage diverged from jawed vertebrates at this time (McCauley and Bronner-Fraser 2002). This established the basic vertebrate visual architecture that enables detailed spatial representation of the visual world.

This fundamental architecture has been conserved across vertebrate evolution (Figure 1.4), suggesting it emerged in the common ancestor of all vertebrates over 500 million years ago (Baden, Euler, and Berens 2020). Nevertheless, while the basic circuit organisation schema is shared across all vertebrate retinas, the circuit inputs have changed as vertebrate species lost and modified their ancestral cone identities (Bowmaker 1998; Baden 2024a). Consequently, the computational strategies implemented within these conserved circuits have also diverged.

For example, chromatic integration strategies are directly contingent on the opsin sensitivity of the photoreceptors, which may range from rod-dominated nocturnal mammals to the tetrachromatic systems found in many fish, birds, and reptiles (Thoreson and Dacey 2019). The specifics of circuit signalling are thus influenced by the animal's ecology and evolutionary history (Baden, Euler, and Berens 2020). The overarching architecture remains, but implementation details change to accommodate shifting ecological demands and physiological constraints. This raises important questions about which aspects of

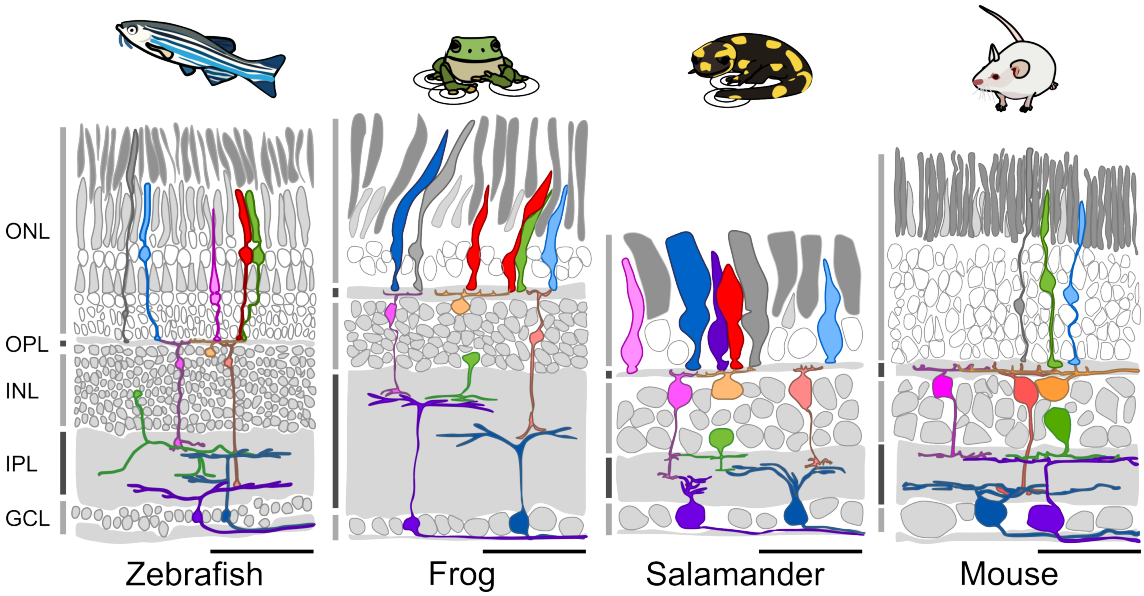

Figure 1.4: Cross-species comparison of retinal structure across aquatic (zebrafish), semiaquatic (frog, salamander), and terrestrial (mouse) species. Nuclear layers are marked in gray and plexiform layers in dark gray. The equivalent demarcations indicate the equivalent retinal layers in the other species. Note the identical neuron types across species. Gross morphology is remarkably conserved, although the details of the circuit implementations vary between species. Scale bar approximates 50 µm. Adapted from https://github.com/BadenLab/Free_to_use_vector_graphics.

retinal processing reflect universal principles of vision versus species-specific adaptations.

1.4.2 Cross-species validation and theoretical framework

Centre-surround antagonism appears to be such a universal principle. It has been identified across the retina in a smorgasbord of terrestrial vertebrate species from mammals such as cats (Enroth-Cugell and Robson 1966; Mcilwain 1964; Hubel and Wiesel 1962; Rodieck 1965), primates (Hubel and Wiesel 1960), and rabbits (Barlow and Levick 1965), to non-mammalian species including fish (Daw 1968; Kaneko 1970; Naka and Nye 1971; Saito, Kondo, and Toyoda 1979; Daw 1968), salamanders (Werblin and Dowling 1969; Werblin 1972; Borges and Wilson 1987), and turtles (Schwartz 1974; Richter and Simon 1975; Yazulla 1976; Ashmore and Copenhagen 1983; Adolph 1988). Based on these reports, spatial antagonism is present across species.

However, deviations have been reported. For example, Saito and Kujiraoka 1982 found carp BCs whose membrane potential only declined moderately as spots exceeded a diameter of 0.5 mm and continued to slightly decline up to the maximum spot size of 2 mm, suggesting an abnormally large and weak surround. In comparison, mouse BCs have centre diameters of only 43–67 µm (Berntson and Taylor 2000), with surround sizes reportedly between 100 and ca. 400 µm. In fact, Saito and Kaneko 1983 reports that 35 out of 54 tested BCs in the carp retina did not exhibit any degree of surround antagonism, such that the majority of cone BCs did not feature any detectable contribution from a RF surround (Saito and Kujiraoka 1982).

Saito and Kaneko speculate these findings may be erroneous due to experimental difficulty. Yet, they are not the only ones to identify surprisingly large and diffuse surround structures in teleost BCs. Table 1.1 summarises the reported stimulus sizes used to probe the surround in BC studies of aquatic and semiaquatic species. The large stimulus sizes, some exceeding millimetres, suggest a radically different ratio between centre and surround in aquatic species, compared to terrestrial mammalian species. Table 1.2 summarises the results of these studies and complements the findings with data from terrestrial mammalian species. The overarching trend indicates that the centre-surround antagonism is spatially broader in aquatic species such as carp and goldfish compared to terrestrial species like mice and primates. Semiaquatic species like salamanders and turtles show moderately large RFs, but still smaller than those of teleosts.

Table 1.1: Stimulus dimensions used in classical center-surround RF studies. Spot stimuli were used to evoke center responses, while annulus stimuli (with specified inner and outer diameters) were used to preferentially stimulate surrounds. N/A indicates stimuli not used in that study.

Species	Spot diameter	Annulus inner ø	Annulus outer ø	Citation
Carp	150 – 300 µm	150 µm – 800 µm	2000 µm - 4000 µm	Toyoda 1973
Carp	100 - 2000µm	N/A	N/A (spot only)	Saito and Kujiraoka 1982
Carp	100 µm	1200 µm	2500 µm	Shimbo et al. 2000
Carp	400 µm	600 µm	2000 µm	Saito and Kaneko 1983
Salamander	100 - 500 µm	100 - 1490 µm	2000 µm	Burkhardt, Bartoletti, and Thoreson 2011
Salamander	100 – 800 µm	N/A	N/A	Marre et al. 2015
Salamander	300 µm	700 µm	2000 µm	Zhang and Wu 2010
Turtle	100 - 1000 µm	400 µm	1600 µm	Schwartz 1974
Turtle	25 – 2500 µm	1000 µm	2500 µm	Richter and Simon 1975

Moreover, spatial nonlinearities have since been identified downstream in the surround of certain salamander Off RGCs, suggesting anisotropic sub-unit distribution and perhaps non-concentric BC RF organsiation (Takeshita and Gollisch 2014). Recently, Swygart et al. 2024 identified that alpha On RGCs in the mouse retina exhibit a surprisingly weak surround, despite a neighbouring On RGC type receiving the same inputs from BCs. These findings may indicate that while centre-surround organisation is indeed a common feature of vertebrate vision, there are notable exceptions and variations across cell types that should be taken into consideration. Perhaps centre-surround antagonism is not a universal principle, but rather a common feature of vertebrate vision that has evolved to meet the demands of spatial encoding in different environments.

1.4.3 Adaptations for spatial integration on land and in air

It is well established that vision needs to undergo evolutionary changes to transfer from water to air, or vice versa (Lamb 2013; MacIver et al. 2017; Swamynathan et al. 2003; Yoshimatsu and Baden 2024; Baden 2024b). For example, chromatic processing is known to differ between aquatic and terrestrial species, with terrestrial species typically exhibiting far simpler chromatic processing (Bowmaker 1998; Baden 2024a). The lens and cornea of terrestrial species are also adapted to refract light in air, while those of aquatic species are adapted to refract light in water (Swamynathan et al. 2003). Accordingly, one may expect the circuitry underlying spatial processing to also exhibit adaptations that reflect

Table 1.2: Center-surround RF measurements across vertebrate species. A horizontal line separates non-mammalian (above) from mammalian (below) species.
Abbreviations: E-phys. = Electrophysiology; 2P = Two-photon imaging; DA = Dark adapted; C.ø = Center diameter; S.ø = Surround diameter (all measurements in µm unless specified)

Common	Species	Type	C.ø	S.ø	Meth.	DA	N	Ref.
Carp	*C. carpio*	Off	150-300	Not specified	E-phys.	Yes	58	Toyoda 1973
Carp	*C. carpio*	On rod/cone	500 (est)	>2000 (est)	E-phys.	Yes	30	Saito and Kujiraoka 1982
Carp	*C. carpio*	Cone	Not specified	Not specified	E-phys.	Yes	59	Shimbo et al. 2000
Carp	*C. carpio*	Off	Not specified	Not specified	E-phys.	No	54	Saito and Kaneko 1983
Goldfish	*C. auratus*	Mixed	100-200	1000-1500	E-phys.	No	109	Kaneko 1973
Salamander	*A. tigrinum*	Cone	100-496	Not specified	E-phys.	No	31	Burkhardt, Bartoletti, and Thoreson 2011
Salamander	*A. tigrinum*	Colour opp.	600 (est)	800 (est)	E-phys.	Yes	135	Hare and Owen 1990
Turtle	*C. serpentina*	Mixed	100-200	Not specified	E-phys.	No	NR	Schwartz 1974
Turtle	*P. s. elegans*	Cone	150-200	>1250	E-phys.	No	91	Richter and Simon 1975
Mouse	*M. musculus*	Cone	67±16	Not identified	E-phys.	Yes	67	Berntson and Taylor 2000
Mouse	*M. musculus*	On	70 (est)	100-200 (est)	2P	Yes	4056	Strauss et al. 2022
Mouse	*M. musculus*	Mixed	56.1±10	255-410	2P	Yes	3540	Franke, Berens, et al. 2017
Macaque	*M. fascicularis*, *P. c. anubis*	Mixed	42-92	467-743	E-phys.	No	12	Dacey et al. 2000

these environmental pressures. However, this is underexplored and poorly understood.

Intriguingly, the morphology of dendritic arborisation in teleost BCs is on a comparable scale to those of terrestrial species (Figure 1.5), yet their spatial integration properties differ. For example, Saito and Kujiraoka 1982 show that dendritic fields of cone BCs in carp range between 47-147 µm with a mean of 90 ± 29 µm (SD). Nevertheless, membrane potential reduction, indicating surround inhibition, only occurred when stimuli exceeded 500 µm. This suggests a disproportionately large surround compared to those expected from mouse studies, despite the relative similarity in dendritic arbour size. Reported RF sizes in teleost are systematically far larger than those of rodents and primates (Table 1.2). Therefore implying that while the dendritic arborisation may be similar, the spatial integration properties of BCs in aquatic species are adapted to a different scale of spatial integration via lateral interactions.

Together, this hints at distinct spatial processing properties between aquatic teleosts and terrestrial mammals. Given that chromatic processing and optics change with territorialisation, it seems plausible that the underlying circuitry should also adapt to the new medium and environment. Supporting this notion, orthologs of the starburst ACs, a key component of lateral processing in mice, have now been identified in the zebrafish retina (Yoshimatsu and Baden 2024; Li, Yu, et al. 2024). This hints that lateral circuits are at least partially conserved across vertebrates, but that their implementation nuances have changed.

This proposal comes with a caveat. One must be careful in comparing studies across species and from different eras of research. Differences in experimental techniques, sample preparation, and analysis methods can introduce significant variability in reported RF properties. For example, the use of different stimulus sizes, light intensities, and recording techniques can all influence the measured RF size and shape. Therefore, while the trends observed in the literature suggest systematic differences in spatial encoding between aquatic and terrestrial species, these findings should be interpreted with caution.

This is further complicated by the lack of modern functional investigations of spatiochromatic RFs in aquatic species. While the morphology of BCs has been extensively studied in zebrafish, the functional properties of their RFs remain largely unknown. Most studies focus on a handful of identifiable types of cells, and the functional properties of BCs are often inferred from morphological data or indirect measurements. This limits our understanding of how each cell type contributes to spatial vision and how these contributions may vary across species. Therefore, while the morphological similarities between terrestrial and aquatic species suggest that the basic architecture is conserved, the functional properties of BCs and their role in spatial computation remain poorly understood.

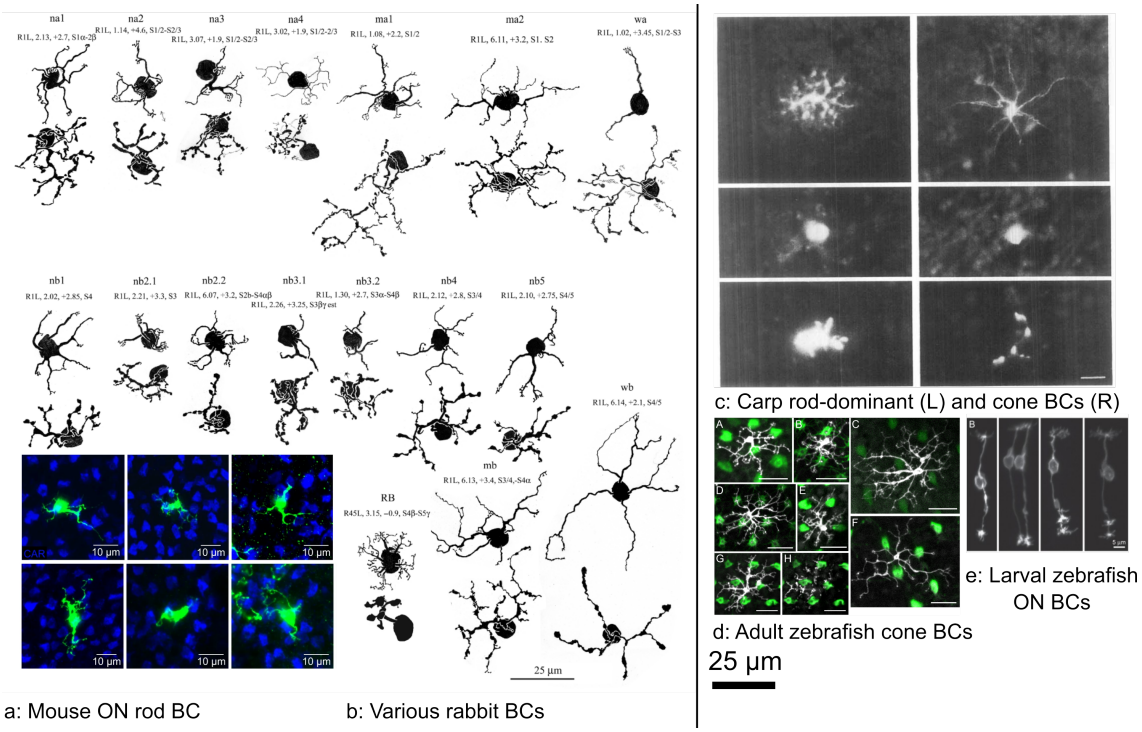

Figure 1.5: Example BC dendritic arbours in a terrestrial mammal (rabbit) and an aquatic species (zebrafish) from various studies, separated by black line. Figures manually scaled to 1:1. **(a)** Example mouse ON rod BCs from Hsiang et al. 2024, *AAV-Grm6-Cre* transfected BC in green and cone arrestin stain in blue. **(b)** 16 different types of Golgi-stained rabbit bipolar cell morphology from Famiglietti 2025 showing dendritic branching patterns. Scale bar 25 µm. **(c)** Dye-injected rod (left) and cone ON (right) BCs from Saito and Kujiraoka 1982 showing dendrites (top), cell body (middle), and axons (bottom). **(d)** Z-axis projection of dendritic tree of zebrafish cone BCs in transgenic zebrafish from Li, Tsujimura, et al. 2012. White shows EGFP-positive BC, green denotes SWS1 or SWS2 positive cones. Innset letters from original publication. Innset scale bar 10 µm. **(e)** Transverse view of maturing zebrafish cone BCs at 5 dpf from Schroeter, Wong, and Gregg 2006, showing *nyx::MYFP* positive BCs showing dendritic arbours at the top and immature terminals at the bottom.

1.5 Aims

Aim 1: Characterise the larval zebrafish bipolar cell RFs

Despite zebrafish being a model organism for vision research, surprisingly little is understood about how each cell type in the retina contributes to spatial vision. RF properties such as size, polarity, and morphology throughout retinal cells remain largely unknown. This thesis will establish the morphological characteristics of larval zebrafish BC RFs and provide the first systematic comparison with other vertebrate species. I will determine how centre-surround antagonism manifests in zebrafish BCs and quantify the spatial integration properties that underpin early visual processing in this aquatic model.

Aim 2: Identify potential chromatic biases in spatial integration

The tetrachromatic inputs from the outer retina may be leveraged in spatial computations, particularly given that the wavelength spectrum attenuates rapidly in water and aquatic

environments feature distinct spatial characteristics compared to terrestrial scenes. I will systematically characterise differences in RF size and colour integration between different BC types to establish how spatial integration varies across the tetrachromatic pathway. This analysis will reveal the extent to which chromatic channels exhibit distinct spatial integration patterns and determine whether spectral and spatial processing are interdependent at the BC level.

Aim 3: Evaluate spatial dependency of IPL organisation

The IPL stratification of BCs varies systematically with polarity and colour, but the relationship between stratification patterns and spatial integration properties remains unknown. I will determine whether the stratification pattern of zebrafish BCs terminals in the IPL correlates with their spatial integration characteristics. Specifically, I will establish whether BCs with different RF sizes or chromatic preferences exhibit distinct stratification patterns, and test whether spatially antagonistic cells stratify preferentially between the ON and OFF sublaminae. This analysis will reveal the organising principles that link morphological positioning to functional properties.

Aim 4: Establish the role of amacrine cells in IPL spatial processing

To achieve a mechanistic understanding of how amacrine cells shape RF properties, I will pharmacologically block lateral interactions and quantify the resulting changes in spatial antagonism. This pharmacological approach will establish the extent to which any centre-surround antagonism depends on horizontal or amacrine cell chemical interactions. By comparing spatial and chromatic properties before and during lateral circuit blockade, I will determine the specific contributions of lateral inhibition to BC RF organisation and identify the circuit mechanisms underlying spatial processing in the zebrafish outer retina.

2 | Methods

2.1 Animals

2.1.1 Husbandry

Research was conducted using transgenic zebrafish (*Danio rerio*). Fish were reared based on standard protocols of zebrafish care. All procedures were conducted in accordance with the UK Animals (Scientific Procedures) act 1986, and the UK Home Office guidelines. All persons involved in research are valid licence holders, and the procedures have been approved by the named individuals in the University of Sussex animal welfare committee under the establishment licences. Fish were housed at the zebrafish facility and kept on a 14:10 day/night cycle with gradually rising and falling light levels. Day-to-day care was completed by facility technicians. Fish were fed three to four times a day, depending on age. In agreement with the licences, fish were housed up to an age of 24 months.

2.1.2 Egg collection and rearing

One week prior to experiments, zebrafish were sexed and either paired or grouped into separated breeding tanks in the evening. Eggs were collected approximately at noon on the following day. Crossings were typically between AB wild type fish and *Casper* mutants; a pigment-deficient phenotype that lacks melanophores and iridophores (White et al. 2008). *Crystal* phenotype mutants (Antinucci and Hindges 2016) were occasionally used, but were not favoured due to poor yields. *Roy* were also used as approximately a quarter of their offspring exhibit the *Casper* phenotype (Antinucci and Hindges 2016; White et al. 2008). In-crossing was occasionally used when outcrossing failed, although outcrossing was preferred. Zebrafish bred for line maintenance were always outcrossed.

Eggs were collected the next morning. Tank water was strained to isolate eggs, which were then carefully rinsed in reverse osmosis (RO) water, and placed in 100 mm Petri dishes with approximately 50 mL of aquarium water. Water was exchanged daily for the first three days. Water was then exchanged as needed, typically every 1–3 days depending on water quality such as presence of fungi or excessive microorganism growth. Unfertilised eggs and malformed larvae were discarded continuously. To further prevent pigmentation, larvae were exposed to 200 µM phenylthiourea (PTU) (Karlsson, von Hofsten, and Olsson 2001). On the first day 0.5 ml of PTU was added to the dish, followed by 1 ml on every

water change.

Larvae were kept at 28.5 ℃ in a temperature-controlled incubator, on a 12:12 day/night cycle. Coinciding with egg yolk depletion and onset of feeding behaviours (see subsection 1.2.4), at 5 dpf onwards the larvae were fed at regular intervals with dry powdered food (Gemma Micro 75, Skretting). Previously, feeding was conducted less frequently, but this was observed by multiple lab members to result in the unreported effect of higher incidence of UV-dominant responses in the photoreceptors. Accordingly, food was added to dishes at least once a day, and a few hours prior to experiments.

2.1.3 Larval selection and screening

At 5–6 days post-fertilisation (dpf) larvae were selected for experiments. Imaging the retina requires phenotypes lacking pigmentation in the eye for optical access. Therefore, larvae with AB or *Nacre* phenotype were screened out, leaving *Crystal*/*Casper* phenotype larvae. Next, the remaining larvae were screened for genetic expression of the required fluorescence reporter. This was conducted under a bifocal epifluorescence with dichroic mirrors and filters allowing excitation of the target fluorophore. For nearly all transgenic lines used, the fish co-expressed a red heart marker (cmlc2-RFP) to simplify screening. In instances where no such marker was present, fish were instead screened for green fluorescent protein (GFP) within the retinal structures identified as a dim green light emanating from within the eyes. Larvae between 7–9 dpf were used for experiments.

2.2 Anaesthesia

For screening, larvae were anaesthetised with ethyl 3-aminobenzoate methanesulfonate, also known as Tricaine (Leyden et al. 2022). The solution was made up 400 mg of Tricaine powder (Sigma Aldrich, Cat. A-5040) in 97.9 mL double-distilled water, buffered with 2.1 mL M Tris (pH 9) to adjust the solution to approximately 7 pH. A few minutes prior to screening, 0.5 mL Tricaine solution was pipetted into the dish. In most instances this was suficient to seize movement. Occasionally, if movement still persisted, another 0.5 mL of Tricaine solution was added. Dosage never exceeded 1 mL. All larvae not discarded made full recovery from this procedure. Care was taken to screen fish the day prior to experimentation, to avoid any potential side effects of anaesthesia.

2.3 Sample preparation

Prior to imaging, larvae were mounted in a miniature aquarium (Figure 2.3). Chamber designs are based on those described in (Franke, Maia Chagas, et al. 2019), although simplified. First, a thin cover slide (24 x 50 mm, VWR) is glued onto a recessed slot in a 3D printed chamber (printed with a Prusa i3 MK3S+ printer, using Prusament PETG filament). Matte black filament was chosen where applicable in an effort to reduce reflections. The bracket is designed with the same dimensions as a conventional microscopy slide (75 x 25 mm). A 3D printed support bracket is then glued to the thin glass slide, to hold water

and agarose. Another coverslip is then snapped in half length-wise and glued to the side of the chamber. This window acts as an interface between air and water, allowing the fish to see through without distortion. Together, this forms a small water-tight chamber where the larvae can be mounted. Fish larvae exclusively respire via diffusion of oxygen through the skin before 11 dpf (Hughes, Zimmer, and Perry 2019; Jacob et al. 2002; Pelster and Burggren 1996). Thus, this chamber design is sufficient to provide a constant supply of oxygen.

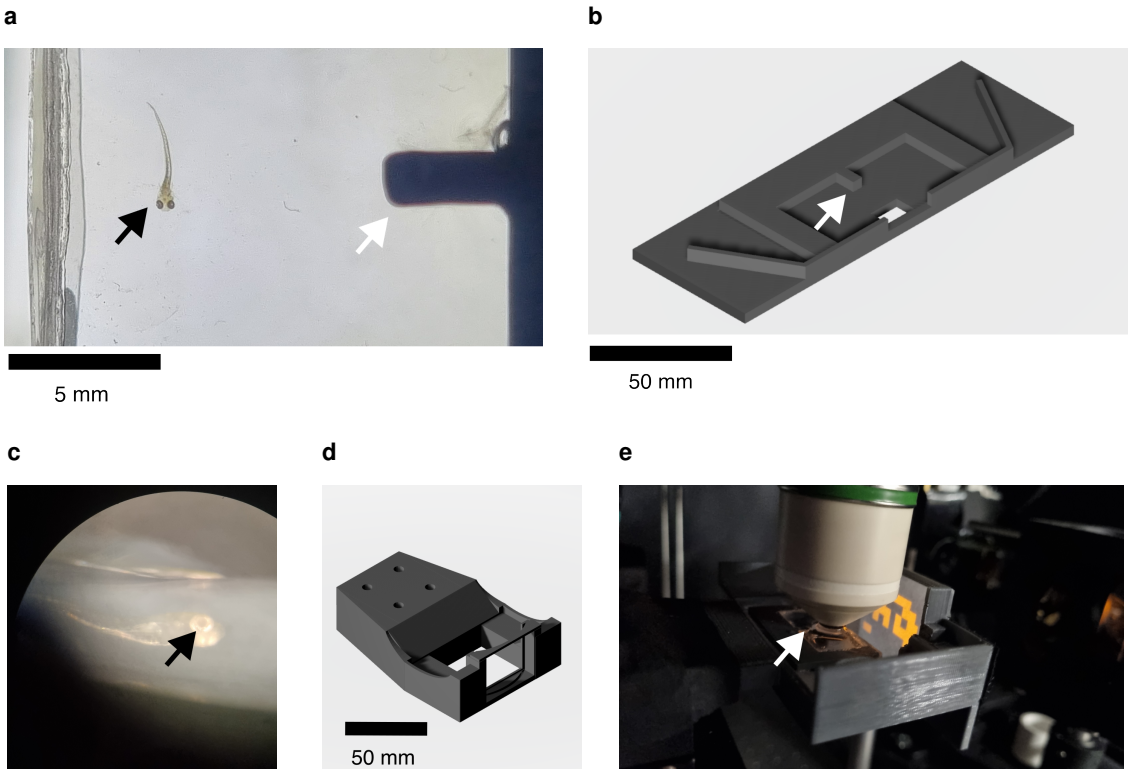

Figure 2.1: Sample preparation, mounting chamber, and cinema design. **(a)** 7-9 dpf zebrafish were mounted for monocular stimulation. For illustration, the sample was here mounted on a transparent slide. Black arrow shows the stimulated eye. White arrow shows a reference point on the chamber used for alignment such that the sample is centred on the stimulator area. **(b)** Chamber design, showing the same reference point as in **(a)**. The chamber is designed to block stray or ambient light from the perspective of the sample. **(c)** The sample as viewed through the glass window of the chamber using a stereoscope with 10x magnification, showing clear line of sight despite the agarose layer. **(d)** The design of the cinema, in which the sample preparations are mounted for imaging and stimulation. The cinema is designed to allow the objective to hover over the sample, while blocking stray or ambient light. **(e)** The final experimental assembly, showing the sample mounted in the chamber and placed in the cinema, with the objective positioned above the sample. White arrow denotes the common reference points between panels **(a)** and **(b)**. Zebrafish sample is too small to be visible in this image, but is positioned as in **(a)**.

Larvae are extracted from the Petri dish with a 3 mL pipette, and placed in a water droplet. Excess water is removed using a fine a 0.5 mL pipette, such that the larvae are only covered in a thin film of water. 1.5% agarose solution, constantly heated at 60 ℃, is extracted and allowed to cool for approximately 20 s before approximately 1 mL of solution is placed on the larvae. The larvae embedded in agarose is then picked up with a pipette before the solution solidifies, and transferred to the mounting chamber. Once deposited,

there is an approximately 60 s window before the agarose solution solidifies. During this time, the larva is manipulated with fine forceps or a probe under a stereoscope to ensure the larvae is in the correct position and orientation, with one eye looking out of the chamber window. The fish were mounted at a slight upwards angle to facilitate imaging, allowing for monocular stimulation with optical access for microscopy. Additional warm agarose was added between the solidifying agarose droplet and window, in effort to further reduce distortions due to medium change. Finally, the remaining space in the chamber is filled with water from the fish tanks. The low concentration of agarose is sufficient to allow diffusion of oxygen, and does not have any discernable optical properties that differ from water once submerged.

2.4 Pharmacology

2.4.1 α-bungarotoxin injection

After fish were mounted, oculomotor movements must be removed to ensure a constant fixation point and facilitate imaging over the same field of view (FOV). For this purpose, α-bungarotoxin (α-BTX), an antagonist of nicotinic acetylcholine receptors (nAChRs), was injected into the extraocular muscles behind the eye. This prevents acetylcholine from binding to nAChRs postsynaptically at the neuromuscular junction, in effect causing local and irreversible paralysis. α-BTX was diluted from a 10 x stock (2.5) of 1 mg α-BTX in 50 µL of PBS pH 7.4. The dilutant buffer was made of 3 volume parts 0.1 M KCl and 1 part phenol red. The α-BTX solution was diluted to a ratio of 1:9 injection buffer.

A glass micropipette was pulled from a borosilicate glass capillary (World Precision Instruments, 1.5 mm outer diameter, 0.86 mm inner diameter) using a micropipette puller (Narishige PC-10). The resulting micropipette had a tip diameter of approximately 65 µm, easily piercing tissue with minimal damage. The micropipette was then loaded with 2.5 µL of the α-BTX solution using a 20 µL loading pipette (Eppendorf).

Injections were done at approximately a 45° angle from above the agarose-embedded animal. The micropipette was inserted approximately 10-20 µm into the tissue between the eye and the skull, aiming for the extraocular muscles. A micromanipulator was used to control the position of the micropipette. The injection volume was approximately 2 nL, and was delivered by an OpenSpritzer (Forman et al. 2017). Given stimuli were monocular, injection behind only the relevant eye was appropriate. The injection was performed under a stereo microscope, and care was taken to avoid damaging the eye or piercing the brain. This procedure was sufficient to stop eye movements in nearly all cases. Occasionally, particularly bright and transient stimuli would still result in the extraoccular muscle twitching, in which case the injection was repeated.

2.5 Transgenics

2.5.1 RibeyeA:SyjGCaMP8m

The majority of experiments were carried out with transgene *RibeyeA:SyjGCaMP8m*, in order to investigate the spatiochromatic integration of information in bipolar cells. This transgenic line was previously used for similar experiments in Wang et al. 2023. Expression was characterised by the presence of the genetically encoded calcium indicator GCaMP in the pre-synaptic terminal of the bipolar cell. The *Ribeye* gene is associated with synaptic ribbons (Schmitz, Königstorfer, and Südhof 2000; Magupalli et al. 2008), and *RibeyeA* specifically labels bipolar cell terminals (Wan, Almers, and Chen 2005). Thus, it is a convenient site for detecting calcium signals related to cell output.

In short, GCaMP consists of a GFP protein bound to a calmodulin (CaM) protein in such a way that the GFP emits more light when bound to Ca^{2+} due to a conformational change of the CaM protein (Nakai, Ohkura, and Imoto 2001; Chen et al. 2013). Ca^{2+} influx into the synapse is associated with neurotransmitter release (Südhof 2012), thereby acting as a proxy for neuronal activity. jGCaMP8m is a fast, modern variant of GCaMP delineated by a rapid rise and a moderate fall in fluorescence, which nonetheless is nearly tenfold faster than previous generations of GCaMP (Zhang, Rózsa, et al. 2023). The flurophore used here is a synaptophysin-bound variant of jGCaMP8m, restricting expression to synaptic terminals (Dreosti, Odermatt, et al. 2009; Broussard et al. 2018). Hence, *RibeyeA:SyjGCaMP8m* allowed the detection of bipolar cell output *in vivo*.

2.5.2 trb2:SyGCaMP6f

In pilot experiments, tg(*thyroid hormone receptor β2 (trb2):SyGCaMP6f*) was used. Here, the goal was to use the photoreceptors as a read-out of where light scatters and focuses within the retina. For this purpose, we selected a line with GCaMP expression under the promoter for trb2. trb2 is required for differentiation of cone photoreceptor progenitors to express long-wavelength sensitive (LWS) opsin (Ng et al. 2001; Angueyra et al. 2023). In zebrafish, this effectively targets the red cones exclusively (Deveau et al. 2020; Nelson et al. 2022; Suzuki et al. 2013; Balraj, Yoshimatsu, and Nelson 2016). Red cones were chosen because LWS-opsin features the widest encoding range (Endeman, Klaassen, and Kamermans 2013), their opponency to other colours are inherently miniscule (Bartel, Yoshimatsu, et al. 2021), and blocking lateral signalling with 6-cyano-7-nitroquinoxaline-2,3-dione (CNQX) should result in secession of remaining opponency. Thus, allowing estimation of chromatic aberration.

TODO: Decide if I want to include, or whether the data is enough to demo PR RFs

2.5.3 cx55.5:nls TrpR

In a handful of experiments tg(*cx55.5:nls TrpR tUAS:SFiGluSnFR*) was used. Here, a glutamate indicator with extremely fast kinematics was used (Marvin et al. 2018). *cx55.5*

is expressed on the horizontal cell dendrites encoding Connexin55.5 (Ul-Hussain et al. 2008; Chapot, Euler, and Schubert 2017), and as such *SFiGluSnFR* fluoresces in the presence of glutamate post-synaptic to the photoreceptors. This was only used in pilot experiments to probe the plausibility of mapping RFs of individual photoreceptors directly.

2.6 Microscopy

All imaging was performed on a custom-built two-photon fluorescence microscope (Janiak et al. 2022) based on the previously established Eyecup-scope design (Euler, Hausselt, et al. 2009). The system employed a floating, movable objective (Sutter MOM) and was equipped with a mode-locked Ti:Sapphire laser (Coherent ChameleonVision-S) serving as the excitation source. Images were acquired using a water immersion objective (Zeiss W Plan-Apochromat 20x/1.0 DIC M27). For GCaMP8m imaging, the excitation wavelength was tuned to 920 nm. Emitted photons were filtered through a 527 nm bandpass filter (ET527/70 M-2P) and collected via GaAsP photodetectors (H10770PA-40, Hamamatsu), which were subsequently upgraded to H11526-20-NF (Hamamatsu) detectors during the course of experiments. In early experiments, PMT signals were amplified using a Thorlabs TIA60 amplifier with an input noise floor of 4.8 pA/Hz$^{1/2}$. This was since upgraded to the low-noise current amplifier (SR 570, Stanford Research Systems) with an improved input noise floor of 5 fA/Hz$^{1/2}$, representing a substantial overall improvement in signal-to-noise performance.

Image acquisition was controlled by ScanM, a custom-written software package implemented in IGOR Pro 6.3 (WaveMetrics) running on a Windows machine. Acquisition parameters were adjusted according to experimental requirements. Typically, the configuration was 128 × 64-pixel images captured at 15.625 Hz, resulting in scan fields of approximately 50–60 µm across at 2.5 times digital zoom. Scan configuration varied depending on the specific experiment, with careful attention paid to ensuring that acquisition frequency always exceeded the Nyquist frequency of presented stimuli to prevent aliasing artifacts. This setup enabled quantification of neuronal responses from genetically encoded fluorescent proteins expressed in specific retinal cell populations *in vivo*.

2.7 Visual stimulation

2.7.1 Design

Visual stimulation was delivered using an arbitrary-spectral stimulator based on Lightcrafter (LcR) 4500 projectors as described in (Franke, Maia Chagas, et al. 2019). This system (Figure 2.2) employs two coupled LcRs configured as RGB and UV projectors, addressing the limitations of traditional LCD screens which cannot emit ultraviolet light while maintaining high spatial resolution. The system utilizes custom LED banks fitted with specific LEDs targeting zebrafish opsin sensitivities: a red LED (588 nm, B5B-434-TY Roithner), green LED (470 nm, SMB1N-D470-02 Roithner), blue LED (420 nm, SMB1N-420H-02 Roithner),

and UV LED (365 nm, LZ1-10UV0R-0000 OSRAM). Each LED was placed behind a matched band pass filter (FF01-586/20 (Semrock), ET480/40x (Chroma), ET420/40m (Chroma), and FF01-932 370/36 (Semrock), respectively) to narrow the spectral output further.

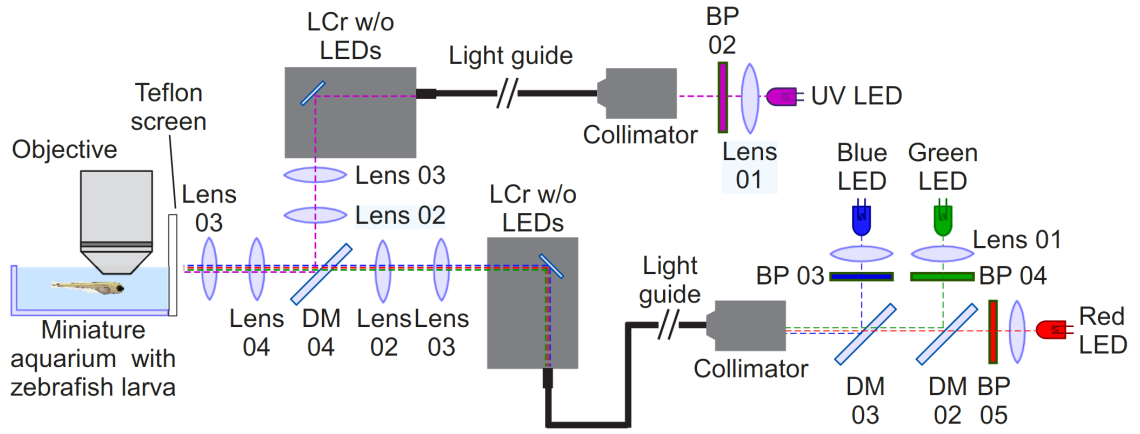

Figure 2.2: Tetrachromatic stimulator optical schematic, figure from Franke, Maia Chagas, et al. 2019. The system employs two LcR 4500 projectors configured for RGB and UV light delivery. Custom LED arrays (red: 588 nm, green: 470 nm, blue: 420 nm, UV: 365 nm) are coupled through light guides and collimators, with dichroic mirrors (DM) combining the optical paths. Bandpass filters (BP) ensure narrow spectra, whilst lenses focus the combined light through the projection system onto a tracing paper canvas adjacent to the zebrafish preparation in the miniature aquarium. The optical path is synchronized with two-photon scanning to prevent PMT interference.

a **b** **c**

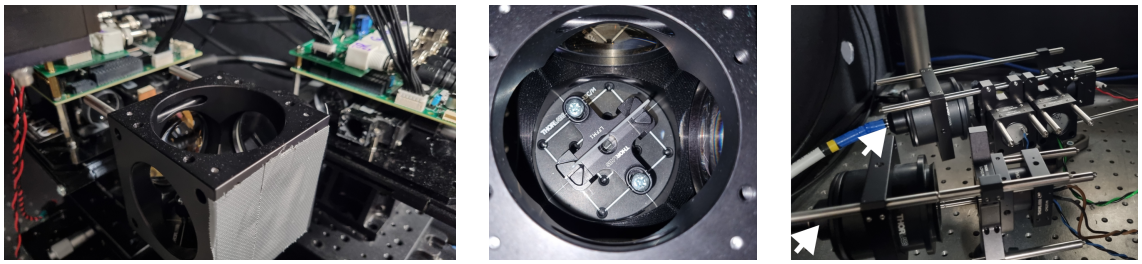

Figure 2.3: Microscope and stimulator setup. (a) The stimulator setup from within the microscope cage, showing the two LcRs in the background and the dichroic mirror in the foreground. The dichroic mirror is used to combine the outputs of the two LcRs into a single beam. **(b)** View of the dichroic mirror cube in **(a)** (DM04 in Figure 2.2). **(c)** The LED banks used for visual stimulation. Two LED banks are used, one for the RGB LcR and one for the UV LcR. Arrows show light guides that each lead to one of the LcRs. LED banks are positioned outside the microscope cage to avoid light bleed.

To eliminate cross-talk between the photomultiplier tube (PMT) and stimulator, LEDs were synchronized using a TTL blanking signal from ScanM, preventing LED activation during the galvanic mirror scanning phase and thus avoiding light artifacts on the PMT. The projector outputs were combined using a dichroic mirror and projected onto a 160 mm by 300 mm canvas fashioned from tracing paper and positioned adjacent to the zebrafish preparation.

2.7.2 Spectral calibration

LED output power was calibrated to match the natural photic environment of zebrafish prior to experimental recordings. This calibration ensured stimulus intensities and spectral content remained ecologically relevant to the zebrafish visual system (Nevala and Baden 2019; Zimmermann et al. 2018). Moreover, it has been observed that high-intensity UV stimulation could suppress the responses of other photoreceptors and subsequently silences other parts of the visual system (Zhou et al. 2020). Thus, necessitating careful power control of the UV LED. Together, these considerations ensured that the visual stimuli were biologically relevant and did not induce aberrant responses in the zebrafish retina.

TTL synchronisation as described above resulted in pulse width modulation (PWM) of LED emission. This was compounded by pre-existing differential PWM across RGB channels due to the LcR's digital light processing chip optimisation for human colour perception. Hence, all calibration steps were performed while the microscope was scanning at the same rate as during experimental recordings, ensuring that the calibration reflected the actual conditions under which cellular responses were recorded.

Spectral calibration commenced with measurement of individual LED output spectra using a calibrated spectrometer (Thorlabs CCS200/M) positioned at the LcR output to verify alignment with zebrafish opsin absorption spectra (Zimmermann et al. 2018; Nevala and Baden 2019; Yoshimatsu, Bartel, et al. 2021). Peak emission wavelengths were recorded for subsequent reference during power calibration procedures.

Power measurements were then conducted using a calibrated power metre (Thorlabs PM100D) positioned corresponding to the zebrafish eye location, approximately 160 mm from the projector output. All measurements employed 250 ms integration periods with real-time monitoring via Thorlabs software. To ensure measurement accuracy under experimental conditions, all calibrations were performed during active scanning with TTL blanking signals engaged, accounting for the asymmetric brightness reduction caused by LED PWM.

Power adjustment followed a systematic hierarchical protocol: red LED output was set to its maximum output allowed by the LED driver, through forward voltage adjustment. This was approximately 0.8 $\mathrm{mW\,cm^{-2}}$ measured from the position of the sample (Figure 2.4b) and 1.2 $\mathrm{mW\,cm^{-2}}$ as measured in front of the screen (Figure A.1). Measurements were sensitive to probe placement, hence some variability. Subsequently, remaining channels were calibrated to a ratio of 1:0.5:0.25:0.125 (R, G, B, UV) relative to the red channel Figure 2.4. The complete calibration procedure was repeated throughout the project to account for potential LED ageing, thermal drift, or environmental variations, ensuring consistent spectral alignment with zebrafish opsin absorption spectra as demonstrated in Figure 2.4a.

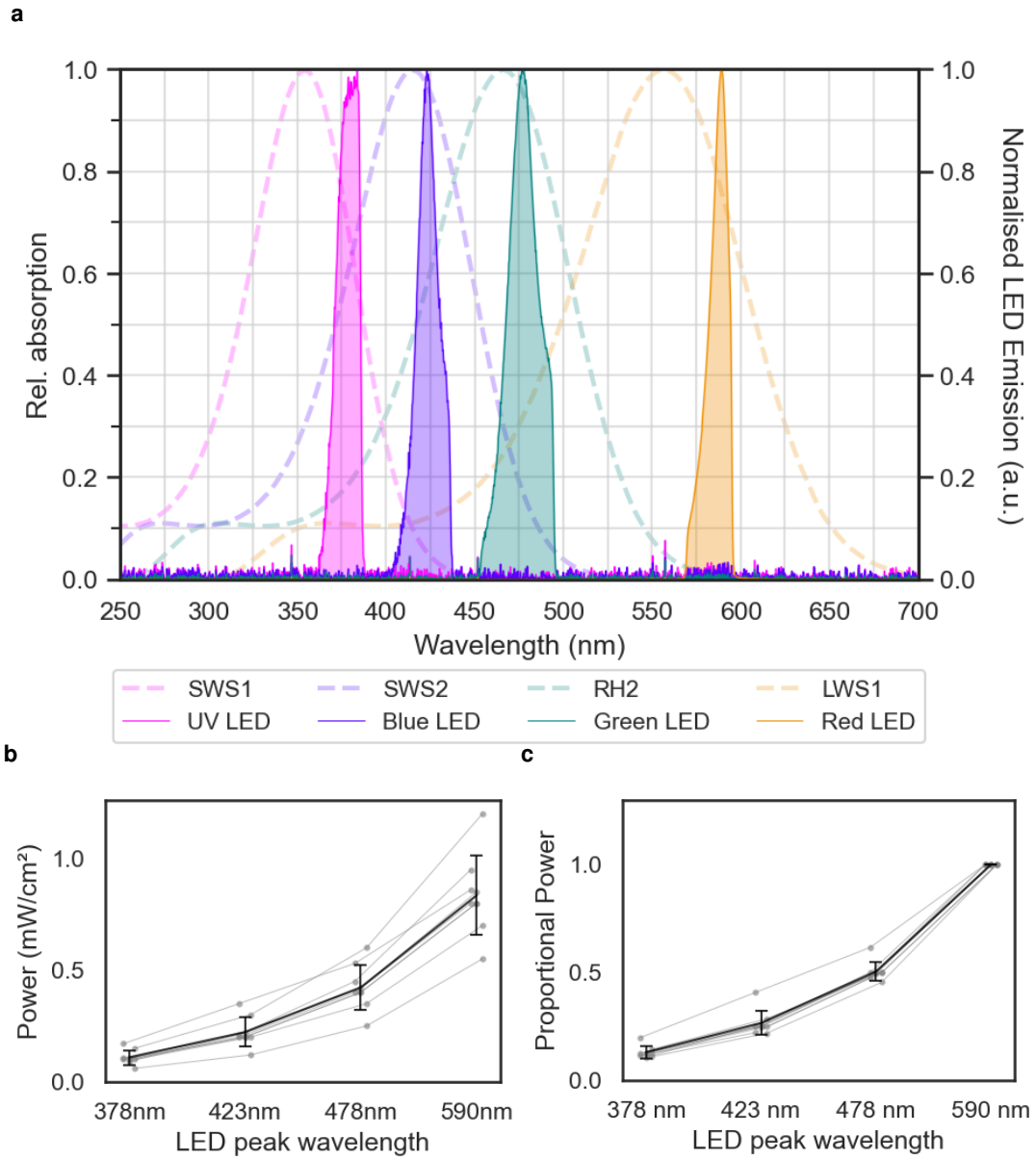

Figure 2.4: LED characterisation and power calibration. **(a)** LED spectrometer measurements. The figure shows the spectral output of the LEDs used for visual stimulation, with the red LED (588 nm), green LED (470 nm), blue LED (420 nm), and UV LED (365 nm) highlighted. The spectral sensitivity curves of zebrafish photoreceptors are overlaid for comparison, illustrating the alignment of the LEDs with the opsin absorption spectra. Note that amplitudes are arbitrary (normalised to 1) for illustration, and do not represent the actual power output of the LEDs. **(b)** Absolute power output (mW cm^{-2}) for each LED wavelength showing individual session measurements (faint grey lines) and average power output (bold lines, mean ± SD). UV LED: 0.11 ± 0.03 mW cm^{-2}, B LED: 0.22 ± 0.07 mW cm^{-2}, G LED: 0.42 ± 0.10 mW cm^{-2}, R LED: 0.83 ± 0.18 mW cm^{-2} (n=9). **(c)** Same data normalized to the red channel to illustrate the proportional LED ratios used for calibration (target ratios: UV:B:G:R = 0.125:0.25:0.5:1). UV LED: 0.13 ± 0.03, B LED: 0.27 ± 0.06, G LED: 0.50 ± 0.04, R LED: 1.00 ± 0.00. Additional measurements taken in front of the projection screen are provided in (Appendix Figure A.1).

2.7.3 Spatial calibration and alignment

With two projectors, careful alignment of their projections was essential to ensure that visual stimuli were presented correctly without offsets or misalignments. Care was taken to minimise chromatic aberration, which occurs when different wavelengths of light focus at different points, leading to fringing and distortion.

Each projector was equipped with a movable lens, allowing for fine adjustments of focus and alignment. Additionally, each projector was mounted on a movable XYZ stage allowing fine positioning of the projections to facilitate alignment. The dichroic mirror cube could be rotated, allowing for coarse alignment of the projectors.

The alignment procedure began with coarse alignment by rotating the dichroic mirror cube such that the red and UV channels roughly overlapped when displaying a full field. The projectors were then aligned by displaying an interlacing pattern of red and UV boxes, and the lenses were moved such that the red and UV channels were mostly aligned and boxes were uniform sizes without distortion. Finally, fine alignment was performed using the same pattern whilst moving the projectors on their XYZ stages. The goal was to ensure that the red and UV boxes perfectly interlaced, with no distortions or overlap (Figure 2.5). The procedure was repeated at the beginning of every imaging session to maintain alignment.

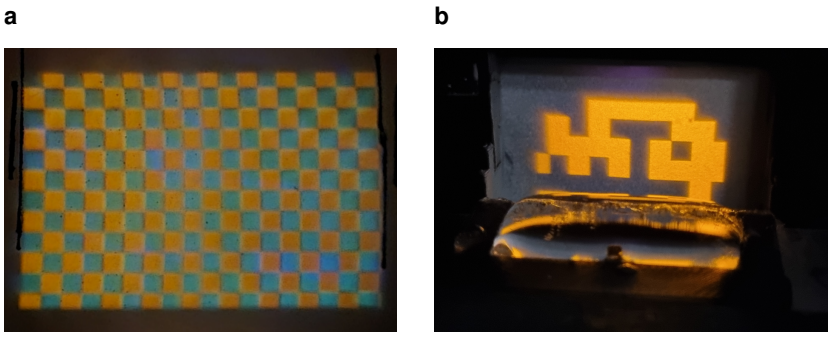

Figure 2.5: Projector alignment demonstration. (a) Interlacing pattern of red and UV channels showing successful alignment with uniform, non-distorted boxes. **(b)** Spatial centering verification showing the aligned projection relative to the zebrafish preparation in the imaging chamber.

2.8 Stimulus design

Stimuli were designed and presented using the open-source software QDSpy (http://qdspy.eulerlab.de/), implemented in Python and supporting up to 6 arbitrary colour channels. The system was configured such that stimuli were distributed across both LcRs, with RGB channels on one projector and UV on the other. Colour and intensity of QDSpy's arbitrary stimulus objects were controlled by scripts and displayed through the LcR's digital light processing chip. Together, this system enabled rapid prototyping of stimuli and adjustment of stimulus parameters such as durations and colour intervals to accommodate various experimental protocols while maintaining consistency for direct

comparability across recordings.

2.8.1 Basic stimulus parameters

For spatiotemporal receptive field (STRF) characterisation, we employed white noise stimuli presented as spatially randomised chequerboards optimised for two-photon calcium imaging constraints. Chequerboard stimuli were displayed at 60 Hz on a screen comprising approximately 54° × 86° visual angle, with larvae positioned 16 mm from the display surface. The temporal update frequency was standardised to 5 Hz to balance stimulus variation with calcium indicator dynamics. Each chequerboard frame was constructed with spatially uniform random contrast distribution, where individual pixels were assigned either 0% or 100% contrast with equal probability, ensuring that the temporal average across all frames approached 50% contrast (Chichilnisky 2001). Each experimental session presented up to 30,000 unique stimulus frames, though practical imaging constraints typically limited recordings to approximately 15,000 frames due to photobleaching considerations, tissue viability, and sample drift.

2.8.2 Super-resolution enhancement

We implemented a recently developed super-resolution approach to overcome spatial sampling limitations (Pamplona et al. 2022). Each chequerboard frame was systematically jittered on an underlying lattice, with spatial shifts corresponding to 25% increments of the chequerboard's spatial frequency. This technique effectively increases the spatial resolution of RF estimates by providing sub-pixel sampling precision, which is particularly advantageous when using larger spatial frequencies that might otherwise undersample fine RF structure (Pamplona et al. 2022; Gupta, Młynarski, Symonova, et al. 2022). Detailed information can be found in chapter 3 subsection 3.2.3, and specific stimulus parameters are given in each following chapter.

2.8.3 Chromatic variants

Stimuli were presented in multiple chromatic configurations to probe colour-specific processing. Primary experiments utilised alternating monochromatic chequerboards in red, green, blue, and UV. The colour sequences were not randomised, but rather presented in a fixed order under the assumption that the retina would not adapt to colour patterns, especially since the spatial content varied randomly. We did however see adaptation to a given colour within its epoch. Hence, a chromatic epoch of 100 frames (20 s) before switching to the next colour channel was chosen for all RF mapping experiments with alternating chromatic content. Although pilot experiments explored bichromatic stimulus combinations (red-green, red-UV), monochromatic presentations were adopted for the majority of experiments to facilitate linear interpretation of chromatic integration mechanisms.

2.9 Data processing

2.9.1 Fluorescence pre-processing

Acquired two-photon imaging data were pre-processed using ret_preproc (https://github.com/eulerlab/ret_preproc), which serves as the backbone for loading ScanM-acquired data and contains core pre-processing and analysis tools implemented in Igor Pro. Additional analysis procedures were performed using the Baden Lab OS scripts collection (https://github.com/BadenLab/Igor_scripts), which has diverged from the original ret_preproc analysis components following continued development. The pre-processing pipeline consisted of the following sequential operations:

1. **Data import:** Raw imaging data and trigger channel information were loaded into IGOR Pro using ScanM acquisition software.
2. **Detrending:** A detrending algorithm was applied to by fitting a logarithmic decay function to the temporal dimension and subtracting it to account for calcium indicator bleaching during the experiment.
3. **Stimulus synchronisation:** The trigger channel was binarised to provide a one-dimensional readout of stimulus timing at line-speed, ensuring precise alignment of visual stimulation with image acquisition.
4. **Motion correction:** To mitigate spatial drift, images were registered using a rigid registration algorithm that compared pixel values frame-by-frame, aligning each frame with the previous frame to maintain consistent spatial coordinates throughout the recording.
5. **Responding cell identification:** Correlation metrics were calculated over time across the imaging stack to identify responding bipolar cell terminals, with these metrics serving as thresholds for subsequent region of interest (ROI) determination.

2.9.2 ROI placement and signal extraction

ROI placement was performed manually, as standard automated methods often merged neighbouring cells and produced mixed fluorescence readouts. ROIs were positioned using a correlation map, calculated as the mean correlation between each pixel's time series and all neighbouring pixels, supplemented by visual inspection of the average projection.

The correlation map highlighted regions of high temporal correlation, identifying active terminals, whilst the average projection provided spatial context for terminal boundaries. For terminals with low activity, the correlation map provided insufficient contrast, but the average projection enabled identification of terminal locations that could still yield spatiotemporal RFs from sparse responses over extended recording periods (e.g., 10 minutes).

Where terminal boundaries remained ambiguous, ROIs were positioned to maximally separate suspected terminals, avoiding spatial summation that could artificially inflate RF complexity. This approach ensured that fluorescence traces reflected individual bipolar cell activity rather than mixed signals from multiple terminals.

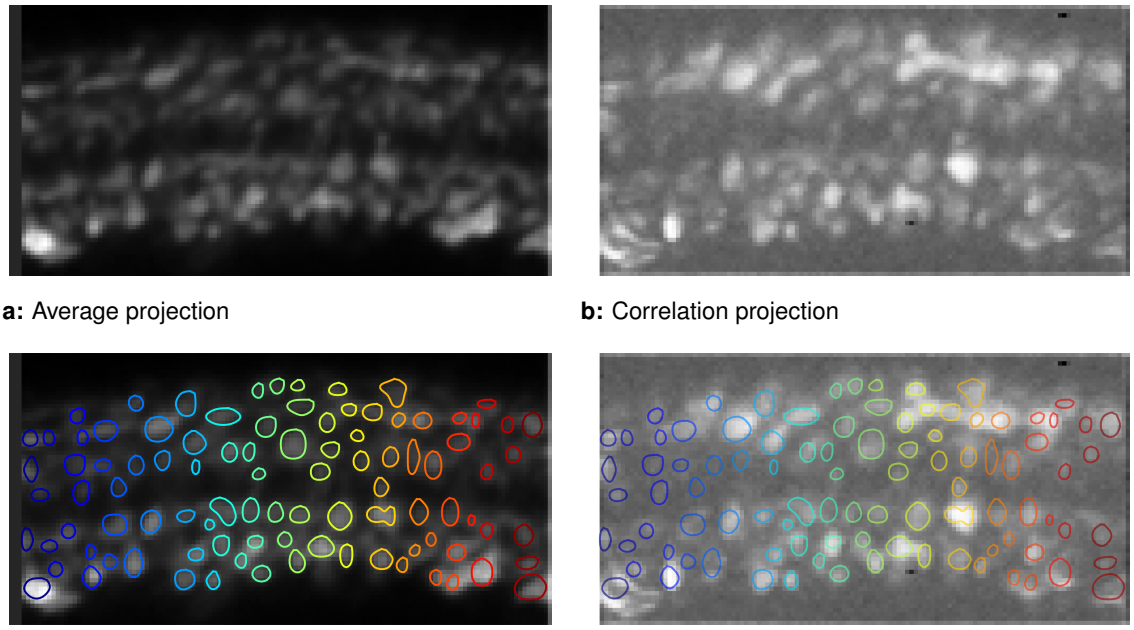

a: Average projection

b: Correlation projection

c: Average projection with ROIs

d: Correlation projection with ROIs

Figure 2.6: Example imaging stack projections and ROI placement. The figure illustrates the manually placed ROIs. **(a)** Average projection of the imaging stack, showing the overall fluorescence distribution across the stack. This clearly shows the bipolar cell terminals in the retina. **(b)** Correlation projection of the imaging stack, highlighting regions of high correlation between pixels, aiding in the identification of active bipolar cell terminals. **(c)** Average projection with manually placed ROIs, each encompassing an individual bipolar cell terminal. The ROIs are drawn to exclude neighbouring terminals, ensuring that fluorescence traces reflect the activity of individual cells. **(d)** Correlation projection with ROIs, illustrating the same ROIs placed on the correlation map.

2.9.3 Fluorescence post-processing and analysis

Following ROI placement, fluorescence traces were extracted and Z-scored to enable comparison across cells and experimental sessions. Z-scoring was performed using the mean and standard deviation calculated from a baseline period (minimum 10 seconds, extended when possible) during which no visual stimulus was presented. This yielded normalised traces with zero mean and unit variance during baseline, with stimulus-evoked responses expressed as standard deviations from baseline fluorescence. This approach follows established calcium imaging protocols (Bartel, Yoshimatsu, et al. 2021; Wang et al. 2022; Yoshimatsu, Schröder, et al. 2020).

Post-processed fluorescence data were analysed using Pygor, a custom Python package extending the IGOR Pro workflow. Pygor imports H5 files from the OS scripts pipeline, employing dataclasses for batch processing across experimental sessions. The package includes modules for data visualisation, statistical analysis, and STRF

analysis of multidimensional RFs with spatial, temporal, and chromatic components (https://github.com/simbru/pygor). Analysis employed standard Python libraries: Matplotlib and Seaborn for visualisation, scikit-image and scipy.ndimage for image processing, Numpy and Pandas for data manipulation, and Scikit-learn for dimensionality reduction and clustering, and Napari for interactively exploring multi-dimensional data.

2.9.4 Statistical analysis

Statistical analysis employed scipy.stats and statannotations libraries. For STRF analysis, bootstrap testing assessed RF significance across spatial and temporal dimensions. Statistical significance was set at $p < 0.05$ using two-tailed tests. Data were assessed for normality, heteroscedasticity, and independence assumptions, with parametric or non-parametric tests selected accordingly (Field 2007). Specific analyses are detailed in relevant results sections.

2.9.5 RF mapping

Spatiotemporal RFs were mapped using a novel (CCA) algorithm developed specifically for calcium imaging data. Unlike traditional spike-triggered averaging approaches, CCA leverages the graded nature of calcium signals directly, cross-correlating each stimulus pixel's temporal history with fluorescence traces to generate spatiotemporal RFs. This approach circumvents the need for spike deconvolution whilst maintaining sufficient temporal precision to capture bipolar cell response dynamics at 5 Hz stimulus presentation rates.

The method enables systematic analysis of chromatic integration across multiple spectral channels using calcium imaging, providing population-level spatial sensitivity maps that complement single-cell electrophysiological approaches. This enables linear characterisation of spatial and chromatic integration properties across multiple spectral channels. Post-processing includes automated centre-surround segmentation (see chapter 3), quality control, and standardised output formatting for systematic analysis across experimental sessions.

Detailed methodology and implementation specifics are provided in Chapter 3, with software available at: https://github.com/simbru/pygor/tree/main/src/pygor/strf.

3 | In-Vivo Estimation of Bipolar Cell RFs Using Calcium Imaging and Correlation Analysis

3.1 Introduction

3.1.1 Background

Bipolar cell spatial properties have been characterised across various vertebrate species using methodologies that have evolved substantially over the past century. As described in chapter 1, pioneering studies employed single-cell electrophysiology with simple stimuli displayed through various projector setups (Talbot and Kuffler 1952; Saito, Kondo, and Toyoda 1979). However, bipolar cells have remained notoriously difficult to investigate, with experiments generally having low throughput. Schreyer and Gollisch 2021 attributes this disparity to several practical challenges: bipolar cells sit in an anatomically inconvenient position in between photoreceptor and ganglion cell layers, their small cell bodies make intracellular recording difficult, and they signal mostly through graded potentials rather than more easily detectable action potentials.

White noise RF mapping protocols and multi electrode arrays have substantially improved throughput compared to traditional single-cell approaches whilst maintaining spatial precision (Spira and Hai 2013; Pamplona et al. 2022; Gupta, Młynarski, Sumser, et al. 2023; Field et al. 2010). However, electrode arrays cannot capture bipolar cell potentials due to their anatomical location. Despite methodological advances, bipolar cells have received considerably less attention than photoreceptors and ganglion cells. However, the development of two-photon microscopy and genetically encoded calcium indicators have created new opportunities for *in vivo* investigation of retinal circuits, allowing investigation of retinal processing in an intact animal.

Here, we present a novel approach for the *in vivo* estimation of bipolar cell RFs using calcium imaging and reverse-correlation analysis. By employing opsin-targeted shifting coloured binary noise, we aim to extend the existing characterisation of larval zebrafish bipolar cell RFs. We demonstrate that CCA can effectively extract spatiotemporal RFs

from calcium imaging data, revealing distinct spatial and temporal patterns of activity in response to chromatic stimuli. This approach provides a powerful tool for investigating the functional properties of bipolar cells in the intact retina, offering insights into their role in early visual processing.

3.1.2 Motivation

A handful of *in vivo* studies have estimated bipolar cell RFs in zebrafish larvae using two-photon calcium imaging, yet no assessment of the relationship between space and colour integration has been conducted. Antinucci and Hindges 2016 used moving bars and gratings to demonstrate orientation tuning in some bipolar cell terminals. They used a commercially available LCD screen with unspecified wavelengths. Johnston, Seibel, et al. 2019 employed filtered back projection for rapid RF mapping (Johnston, Ding, et al. 2014), showing that some bipolar cells exhibit elongated RFs sufficient to generate weak orientation selectivity. This study used a single wavelength (red, wavelength unspecified) from a commercial projector at relatively dim light levels (12.7 $\mathrm{nW\,mm^{-2}}$ (Johnston, Seibel, et al. 2019)). Both studies relied on commercial display systems designed for human vision, which provide suboptimal stimulation of zebrafish cones.

While these studies assessed spatial integration in zebrafish bipolar cells, they did not address integration across spectral channels nor use wavelengths matched to zebrafish cone opsins. This represents a critical gap given that zebrafish possess ancestral tetrachromatic vision with complex visual circuits. Yet, we do not know whether they use colours across space for sophisticated spatial integration or whether spectral channels simply sum to form broadband spatial responses as observed in mammals. Building on these advances, systematic multichromatic RF mapping using opsin-targeted wavelengths represents the essential next step to understand how early visual circuits combine colour information in ancestral vertebrate systems, potentially revealing discrete functional roles for individual chromatic channels that have been lost in derived visual systems.

3.1.3 Significance

We sought to develop a method for *in vivo* estimation of bipolar cell RF colour components using calcium imaging and reverse-correlation analysis. We apply opsin-targeted shifting coloured binary noise to extend the existing characterisation of larval zebrafish bipolar cell RFs. By decomposing spatial integration into its constituent spectral channels, we aim to gain insights into the role of chromatic organisation of bipolar cell RFs in early visual processing. This represents the first multichromatic, *in vivo* high-resolution estimation of bipolar cell RFs using calcium imaging. Thus, expanding on and complementing previous efforts in understanding bipolar cell spatial integration and the circuits involved, providing a foundation for future studies investigating spatiochromatic visual processing in bipolar cells. Here, we present our multichromatic mapping technique and demonstrate its effectiveness in capturing spatial and chromatic RFs.

3.2 Experimental design

3.2.1 Imaging parameter optimisation

Functional imaging experiments of bipolar cell terminals presented various challenges. First, bipolar cell terminals are small, typically only a few µm in diameter (Schroeter, Wong, and Gregg 2006; Zhao, Ellingsen, and Fjose 2009). The small size of these structures made it difficult to achieve a high number of separable ROIs within a scan field without significantly sacrificing on temporal resolution. We were operating with a diffraction limited microscope configuration, at the practical limits of our imaging system. With 20x optical magnification and typically around 1.5 to 2x digital zoom, this yielded a field of view of approximately 20-30 µm in width (2:1 aspect ratio), enough to resolve approximately between 30 to 80 ROIs depending on signal-to-noise conditions and transparency of the given sample. To balance imaging acquisition frame rate and spatial resolution, we opted for 1ms line speed at 128×64 pixel resolution, yielding a 15.625 Hz frame rate.

3.2.2 Stimulus temporal frequency

In accordance with the Nyquist theorem, this limited the temporal frequency of our stimulation to 7.8125 Hz. However, we also needed to account for the dynamics of the calcium indicator and synaptic calcium flux. The *jGCaMP8* family of indicators are generally described as having ultra-fast kinetics allowing tracking of individual spikes up to 50 Hz (Zhang, Rózsa, et al. 2023). The *jGCaMP8m* variant used in this study has a rise time of approximately 2 ms and a decay time of around 20 ms (Zhang, Rózsa, et al. 2023). This theoretically allows for a high temporal stimulation frequency.

Larval zebrafish bipolar cells can exhibit transient or sustained response kinetics (Wang et al. 2023). In fact, bipolar cells can exhibit both graded potentials (Morgans 2000; Westbrook 1994; Schreyer and Gollisch 2021) and spikes (Baden, Berens, Bethge, et al. 2013; Baden, Espotsi, et al. 2011). About 65% of zebrafish bipolar cell terminals generate spike-like electrical activity with a half-rise time of approximately 65 ms (Dreosti, Esposti, et al. 2011). Given these kinetics, we determined that a stimulus interval of 200 ms was appropriate. This frequency is slow enough to allow the calcium indicator to accurately track the graded responses of bipolar cells without significant temporal overlap between successive stimuli. Therefore, we optimised between stimulation rate and fluorophore kinetic and established a stimulus temporal frequency of 5 Hz, maintaining temporal resolution sufficient to detect synaptic release events.

We chose simple, cyclical 100-frame epochs per colour (20-second intervals) for multichromatic mapping, optimising between data sufficiency and chromatic decomposition feasibility. Early experiments attempted sequential single-colour sessions but suffered from drift-induced ROI misalignment between recordings. Colour cycling within individual experiments resolved this limitation, maintaining ROI consistency across spectral conditions whilst providing the flexibility to terminate experiments while retaining balanced chromatic sampling. The 20-second epoch duration minimised neuronal adaptation whilst

reducing correlation artifacts from colour transitions (Figure 3.1). We adopted sequential spectral decomposition as our systematic baseline, reserving simultaneous chromatic stimulation for future exploration.

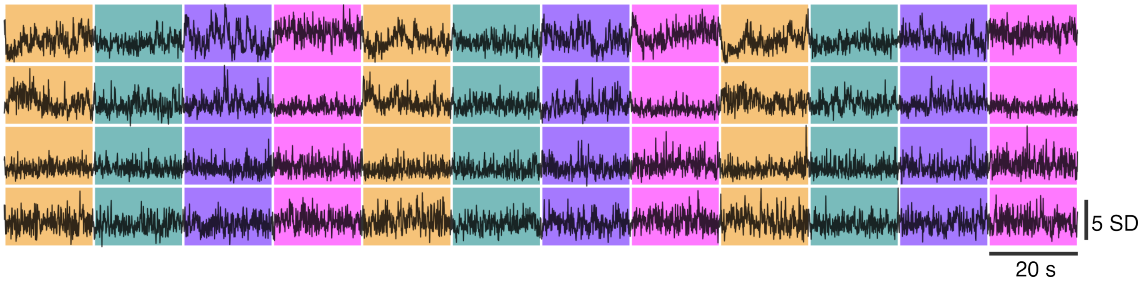

Figure 3.1: Example calcium traces during multichromatic stimulation. Four representative ROIs showing calcium fluorescence responses during alternating colour epochs. Orange, teal, purple, and magenta backgrounds indicate different spectral stimuli, corresponding to red, green, blue, and UV wavelengths aligned to the fish's opsins as perceived in human vision. The first pair of ROIs show clear colour preference as demonstrated by shifts in response amplitude between colours. Note the second ROI from the top shows a pronounced sensitisation to the onset of red, necessitating a longer stimulation duration for each colour block. The second pair of ROIs show more consistent baselines throughout the stimulation period, indicating broad-band response. Scale bars: 5 SD (vertical), 20 s (horizontal).

3.2.3 Stimulus spatial frequency

In spike-triggered average (STA)-like approaches the spatial frequency of the stimulus is a critical parameter that influences the resulting RF estimates. The spatial frequency determines the level of detail in the STRF estimation, and higher spatial frequencies can reveal finer features of the RF. However, the choice of spatial frequency must also consider the limitations imposed by the animal's visual system and the experimental setup. Fine spatial frequencies may not be optimally resolved depending on the cell's spatial integration properties, resulting in sparse responses that require longer imaging times. If spatial frequencies are too fine, they will effectively be interpreted by a spatially integrating cell as a mean grey.

Early in the project, a series of papers were published demonstrating a shuffled white noise approach to STA (Pamplona et al. 2022; Gupta, Młynarski, Symonova, et al. 2022), which is quickly gaining popularity in the field. In short, a given pixel size is selected and the stimulus is then pseudo-randomly shuffled on an underlying lattice, leading to upscaling in the STA calculation. This super-resolution methodology addresses imaging duration constraints of two-photon calcium imaging compared to traditional electrophysiological approaches. Whilst electrophysiological STA experiments typically employ recording durations of 30–240 minutes (Field et al. 2010), two-photon recordings are typically constrained to 15–20 minutes in a single imaging plane due to photobleaching and sample drift artefacts common in larval zebrafish preparations. The enhanced spatial sampling provided by the super-resolution approach allows larger block sizes to be used. This maximises the probability of adequately stimulating RF centres within these temporal constraints, thereby improving the reliability of RF characterisation under imaging conditions.

To optimise for SNR in order to gain an initial understanding of multichromatic RFs, the majority of experiments were conducted with 10° boxes. The underlying noise array is 10 by 6 and upscaled to 40 by 24 by via 25% increment shuffling. Measuring and calculating the actual stimulus size after simulator calibration yielded a size of 9.48°, resulting in 2.37°-wide pixels after upscaling. Thus, 2.37 was consistently used as the scaling factor between stimulus pixels and visual degrees throughout the rest of this thesis.

3.3 Methods

3.3.1 Aligning the stimulus and scan plane

Zebrafish were mounted for monocular stimulation perpendicular to the window of the mounting chamber as described in chapter 2 section 2.3. The sample was then transferred to the imaging setup, placed under the objective, and the initial scan plane was centred on the eye. Once the IPL was identified by its fluorescence, a series of diagnostic stimuli were then played to ensure the sample, scan plane, and stimuli were aligned. In short, these consisted of sets of bar and box stimuli presented at various locations on the screen. This allowed an initial assessment of spatial alignment and responsiveness, as changes in fluorescence could be observed and plotted in a live read-out.

3.3.2 Drift mitigation and registration

These experiments required relatively long recording times with high magnification, exaggerating drift at the risk of losing ROIs over time. Various suspected factors contributed to sample drift including agarose settling and saturating with water over time, output from the laser heating up the agarose causing expansions, movement from the animal, and ambient temperature changes. If terminals were in risk of drifting out of the scan FOV in the X or Y axes, the scan plane could be carefully adjusted to maintain alignment. Drift in the X and Y planes were then corrected effectively using simple rigid registration procedures. Successful registration was confirmed by comparing average or standard deviation projections of the scan stack before and after registration, assessing obvious directional artefacts in the FOV.

If individual terminals could be resolved and segmented, drift mitigation and registration were deemed successful. Occasionally, scan plane repositioning was inaccurate leading to loss of the same terminals after adjustment. These experiments were discarded to avoid artefactual RF mappings. Experiments could also exhibit irrecoverable Z drift, in which case experiments were also discarded as single-plane imaging did not allow for Z correction.

3.3.3 Reverse correlation analysis

We developed the CCA algorithm inspired by classic STA calculations (Chichilnisky 2001) to identify stimulus patterns that correlate with calcium fluorescence changes. To circumvent the limitation of not having direct spike readouts from two-photon imaging, we instead

leverage the graded calcium responses. The algorithm exploits calcium signals' inherent graded nature rather than attempting discrete events from spike-estimation.

Algorithm implementation

CCA cross-correlates each stimulus pixel's history with corresponding fluorescence traces, using frame-precise synchronisation between stimulus history and calcium impinging over a specified window, here 1.3 s. Multi-spectral stimuli (e.g., R, G, B, UV) are organised in 3D arrays with colour lookup tables, enabling systematic analysis of chromatic integration. The CCA is thereby derived by cross-correlating the stimulus history with the calcium trace for each ROI and for each colour, approximating the RF's spatial, chromatic, and temporal characteristics.

Algorithm 1 Spatiotemporal Receptive Field Analysis

```
Input: calcium traces, visual noise patterns, trigger times
Output: spatiotemporal RF maps
// Setup
Load analysis parameters (temporal windows, colour channels, etc.)
Validate required data exists (imaging data, ROIs, stimulus patterns)
Interpolate noise pattern to frame-precision
Generate colour channel lookup table:
for each frame in noise stimulus do
    Assign colour channel based on stimulus parameter (frames per colour)
end for
// Main RF calculation
Initialize result arrays for correlations and statistics
for each ROI do
    Extract calcium fluorescence trace for ROI
    for each colour channel (red, green, blue, UV) do
        Filter trace to include only frames with this colour stimulus
        // Calculate spike-triggered average for each stimulus pixel
        for each pixel in visual stimulus do
            Cross-correlate filtered calcium trace with pixel intensity over time
            Extract temporal window around peak correlation
            Store as spatiotemporal filter for this pixel
            Normalise by mean stimulus intensity
        end for
        Save complete RF map for this ROI and colour
    end for
end for
```

This implementation integrates with the broader preprocessing pipeline, requiring detrended imaging data, ROI masks, and trigger timing as inputs, whilst generating STRF correlation and standard deviation maps for downstream analysis. The script implements the CCA algorithm in IGOR Pro, and is available on GitHub: https://github.com/BadenLab/Igor_scripts.

3.3.4 Post-processing and segmentation

Post-processing of the CCA calculated STRF employs automated border masking and Z-score normalisation against non-signal frames. Centre-surround segmentation was done by agglomerative clustering to partition each STRF into three temporal clusters representing centre, surround, and noise components. For clustering, time series from each pixel in the calculated STRF were extracted and centred on their first index such that all time series were started from 0. Clustering was then performed, yielding three cluster centres. The labels for each centre was then be reshaped back to the original spatial structure, and pixel time series were extracted conditionally based on these labels. The average time series within each cluster were then calculated from all pixels assigned to that cluster. This yields an estimated centre-, surround, and background time series. Clustering was performed for all STRFs. Quality control excluded averaged cluster time series with peak amplitudes below 2 standard deviations.

Conditional merging prevents over-segmentation artifacts: clusters with high correlation (Pearson's $r > 0.95$, covariance > 2) or low variance (< 0.6125) are consolidated, whilst absent surround regions trigger centre cluster reunification to avoid spurious fragmentation. The merging allowed for all clusters to be merged into a single time series in cases where no signal was identified. For visualisation, spatial profiles of STRFs are extracted through temporal collapse via variance projection, and polarity added by assessing each pixel's time kernel characteristics and multiplying it with the spatial profile. Code for the post-processing procedures are available on GitHub: https://github.com/simbru/pygor/tree/main/src/pygor/strf.

3.3.5 Exclusion criteria

Experiments were excluded for excessive spatial drift, signal-to-noise ratios below 2 standard deviations above baseline, evidence of photobleaching, or compromised tissue integrity. Recordings with insufficient duration ($<$ 1000 frames per colour channel) were excluded from STRF analysis. Computed STRFs were excluded for low signal amplitude as described above, abnormally large spatial extents or elongations for all ROIs indicating systematic errors like sample drift. In tetrachromatic experiments, exclusion criteria were applied per colour channel. Sub-threshold colour channels were treated as non-responsive. STRFs from a given ROI were only excluded from analysis if all colour channels were sub-threshold.

3.3.6 Photobleaching

Bleaching the fluorophore represents a significant concern in long-duration calcium imaging experiments, potentially compromising signal quality and introducing systematic bias in fluorescence measurements. As such, consecutive imaging of the same ROIs was untenable, and laser power was deliberately reduced for diagnostic stimuli to preserve the sample. Figure 3.2 illustrates the photobleaching of a representative scan plane after 50 minutes of imaging, next to unscanned neighbouring regions. This effect also

extends to the Z axis, leading to a reduction in signal intensity within a few microns of the scanned plane. Care was always taken not to overlap with already scanned regions when conducting experiments over multiple scan planes. As seen in Figure 3.2, this could be easily determined by visual inspection of the imaging plane prior to imaging.

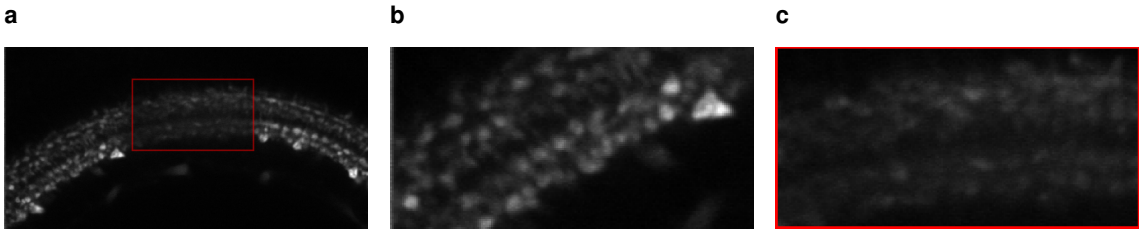

Figure 3.2: Representative example of photobleaching effects in calcium imaging data. (a) Zoomed out view of an imaging plane after 30 minutes of recording. Red rectangle indicates FOV of recording and the resulting photobleaching. Neighbouring regions outside the scan plane are unaffected. **(b)** High-contrast region outside the scan plane maintaining signal integrity after the experiment. **(c)** Low-contrast region (red border) exhibiting substantial signal degradation due to photobleaching, demonstrating the effect of photobleaching.

3.4 Results

We developed an in-vivo method for estimating bipolar cell RFs using two-photon calcium imaging combined with colour-varying spatiotemporal binary noise stimuli and a cross-correlation analysis algorithm. This approach enabled detailed mapping of the spatial, temporal, and chromatic properties of bipolar cell RFs in the intact retina. 27 successful imaging sessions were conducted for the core data collection using four separate colour channels: red (588 nm), green (470 nm), blue (420 nm), and UV (365 nm) with a box size of 9.48° at 25% upscaling giving pixel resolution of 2.37°.

3.4.1 Iterative spatial stimulation for aligning scan plane with stimulus

Prior to experiments, alignment of the central retina with the stimulus presentation was assessed. Series of iterative stimuli were played to identify the location of stimuli presentation relative to the imaging plane. The screen was segmented into 9 regions and a 1 s bright box stimulus was flashed within each region. Traces were viewed live and averaged to produce a response profile for each region.

We aimed for centre alignment in order to accurately capture any potential broad RF structures. As such, STRFs are positioned away from the edge of the stimulation area, in order to reduce the incidence of artefactual or partially captured RFs that can lead to ambiguous assessment of spatial morphology. Figure 3.3a-c demonstrates a representative example of the spatial relationship between stimulus location and response amplitude under optimal conditions. In contrast, Figure 3.3d-e shows misalignment on the X and Y axis relative to the stimulus presentation area.

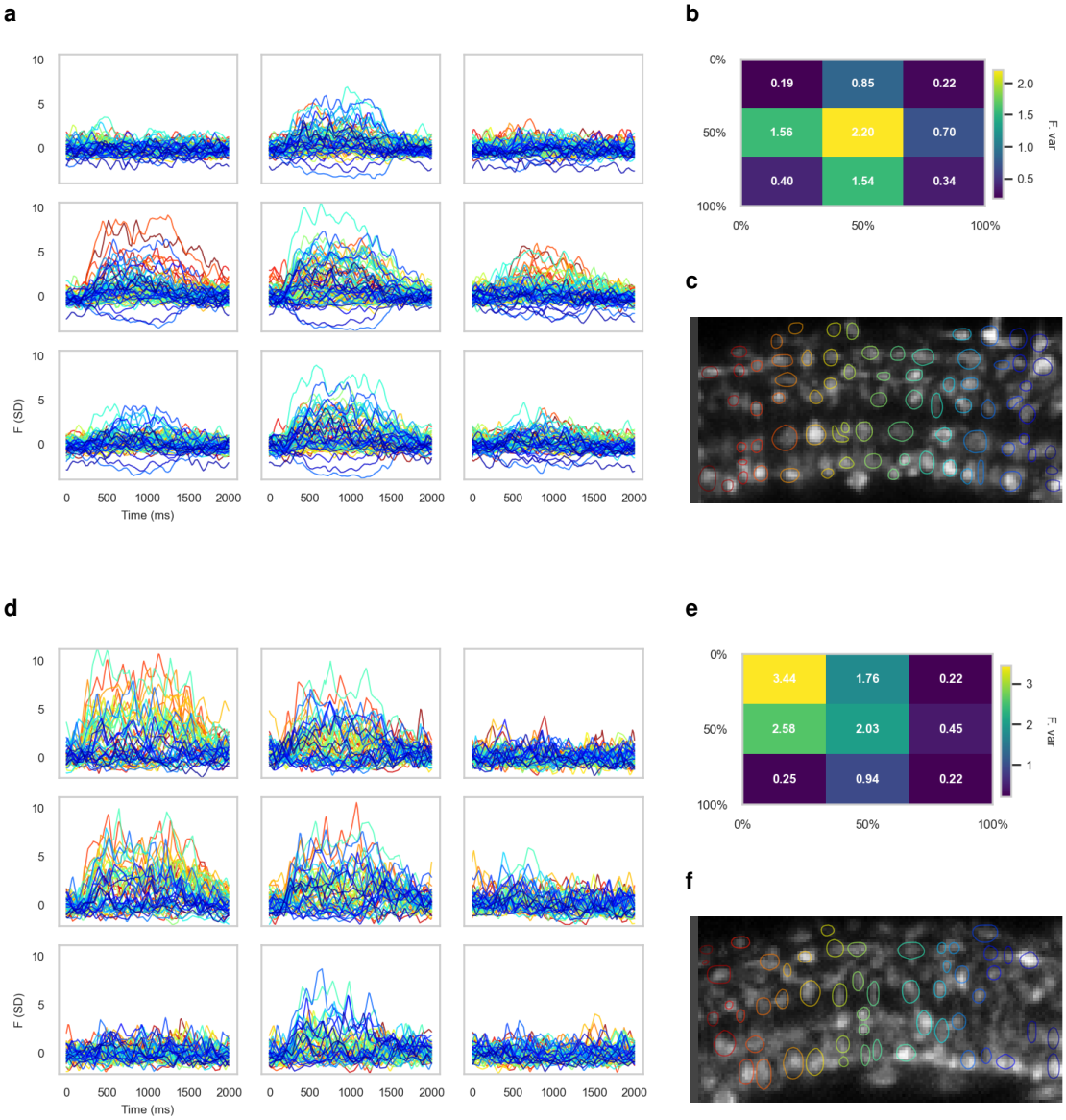

Figure 3.3: Scan plane alignment demonstration showing optimal alignment between stimulus and imaging plane. (a) Calcium traces from individual bipolar cells showing clear, consistent responses across the 3×3 stimulus grid. **(b)** Spatial heatmap of response amplitudes demonstrating coherent receptive field structure. **(c)** ROI locations overlaid on the scan plane, from which Figure 3.3b and Figure 3.3a are derived. **(d)** As above, but demonstrating misalignment between presentation area and FOV. **(e)** Corresponding heatmap. **(f)** Corresponding ROI locations.

3.4.2 Reverse correlation reveals spatiotemporal structure of RFs

After confirming alignment, binary noise was presented while calcium imaging was performed. Figure 3.4 demonstrates an example of the CCA using broadband binary noise, combining all spectral channels from UV to Red. Calcium signals (Figure 3.4a) were extracted from ROIs within the scan plane Figure 3.4b. The stimulus history for each pixel was cross-correlated with the calcium trace over a temporal window. Figure 3.4c shows the stimulus history for the 100 most strongly correlated pixels within the STRF over an arbitrary 15 s period. Figure 3.4d shows the result of CCA for the same ROI. Figure 3.4e and Figure 3.4f shows the same analysis for background pixels. Figure 3.4g shows the resulting spatial characteristics by mapping temporal amplitude (z-scored) back onto the spatial position of each pixel. Figure 3.4h shows the relationship between z-scoring and raw cross-correlation values. Due to the linear relationship, metrics throughout the rest of the thesis are presented in SD units to facilitate comparison across experiments.

Additional examples of cross-correlation analysis applied to bipolar cell terminals with weak responses and absent RF structure are provided in Appendix section A.3.

3.4.3 Segmentation of RFs

The STRFs calculated by CCA are three-dimensional matrices representing stimulus history over the specified time window in both spatial and temporal domains. To identify spatial structure and extract corresponding temporal signals, we applied clustering to the extracted STRFs (subsection 3.3.4). Time courses for each pixel in the STRF were extracted and agglomerative clustering was performed to delineate distinct functional zones within each RF.

Figure 3.5 demonstrates this process for two individual representative RFs. Figure 3.5a shows all time series extracted from every pixel in a STRF, with spatial characteristics in Figure 3.5d. Figure 3.5b shows initial clustering with corresponding spatial locations in Figure 3.5e. The two similar time series were merged according to the covariance threshold, resulting in segmentation shown in Figure 3.5c and Figure 3.5f.

Figure 3.5g shows a RF with spatial antagonism. The clustering process grouped time series by their characteristic shapes (Figure 3.5h), with distinct time series exhibiting opposing polarities and unique temporal dynamics. The automated segmentation algorithm left centre, surround, and background signals intact, with functional zones delineated in Figure 3.5i.

3.4.4 Multichromatic RF

To extend CCA to multiple spectral channels, we presented the same binary noise stimulus with alternating chromatic content and calculated separate STRFs for each colour channel.

Figure 3.6 summarises the workflow for multichromatic RF mapping with a representative example. Fluorescence traces are extracted from an ROI as in Figure 3.4. Figure 3.6a

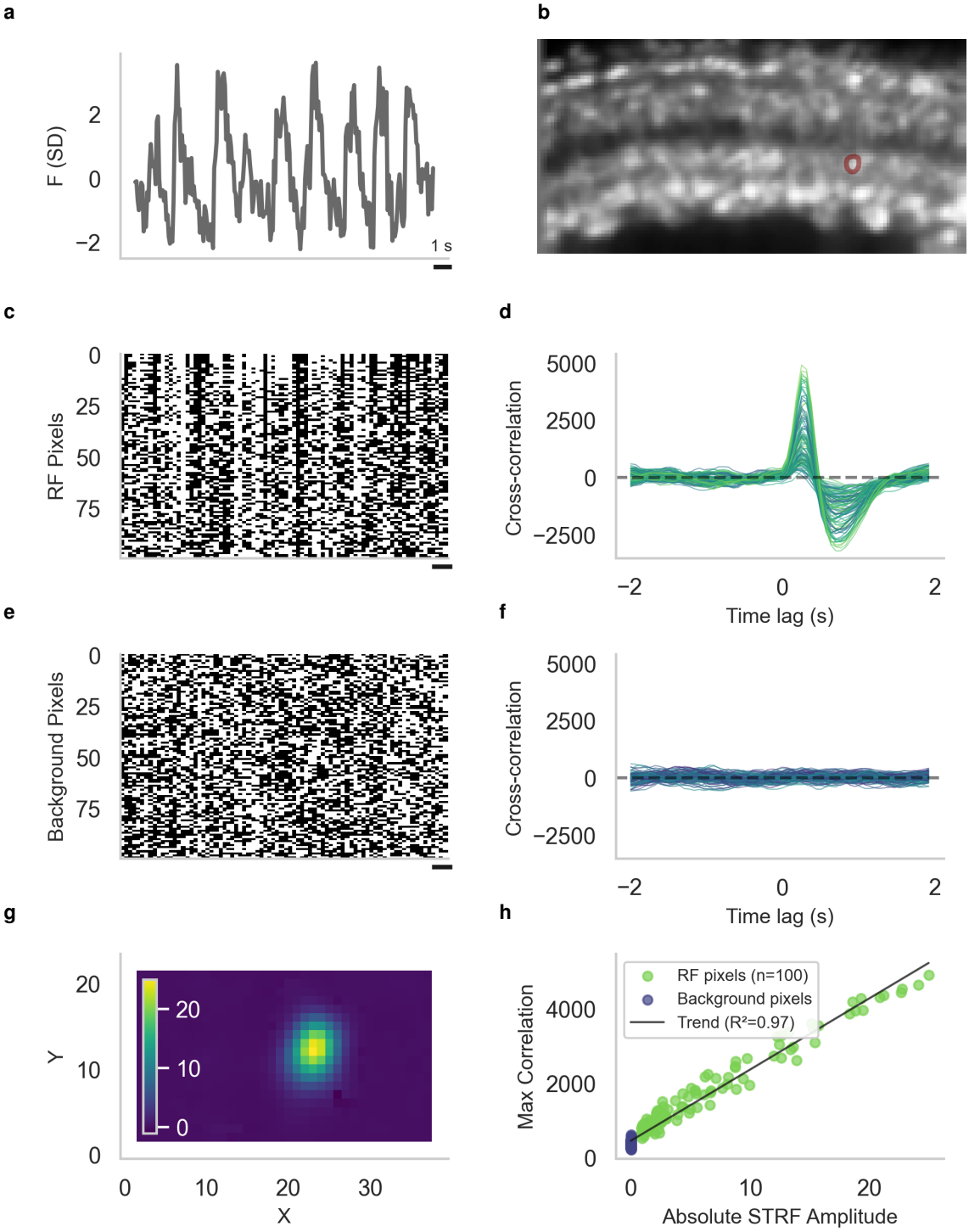

Figure 3.4: Validation of calcium imaging-based RF mapping through cross-correlation analysis. **(a)** Calcium fluorescence responses (SD) from a single bipolar cel terminal during spatial binary noise presentation, demonstrating robust temporal dynamics. **(b)** The analysed ROI within the retinal tissue scan plane. **(c)** Stimulus history for top 100 high-amplitude STRF pixels over a 15 s window, demonstrating temporal correlation. Note that these represent a flattened view of the spatially arranged pixels that make up the centre of the RF. **(d)** Cross-correlation functions between ROI fluorescence and centre-driving pixels, revealing characteristic temporal profiles of the STRF, akin to STA. **(e)** Control stimulus time series from background pixels with minimal STRF amplitudes. Note the lack of stimulus coherence. **(f)** Cross-correlation functions for background control pixels, demonstrating negligible correlation and confirming spatial selectivity of the RF mapping. **(g)** Spatially-organised STRF map derived from cross-correlation analysis, revealing the RF's spatial characteristics. Note the outer two pixels are ignored due to edge effects of shuffled noise. **(h)** Quantitative validation showing linear relationship (R^2 = 0.97, n = 100 pixels) between STRF amplitude and maximum cross-correlation strength, confirming that spatial RF structure emerges from systematic correlation patterns.

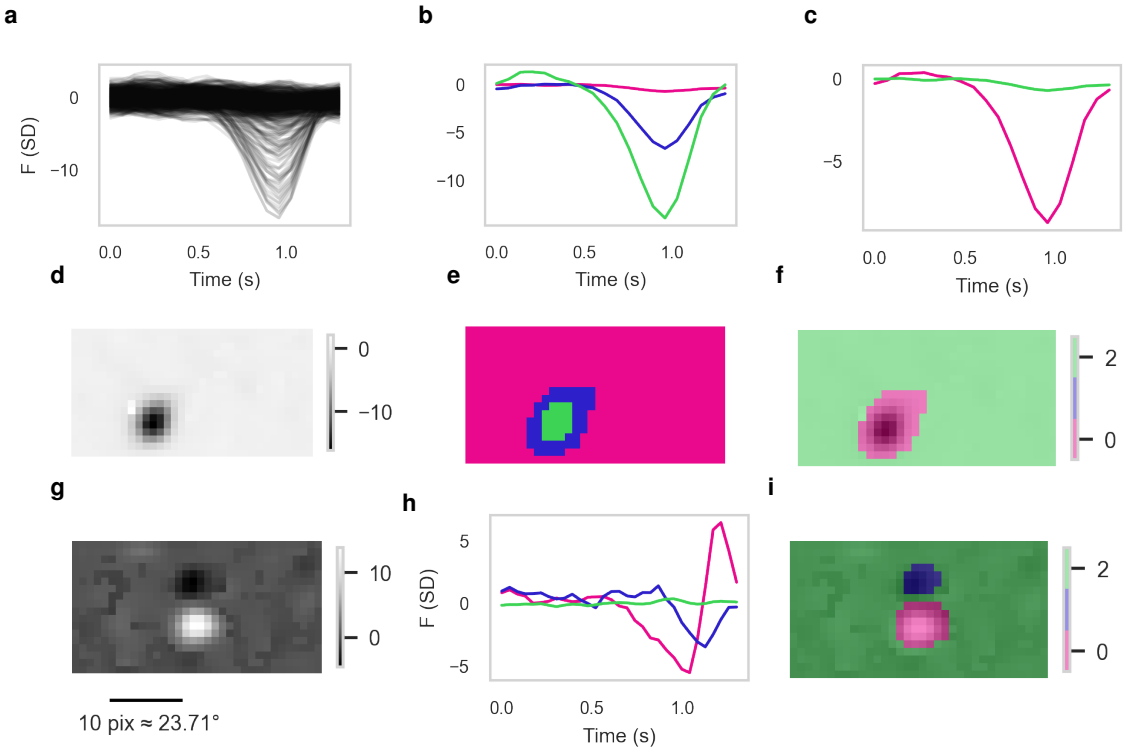

Figure 3.5: Demonstration of segmentation algorithm, showing sequential stages of the clustering-based segmentation analysis. Representative examples showing the automated clustering approach for partitioning spatiotemporal receptive fields into functional components. **(a)** All time series as extracted from example STRF in Figure 3.5d. **(b)** Clustering centres of agglomerative clustering of time series into 3 clusters, with each cluster represented by a different colour. **(c)** Result of cluster merging, here based on a variance criterion. **(d)** Example spatial projection of STRF used for example. **(e)** Spatial position of pixel location for each time series used for clustering, by reshaping the underlying clustering labels. **(f)** Final clustering labels applied spatially after the cluster merging, representing the segmented receptive field. **(g)** Second example spatial projection from different STRF with spatial antagonism for comparison. Time series were extracted is in Figure 3.5a. **(h)** Clustering centres for the second example showing different temporal dynamics for centre and surround components. **(i)** Final segmentation result for the second example, demonstrating method generalisability.

shows a representative calcium signal from a single ROI, aligned to the stimulus presentation history over 80 s from the 50 pixels with the highest cross-correlation, visualised in Figure 3.6b. Figure 3.6c illustrates the cross-correlation analysis for each colour channel. The spatial properties were extracted by separately collapsing the temporal domains (Figure 3.6d, each colour aligned to their corresponding panel above).

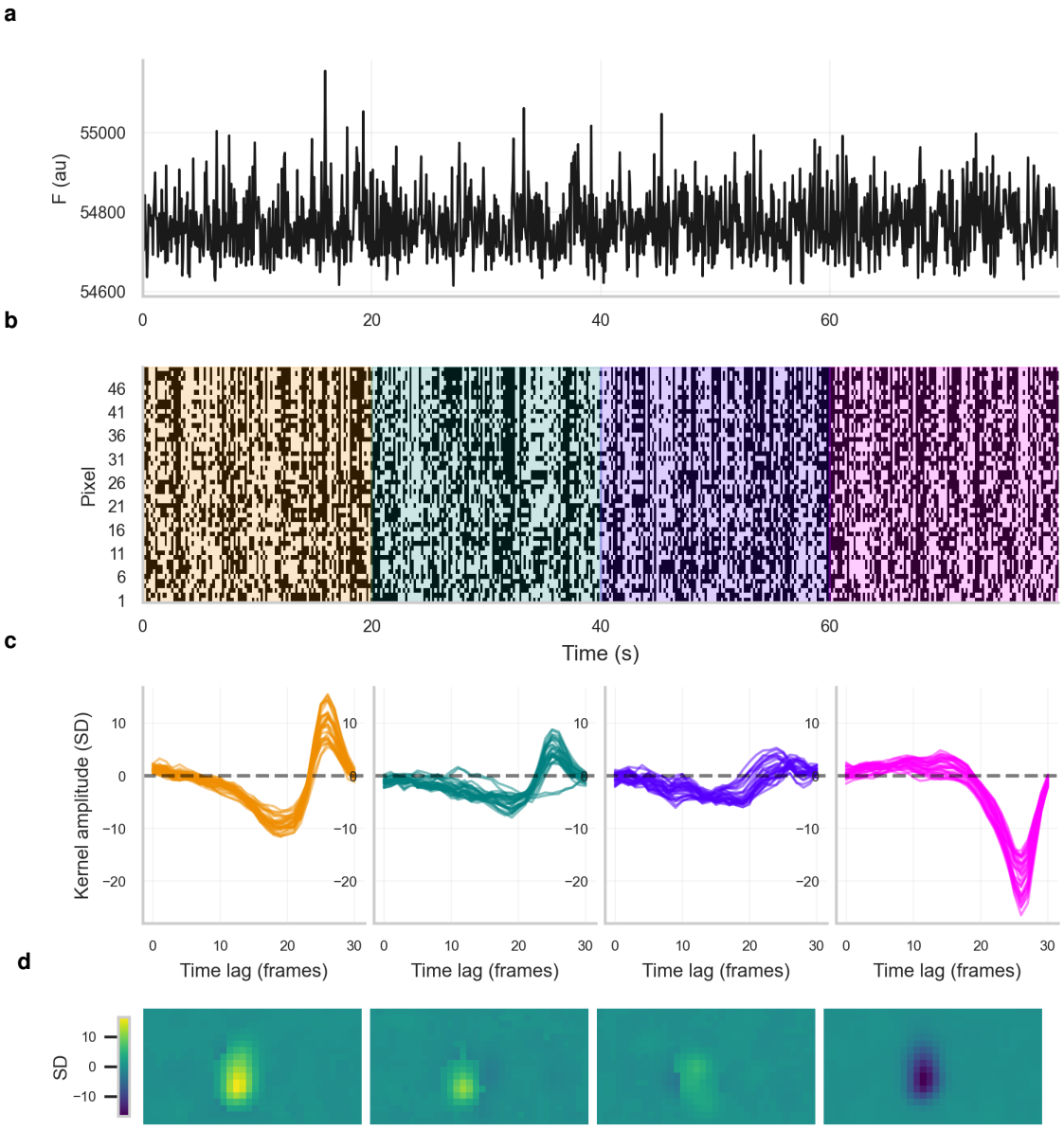

Figure 3.6: Demonstration of multichromatic CCA. (a) Fluorescence response trace from a representative bipolar cell terminal during multichromatic visual stimulation. The trace shows calcium signal over an 80-second recording window. **(b)** Stimulus history for top 50 pixels based on amplitude in the STRF, showing the temporal alignment between fluorescence and stimulus history. Colour-coded bands represent the continuous tetrachromatic noise stimulation across four spectral channels. **(c)** Temporal correlation kernels for each colour channel, here showing the top 95th percentile of spatially responsive pixels. **(d)** Spatial RF maps for each colour channel, computed using multichromatic reverse correlation and derived from the collapsed time-kernels for each pixel.

3.4.5 Comparison with simple spatial stimuli

To validate that the spatiotemporal characterisation truly captured the spatial extents of the RFs, we compared CCA with simple static bar stimuli. Fifteen-degree bars with positive and negative contrast were presented sequentially across the screen in vertical and horizontal orientations. Positive bars (+100%) were presented from a dark background and negative bars (-100%) from a uniform white background. Bars were presented for 2s with 2s inter-stimulus intervals.

Peak response amplitudes were extracted for each bar position to generate spatial tuning profiles for each orientation and contrast polarity (Figure 3.7b). Figure 3.7b-d demonstrate representative examples of strong alignment between spatial tuning functions from bar stimuli and CCA-derived STRFs, confirming that CCA effectively captures both spatial characteristics and polarity of bipolar cell RFs.

3.4.6 Comparison with simple chromatic stimuli

We asked to what extent the CCA derived STRFs could predict full-field chromatic responses of bipolar cells. Figure 3.8 shows a representative experiment where multi-chromatic RF mapping was paired with full-field flash stimulation. RFs were mapped as described above. Example RFs' spatial and temporal characteristics are shown alongside their corresponding full-field responses. Four colours were flashed from dark, each for 2 s followed by a 2 s return to dark.

The overall polarity of cells per colour channel in the RF corresponded to responses seen in full-field flashes, including mixed ON and OFF responses for different wavelengths. Response amplitudes were also captured in the STRF, with some ROIs showing uniform amplitudes across colour channels while others were more selective.

3.4.7 Core data collection summary and validation

Figure 3.9 summarises the main data collection efforts and simple metrics for all mapped RFs in the core data collection. The total number of ROIs was 1122 (Figure 3.9a). Of 4,488 STRFs calculated (4 per ROI), 1904 passed the signal threshold criterion of > 2 standard deviations, yielding 848 ROIs with at least one colour STRF above threshold (Figure 3.9c). Recording durations averaged 22.7 ± 11.1 minutes (Figure 3.9b). A positive correlation was observed between recording duration and signal strength (r = 0.722, Figure 3.9e). The stimulus presentation maintained precise temporal synchronisation (202.9 ± 1.3 ms intervals vs. intended 200 ms, Figure 3.9f). The average maximum response amplitude across all ROIs and colours was 8.83 ± 3.65 (SD). Chromatic selectivity analysis where lower values indicate broadband responses and higher values reflect wavelength-specific tuning revealed diverse spectral preferences (mean: 0.31 ± 0.14, Figure 3.9d) across the sampled population.

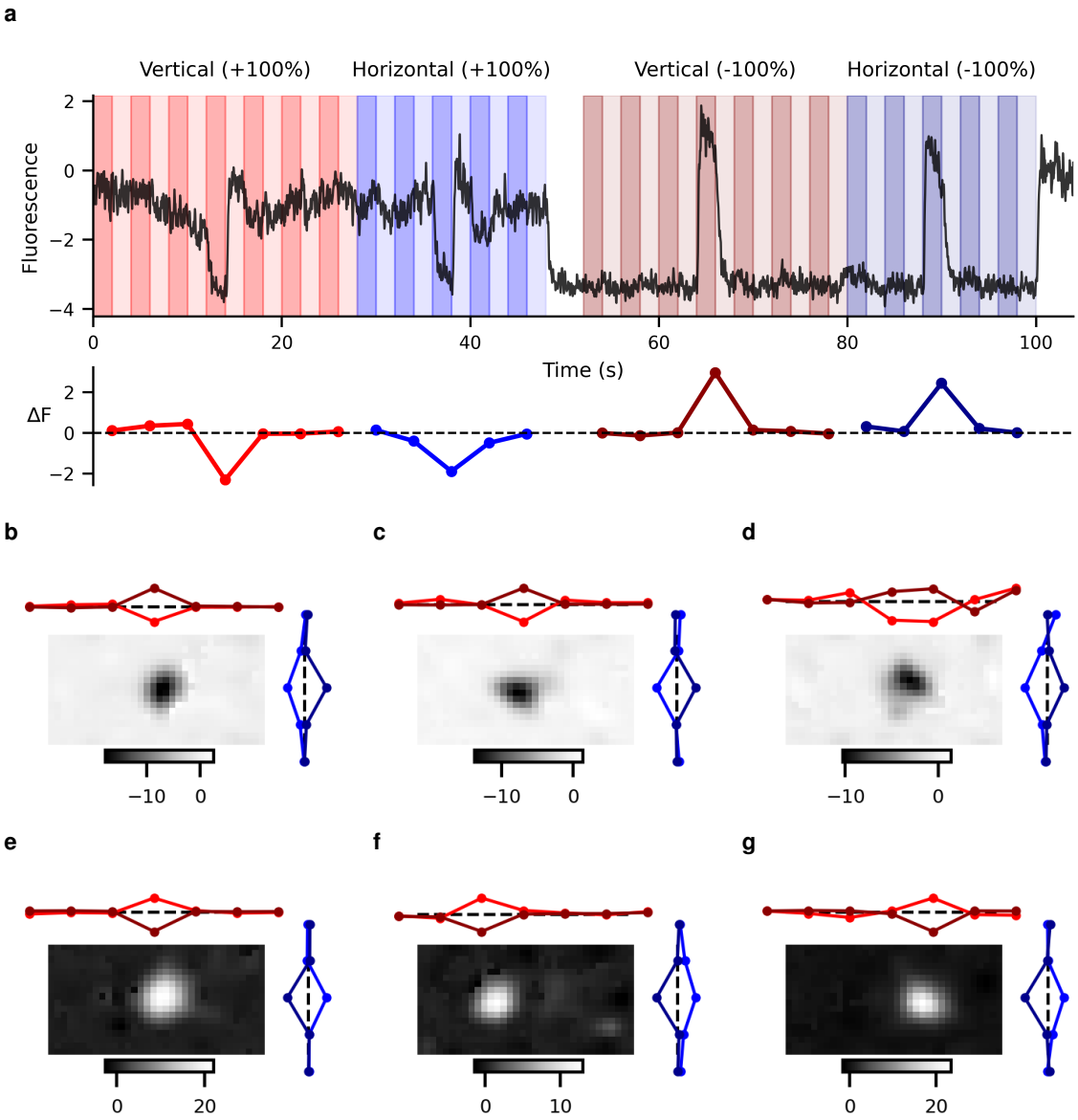

Figure 3.7: Receptive field mapping technique accurately captures spatial characteristics of bipolar cells. Bar-stimulus experiments demonstrate detailed spatial profiling beyond what simple orthogonal stimuli can reveal. **(a)** Sequential bar presentation at vertical and horizontal positions with 15° spacing, covering the entire visual field. Dark-to-white bars (100% contrast) were presented for 2 seconds followed by 2-second inter-stimulus intervals (shaded regions). White-to-dark bars (0% contrast) followed the same timing pattern. Full-field flashes at 50s and 100s (unshaded regions) reversed contrast polarity between epochs. Spatial tuning functions extracted from each epoch are shown beneath in corresponding colours. **(b-g)** Representative examples demonstrating the method's ability to precisely map receptive field structure and spatial tuning profiles, revealing spatial organisation and polarity of bipolar cell receptive fields.

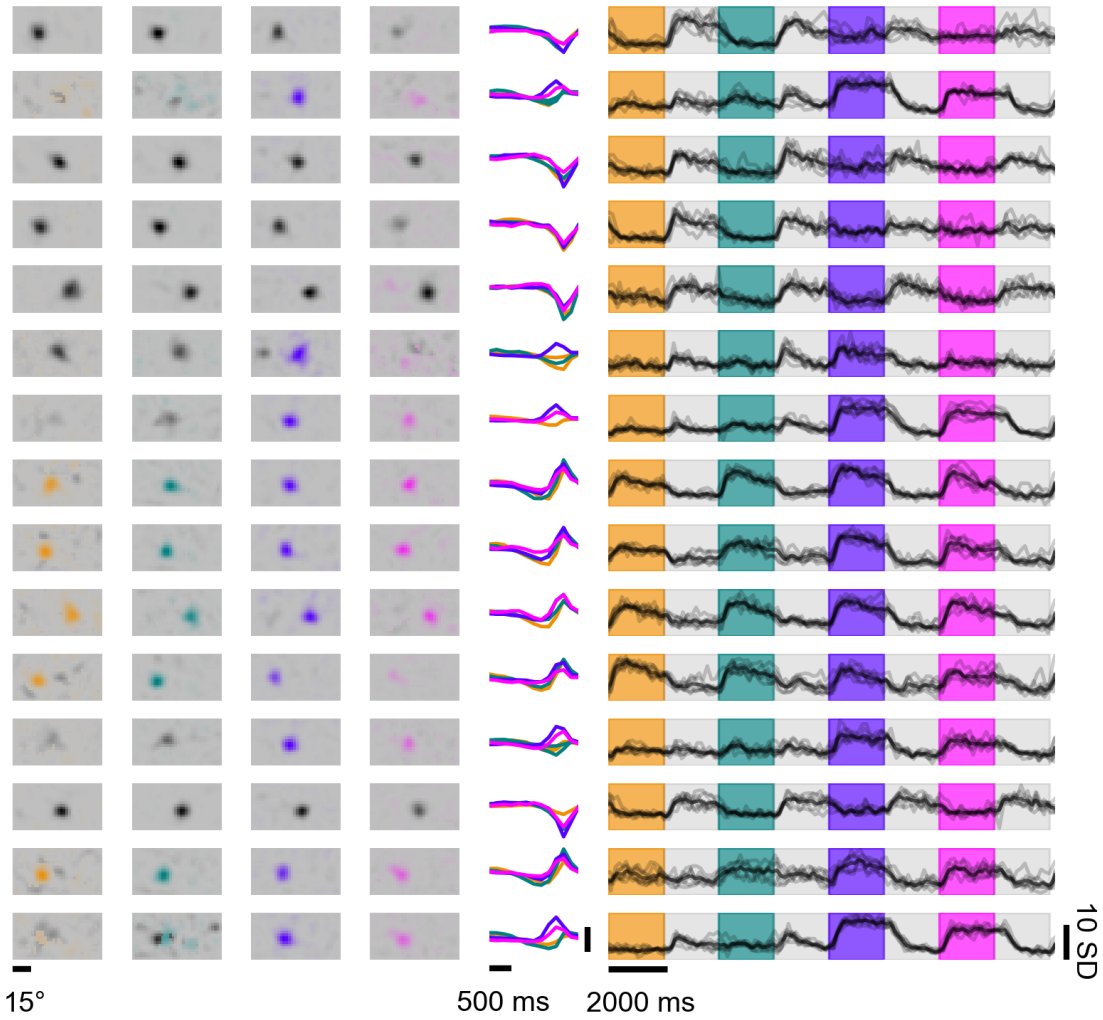

Figure 3.8: Multichromatic RF mapping technique effectively captures bipolar cell colour integration. Example RFs with corresponding full-field flash responses. Each row represents a single ROI. Left columns show representative RFs for red, green, blue, and UV wavelengths, demonstrating diverse spatiochromatic integration. The middle column shows the corresponding temporal dynamics of RF centres (scale bar 10 SD). Right column shows fluorescence traces during chromatic full-field flashes, demonstrating alignment between RF polarity and chromatic integration strength for each ROI.

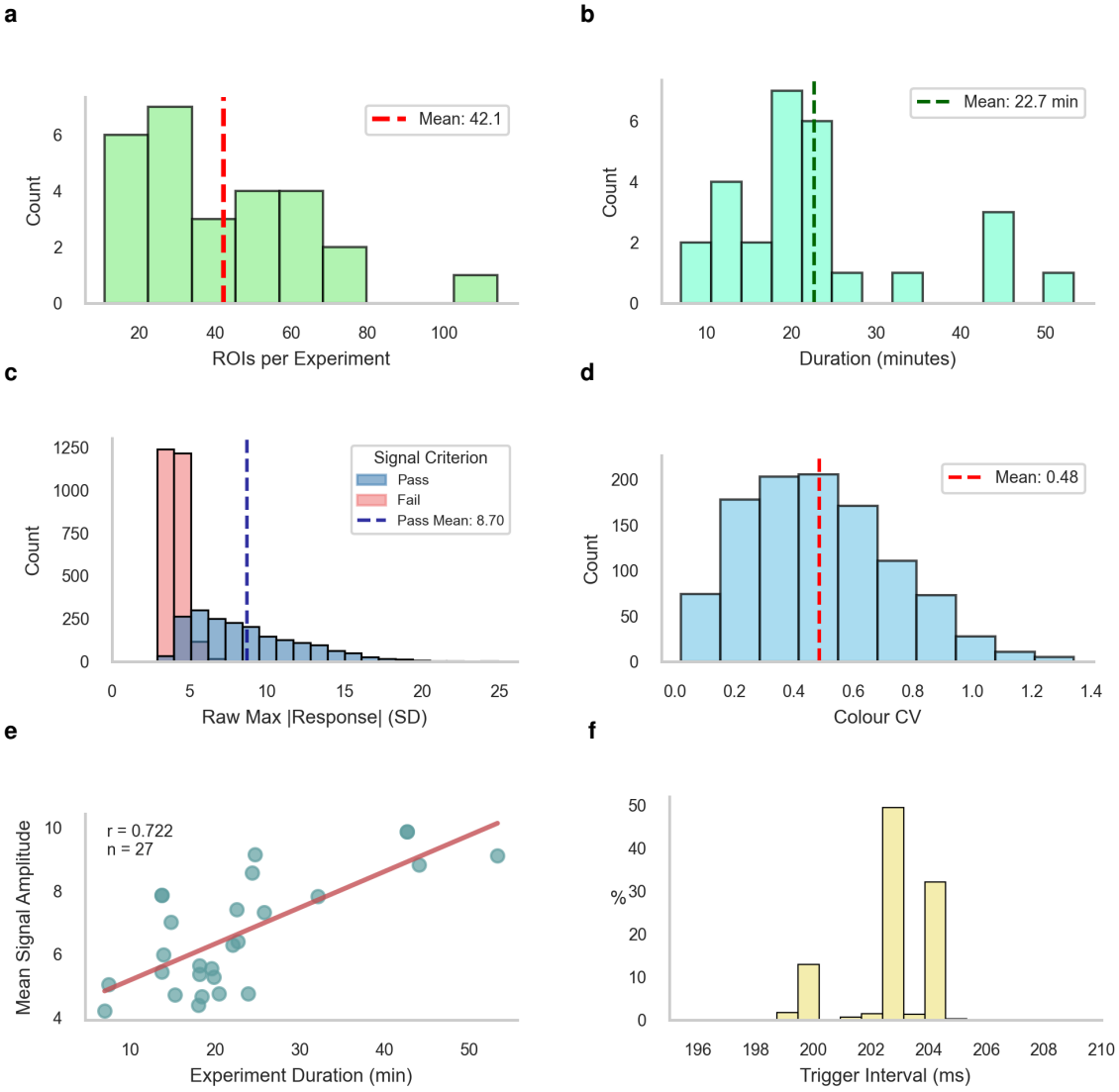

Figure 3.9: Methodological validation of multichromatic CCA approach for zebrafish bipolar cell recordings. (a) ROI count per experiment (n=27, mean: 41.5, range: 11-114). **(b)** Recording duration distribution (22.7 ± 11.1 min) showing extended sessions essential for robust reverse correlation analysis. **(c)** STRF amplitude distribution; red indicates failed signal quality, blue indicates pass. Quality criterion effectively separates signal from noise. **(d)** Measurement of spectral integration distribution (coefficient of variation, mean: 0.48 ± 0.14) indicating chromatic selectivity, with lower values showing broadband responses and higher values reflecting wavelength-specific tuning. **(e)** Duration vs amplitude correlation (r = 0.722) supporting longer recordings for robust characterisation. **(f)** Trigger interval precision (202.9 ± 1.3 ms) ensuring reliable CCA computation.

3.5 Discussion

3.5.1 Decoding RFs from synaptic calcium

We demonstrate RF mapping in vivo using two-photon imaging. The CCA uses calcium imaging data and binary spatiochromatic noise to characterise integration properties of bipolar cells. Because calcium influx at the synapse is intimately linked with synaptic

release at the bipolar cell synapse (Südhof 2012; Kaneko, Pinto, and Tachibana 1989; Pan et al. 2001), and the transgenic line (*RibbeyeA:SyjGCaMP8m*) enables robust readout of calcium dynamics at the bipolar cell's ribbon synapse (Dreosti, Odermatt, et al. 2009; Magupalli et al. 2008; Zhang and Looger 2024), we can accurately track bipolar cell activity. By cross-correlating calcium signals for each ROI with stimulus history, we identify the average stimulus patterns preceding bipolar cell activation, thereby approximating the RF.

The resulting STRFs reveal distinct spatial and temporal patterns of activity, capturing both the stimulus area and polarity that drove calcium fluctuations in bipolar cell terminals. The temporal alignment between calcium dynamics and binary noise in Figure 3.4 and Figure 3.6 demonstrates the effectiveness of the correlation approach. Background pixels showed no appreciable cross-correlation in Figure 3.4e, Figure 3.4f, and Figure 3.4h, indicative of no RF contribution. Taken together, this approach accurately captured the spatial morphology and polarity of the bipolar cell RFs Figure 3.7.

Dissecting colour responses

Zebrafish bipolar cell spectral integration is diverse and complex (Wang et al. 2023; Bartel, Yoshimatsu, et al. 2021; Li, Tsujimura, et al. 2012). Therefore, it was important to capture the chromatic components of their RFs. The CCA also extended the analysis to include multichromatic stimuli, allowing for comprehensive estimation of bipolar cells chromatic integration. Figure 3.6 demonstrates the ability to capture distinct spatiochromatic components of bipolar cell RFs, revealing integration patterns across different wavelengths. In Figure 3.6 the highest response amplitudes in the temporal domain come from the Red and UV channels, with the Green and Blue channels having comparatively subdued but still present signals. Moreover, the Red channel reveals opposing polarities with distinct temporal characteristics. The Red channel and opposing UV channel have substantial spatial overlap, and would likely cancel out under broadband white stimulation. Therefore, the multichromatic CCA approach decomposes spatiochromatic integration that would be obscured under traditional broadband spatial stimulation.

Moreover, the correspondence between full-field flashes and chromatic RF components shown in Figure 3.8 validates this. For each ROI, the spectral integration aligned with its full-field flash response, with overall polarity corresponding to responses seen in full-field flashes and response amplitudes captured in the STRF. Response amplitudes were also captured in the STRF, with some ROIs showing uniform amplitudes across colour channels while others were more selective. This suggests that CCA can predict full-field responses based on RF properties, and that spectral integration of bipolar cells can be linearly decomposed via CCA. The alignment in tuning functions with RF centres, and the corresponding RF polarity capturing peak and suppression responses for negative and positive contrast, demonstrates the validity of our approach. While both methods reveal similar spatial tuning properties, the CCA approach provides a more comprehensive view of the RF structure by capturing full spatiotemporal dynamics rather than static spatial profiles alone.

3.5.2 Dissecting method performance across experiments

The ability to simultaneously characterise up to 100 bipolar cell RFs represents a substantial advance in throughput for this challenging cell type (Figure 3.9a). While electrode arrays achieve higher throughput for accessible neurons, bipolar cells occupy an anatomically inconvenient position between photoreceptor and ganglion cell layers that has historically limited experimental access. By targeting the final integrated output of each cell's upstream processing, the synaptic terminals, our approach captures RF properties at the most functionally relevant location. Recording durations of 22.7 ± 11.1 minutes (Figure 3.9b), while longer than typical *in vivo* two-photon experiments, are comparable to or shorter than traditional electrophysiology sessions. The strong correlation between recording duration and signal strength (r = 0.722, Figure 3.9e) supports the stochastic nature of RF mapping: extended recordings increase the probability of adequately stimulating each cell's RF, thereby improving signal-to-noise ratios and RF reconstruction fidelity. Importantly, this comprehensive characterisation captures spatial integration, polarity, and chromatic responses within single experiments, eliminating the need for multiple stimulus protocols whose recording times would nevertheless add up.

The diversity of chromatic selectivity values (0.31 ± 0.14, Figure 3.9d) demonstrates the method's capacity to capture the full spectrum of spectral integration properties, from broadband responses (low values) to highly wavelength-specific tuning (high values). This physiologically realistic distribution validates that our approach effectively characterises the chromatic diversity present in bipolar cell populations. The 2 SD signal quality criterion (Figure 3.9c), adhering to established statistical principles of normal distributions, effectively separated signal from noise while maintaining sufficient sensitivity to capture weaker but genuine responses. Precise temporal synchronisation (202.9 ± 1.3 ms intervals, Figure 3.9f) confirmed reliable 5 Hz stimulation throughout experiments, ensuring consistent correlation analysis across all recordings.

3.5.3 Balancing RF mapping and imaging constraints

The parameter space was particularly challenging because we needed to simultaneously optimise across three dimensions: spatial resolution, chromatic sampling, and temporal precision. We ultimately prioritized spatial characterisation, ensuring sufficient colour cycles (described in subsection 3.2.3), while accepting lower temporal refresh rates. Our final spatial resolution of 2.37° after calibration aligns closely with previous zebrafish RF mapping (Johnston, Ding, et al. 2014), while the shuffled white noise approach enabled robust characterisation with larger stimulus blocks.

Achieving high-quality 20+ minute recordings requires careful balance between laser power and photobleaching constraints (Figure 3.2). Too little power compromises SNR for detecting weak responses, while excessive power limits recording duration through fluorophore bleaching. Low-noise preamplifiers and more sensitive PMTs substantially improved signal-to-noise ratios throughout development, enabling detection of the graded bipolar cell responses that drive this stochastic mapping approach. This connects directly

to our validation finding that extended recording durations improve RF reconstruction quality (Figure 3.9e): with sufficient sampling time and optimised imaging parameters, our chosen stimulus blocks reliably capture RF structure.

3.5.4 Clustering for RF segmentation

The motivation for clustering was to identify potential spatial antagonisms, such as those described by centre-surround models. The agglomerative clustering is done purely on the temporal dynamics of each pixel's response, and makes no assumptions of spatial position. This process allowed us to delineate distinct functional zones within each RF, and enabled extraction of their corresponding time series (Figure 3.5). Note that clustering on simple temporal dynamics can lead to artificial segmentation of simple centre responses, resulting in similar temporal characteristics separated only by amplitude. This is due to the approximately Gaussian distribution of the RF. The conditional merging step mitigates over-segmentation artefacts by consolidating clusters with high correlation or low variance, while ensuring that absent surround regions do not lead to spurious fragmentation. Nevertheless, as demonstrated in Figure 3.5g-i, the method can also successfully identify spatial antagonism when present. This approach effectively balances sensitivity to genuine functional distinctions with robustness against noise-induced artefacts. Functional segmentation of the RFs was successful, facilitating systematic analysis in following chapters.

3.5.5 Limitations of CCA

The CCA approach effectively captures the spatiotemporal and chromatic properties of bipolar cell RFs. However, several limitations should be considered. First, the method requires relatively long stimulation times, as evidenced by the STRF amplitudes increased as a function of recording time (Figure 3.9b, Figure 3.9e). Moreover, high-quality recordings with low noise are also necessary.

Since the CCA approach estimates stimulus patterns associated with calcium responses, the method trades temporal precision for spatial coverage and experimental throughput. While CCA captures spatial organisation effectively, the temporal dynamics reflect calcium indicator kinetics rather than precise neural timing. Electrophysiological STA experiments using spike trains will generate temporal components whose durations are typically in the 100 ms range (Chichilnisky 2001; Seifert et al. 2023; Cooler and Schwartz 2021), whereas the duration of our calcium-based STRF temporal components are typically around 1 s. As such, the method is optimised for spatial characterisation, with temporal information serving primarily to identify response windows rather than measure precise neural computation timing.

Another limitation is the assumption of linearity inherent in reverse correlation techniques. The CCA approach captures linear integration properties across large neural populations through linear correlation analysis between stimulus and calcium signals. Unlike electrophysiological methods that can separate linear integration from nonlinear transformations

(Chichilnisky 2001; Schreyer and Gollisch 2021), our approach assumes a monotonic relationship between neural activity and calcium fluorescence. It is unknown to what extent this assumption holds for all bipolar cell types.

We did not perform deconvolution of calcium signals, as the temporal kinetics of the calcium indicator (*jGCaMP8m*) were sufficiently fast to capture the presynaptic activity of BC in response to a 5 Hz stimulus. However, deconvolution could be applied in future iterations of the algorithm to further refine the temporal resolution of the RF estimates.

Finally, the approach does not account for potential crosstalk between spectral channels or nonlinear interactions between chromatic inputs. Future experiments should investigate different chromatic decomposition strategies, including stimuli with mixed chromatic content which may facilitate exploration of nonlinear spectral integration. Because the parameter space was relatively large (space, time, colour), we could not control for every combination or version of the stimulus protocols. Therefore, future experiments should consider varying colour epochs and introduce pseudo-random colour patterns to further optimise the balance between experimental duration and RF characterisation quality.

3.6 Summary

We successfully developed and validated an *in vivo* method for estimating bipolar cell RFs using multichromatic spatiotemporal noise and calcium imaging. The CCA algorithm effectively recovered RF structure across multiple spectral channels, revealing both spatial organisation and chromatic integration properties of bipolar cells in the intact zebrafish retina. This approach provides a foundation for systematic investigation of colour processing in early visual circuits and demonstrates the feasibility of high-throughput RF mapping in vertebrate retinal circuits. Next, we look at the systematic application of this method to explore the functional organisation of bipolar cells in the larval zebrafish.

4 | Chromatic integration supersedes spatial antagonism in most zebrafish bipolar cells

4.1 Introduction

4.1.1 Background

Classical retinal theory from mammalian models posits that spatial complexity drives functional diversity through centre-surround antagonism. This canonical mechanism (Field et al. 2010; Turner, Schwartz, and Rieke 2018; Freed, Smith, and Sterling 1992; Balasubramanian and Sterling 2009) in part emerges at the level of BCs, where dendritic stratification into the OPL creates the RF centre and lateral interactions within both the OPL and IPL shapes antagonistic surrounds. This enables feature detection (Marr, Hildreth, and Brenner 1980; Zhang, Kim, et al. 2012; Baden, Berens, Franke, et al. 2016) and diversification of information at the input and output layers of the retina (Hsiang et al. 2024; Franke, Berens, et al. 2017; Kramer and Davenport 2015). Surround antagonism therefore shapes spatial processing, building feature selectivity through downstream summation of RFs.

In adult teleosts, lateral inhibition has been found to generate centre-surround organisation (Kaneko 1970; Naka and Nye 1971; Saito, Kondo, and Toyoda 1979; Daw 1968), with some BCs featuring complex spectral integration in the form of double opponency (Kaneko and Tachibana 1981; Shimbo et al. 2000; Wong, Adolph, and Dowling 2005). However, uncertainty persists regarding the prevalence of centre-surround organisation, with mixed results in its characterisation. For example, Saito and Kaneko 1983 reported that more than half of carp BC RFs did not have detectable surrounds. Moreover, it appears that only approximately 25% of adult carp BCs exhibit double opponency despite the abundance of spectral information (Shimbo et al. 2000).

Additionally, when RF surrounds are identified in BCs of aquatic species they regularly appear larger and more diffuse than in terrestrial vertebrates. This is evidenced by the substantially larger stimuli required to probe surrounds in fish compared to rodent

studies (see Table 1.2, Table 1.1, and subsection 1.4.2). In rodents, however, robust centre-surround antagonism in BCs has been shown to be near-ubiqitous for BC and their contribution crucial for spatial processing (Franke, Berens, et al. 2017; Hsiang et al. 2024; Strauss et al. 2022). Perhaps these differences in teleosts surround antagonism reflect adaptations to underwater visual environments, as compared to the comparatively simple visual systems of terrestrial mammals (Lamb, Collin, and Pugh 2007; Baden 2024a).

One explanation for this discrepancy may be the fundamental difference in input complexity between the two branches of vertebrates. Teleosts generally have superior spectral encoding compared to mammals (Behrens et al. 2016), with four cones as compared to the typical two-cone visual systems of most mammals (Carleton et al. 2020). The ancestral photoreceptor diversity possessed by zebrafish for example has been shown to enable impressive chromatic functional organisation (Endeman, Klaassen, and Kamermans 2013; Yoshimatsu, Bartel, et al. 2021). Accordingly, we may expect downstream integration and processing to differ from mammalian models.

4.1.2 Motivation

Although the zebrafish retina has been extensively studied, many functional questions remain unanswered. The morphological diversity of adult zebrafish BCs is well-established, with at least 17 morphological and up to 21 transcriptomically distinct cone BC types identified (Hellevik et al. 2024; Connaughton 2011), each exhibiting distinct patterns of cone integration (Li, Tsujimura, et al. 2012). Their functional characteristics have been explored, revealing systematic yet highly diverse spectral integration (Bartel, Yoshimatsu, et al. 2021; Zimmermann et al. 2018). While spatial processing has been partially investigated, with reports of varying degrees of orientation selectivity (OS) across the BC population (Antinucci, Suleyman, et al. 2016; Johnston, Seibel, et al. 2019), how spectral integration interacts with spatial processing in zebrafish BCs remains unclear.

4.1.3 Objectives

To address these knowledge gaps, we systematically characterised the spatiochromatic integration properties of larval zebrafish BCs using in vivo two-photon imaging to estimate tetrachromatic RFs. This approach enabled analysis of spatiotemporal properties and integration types across all four spectral channels. Based on findings in adult teleosts (Kaneko and Tachibana 1981; Shimbo et al. 2000; Wong, Adolph, and Dowling 2005) and previous reports of centre-surround incidence in larval zebrafish (Antinucci, Suleyman, et al. 2016; Johnston, Seibel, et al. 2019), we hypothesised that spectral channel identity would drive BC functional diversity through distinct spatial characteristics, with most BCs exhibiting detectable surround structures and predictable spectral biases in spatial extents.

4.1.4 Key findings

Contrary to these expectations, BC RFs exhibited simple spatial organisation with weak or absent surrounds across individual spectral channels. Instead, spectral channel identity

emerged as the primary determinant of spatial extent whilst radically altering temporal kinetics. Functional clustering revealed archetypal integration types demonstrating the importance of centre-driven spectral integration in generating diversity. Additionally, a rare subset of BCs displayed complex spatial organisation with non-concentric surrounds, typically within one or two cone channels, representing a distinct pathway.

4.2 Methods

4.2.1 Quality control filtering

RF measurements occasionally contained outliers due to segmentation failures, characterised by implausibly large areas or diameters. ROIs were flagged for removal if any of their four colour channels (R, G, B, UV) exceeded 99th percentile thresholds for area or diameter, resulting in removal of 30 ROIs (2.8% of dataset). This approach minimised loss of potentially valid biological measurements whilst removing clear segmentation failures.

4.2.2 Quantification of inner plexiform layer stratification

To quantify IPL stratification, we calculated the relative depth of each region of interest (ROI) within the IPL. The orientation of the scan plane relative to the IPL was noted. A border was drawn manually at the inner and outer IPL boundaries, and the distance from the inner to outer border was calculated. The position of each ROI was then normalised to this distance, yielding a relative depth value between 0% (inner IPL boundary) and 100% (outer IPL boundary). This allowed comparison of stratification patterns across scans.

4.2.3 Quantification of spatial and temporal features

Spatial RFs were segmented into centre and surround components using clustering of temporal kernels per pixel (detailed in chapter 2). Area was calculated as the number of pixels in the centre cluster multiplied by the area per pixel (2.37 $^{\circ 2}$); diameter, eccentricity, and orientation were derived from weighted principal component analysis (PCA) of significant pixels (>1 SD from mean) within the centre region. PCA calculated the covariance matrix of pixel coordinates weighted by response amplitude, with eigenvalue decomposition yielding major and minor axes. Eccentricity was derived as:

$$\text{Eccentricity} = \sqrt{1 - (b/a)^2} \tag{4.1}$$

where a is the major axis and b is the minor axis.

Temporal properties were calculated from extracted centre temporal kernels. The biphasic index was calculated as:

$$\text{Biphasic index} = 1 - \left| \frac{b - a}{a + b} \right| \tag{4.2}$$

where a represents the area under the negative phase and b represents the area under the positive phase of the temporal kernel. This metric quantifies the degree of biphasic

character, with values approaching 1 indicating balanced positive and negative phases, and values approaching 0 indicating monophasic responses. Spectral centroid was computed from the Fourier transform of temporal kernels as:

$$\text{Spectral centroid} = \frac{\sum(\text{frequencies} \times \text{spectrum})}{\sum(\text{spectrum})} \tag{4.3}$$

This measure quantifies the temporal frequency content, with higher values indicating faster temporal dynamics. Response latencies were identified as the timing of the final peak or trough in the centre temporal response, representing the latest major deflection in the signal.

To quantify spatial opponency of RFs we calculated two complementary metrics. The antagonism index measures functional balance between opposing regions:

$$\text{Antagonism index} = 1 - \frac{|C| - |S|}{|C| + |S|} \tag{4.4}$$

where C and S represent centre and surround response magnitudes from the time kernels with opposite polarity. Values approaching 1 indicating balanced opponency (equal amplitude in centre and surround) and 0 indicating complete centre dominance. If no opposing polarity region was detected, the antagonism index was set to 0.

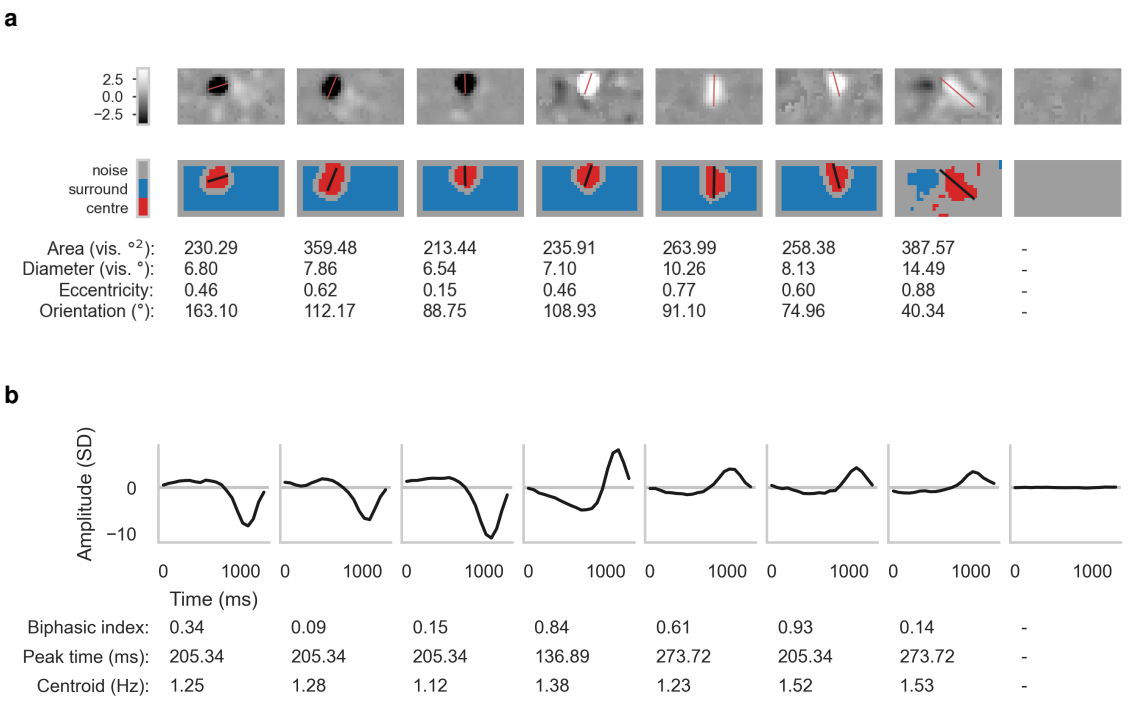

Figure 4.1: Spatial and temporal statistics demonstration of receptive field properties. (a) Spatial statistics showing receptive field maps and quantitative measures. Heatmap values are normalised to the 99th percentile of the plotted spatial maps. **(b)** Temporal statistics of the segmented centre component showing response time courses and quantitative temporal measures, corresponding to the spatial maps in the row above.

4.2.4 Functional clustering

To identify functional cell types within the BC population, we performed hierarchical clustering on multidimensional RF features. Five feature categories were extracted from each ROI's tetrachromatic RFs: response polarity (-1 for On, 1 for Off, and 2 for spatially antagonistic), major axis length, minor axis length, and biphasic index. Other metrics were tested but ultimately degraded clustering performance. This yielded 20 feature dimensions (5 categories × 4 spectral channels). Missing values (for example if an ROI showed no responses to a specific colour channel) were replaced with zeros, and features were standardised using z-score normalisation. Agglomerative hierarchical clustering from `scikit-learn` was then performed.

4.2.5 Statistical analysis

Non-parametric tests were used throughout due to non-normal data distributions. Kruskal-Wallis tests assessed differences across multiple groups, with Dunn's test for post-hoc pairwise comparisons. Mann-Whitney U tests compared two groups. Effect sizes were calculated using eta-squared for Kruskal-Wallis and ranked correlation for Mann-Whitney U tests. Significance was set at $p < 0.05$, with Bonferroni correction applied for multiple comparisons.

Principal Component Analysis (PCA) was performed on spatial receptive field properties for shape quantification, using weighted covariance matrices of pixel coordinates. For functional clustering, features were normalised using `Normalizer` with L2 from `scikit-learn`, which normalizes features by removing the mean and scaling to unit variance, ensuring all features contribute equally to clustering regardless of their original scale or units. Agglomerative hierarchical clustering used Ward linkage was applied directly to the standardised features. Cluster quality was evaluated using silhouette score (average score: 0.385) and the Calinski-Harabasz index (235.847). Dimensionality reduction for visualisation employed both PCA and t-distributed Stochastic Neighbour Embedding (t-SNE) to reveal cluster structure in high-dimensional feature space. All statistical analyses were performed in Python using `scipy.stats`, `pingouin`, `scikit-learn`, and `numpy`.

4.3 Results

4.3.1 Biases in encoding polarity across spectral channels

BC RFs were mapped using a tetrachromatic noise stimulus (R, G, B, and UV channels) and reverse correlation analysis as described in chapter 2. This yielded spatiotemporal RFs for each colour channel, which were then segmented such that the spatial and temporal properties could be described. Out of 4,240 RFs (4 per ROI) 2,051 contained STRFs that met the inclusion criteria. For this analysis we extracted the area, diameter, eccentricity, and orientation of the receptive field centre. We also calculated the biphasic index of the temporal kernel, estimated the latency, and extracted the frequency of the

temporal signal as the spectral centroid. Example receptive fields, their segmentation, and corresponding extracted metrics are shown in Figure 4.1.

1,052 RFs were classified as On-encoding (51.3%) and 999 as Off-encoding (48.7%), depending on the polarity of the time kernel. Different spectral channels exhibit distinct polarity biases (Table 4.1). R and G channels are Off-biased (61.6% and 63.9% Off, respectively), while B and UV channels show strong On bias (66.1% and 71.7% On, respectively).

Table 4.1: Incidence of On and Off receptive fields by spectral channel. Counts, percentages and On:Off ratio are shown for each cone channel (R, G, B, UV).

Cone Channel	Off n	On n	Total	% On	% Off	On:Off
R (580 nm)	392	244	636	38.4%	61.6%	0.62
G (478 nm)	315	178	493	36.1%	63.9%	0.57
B (420 nm)	186	362	548	66.1%	33.9%	1.95
UV (365 nm)	106	268	374	71.7%	28.3%	2.53
Total	999	1052	2051	51.3%	48.7%	1.05

4.3.2 Bipolar cell receptive field cone channels vary subtly but predictably in their spatiotemporal properties

Next, we characterised the spatial and temporal properties of RFs by spectral channel. RFs were pooled irrespective of integration type but categorised by their corresponding spectral channel, allowing broad characterisation of spatiotemporal properties that may depend on spectral tuning.

Receptive field areas varied significantly across spectral channels (Kruskal-Wallis $H = 28.89$, $p < 0.001$). All values reported as mean ± SD. The R channel showed the largest areas (245.6 ± 136.4 °²) with the highest variability (Figure 4.2a), followed by G (228.8 ± 111.4 °²), while B and UV channels were smaller (207.2 ± 86.1 °² and 213.2 ± 80.1 °², respectively). Post-hoc comparisons confirmed that R and G areas were significantly larger than B and UV (Dunn's test, $p < 0.01$). Diameter measurements provided supporting evidence (Figure 4.2b), with R channels showing the largest diameters (7.95 ± 1.93°) compared to B channels (7.60 ± 1.50°, $p = 0.042$). Although these measurements were statistically significant, they represent a diameter difference of less than 0.5°. Encoding polarity (On, Off) showed no significant effect ($p > 0.4$).

To identify systematic differences in RF shape depending on spectral channel, we examined eccentricity and orientation. Eccentricities were nearly uniform across all channels with means of approximately 0.58 and standard deviations of 0.156-0.166, indicating slightly elliptical RFs extents (Kruskal-Wallis $H = 0.19$, $p = 0.98$). Orientation distributions were broadly similar across spectral channels (Figure 4.2d), indicating no meaningful directional bias by spectral channel. However, all spectral channels showed a peak at 90°, indicating vertically elongated receptive fields. As indicated by the moderate eccentricity

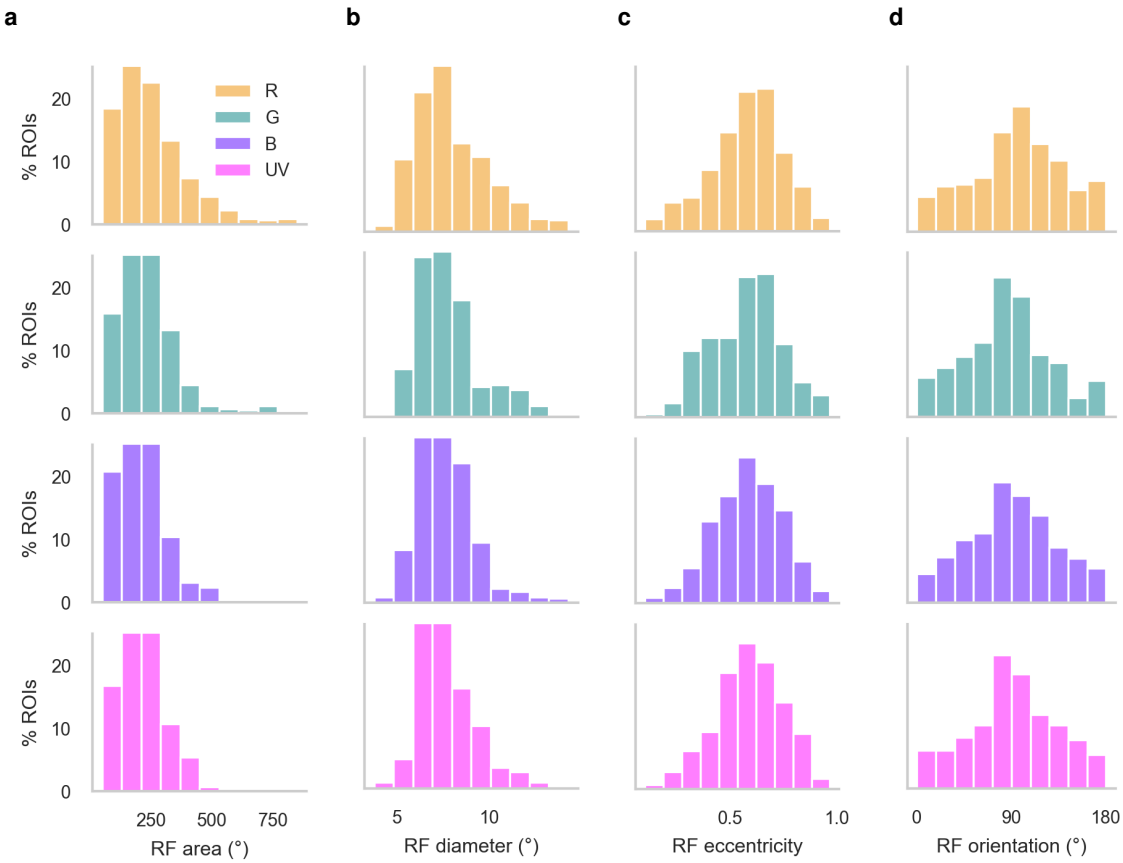

Figure 4.2: Receptive field spatial properties vary systematically across spectral channels. Each column contains feature measurements with spectral channels as rows. **(a)** RF area distributions across spectral channels, measured as the total of segmented pixels and scaled by pixel-to-degree factor of 2.37. **(b)** Equivalent diameter distributions, here derived from PCA to identify the major axis of RF. **(c)** RF eccentricity distributions derived from PCA. **(d)** RF orientation distributions, as the angle between the major axis and the STRF. All plots share the same y-axis scale.

values (Figure 4.2c), these elongations were consistent across spectral channels. No significant shape differences within any colour channel ($p > 0.4$) were found when separated by encoding polarity.

R and G channels consistently produced larger and more variable RFs than B and UV channels. Encoding polarity showed no influence on spatial characteristics, and RF shape properties remained uniform across all spectral channels. Substantial variability existed within each spectral channel (coefficients of variation ranging 0.38-0.56 for areas).

4.3.3 Temporal receptive field properties vary by polarity and cone channel

Next, we wanted to understand whether temporal properties of RFs depend on spectral channel. The biphasic index revealed significant spectral differences in temporal complexity within polarity groups (Kruskal-Wallis $H = 95.63$, $p < 0.001$; detailed statistics in Table A.1). On RFs exhibited substantial biphasic character with clear spectral gradients, while Off RFs remained consistently monophasic across all cone channels. Within On responses, G and R channels showed the strongest biphasic character. B On RFs exhibited surprisingly low biphasic index (0.315 ± 0.289), indicating a more simplified temporal profile and sustained responses compared to the rest of the On system. Similarly, inspecting the distribution of values for On UV also reveals a surprisingly flat distribution (Figure 4.3a), indicating a large proportion show sustained temporal encoding despite their encoding polarity.

Spectral centroid analysis (Figure 4.3b) likewise demonstrated both colour and polarity effects on temporal balance (colour: Kruskal-Wallis $H = 107.00$, $p < 0.001$; polarity: Mann-Whitney $U = 524{,}896$, $p < 0.001$). On RFs exhibited higher spectral centroid values (1.379 Hz ± 0.278 Hz) compared to Off RFs (1.233 Hz ± 0.260 Hz), indicating faster response kinetics. UV-sensitive responses showed the fastest centroids (1.396 Hz ± 0.290 Hz), followed by G (1.375 Hz ± 0.266 Hz), R (1.275 Hz ± 0.270 Hz), and B (1.227 Hz ± 0.263 Hz), revealing systematic spectral differences in temporal kernels (Figure 4.3b). Response latency varied significantly by spectral channel (Kruskal-Wallis $H = 221.42$, $p < 0.001$) but showed no polarity dependence (Mann-Whitney $U = 413{,}491$, $p = 0.346$, Figure 4.3c). R and G channels showed the shortest response latencies (228 ± 62 ms and 229 ± 68 ms, respectively), whilst UV and B channels exhibited longer response latencies (256 ± 70 ms and 275 ± 98 ms, respectively). Both encoding polarity and spectral channel identity influenced RF temporal characteristics, with longer wavelengths exhibiting shorter integration times than shorter wavelengths.

4.3.4 Multichromatic integration types reveal distinct processing strategies

Given the heterogeneous spatiotemporal properties across individual spectral channels, we next investigated how multichromatic integration types affected receptive field characteristics (Figure 4.4). ROIs were categorised into three integration types based on their responses across cone channels: On (responding to light onset only, 43.3%), Off (responding to light offset only, 37.1%), and Opponent (mixed polarity across spectral

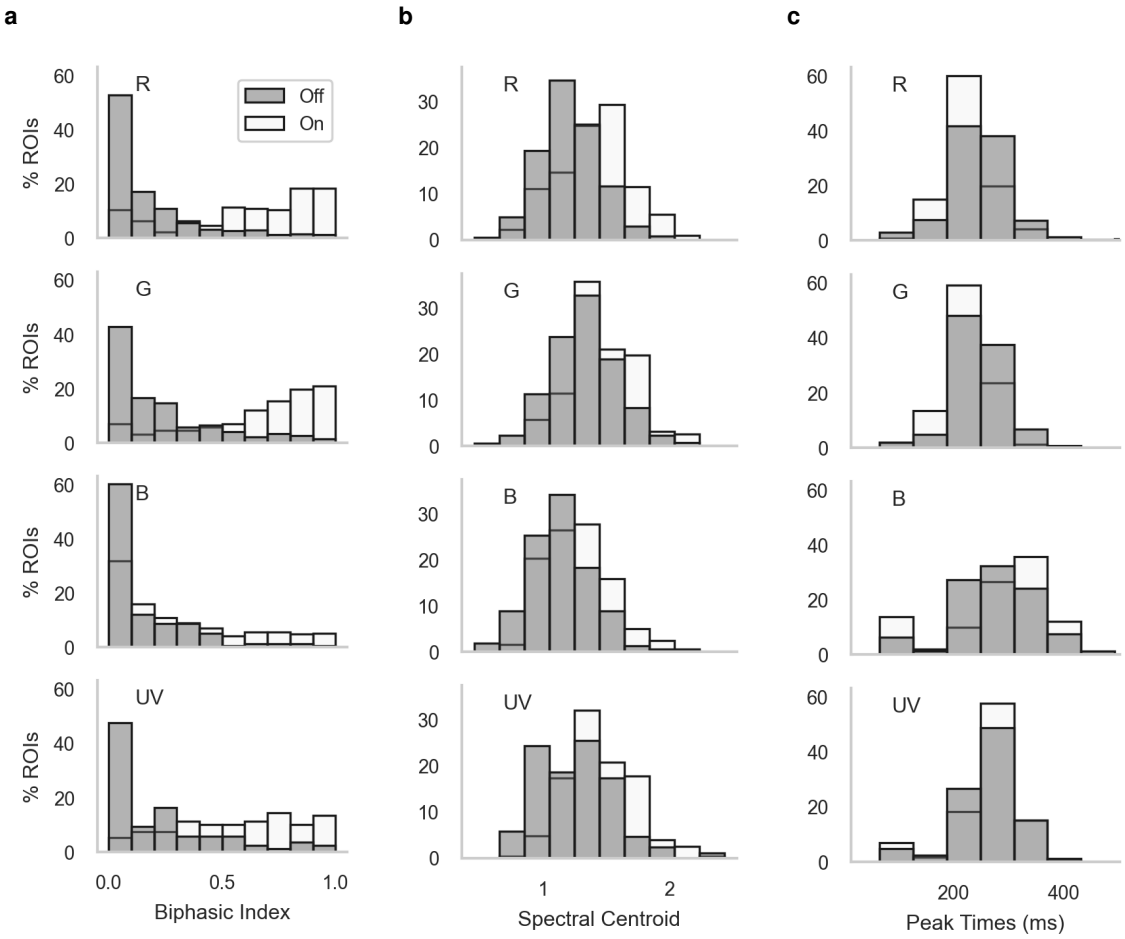

Figure 4.3: Temporal properties vary systematically across spectral channels. **(a)** Biphasic index distributions indicating the degree of temporal complexity in RF responses, where higher values suggest more biphasic (ON-OFF) characteristics. **(b)** Spectral centroid distributions representing the temporal balance of RF responses across the time course. **(c)** Peak times distributions showing the timing of maximum response for each spectral channel, measured in milliseconds from stimulus onset.

channels, 19.7%). On average, Off ROIs integrated 2.4 ± 1.1 spectral inputs per terminal, On ROIs 2.2 ± 1.2 spectral inputs per terminal, and Opponent ROIs 2.9 ± 0.7 spectral inputs per terminal.

Integration type strongly influenced receptive field size, but only for short-wavelength channels (Figure 4.5). G, B, and UV channels showed significant polarity effects, while the R channel showed no differences. In B and UV channels, Off terminals exhibited consistently smaller diameters (B: 7.04 ± 1.15°, UV: 7.10 ± 1.12°) compared to both On (B: 7.79 ± 1.68°, UV: 7.73 ± 1.50°) and Opponent cells (B: 8.06 ± 1.52°, UV: 7.96 ± 1.49°). Off terminals showed marked spectral heterogeneity, with sizes varying between long-wavelength (R: 8.11 ± 2.04°, G: 7.91 ± 1.99°) and short-wavelength channels (B: 7.04 ± 1.15°, UV: 7.10 ± 1.12°). In contrast, On and Opponent cells maintained uniform sizes across all spectral channels. Receptive field shape remained consistent across all integration types and spectral channels.

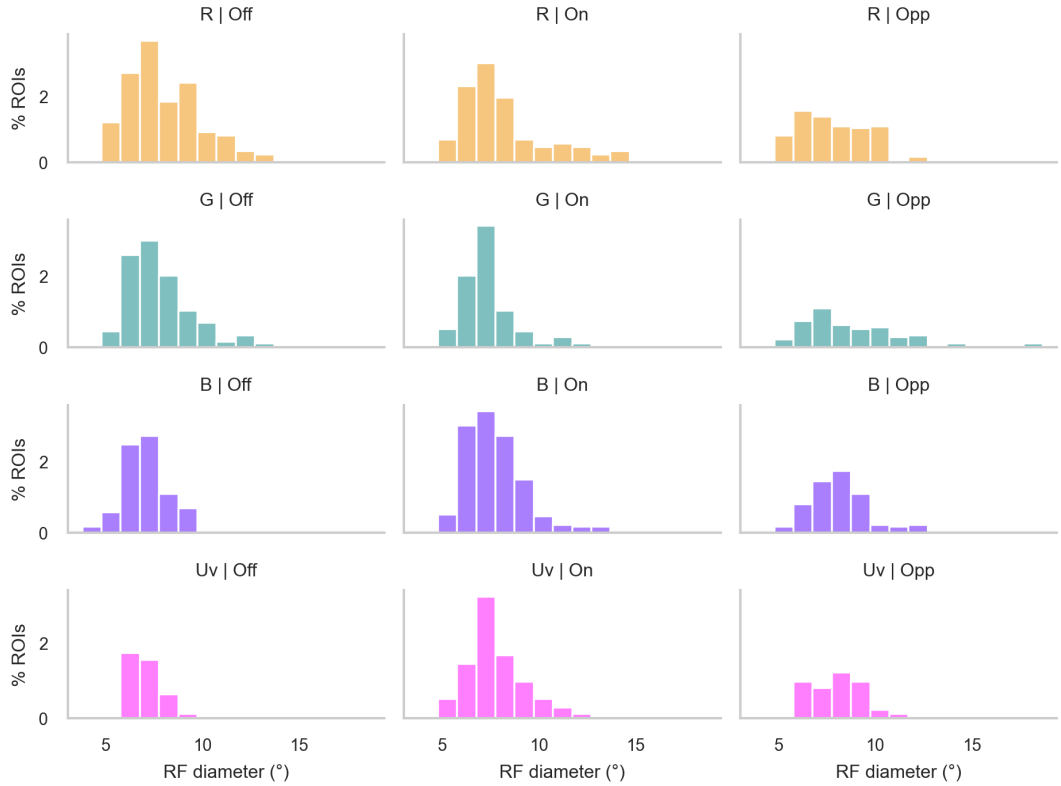

Figure 4.4: Exploratory analysis of receptive field diameter by polarity and colour channel. Distribution histograms show RF diameter patterns across R, G, B, and UV channels (rows 1-4) for Off, On, and Opponent terminals (columns). While distributions largely overlap, subtle systematic differences emerge, particularly in B and UV channels where Off terminals exhibit distinct diameter patterns compared to On and Opponent terminals.

Integration types varied in their temporal kinetics (Figure 4.6). Two-way ANOVA revealed that both integration type and spectral channel significantly influenced temporal characteristics, with particularly strong effects on biphasic index (integration type: $F = 370.531$, spectral channel: $F = 50.342$, both $p < 0.0001$). Off cells exhibited slow, sustained temporal responses across all wavelengths, exemplified by B-sensitive Off cells showing the slowest

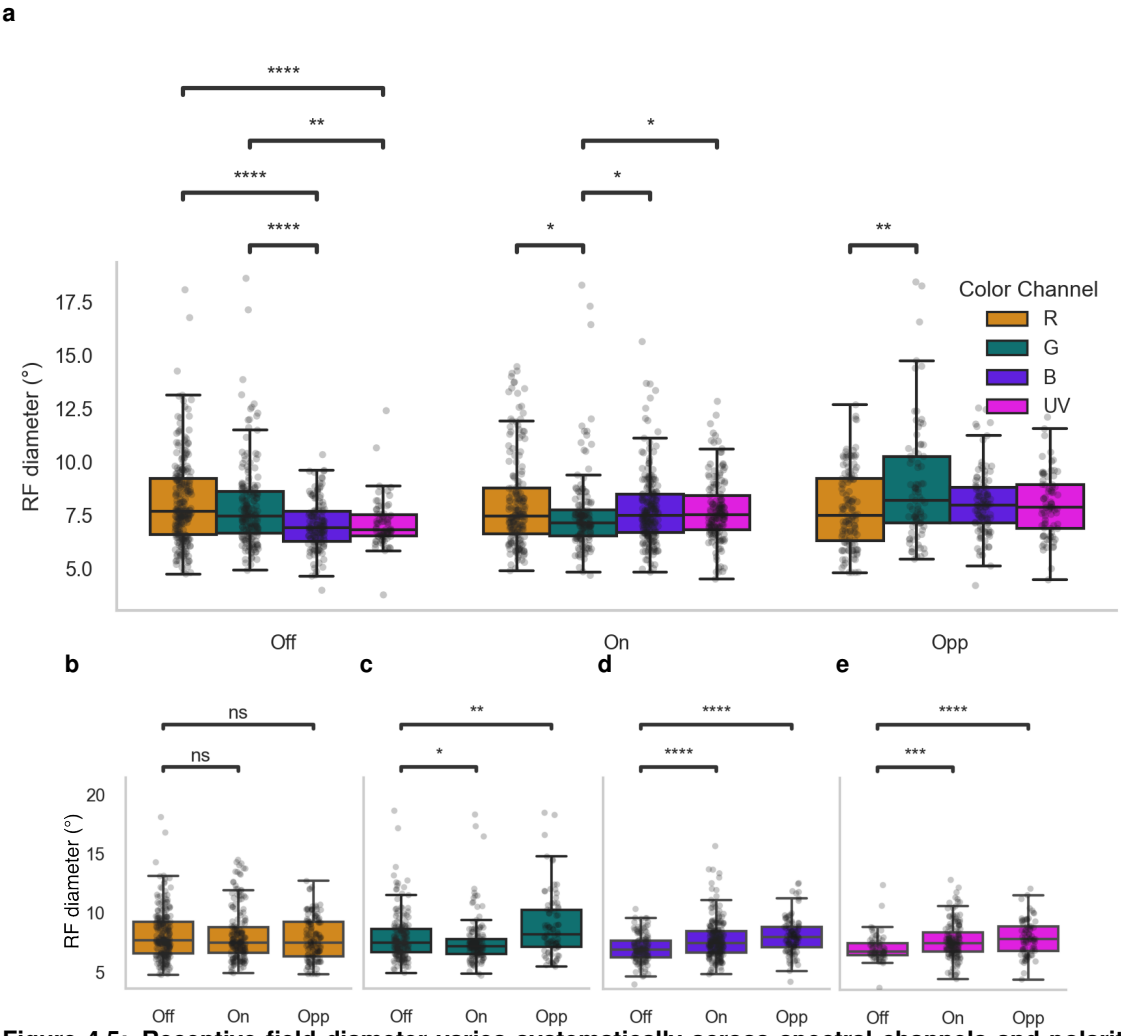

Figure 4.5: Receptive field diameter varies systematically across spectral channels and polarity types. (a) Overview of RF diameter patterns across all colour channels within polarity categories. Off cells show marked spectral heterogeneity, while On and Opponent cells maintain more uniform diameters across channels. **(b)** R channel diameter comparison across polarity types (Kruskal-Wallis H = 1.543, p = 0.462, $\eta^2 = 0.000$) shows no significant differences between Off (8.11 ± 2.04°), On (8.09 ± 2.20°), and Opponent cells (7.80 ± 1.82°). **(c)** G channel diameter varies significantly by polarity (H = 17.139, p = 0.0002, $\eta^2 = 0.037$), with differences between Off (7.91 ± 1.99°) vs Opponent (8.89 ± 2.78°, p = 0.017) and On vs Opponent (7.58 ± 1.98° vs 8.89 ± 2.78°, p = 0.0002). **(d)** B channel shows the strongest polarity effects (H = 33.081, p $<$ 0.0001, $\eta^2 = 0.069$), with Off cells (7.04 ± 1.15°) significantly smaller than both On (7.79 ± 1.68°, p = 0.0001) and Opponent cells (8.06 ± 1.52°, p $<$ 0.0001). **(e)** UV channel diameter differs significantly by polarity (H = 19.436, p = 0.0001, $\eta^2 = 0.058$), with Off cells (7.10 ± 1.12°) smaller than both On (7.73 ± 1.50°, p = 0.0005) and Opponent cells (7.96 ± 1.49°, p = 0.0003). Statistical significance indicated by asterisks: ns p $>$ 0.05, * p $\leq$ 0.05, ** p $\leq$ 0.01, *** p $\leq$ 0.001, **** p $\leq$ 0.0001.

centroids (1.138 Hz ± 0.266 Hz) and most monophasic profiles (biphasic index: 0.145 ± 0.195). On cells showed the opposite pattern: rapid, transient temporal kinetics, with G-sensitive On cells displaying the fastest centroids (1.450 Hz ± 0.266 Hz) and strongest biphasic character (0.663 ± 0.281). Opponent cells occupied an intermediate temporal position, with moderate delays and biphasic characteristics that varied across spectral channels. The biphasic index showed particularly strong effects, with integration type explaining substantially more temporal variance than spectral channel.

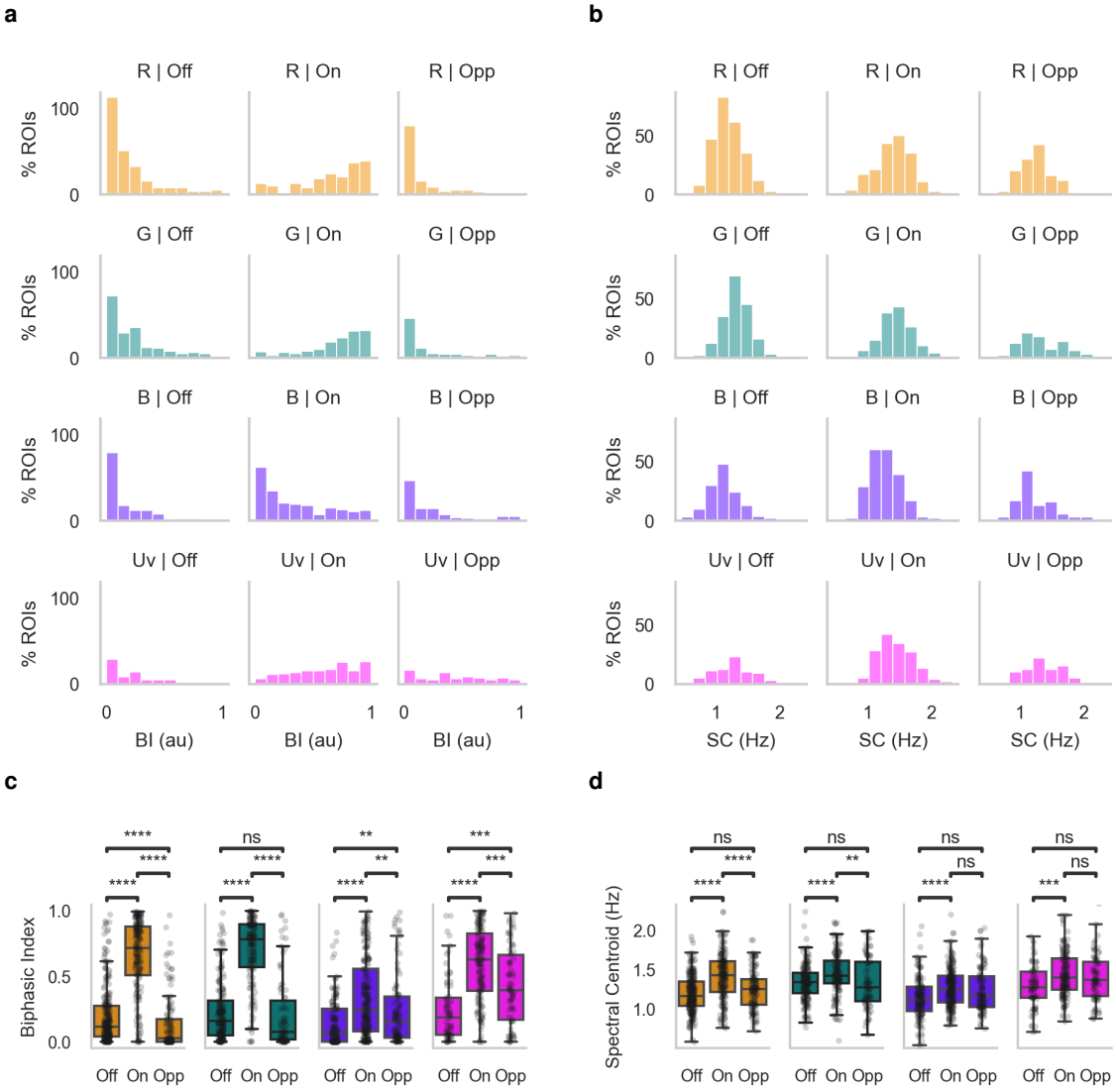

Figure 4.6: Temporal properties analysis by polarity categories. (a) Biphasic index distributions across Off, On, and Opponent cells showing the degree of temporal complexity in RF responses. **(b)** Spectral centroid distributions representing the temporal balance of RF responses across polarity categories. **(c)** Biphasic index statistical comparison across polarity types. Within-category colour effects: Off ($H=24.174$, $p<0.0001$), On ($H=140.962$, $p<0.0001$), Opponent ($H=61.352$, $p<0.0001$). Between-category polarity effects within colours: R ($H=229.193$, $p<0.0001$), G ($H=165.963$, $p<0.0001$), B ($H=46.898$, $p<0.0001$), UV ($H=65.412$, $p<0.0001$). **(d)** Spectral centroid statistical comparison across polarity types. Within-category colour effects: Off ($H=61.652$, $p<0.0001$), On ($H=54.811$, $p<0.0001$), Opponent ($H=18.812$, $p<0.001$). Between-category polarity effects within colours: R ($H=65.684$, $p<0.0001$), G ($H=21.993$, $p<0.0001$), B ($H=21.305$, $p<0.0001$), UV ($H=13.698$, $p<0.01$). Statistical significance annotations show pairwise Mann-Whitney U test with Bonferroni correction results between polarity categories (ns: $p > 0.05$; *: $p \leq 0.01$; **: $p \leq 0.001$; ***: $p \leq 0.0001$; ****: $p \leq 0.00001$).

4.3.5 Spectral content and polarity predict IPL stratification

We examined IPL depth distributions using polarity-based and integration-type analyses (Figure 4.7, Figure 4.8). This confirmed classic On/Off laminar organisation whilst revealing spectral stratification patterns. Off RFs distributed in outer IPL with longer wavelengths (R, G) more Off-biased than shorter wavelengths (B, UV). On encoding was most prominant in the 4th decile across channels, although the shorter wavelengths exhibited more distributed stratification with secondary peaks. Both B and UV showed strong in 2nd decile peaks, with increased stratification also in the 6th and 7th deciles, respectively.

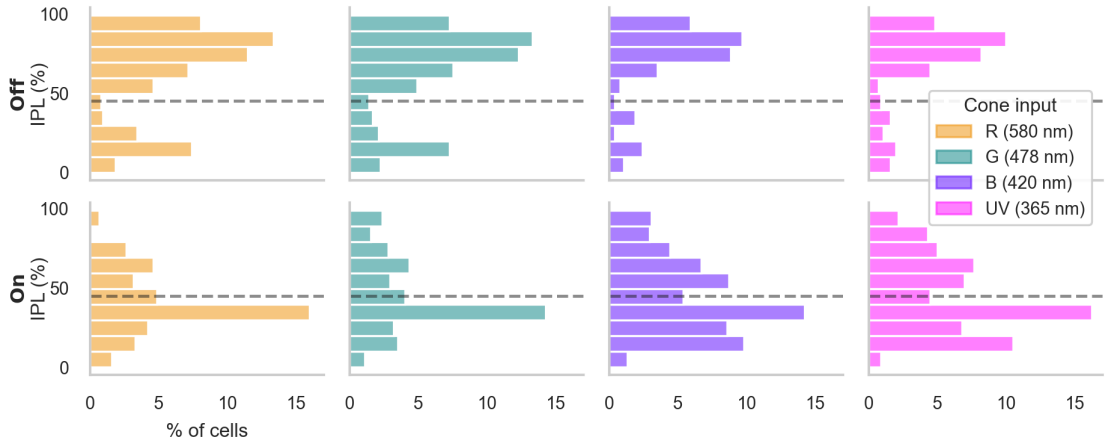

Figure 4.7: IPL stratification patterns by cone input type and polarity. Distribution of BC terminal ROIs across IPL depth (0% = ganglion cell layer, 100% = inner nuclear layer) organized by cone input and RF encoding polarity. Data is normalized so that within each cone input column, all bars sum to 100% across polarities and depth bins. Dashed horizontal line indicates the IPL threshold separating Off (above) and On (below) sublaminae. Off encoding shows fairly even distribution in the upper IPL with bias towards 7th-8th deciles and a distinct 2nd decile peak representing displaced Off terminals. Longer wavelengths (R, G) are more Off-biased than shorter wavelengths (B, UV). On encoding reveals predominant 4th decile stratification varying by spectral channel, with R and G showing stronger 4th decile dominance whilst B and UV exhibit more balanced distribution with secondary peaks in 6th-7th deciles.

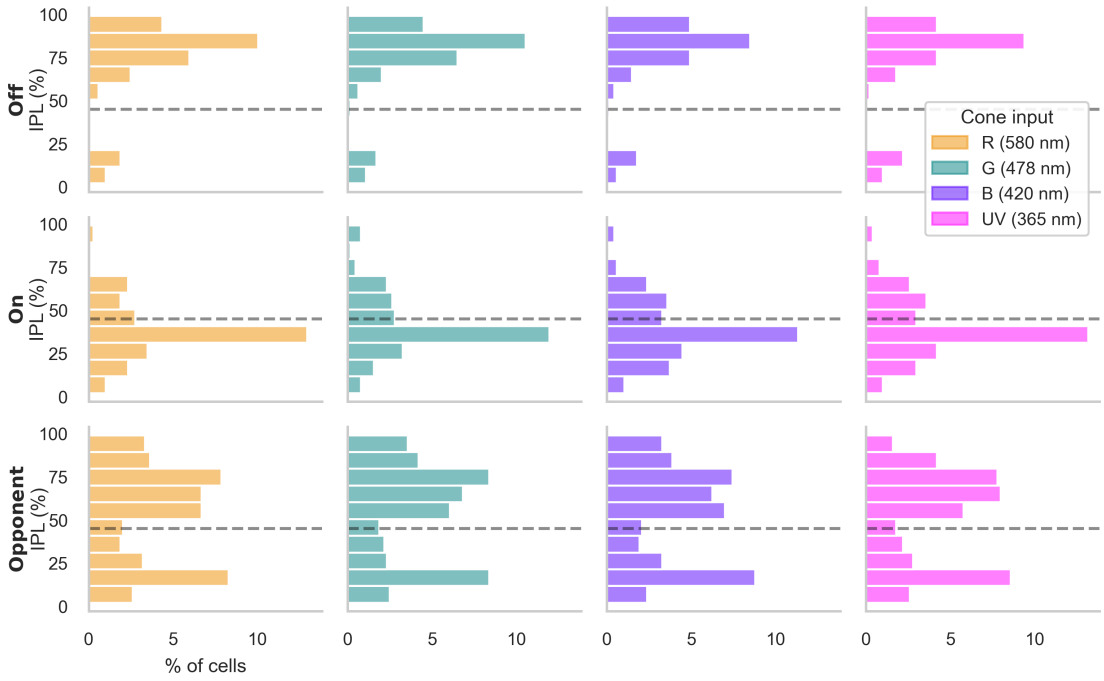

Figure 4.8: IPL stratification patterns by cone input type and integration type. Histograms showing the distribution of bipolar cell terminal depths within the IPL across different colour channels and integration types. Data is normalized so that within each cone input column, all bars sum to 100% across categories and depth bins. All spectral channels show strong 4th decile stratification in the On sublaminae. Off terminals remain relatively consistent across spectral channels with secondary peaks in 2nd decile indicating displaced Off terminals. Opponent terminals show distinct 2nd decile stratification, contrasting sharply with pure On types' 4th decile dominance, creating apparent homogenisation compared to the polarity-based analysis.

Comparing the two approaches revealed that apparent displacement in the polarity analysis was largely attributable to Opponent integration. Excluding Opponent ROIs, only 18.4% of pure On terminals stratified in Off sublaminae versus 11.5% of Off terminals in On sublaminae (See Appendix Table A.4). Opponent terminals showed distinct 2nd decile stratification, contrasting with pure On types' 4th decile dominance.

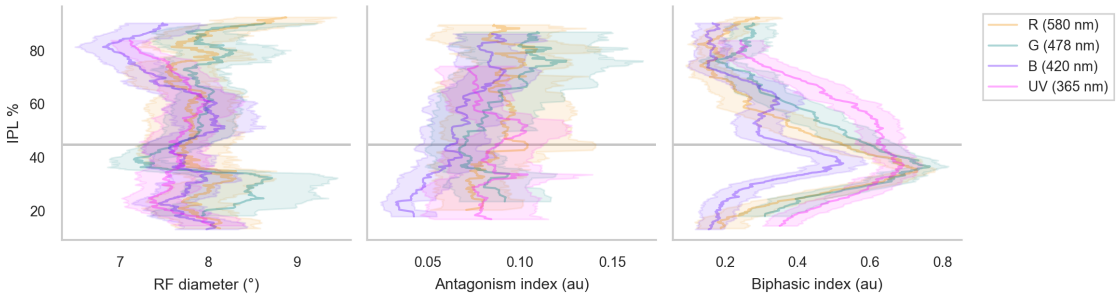

Figure 4.9: IPL stratification effects on spatiotemporal properties. Scatter plots show relationships between IPL depth (y-axis, 0% = inner boundary, 100% = outer boundary) and spatiotemporal metrics across spectral channels (R, G, B, UV) and integration categories (Off, On, Opponent). **Left column:** RF diameter shows minimal depth-dependent organisation (largest $r^2 = 0.017$). **Middle column:** Antagonism index exhibits weak stratification effects with modest correlation only in B channel On cells ($r^2 = 0.078$). **Right column:** Biphasic index demonstrates robust ON/OFF laminar organisation with strong category effects ($\eta^2 = 0.23$) and polarity-dependent stratification patterns. Trend lines show locally weighted scatterplot smoothing. Despite statistical significance in many comparisons due to large sample sizes (n > 1,800 RFs), effect sizes reveal that spatial properties show negligible IPL organisation whilst temporal properties confirm expected laminar segregation.

To determine whether spatiotemporal properties change as a function of IPL stratification, we performed statistical analyses within both spectral channel and integration type categories. The analysis revealed fundamentally different patterns for spatial versus temporal properties (Figure 4.9, Figure A.6).

Spatial properties showed minimal depth-dependent organisation. RF diameter exhibited no meaningful wavelength-specific stratification patterns across IPL depth, whilst antagonism indices showed weak associations with stratification depth. The strongest spatial-depth relationship was observed in B channel On cells, but remained modest. These minimal spatial effects suggest that IPL connectivity does not create systematic spatial gradients.

In contrast, temporal properties demonstrated robust laminar organisation consistent with classic ON/OFF pathway segregation. Biphasic index showed strong stratification effects, confirming that temporal integration characteristics reliably predict anatomical placement within IPL sublaminae. The heterogeneity observed in opponent terminals reflected their mixed On/Off signalling rather than systematic depth-dependent organisation, supporting the view that IPL organisation primarily reflects polarity-based pathway segregation rather than gradients in spatial or chromatic processing.

4.3.6 Clustering analysis reveals spectral organisation of bipolar cell receptive fields

In order to characterise the functional diversity of bipolar cells, we performed clustering analyses on their spatiotemporal receptive field properties. Recent transcriptomic studies have identified distinct molecular signatures of 21 cone BCs (Hellevik et al. 2024). Accordingly, we performed agglomerative hierarchical clustering on spatial and temporal metrics and specified 21 clusters to match expected bipolar cell diversity. The resulting clusters revealed distinct spatiotemporal processing strategies, with clear functional differentiation across spectral channels. Stratification within the IPL was specifically withheld in order to examine anatomical feasibility of the clustering based on spatiotemporal features.

Clustering faithfully captured the expected stratification patterns as predicted by the ROI's response characteristics. Off-encoding clusters stratified in deep layers of the IPL while On-encoding clusters typically stratified in shallow layers. Clustering yielded 7 pure Off clusters (n = 284, 34.2%), 9 pure On clusters (n = 411, 49.5%), and 5 Opponent clusters (n = 138, 16.6%), closely matching the overall population statistics (subsection 4.3.4). Clusters varied in size from 10 to 82 cells, with silhouette scores ranging from 0.101 to 0.550, indicating moderate cluster separation (detailed cluster metrics in Table A.2). Dimensionality reduced visualisations (PCA and t-SNE) confirmed clusters segregation (Figure 4.11).

Off clusters (C0, C1, C2, C3, C13, C16, and C18) were characterised by slow, monophasic temporal profiles and larger spatial extents. Their spectral content varied systematically in the number of cone channels integrated, showing a gradient from single-channel R (C1, C3) to block-wiring of R/G (C0, C2, C16) and tetrachromatic integration (C13). All Off clusters stratified predominantly in the outer half of the IPL, confirming their Off identity.

On clusters (C4, C7, C8, C10, C11, C12, C15, C17, C19, C20) represented the most diverse spectral integration types, encompassing a wide range of cone channel combinations and temporal kinetics. These varied from single-channel (C4, C6, C7, and C12) to block-wiring of B/UV (C11), R/G (C12), and R/G/B (C20). C19 exhibited full tetrachromatic integration, separated subtly by their temporal kinetics. Intriguingly, C20 exhibited relatively strong spatial antagonism across R/G/B channels, a feature not observed in other clusters. All On clusters stratified primarily in the inner half of the IPL.

The opponent clusters (C6, C9, C14, C16, and C17) all exhibited strong opponency. C6 and C17 exhibited distinct R Off vs UV On and R Off vs B On opponency, respectively, with clear spectral gaps. C9 showed G Off vs B/UV On and C16 showed R/G Off vs B/UV On. Again, one cluster differentiates itself by exhibiting strong spatial antagonism (C14), with R/G On vs UV Off. This cluster exhibited detectable antagonism in all channels. C0 may have exhibited weak R vs. B/UV opponency, but this could be a clustering artefact due to poor reconstruction. Nevertheless, the strongly opponent clusters all appear to be bistratifying. In common, the short wavelengths were On and the long wavelengths Off.

Figure 4.10: Functional clustering of bipolar cell receptive fields reveals spectral organisation. Reconstructed cluster averages as rows, with ID, and number of ROIs in cluster. Clustering analysis based on spatiotemporal receptive field properties demonstrates that spectral channel identity, rather than spatial complexity, drives functional diversity in the bipolar cell population.

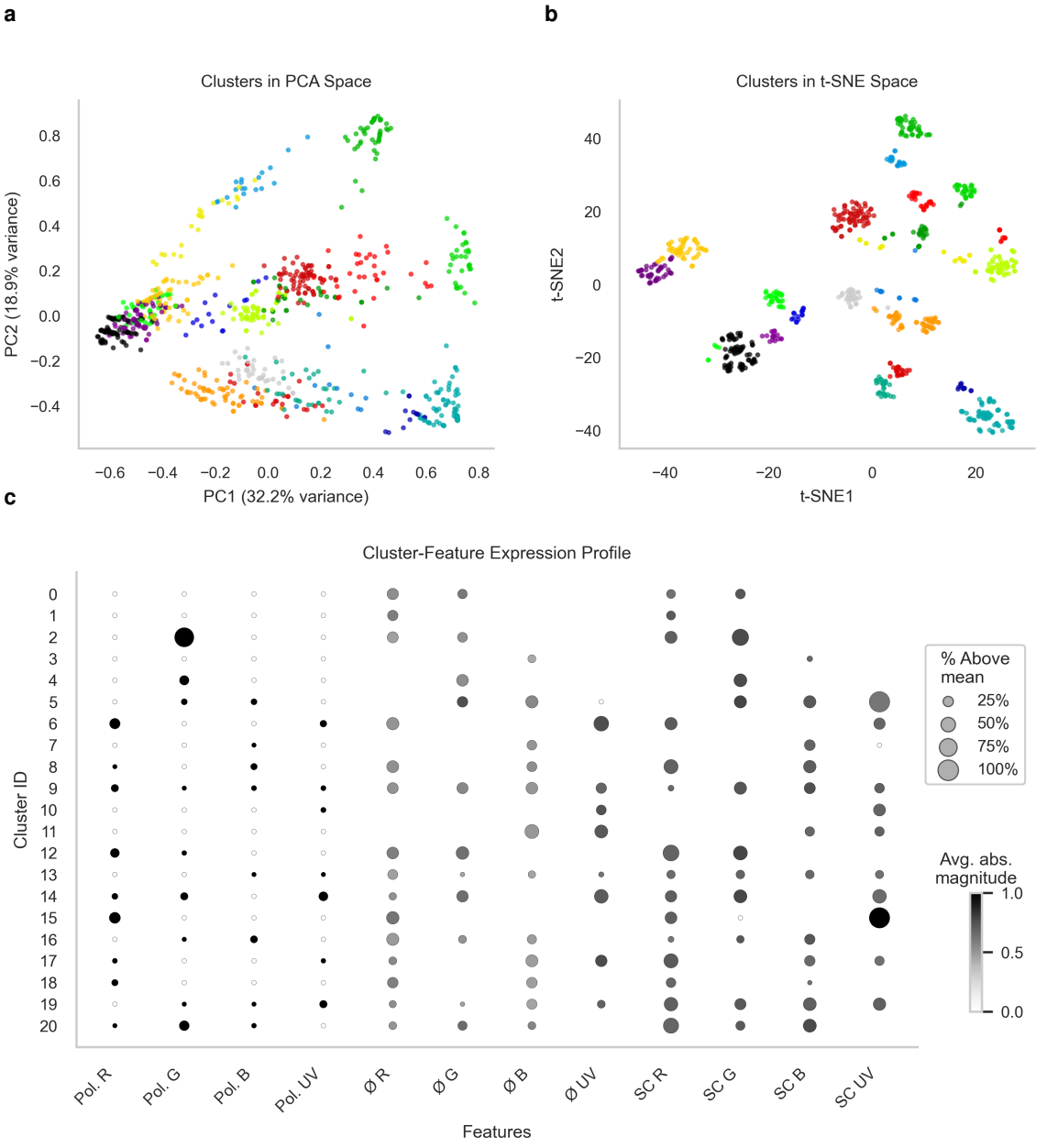

Figure 4.11: Dimensionality reduction visualisation of bipolar cell clustering. (a) Principal Component Analysis (PCA) projection showing separation of functional clusters based on the first two principal components. **(b)** t-distributed Stochastic Neighbour Embedding (t-SNE) visualisation reveals local neighbourhood structure within the clustering space. **(c)** Cluster-feature expression profile showing the percentage of cells above threshold (dot size, threshold = mean + 0.5 SD) and average magnitude among active cells (colour intensity) for a curated subset of discriminative spectral and temporal features across all 21 clusters. This subset highlights the most informative response properties for functional type classification (complete 20-feature profile in Figure A.5). Both methods demonstrate clear segregation of bipolar cell types according to their spectral and temporal response properties.

4.3.7 Surround contribution is overall weak

To further investigate surround contributions, we applied the centre-surround detection algorithm described in chapter 3 to identify RFs exhibiting spatial antagonism. The antagonism index was calculated as the balance of centre vs. surround contribution, with 1 denoting equal balance and 0 denoting total centre dominance. Centre-surround organisation was predominantly weak across the bipolar cell population (antagonism index: 0.045 ± 0.056, median: 0.026, range: 0.000-0.344). Statistical analysis revealed significant differences between clusters ($F = 3.811$, $p < 0.001$, $\eta^2 = 0.088$), with cluster identity explaining 8.8% of variance in opponency index. Integration categories showed no significant differences ($F = 1.299$, $p = 0.273$, $\eta^2 = 0.003$). Spectral channel analysis revealed modest but significant differences ($F = 5.618$, $p < 0.001$, $\eta^2 = 0.009$), with UV channels showing slightly higher opponency indices (0.054 ± 0.077) compared to other channels (R: 0.039 ± 0.066, G: 0.049 ± 0.073, B: 0.037 ± 0.062).

4.3.8 A subset of bipolar cells exhibit strong centre-surround organisation

A rare subset displayed robust centre-surround structure with substantially higher antagonism indices, contributing to the spatially antagonistic clusters. We defined the threshold for these ROIs as a spatial antagonism index of 0.33 to effectively separate this minority from the main population. 94.2% of ROIs fell below this threshold, showing minimal spatial antagonism. However, 5.8% ($n = 47$) of BC terminals exhibited significantly stronger spatial antagonism (antagonism index: 0.493 ± 0.167) than the main population (Mann-Whitney $U = 191{,}825$, $p < 0.001$).

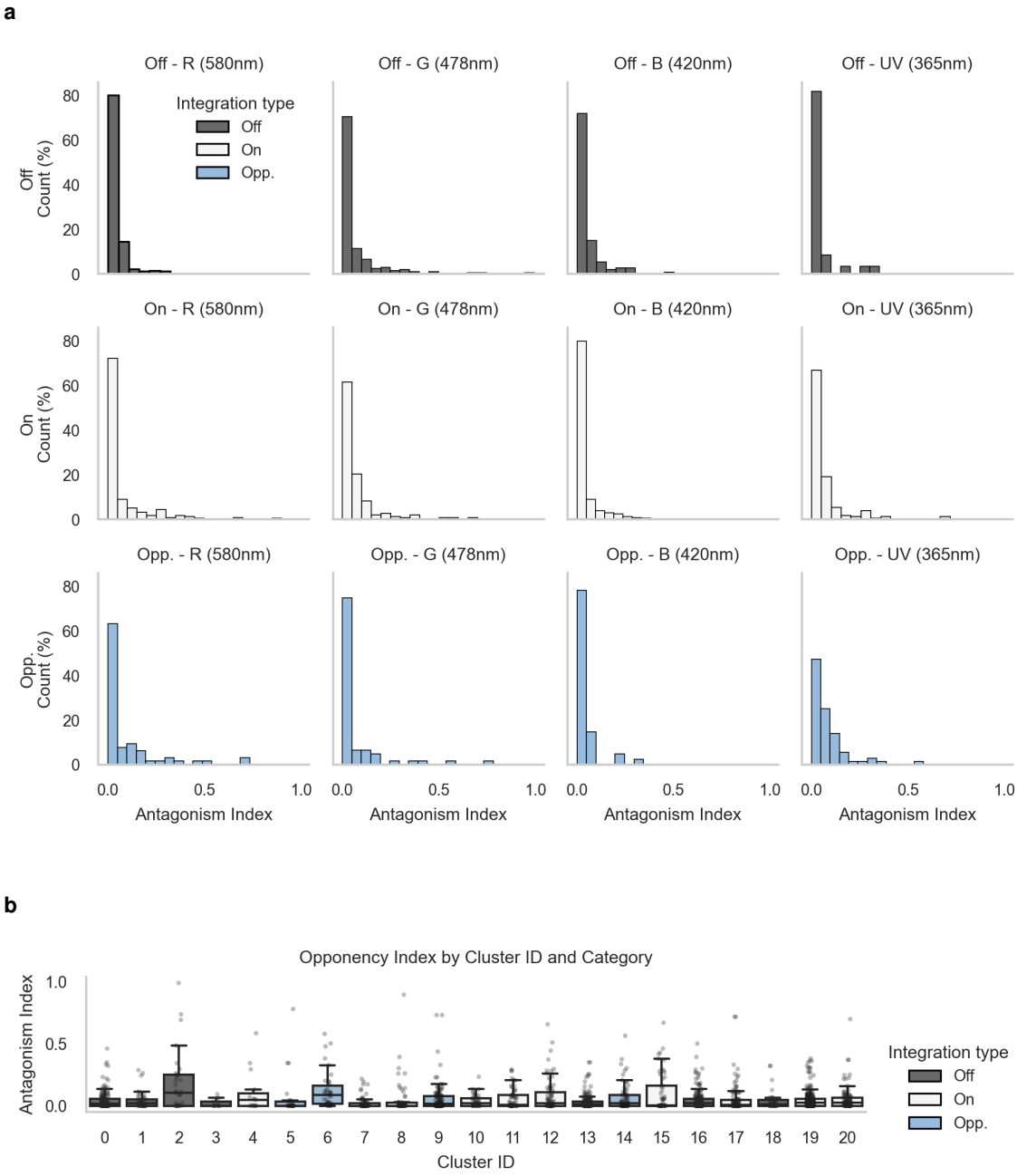

Figure 4.12: Center-surround analysis across colour channels and functional categories. (a) Distribution of antagonism indices across encoding types and colour channels (R, G, B, UV). **(b)** Antagonism index by cluster ID and category. Boxplots show the distribution of antagonism indices across all clusters, grouped by their functional category (OFF, ON, Opponent). Individual data points are overlaid as semi-transparent dots. Most clusters exhibit minimal surround structure regardless of their encoding type. Statistical analysis: Category effect ($F=1.299$, $p=0.273$, $\eta^2=0.003$, n=284/411/138 ROIs for Off/On/Opponent), Cluster effect ($F=3.811$, $p<0.001$, $\eta^2=0.088$, 21 clusters, 10-82 ROIs per cluster).

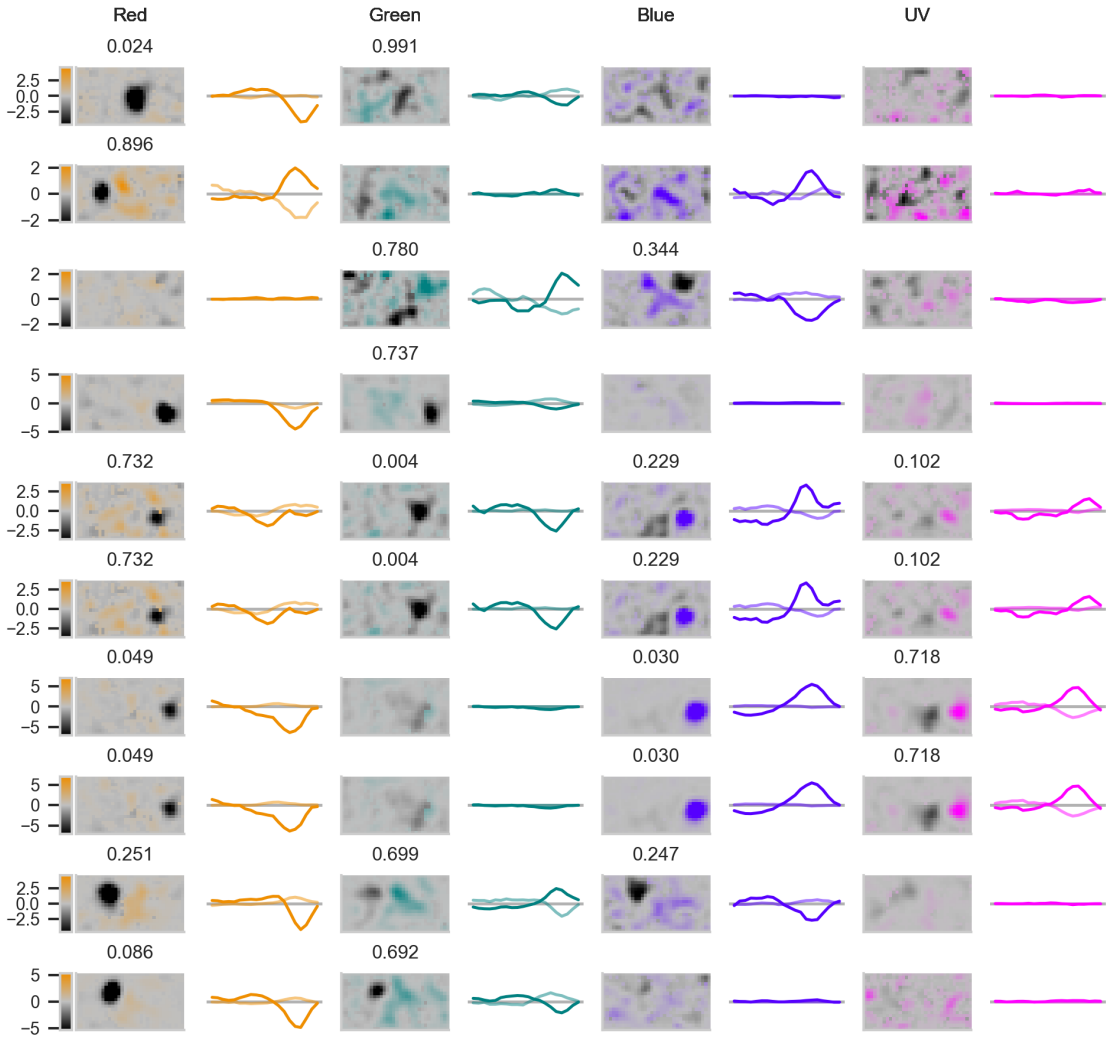

Figure 4.13: Spatial and temporal profiles of the 10 most spatially antagonistic ROIs. Centre-surround organization across spectral channels showing surround contribution as a percentage and opponency index above each RF. No score indicates that no signal was detected in the given channel. Each row represents a single ROI, and the columns its spectral content. The colour bar is representative for the colour map for all subplots, normalised within each row.

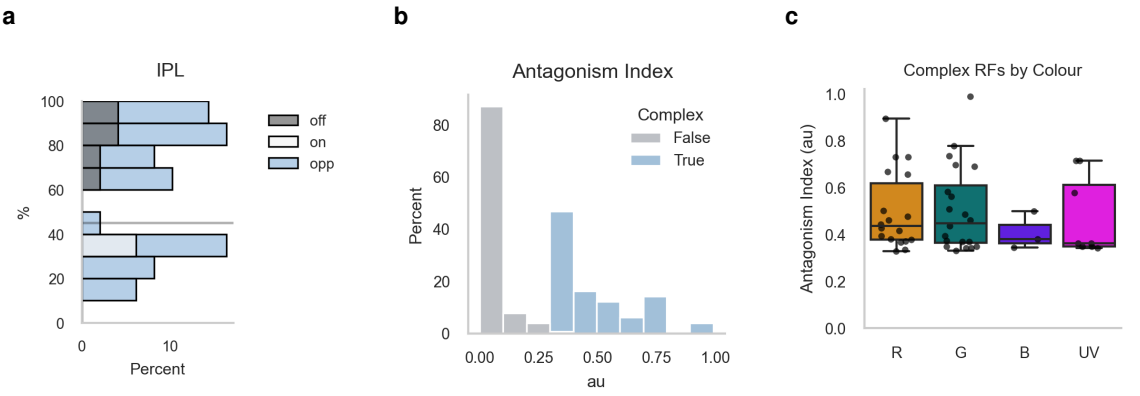

Figure 4.14: Statistical summary for strongly antagonistic bipolar cell receptive fields. (a) IPL distribution of ROIs yielding complex RFs. Note the bimodal distribution among the On and Off layer. This reflects the centre-component's true identity rather than being bistratifying BCs. **(b)** The distribution in antagonism index, shown for complex and non-complex cells, normalised within their categories. **(c)** Spatial antagonism index by colour channel for spatially complex RFs (antagonism index > 0.33).

4.4 Discussion

4.4.1 Spectral channel identity and encoding polarity are the primary determinants of bipolar cell receptive field characteristics

Larval zebrafish present a unique opportunity to investigate in-vivo how spectral complexity influences spatial organisation in bipolar cells. Each of their four cone types exhibit distinct spectral sensitivities, temporal kinetics, and gain properties (Endeman, Klaassen, and Kamermans 2013; Yoshimatsu, Schröder, et al. 2020; Carleton et al. 2020), creating systematic differences in photoreceptor inputs. BCs actively leverage this tetrachromatic diversity through systematic spectral integration types (Bartel, Yoshimatsu, et al. 2021; Wang et al. 2023; Zimmermann et al. 2018), constructing distinct spectral channels through selective convergence and opponent mechanisms.

However, the full chromatic repertoire of spatial integration in zebrafish BCs remains underexplored. Recent studies have investigated temporal and chromatic encoding in larval zebrafish BCs (Bartel, Yoshimatsu, et al. 2021; Wang et al. 2023; Zimmermann et al. 2018). Moreover, a handful of studies have investigated spatial encoding (Johnston, Seibel, et al. 2019; Antinucci, Suleyman, et al. 2016). However, these studies used only R light stimulation, which drives only a subset of BCs (Zimmermann et al. 2018; Bartel, Yoshimatsu, et al. 2021). Whether spatial characteristics are consistent across all spectral channels, and how they relate to chromatic integration types, remains unknown.

Here, we show that spatial antagonism in the larval zebrafish BC population is overall weak, with only a small subset (5.8%) exhibiting strong centre-surround organisation (Figure 4.12b). Instead, spectral channel identity and encoding polarity are the primary determinants of RF spatiotemporal characteristics. Longer wavelengths (R, G) produce larger, more variable RFs with slower temporal kinetics, while shorter wavelengths (B, UV)

yield smaller, more uniform RFs with faster kinetics (Figure 4.2a, Figure 4.3b). Encoding polarity further modulates these properties, with Off RFs showing simple monophasic profiles and On RFs exhibiting complex biphasic kinetics. Anatomically, these functional types stratify predictably within the IPL, confirming the strong link between spectral content, polarity, and neuroanatomy.

4.4.2 Tetrachromatic inputs afford diverse bipolar cell receptive field characteristics

Spectral channel identity emerged as the primary determinant of RF spatial characteristics. Receptive field areas followed a consistent pattern of longer wavelengths producing larger and more variable RFs than shorter wavelengths. Moreover, this dichotomy translated to the temporal domain, with longer wavelengths exhibiting slower response kinetics and shorter wavelengths responding faster.

These findings are in line with previous studies of spectral integration in larval zebrafish BCs (Bartel, Yoshimatsu, et al. 2021; Zimmermann et al. 2018), which identified systematic gradients of spectral integration from long to short wavelengths. However, our results extend these findings by demonstrating that spectral channel identity also influences spatial properties. We found a consistent hierarchy of R > G > B > UV in terms of size and size uniformity, although the mean differences in size were modest (around 0.5 ° in diameter on average) (Figure 4.2b). In contrast to spatial extent, RF shape properties showed no spectral dependence (Figure 4.2c). This indicates that while spectral channels influence RF size and variability, they do not alter fundamental spatial organisation patterns.

4.4.3 The interplay between spectral channel and encoding polarity

When looking at the data by cone channels alone, we found that longer wavelengths (R, G) preferentially drive Off pathways (approximately 60% Off), while shorter wavelengths (B, UV) favour On pathways (approximately 70% On) (Table 4.1). Off terminals exhibited simple monophasic temporal profiles consistent with sustained feature encoding. Conversely, On terminals displayed varying degrees of biphasic temporal integration, providing temporal contrast enhancement suitable for detecting transient events like motion, flicker, and moving edges. This biphasic character was strongest in G and R On channels, whilst B and UV On RFs showed surprisingly simplified temporal profiles despite their On identity (Figure 4.3a).

The heterogeneity within the population was further elucidated by examining the interplay between spectral channel identity and the encoding polarity of the measured BC terminals. A terminal's integration type (On, Off, Opponent) significantly influenced its spatiotemporal characteristics. The R channel was the only channel unaffected by integration type, while G, B, and UV channels showed significant polarity effects on RF size (Figure 4.6). Notably, Off terminals exhibited smaller diameters in B and UV channels compared to On and Opponent terminals, indicating distinct processing characteristics for short-wavelength Off signals. Additionally, G RFs were largest in Opponent terminals, but smallest in On

terminals.

Anatomically, this functional organisation mapped predictably onto IPL stratification, with chromatic content and polarity serving as strong predictors of anatomical placement (Figure 4.7). This agrees with previous findings in the larval zebrafish retina (Bartel, Yoshimatsu, et al. 2021), particularly with stratification patterns at the horizon (Zimmermann et al. 2018).

The opponent-specific stratification patterns observed in Figure 4.7 versus Figure 4.8 reflect the integration of long and short wavelength signals by opponent cells. This integration creates intermediate stratification patterns that span multiple spectral channels at the anatomical level. Opponent cells predominantly integrate long (R, G) versus short (B, UV) wavelength signals, as demonstrated by the clustering analysis (Figure 4.10). This long vs short integration pattern explains why the 2nd decile peak appears across all spectral channels in opponent stratification rather than being restricted to specific channels.

Since temporal integration reflected the polarity of the RF, kinetics varied with IPL stratification according to the RF's polarity. However, spatial properties (size, antagonism) showed no meaningful organisation within IPL stratification. This suggests that connectivity in the IPL serves to organise colour information by routing it to discrete sublaminae rather than creating spatial gradients. The spatiotemporal heterogeneity within polarity groups (Figure 4.6, Figure 4.5) indicates that functionally diverse bipolar cell subtypes emerge from the intersection of spectral and polarity dimensions rather than spatial complexity.

4.4.4 Surrounds are overall weak but a subset exhibit strong centre-surround organisation

Spatial antagonism in the form of concentric centre-surround organisation is a foundational principle of retinal processing (Barlow 1961; Marr, Hildreth, and Brenner 1980; Turner, Schwartz, and Rieke 2018). Classical models propose approximately balanced centre and surround contributions, with surround strength typically ranging from 50-100% of centre strength in mammalian models (Dacey et al. 2000; Strauss et al. 2022; Gaynes et al. 2022). Recently, studies in mice have shown that BCs surround interactions mediate spatial computations and contribute to efficient encoding of natural environments (Franke, Berens, et al. 2017; Hsiang et al. 2024). However, most of this understanding derives from studies in terrestrial mammals with dichromatic vision. We expected to see centre-surround antagonism, although were expecting their spatial extents to be larger than in terrestrial mammals based on previous descriptions of teleost BCs (Saito and Kaneko 1983; Toyoda 1973; Burkhardt, Bartoletti, and Thoreson 2011).

We instead found that classical centre-surround organisation was not a dominant feature of bipolar cell RFs in larval zebrafish retina. The vast majority (94.1%) exhibited weak or undetectable surround structure, with over 50% of RFs having an antagonism index below 0.05 indicating negligible surround influence. Instead, functional clustering revealed

21 functional clusters organised primarily around spectral integration types (Figure 4.10), suggesting that tetrachromatic diversity provides sufficient computational resources without requiring complex spatial architectures. Even the most spatially antagonistic clusters had surrounds accounting for only about 7% of their RF signal. Statistical analysis revealed negligible differences across integration categories or spectral channels, suggesting that spectral channel identity rather than spatial complexity drives bipolar cell diversity.

However, a rare subset (5.9%) displayed robust centre-surround structure with substantially higher opponency indices (0.493 ± 0.167), indicating a roughly 35% surround contribution (Figure 4.14). These were primarily found in R, G and UV channels, and were typically from Opponent ROIs (ca. 80%). Intriguingly, their proportion matches the 5% of BCs reported by others (Antinucci, Suleyman, et al. 2016), perhaps hinting at a functionally distinct subset.

4.4.5 Implications for spatial processing in larval zebrafish

The predominance of weak surrounds raises questions about spatial processing mechanisms. Weak surrounds may be sufficient for basic spatial processing while the strongly antagonistic subset handles complex spatial tasks. For example, Johnston, Ding, et al. 2014 showed that 25% of presynaptic and 47% of postsynaptic BCs synapses exhibited OS, perhaps indicating that diffuse surrounds are sufficient for weak spatial nonlinearities.

An alternative explanation is that spatial antagonism in the IPL may emerge through multichromatic interactions rather than within individual spectral channels. This would lean more towards the observations of double opponency in carp BC (Kaneko and Tachibana 1981; Shimbo et al. 2000), generating spatial processing through spectral opponency patterns that are not apparent when examining individual colour channels in isolation. The next chapter directly examines this hypothesis.

Hierarchical clustering based on spatiotemporal receptive field properties successfully identified 21 distinct bipolar cell types that closely matched expected transcriptomic diversity (Hellevik et al. 2024). The clustering yielded 7 pure Off clusters, 8 pure On clusters, and 6 Opponent clusters, each faithfully capturing the expected anatomical stratification patterns within the IPL.

Off clusters were characterised by slow, monophasic temporal profiles and systematically varied in spectral integration from single-channel red to full tetrachromatic convergence. On clusters displayed the greatest spectral diversity, encompassing single-channel responses (UV, red, green, blue) through various block-wiring patterns (B/UV, R/G, R/UV) to full tetrachromatic integration. Opponent clusters demonstrated primarily long-versus-short wavelength comparisons, with strongly opponent types dividing along the red-green versus blue-UV axis. This organisation demonstrates that spectral channel identity, rather than spatial complexity, serves as the primary mechanism for generating bipolar cell functional diversity.

4.4.6 Limitations and future directions

Several limitations should be noted. First, we did not detect any degree of double opponency as expected based on previous teleost descriptions (Kaneko and Tachibana 1981; Burkhardt, Bartoletti, and Thoreson 2011; Shimbo et al. 2000). One explanation is that the sequential colour content of the CCA stimulus (described in-depth in chapter 3) does not allow for simultaneous multispectral stimulation in its current form. We were expecting to see spatial antagonism in multiple colour channels whose sum would be double opponent, but this was not present even in the highly antagonistic terminals.

Another explanation for this is that the developmental stage examined here (5-9 dpf larvae) may not represent mature retinal organisation. Adult zebrafish may exhibit different spatial processing mechanisms, and comparative developmental studies could reveal how spectral-spatial balance evolves with maturation.

In the temporal domain, calcium imaging introduces temporal delays that limit precise temporal characterisation, as evidenced by response latencies exceeding 200 ms due to acquisition rates of 15.625 Hz. Faster imaging techniques could provide more accurate temporal profiles, although at the expense of spatial resolution and experimental throughput. Future experiments should trial glutamate imaging for even faster kinetics and a direct readout of transmission events (Marvin et al. 2018).

Finally, our spatial analysis here presented, primarily in the form of size and shape metrics, may not fully capture the complexity of spatial processing. Integrated spatiochromatic analyses that consider interactions between spectral and spatial dimensions could reveal more nuanced organisational principles. The following chapter directly addresses this limitation.

4.5 Summary

Our investigation reveals a departure from classical retinal processing models in larval zebrafish bipolar cells. Spectral channel identity, rather than spatial complexity, emerges as the primary driver of functional diversity through systematic spectral-polarity patterns with minimal centre-surround antagonism. This contrasts the classical centre-surround models of terrestrial retina RFs and demonstrates that larval zebrafish leverage tetrachromatic integration in the outer retina to achieve diverse BC signalling. In the next chapter we assess whether complex spatial processing emerges through multichromatic interactions rather than as classical spatial antagonism.

5 | Non-classical spatial antagonism in the larval zebrafish retina

5.1 Introduction

5.1.1 Background

The previous chapter showed that larval zebrafish bipolar cells exhibit minimal classical centre-surround organisation, with spectral channel identity emerging as the primary driver of functional diversity. However, classical retinal theory assumes that spatial antagonism arises through approximately balanced concentric centre-surround antagonism (Barlow 1961; Marr, Hildreth, and Brenner 1980). In fact, centre-surround antagonism has been directly demonstrated to mediate spatial processing in the mammalian outer retina (Franke, Berens, et al. 2017; Hsiang et al. 2024; Strauss et al. 2022). This raises a fundamental question: if individual spectral channels show spatially simple organisation, how do bipolar cells achieve the antagonistic spatial processing necessary for visual computations?

The weak surround structure observed in larval zebrafish bipolar cells suggests that alternative mechanisms may generate spatial antagonism. One possibility is that spatial antagonism emerges through systematic relationships between multiple spectral channels rather than within single chromatic pathways. Several lines of evidence support this hypothesis. First, strongly colour opponent cells constitute a significant fraction of bipolar cells (approximately 20%, chapter 4). Second, double opponent cells in carp demonstrate that complex spatiochromatic interactions occur in the teleost outer retina (Kaneko and Tachibana 1981; Shimbo et al. 2000). Third, zebrafish cones exhibit systematic opponent relationships (Bartel, Janiak, et al. 2021), with ACs acting as regulatory circuits that modulate spectral opponency across bipolar cell populations to maintain computational diversity (Wang et al. 2023), providing a substrate for spatiochromatic interactions.

Additionally, the zebrafish environment is predominantly broadband, rather than spectrally pure (see Figure 5.1a, b). Natural underwater scenes are dominated by achromatic content, comprising around 90% of scene variance (Zimmermann et al. 2018). Moreover, zebrafish cone opsins exhibit broad, overlapping spectral sensitivities meaning most natural stimuli simultaneously activate multiple spectral channels (Figure 5.1c, d).

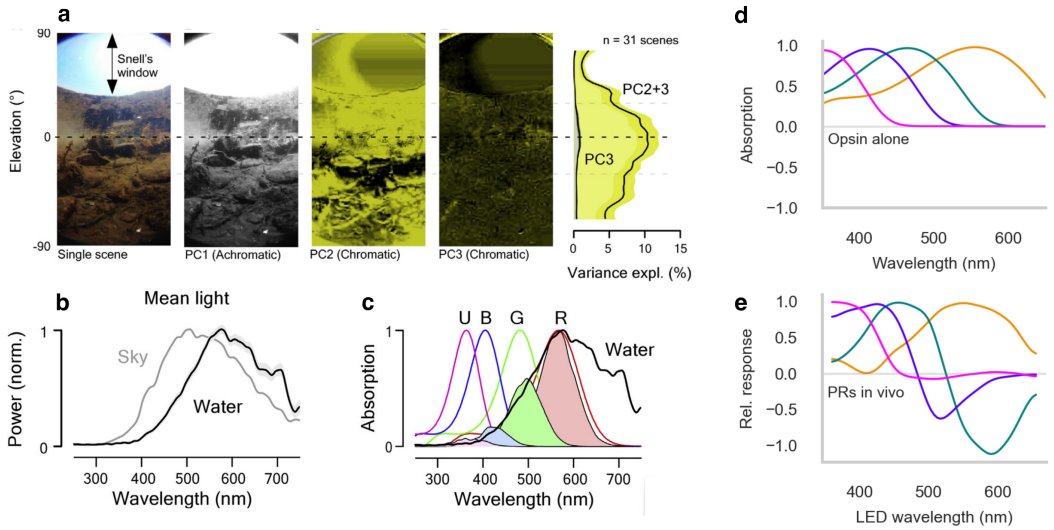

Figure 5.1: Natural visual environments are predominantly broadband rather than spectrally pure. (a) Natural scene statistics from zebrafish habitat showing analysis of hyperspectral image anaylsis using PCA, from Zimmermann et al. 2018. PC1 captures achromatic content (>90% variance), demonstrating that natural scenes are predominantly broadband. PC2-3 capture remaining chromatic content, showing pure colour information represents a minority of natural visual information. Variance analysis across image elevations confirms chromatic content is spatially restricted. **(b)** Mean underwater spectra from zebrafish natural habitat, demonstrating broadband spectral content (Zimmermann et al. 2018). **(c)** Zebrafish opsin complement multiplied with mean underwater spectrum to estimate relative photon catch rates in natural conditions (Zimmermann et al. 2018). **(d)** Log-opsin sensitivity spectra showing overlapping spectral sensitivities across tetrachromatic channels (adapted from Yoshimatsu, Bartel, et al. 2021). **(e)** Photoreceptor responses to spectral steps at 12 different wavelengths (adapted from Yoshimatsu, Bartel, et al. 2021).

5.1.2 Motivation

Given this ecological context, we here used broadband 'white' stimulation to closer approximate natural conditions. We sought to address whether the weak centre-surround structures observed under single-channel stimulation were genuinely weak, or the result of unnatural stimulation conditions. We hypothesised that under broadband conditions, the increased cone output onto BC should more preferably drive spatial integration, and that this in conjunction with the cone opponencies (Figure 5.1e) could increase detectable spatial antagonism yielding classic centre-surround morphologies.

Additionally, since ACs mediate lateral inhibition, disrupting their function should reveal whether they contribute to BC RF organisation despite the observed weak surrounds. If RF sizes increase after AC block, this would indicate that ACs contribute to spatial organisation and confirm that the surrounds, while weak, contribute to spatial processing in the larval zebrafish.

5.1.3 Objectives

To test this hypothesis, we employed three complementary approaches: (1) 'white' stimulation (simultaneous activation of R, G, B, and UV channels) to investigate cross-channel interactions under ecologically relevant broadband conditions; (2) simple stimuli to confirm weak surround antagonism and assess orientation selectivity; and (3) pharmacological blocking of lateral inhibition from ACs to determine their role in spatial organisation and spectral opponency.

5.1.4 Key findings

We found that under 'white' stimulation, spatial antagonism remained low across the population. However, this uncovered a small subset of terminals that had strong spatial antagonism. These spatially antagonistic terminals displayed no response when their entire RF was illuminated and featured orientation selectivity. We found that opponent terminals under the tetrachromatic condition exhibited spatially offset sensitivities with long (R,G) and short (B,UV) wavelengths showing near-oppositional orientations (near 180° separation). Their offsets may explain the strong spatial antagonism observed under 'white' stimulation, suggesting cross-channel interactions enable spatial computations. Pharmacological AC block abolished these wavelength-dependent patterns and reduced spatial antagonism, demonstrating that lateral inhibition shapes cross-channel spatial organisation. Additionally, it revealed that ACs contribute to spatial tuning by sharpening RF centres, implicating the weak surrounds as a functional component of spatial processing.

5.2 Methods

All methods carried out as described in chapter 4, with the following additions.

5.2.1 Broadband 'white' stimulation

For a subset of experiments, we modified the tetrachromatic stimulation approach by activating all four LED channels simultaneously rather than cycling through them sequentially. This broadband condition, which we term 'white' stimulation (RGBUV), used the same shifting noise stimulus except each stimulus box incorporated all LED channels simultaneously. LED power ratios were preserved as described in chapter 2 to maintain consistent natural statistics of light intensities.

5.2.2 Pharmacological block of amacrine cells

In a subset of experiments, a drug cocktail designed to block lateral inhibition in the inner retina was used. This has recently been successfully demonstrated in Wang et al. 2023. In short, the cocktail consisted of gabazine, (1,2,5,6-Tetrahydropyridin-4-yl) methylphosphinic acid (TPMPA), and CNQX at a ratio of 1:1:1 with a 5 µL volume, and blocks $GABA_A$, $GABA_C$, and glycine receptors, respectively. Previous use of this cocktail included 1 mM Alexa 594, but here this was replaced with double-distilled water. The solution was injected intraocularly, through the cornea and between the iris and lens, targetting the retinal vasculature directly. It is likely that the injection occasionally was instead injected into the vitreous and diffused through to the retina. Accordingly, disinhibition was assessed during based on slower response kinetics, baseline shift, and an unmasking of On-Off responses to full-field flashes (Wang et al. 2023). In some cases the injection lead to an 'overdose', causing the retina to oscillate spontaneously. In these cases, the experiment was terminated and the data discarded.

5.2.3 Spectral integration analysis

To quantify how uniformly spectral channels are integrated within individual bipolar cell terminals, we computed the coefficient of variation (CV) of spatial amplitude responses across the four spectral channels (R, G, B, UV) for each ROI. The coefficient of variation was calculated as the standard deviation divided by the mean of the absolute amplitude values across spectral channels:

$$CV = \frac{\sigma}{\mu + \epsilon} \tag{5.1}$$

where σ is the standard deviation, μ is the mean amplitude, and ϵ is a small constant ($1{\times}10^{-10}$) to avoid division by zero. Lower CV values indicate more uniform spectral integration, whilst higher values indicate greater selectivity or dominance by specific spectral channels. For ROIs with all zero amplitudes, CV was set to zero.

5.2.4 Spatial offsets and correlation analysis

Spatial relationships between spectral channels were quantified using two approaches. First, we computed spatial correlations by flattening each spectral channel's receptive

field and calculating pairwise Pearson correlations, yielding a correlation matrix with 1 indicating perfect alignment and 0 indicating no overlap. Channels with no signal were set to NaN to avoid spurious correlations. Additionally, we computed spatial offset vectors by calculating each ROI's 'true' centre as the mean centroid across all spectral channels, then calculating vectors from this reference to each channel's centroid. For non-concentric 'white' receptive fields with clear On and Off lobes, vectors were computed between Off and On lobe centroids.

5.2.5 Additional visual stimuli

To verify the weak surround antagonism findings from chapter 4 and assess orientation selectivity, additional stimulus paradigms were employed following 'white' RF mapping.

Bar stimuli for surround verification

To demonstrate the absence of strong surround antagonism, we employed vertical bar stimuli across the visual field (n=3 experiments). The screen was divided into 15° vertical bars spanning the visual field, with the first and last bars extending beyond screen boundaries. Each bar was flashed for 2 seconds against a dark background, followed by 2 seconds darkness. Stimuli began with bright flashes at each position sequentially. After completing all positions, a 100% contrast step reversed stimulus polarity, and dark flashes were presented in the same sequence against a bright background. The full sequence was repeated 10 times per recording. Responses were assessed qualitatively for evidence of centre-surround antagonism, expecting sign reversal in calcium traces for cells with strong surrounds.

Moving bar stimuli for orientation selectivity

Following RF mapping, a subset of experiments included moving bar stimuli to assess orientation selectivity (n=3 experiments). Fish were grey-adapted for approximately 10 minutes prior to these experiments. Moving bars consisted of gradient-contrast stimuli that ramped from 0% to 100% contrast against a grey background. Each bar was 10° wide × 2 units, presented in On-Off and Off-on sequences (bright bar followed by dark bar, and vice versa). Bars moved at 45°/second across 8 directions: 0°, 45°, 90°, 135°, 180°, 225°, 270°, and 315°. Orientation tuning functions were computed for each responsive ROI by measuring peak response amplitude in each direction. Orientation selectivity was assessed qualitatively by comparing tuning curves and directionality between spatially simple and spatially antagonistic receptive fields.

5.2.6 Statistics

All statistical analyses were performed using Python with SciPy, NumPy, and Pingouin packages. Data were assessed for normality using the Shapiro-Wilk test, with non-parametric alternatives employed when assumptions were violated. Spatial correlations between spectral channels were computed using Pearson correlation coefficients on

flattened spatial receptive field profiles. Average correlation matrices were calculated for each integration type (Off, On, Opponent). Threshold analyses used a correlation cutoff of 0.8 to identify spatially decorrelated receptive fields, with proportions compared between conditions using Mann-Whitney U.

For angular data (spatial offset directions), circular statistics were employed using the Watson-Williams test for comparing mean directions between groups. This test assesses whether two or more samples of angular measurements have the same mean direction, accounting for the circular nature of angular data where 0° and 360° are equivalent. Circular variance was calculated to quantify the concentration of angular distributions, with values approaching 0 indicating highly concentrated distributions and values approaching 1 indicating uniform circular distributions.

5.3 Results

5.3.1 'White' stimulation revealed split-field receptive fields

In a subset of experiments, we changed the stimulation paradigm to present all spectral channels simultaneously, which we refer to as 'white' stimulation. This approach allowed us to investigate how bipolar cell terminals integrate spatial information when all colour channels are active at once, as they are in nature. 21 recordings were performed across 14 fish, yielding 1325 RFs that passed inclusion criteria (chapter 2 , chapter 4). Under this condition spatial antagonism remained weak (antagonism index: 0.039 ± 0.073), yielding simple spatial receptive fields in the vast majority of terminals, consistent with previous findings (chapter 4).

However, a subset of terminals (4.2%) exhibited strongly antagonistic, non-concentric RF structures. These RFs displayed a Gabor-like split-field spatial arrangement, as if an On and Off channel were combined. The IPL stratification pattern of these terminals were similar to that of opponent terminals observed under the standard cycling spectral stimulation (Figure 5.2b, c). The split-field RFs had a substantially higher antagonism index (0.534 ± 0.172). When measuring the angle between their On and Off lobe, they exhibited a distinct 90° bias, with a secondary peak at 0° and 180° (Figure 5.2e).

5.3.2 Simple bar stimulus confirmed spatial profiles

To verify the weak surrounds described in chapter 4, we conducted bar stimuli experiments (n = 3) using sequential 15° vertical bars across the visual field. Most cells showed simple responses with minimal surround antagonism (Figure 5.3). Some Off cells had weak antagonistic deflections approximately 30° from their receptive field centres, whilst On cells showed no detectable surround responses. These results confirmed that bipolar cells exhibit predominantly weak surround antagonism, consistent with antagonism index measurements. The split-field RFs consistently showed only minimal, transient responses to the vertical bars and no response to the contrast steps in the stimulus (Figure 5.3), indicating their On and Off lobes cancel each other when simultaneously stimulated. This

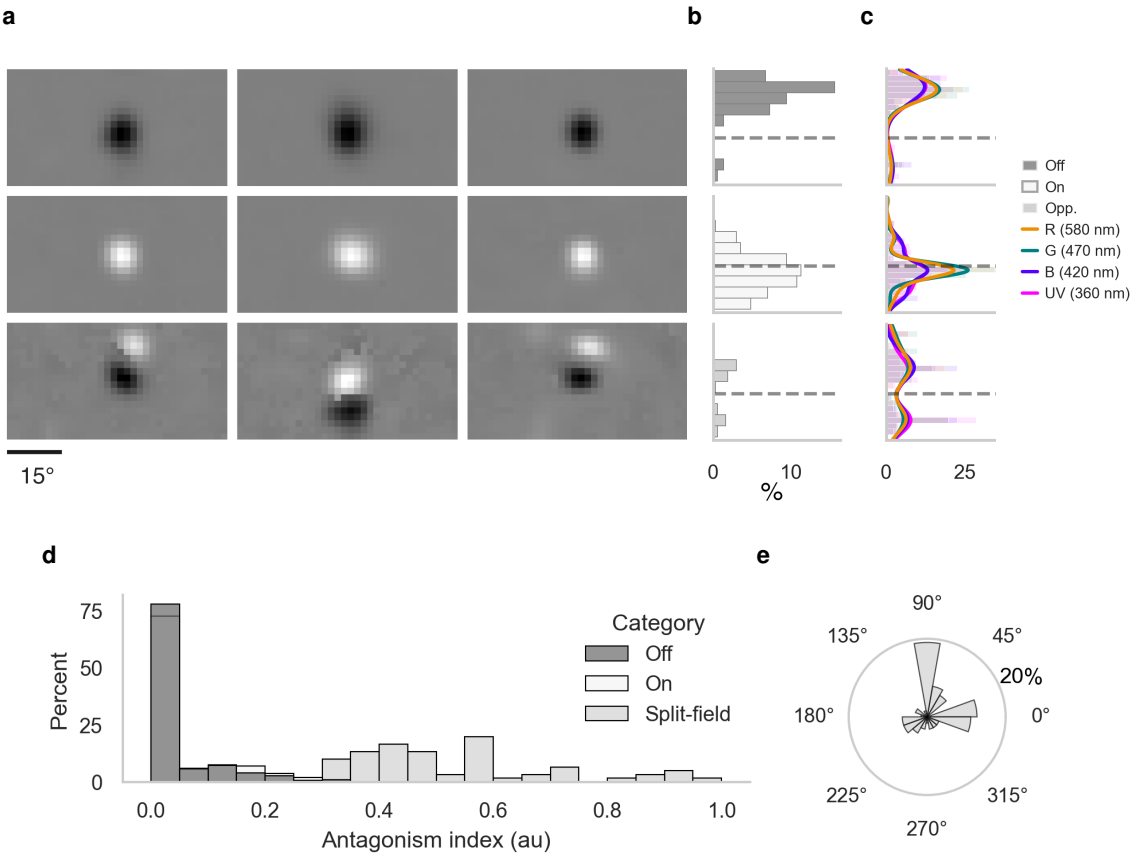

Figure 5.2: Introduction to receptive field analysis. (a) Demonstration of receptive field examples under 'white' stimulation. **(b)** IPL achromatic responses. **(c)** IPL distributions associated with each RF phenotype, and the corresponding distributions for chromatic responses from On, Off, and spectrally Opponent ROIs. **(d)** Distribution of antagonism index values across different categories under 'white' stimulation. **(e)** Polar plot showing orientation distribution of split-field receptive fields.

is consistent with a strong spatial antagonism, and the transient events to bar presentations may be due to differences in temporal kinetics between the lobes.

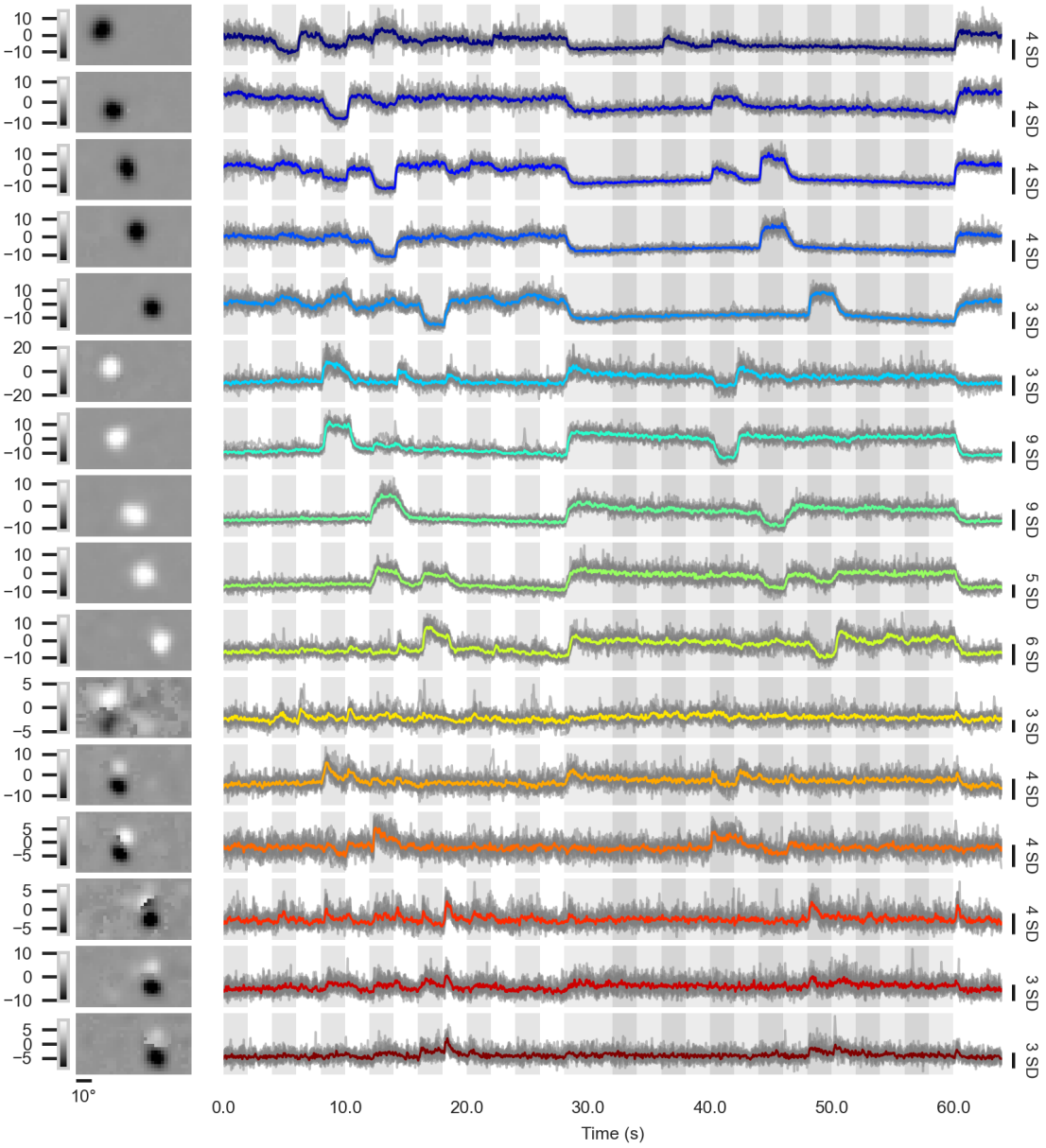

Figure 5.3: Simple vs antagonistic bipolar cell receptive fields. Comparison of receptive field examples from simple bar stimuli showing single strong peaks with minimal surround antagonism versus examples showing strong spatial antagonism under 'white' stimulation, demonstrating Gabor-like split-field organisation.

5.3.3 Strongly antagonistic RFs exhibit orientation selectivity

To test whether the spatially antagonistic terminals were able to encode spatial information in a directionally selective manner, we conducted experiments with moving bars in 8 different directions following RF mapping (n=2 successful experiments). We then computed orientation tuning functions for each terminal and paired the 'white' RF with its corresponding tuning function. This revealed that terminals with strong spatial antagonism consistently exhibited pronounced orientation selectivity (Figure 5.4), whilst spatially

simple RFs typically showed no detectable orientation preference. Although the sample size precludes meaningful statistical analysis, these examples demonstrate that spatial antagonism underlies orientation selectivity in larval zebrafish bipolar cells.

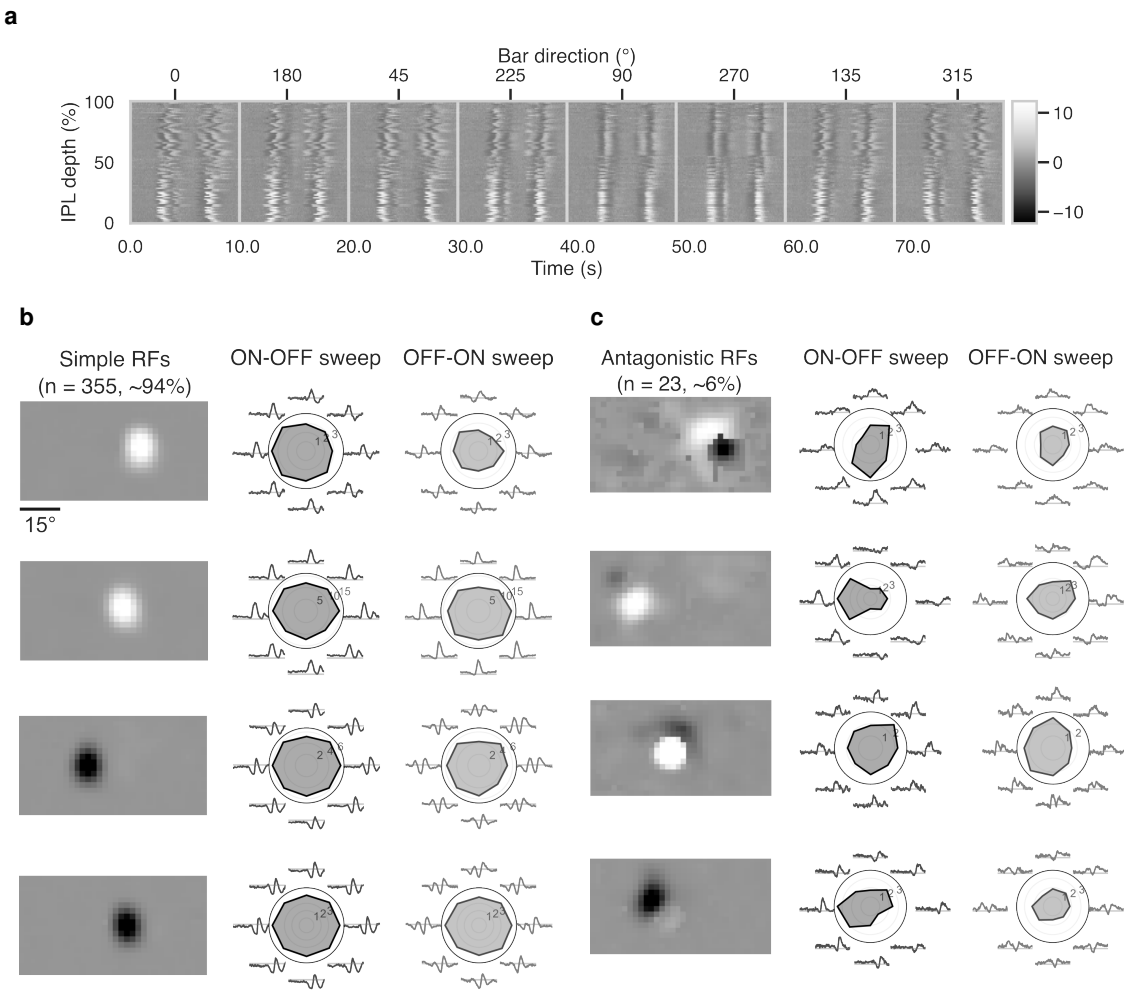

Figure 5.4: Orientation selectivity in bipolar cell responses. (a) Calcium responses across IPL depth during presentation of moving bars at different orientations in one experiment. **(b)** Simple receptive fields showing centre-only responses to ON-OFF and OFF-ON sweeps at different orientations. Examples show typical spatial organisation and temporal profiles. **(c)** Antagonistic receptive fields demonstrating centre-surround organisation with orientation-dependent responses.

5.3.4 Decorrelation of spatial encoding through spectral offsets

Systematic spatial offsets between spectral channels could generate spatial antagonism without classical centre-surround structure. We therefore investigated biases in spatial overlap between spectral channels. For this, we computed pairwise spatial correlations between all spectral channels for each ROI (Figure 5.5). This yielded a correlation matrix for each ROI, with 1 denoting perfect overlap and 0 denoting no overlap (Figure 5.5a). If no signal was present in a channel, correlations involving that channel were ignored to avoid spurious correlations. Figure 5.5b shows a simplified demonstration of the metric, with highly decorrelated spectral channels at the top going towards increasingly correlated RFs at the bottom.

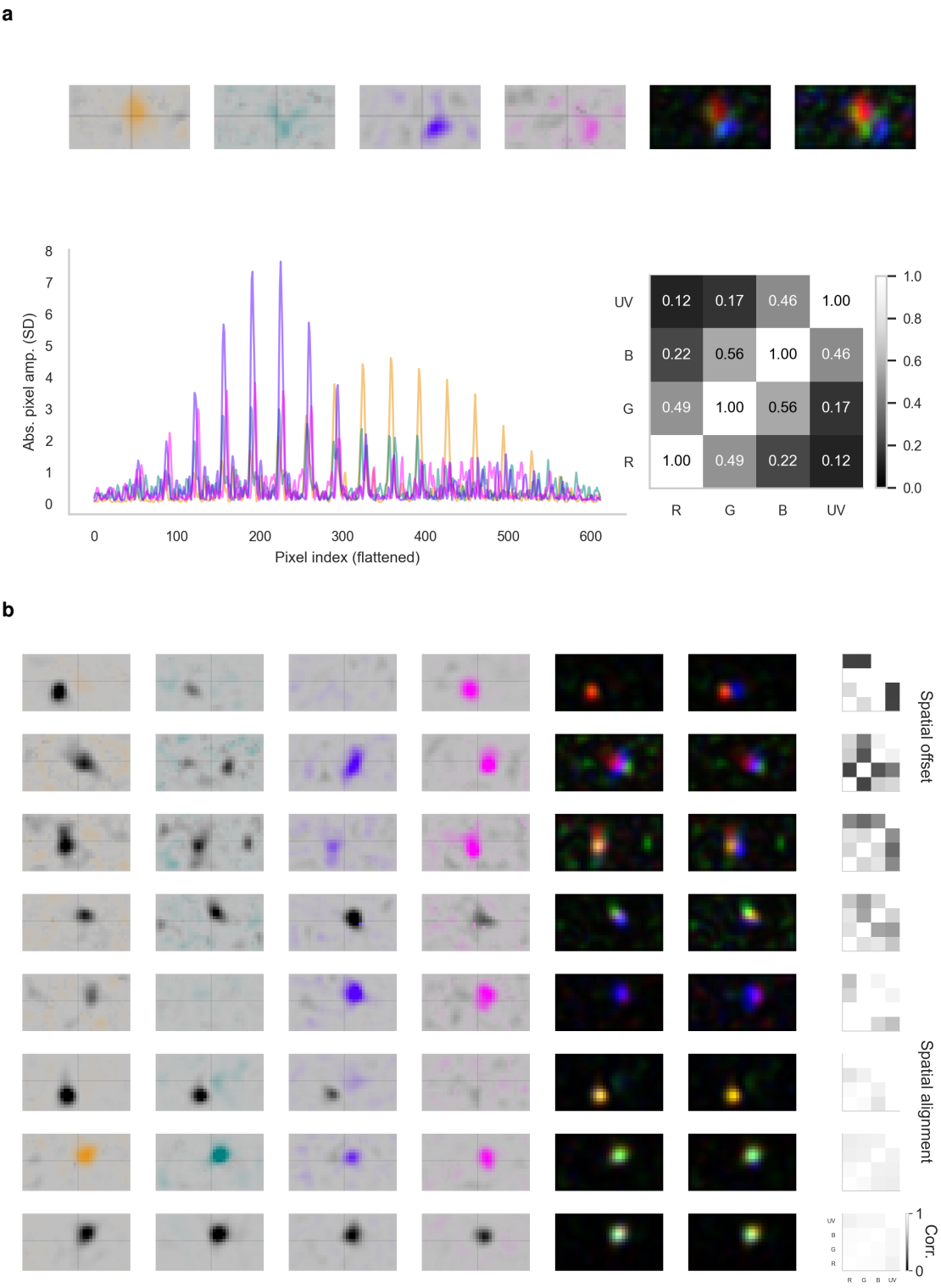

Figure 5.5: Spatial offsets between spectral channels decorrelate spatial encoding. For each ROI, the spatial RF was estimated and time-collapsed giving its spatial profile. The spatial profile for each colour channel was then flattened and pairwise Pearsons' correlations were computed between each channel. This yielded a correlation matrix defining spatial offsets, with 1 denoting perfect overlap and 0 denoting no overlap. **(a)** Example RF demonstrating the spatial correlation metric. **(b)** Simplified demonstrations, with highly decorrelated spectral channels at the top going towards increasingly correlated RFs at the bottom.

We then grouped ROIs by their spectral integration type (Off, On, Opponent) and computed average correlation matrices for each group (Figure 5.6a-d). This revealed that Off ROIs had the highest average correlations between spectral channels (mean pairwise correlation 0.76±0.18), followed by On ROIs (0.69±0.20), with Opponent ROIs showing the lowest correlations (0.57±0.22). This indicates that spectral channels in Opponent ROIs are on average more spatially offset compared to On and Off ROIs.

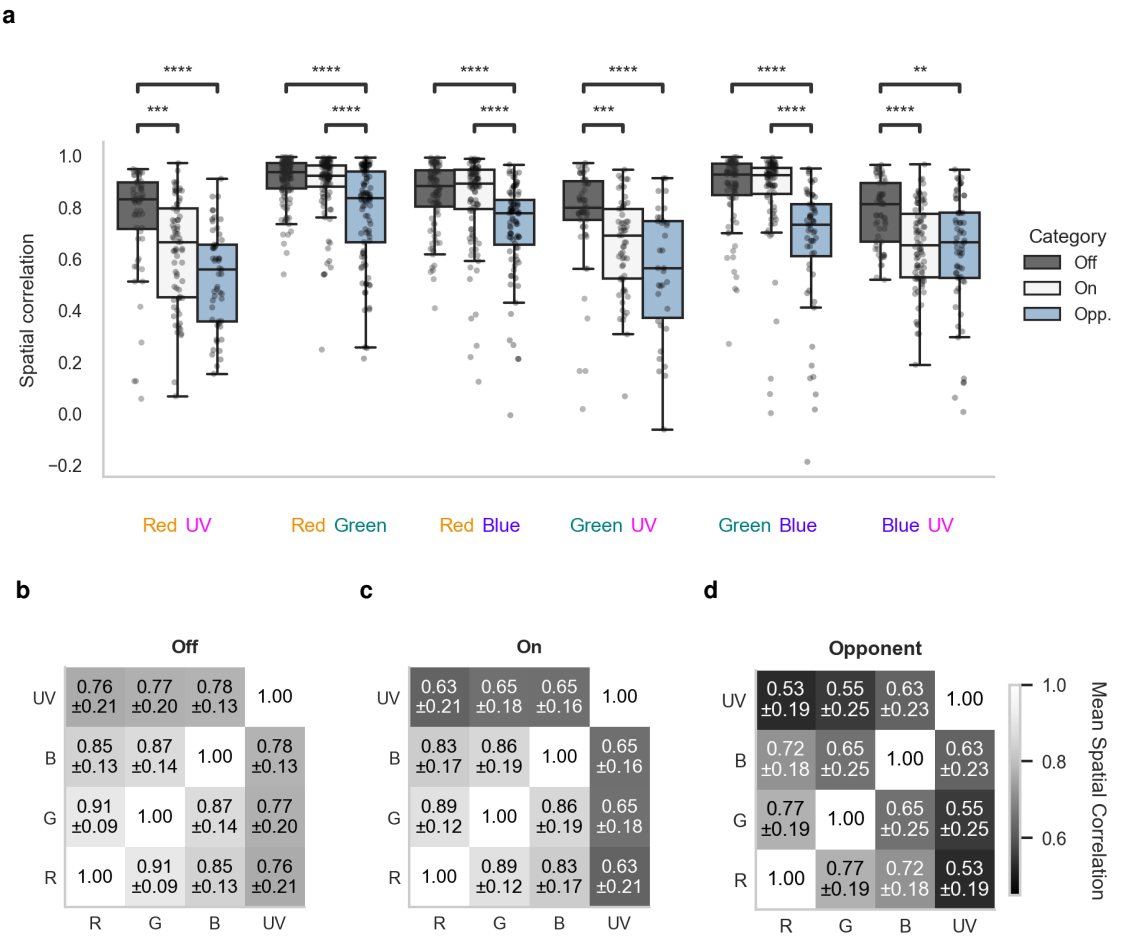

Figure 5.6: Spatial correlations between colour channels reveal integration type-dependent decorrelation patterns. (a) Overview of spatial correlations across all colour channel pairs, grouped by functional category (Off n=221, On n=276, Opponent n=346). Statistical significance levels: ns: $p > 0.05$, *: $p < 0.05$, **: $p < 0.01$, ***: $p < 0.001$, ****: $p < 0.0001$ (Kruskal-Wallis with Bonferroni correction). We saw a clear gradient in mean spatial correlations: Off cells 0.839±0.154, On cells 0.766±0.203, Opponent cells 0.666±0.227. Strongest opponent effects were seen in Green-Blue pairs ($p < 0.0001$), Red-UV pairs ($p < 0.0001$), Red-Green pairs ($p < 0.0001$). **(b-d)** Correlation matrices showing pairwise spatial correlations between Red (R), Green (G), Blue (B), and UV channels for Off (**b**), On (**c**), and Opponent (**d**) functional categories. Values represent mean correlation coefficients ± SD.

5.3.5 The direction of spatial offsets is non-random and aligned to the retinal axes

Having quantified spatial correlations, we examined whether spatial offsets exhibited systematic directional biases by computing offset vectors between spectral channel peaks. This yielded both a magnitude and direction for each channel pair, such that we could

compare their vectors. To examine whether spatial offset patterns vary systematically between spectral channels, we conducted cross-channel comparisons within integration type categories.

Opponent cells showed systematic directional differences between spectral channels (Figure 5.7a). When channels were grouped by wavelength, long wavelengths (R, G) oriented around -141° whilst short wavelengths (B, UV) oriented around +60°, yielding 159.8° separation (Watson-Williams F=164.3, p<0.001). This near-180° opposition was consistent across wavelength extremes: R and UV channels showed 163.7° separation (F=163.1, p<0.001), whilst G and B channels demonstrated 125.7° separation (F=67.7, p<0.001). Spatial offset magnitudes differed between wavelength groups. Short wavelength channels exhibited larger spatial offsets than long wavelengths (2.48±1.51° vs 1.93±1.73°, Mann-Whitney U=24,574, p<0.001), with UV showing the largest individual offsets (3.01±1.46°).

5.3.6 Blocking inner retinal lateral inhibition disrupts spatiotemporal integration

To determine whether lateral inhibition from ACs contributes to spatial tuning despite weak surrounds, we injected a pharmacological cocktail to block GABAergic and glycinergic inhibition from ACs (Figure 5.8). Analysis of RF diameter revealed that AC block caused a significant increase in RF size across nearly all spectral channels and integration types (control: 7.85±1.92°, AC block: 9.65±3.41°, Mann-Whitney U=741,079, p<0.001). The largest increases occurred in Off cells (7.62±1.68° to 10.11±3.33°) and were most pronounced in long wavelength channels. Moreover, the degree of spatial antagonism was significantly reduced following AC block (control: 0.047±0.079, AC block: 0.024±0.064, U=1,514,342, p<0.001), with Opponent cells showing the largest reductions. We also note a general absence of strong UV responses, leading to fewer ROIs with UV data in the AC block condition.

Moreover, AC block abolished wavelength-dependent organisation (Figure 5.7B). The systematic offsets collapsed into flattened distributions lacking directional structure (Figure 5.7C). For UV channels, opponent cell magnitudes decreased from 3.01±1.46° to 1.61±0.80° (Mann-Whitney U=443, p=0.014), whilst the category separation between opponent and off cells reduced from 0.97° to 0.07°.

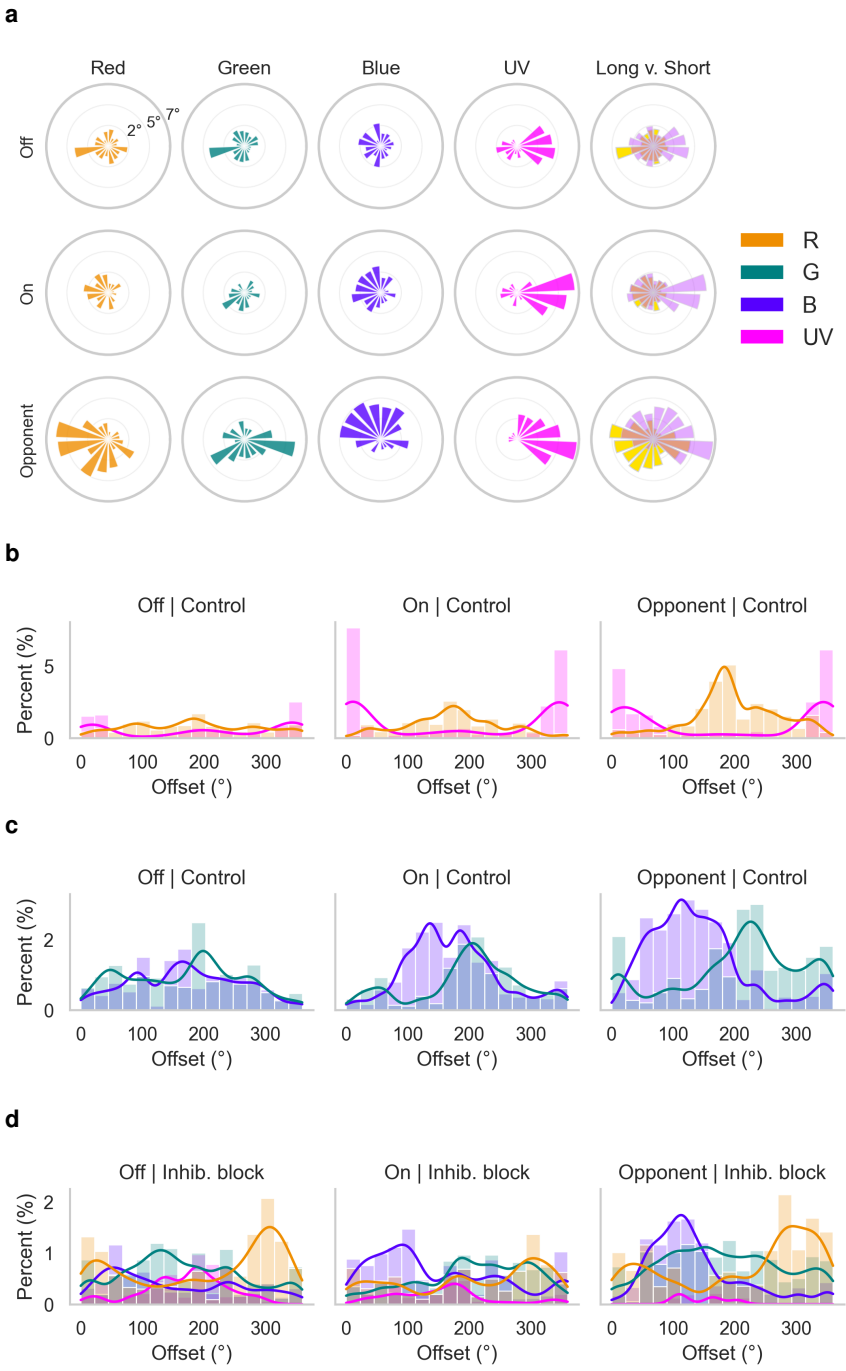

Figure 5.7: Receptive field offset patterns reveal organised spatial structure across integration types. **(a)** Polar plots showing mean RF offset vectors by bin for Off, On, and Opponent ROIs across spectral channels in control conditions. Opponent ROIs (Red n=181, Green n=127, Blue n=129, UV n=92) show systematic organisation with long wavelengths (R+G) orienting around -141°, short wavelengths (B+UV) around +60°, yielding 159.8° separation. UV opponent ROIs show tightest angular organisation (circular variance = 0.310). **(b, c)** Histograms for Red-UV and Green-Blue channel pairs under control conditions. Within opponent ROIs: Red vs UV separation = 163.7° (Watson-Williams F=163.1, p<0.001), Green vs Blue separation = 125.7° (F=67.7, p<0.001). Short wavelengths show larger offset magnitudes than long wavelengths (2.48±1.51° vs 1.93±1.73°, Mann-Whitney U=24,574, p<0.001). **(d-e)** Amacrine cell block condition for Red-UV and Green-Blue pairs showing flattened distributions lacking systematic organisation. Individual channel injection effects: UV opponent magnitudes reduced from 3.01±1.46° to 1.61±0.80° (U=443, p=0.014), Red opponent magnitudes increased (U=5660, p<0.001). Category separation changes: UV opponent-off separation decreased from 0.97° to 0.07°, Red opponent-off separation decreased from 0.85° to 0.59°.

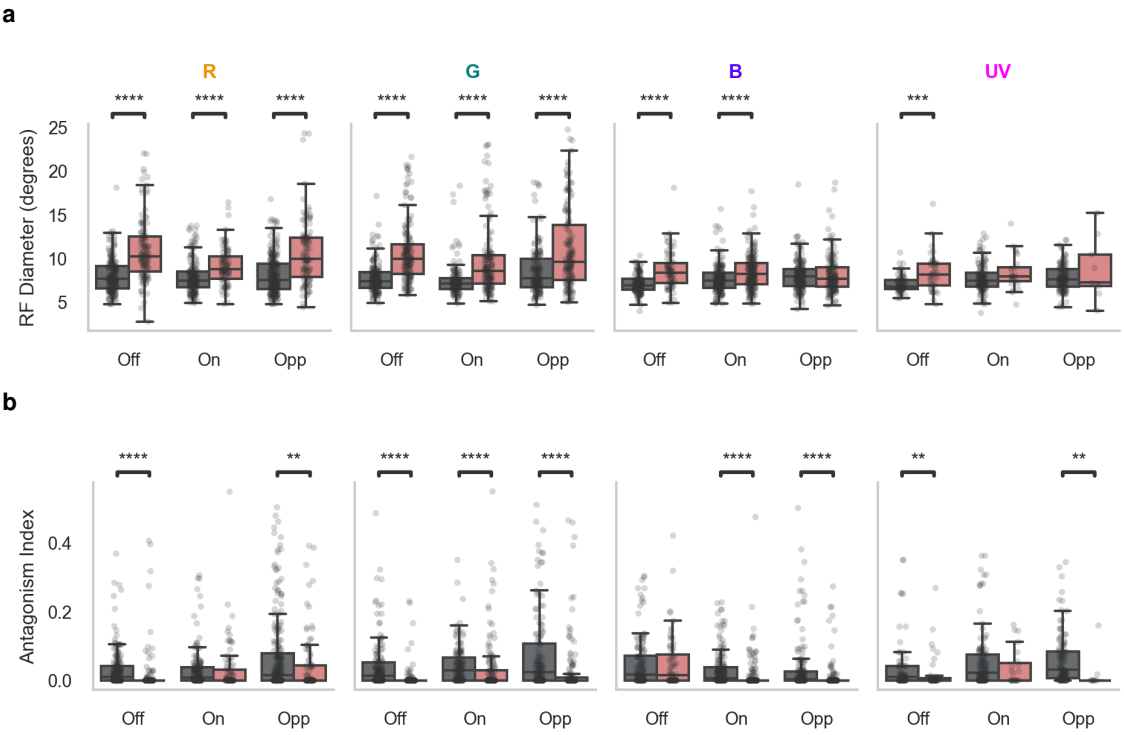

Figure 5.8: AC block leads to dilation of RF sizes and reduction in spatial antagonism. (a) RF diameter comparison across encoding types (Off, On, Opponent) for each spectral channel (R, G, B, UV). Significant increases in RF diameter following AC block across all integration types: Off cells most severely affected (R: U=4,948, p<0.001; G: U=5,064, p<0.001; B: U=2,433, p<0.001; UV: U=973, p<0.001), followed by Opponent cells (R: U=6,821, p<0.001; G: U=7,695, p<0.001), and On cells (R: U=4,670, p<0.001; G: U=5,907, p<0.001; B: U=12,104, p<0.001). **(b)** Opponency index distributions by encoding type and spectral channel. Most pronounced antagonism reductions in G channels across all integration types (Off G: U=18,808, p<0.001; On G: U=13,601, p<0.001; Opponent G: U=14,373, p<0.001). Additional significant effects: Off R (U=15,714, p<0.001), Off UV (U=2,009, p=0.006), On B (U=21,691, p<0.001), Opponent R (U=14,480, p=0.005), Opponent B (U=16,839, p<0.001), Opponent UV (U=836, p=0.004).

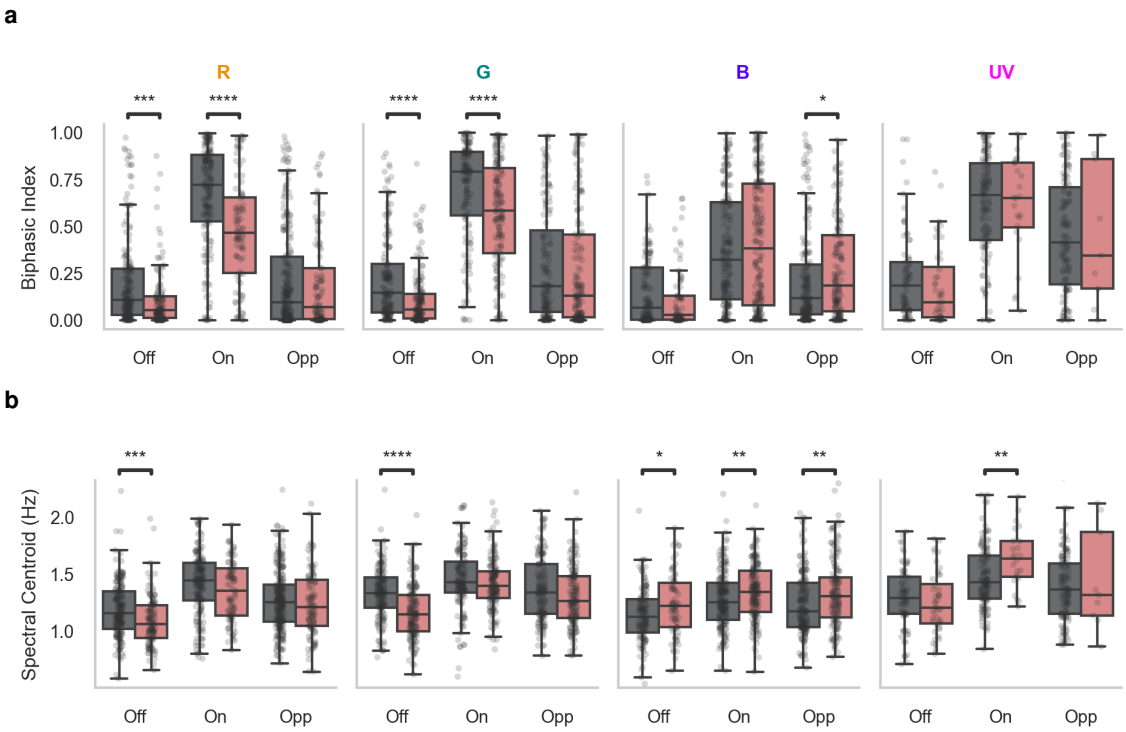

Figure 5.9: AC block disrupts temporal properties. (a) Biphasic index showing temporal complexity across encoding types and spectral channels. Significant reductions in Off and On cells for R and G channels: Off R (U=14,279, p<0.001), Off G (U=16,494, p<0.001), On R (U=10,552, p<0.001), On G (U=13,109, p<0.001). Opponent cells showed minimal changes, with only B channel affected (U=11,020, p=0.047). **(b)** Spectral centroid indicating temporal frequency characteristics. Directional changes with long wavelength channels decreasing in Off cells (Off R: U=14,300, p<0.001; Off G: U=17,625, p<0.001) whilst short wavelength channels increased across integration types (Off B: U=3,743, p=0.020; On B: U=13,489, p=0.006; On UV: U=985, p=0.006; Opponent B: U=10,239, p=0.003).

Temporal integration showed differential patterns, with biphasic index significantly reduced overall (control: 0.351±0.321, AC block: 0.294±0.305, U=1,291,921, p<0.001) but varying by integration type and channel. Off and On cells showed the strongest reductions in R and G channels, with Off cells particularly affected (Off R: 0.197±0.234 to 0.110±0.158, p<0.001; Off G: 0.223±0.227 to 0.113±0.149, p<0.001). Opponent cells were less affected overall, with only the B channel showing significant changes. Spectral centroid showed more subtle directional changes, with long wavelength channels (R, G) generally decreasing whilst short wavelength channels (B, UV) increased, particularly in Off cells.

To assess spectral integration changes, we computed channel coefficient of variation for each ROI. AC block significantly reduced this measure (control: 0.484±0.246, AC block: 0.383±0.219, Mann-Whitney U=832,836, p<0.001, Cohen's d=0.438), indicating more uniform spectral integration and thereby a reduction in tetrachromatic diversity following disinhibition.

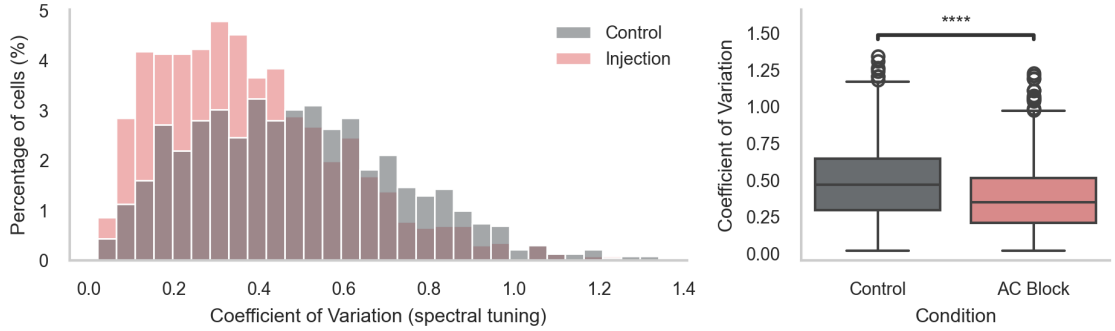

Figure 5.10: Coefficient of variation analysis shows homogenisation of spectral integration. Left: Distribution of coefficient of variation values across spectral channels for control (grey) and AC block (pink) conditions. **Right:** Boxplot comparison showing significant reduction in coefficient of variation following AC block (Mann-Whitney U test, p<0.001), indicating more uniform spectral integration and reduced diversity in spectral channel responses after lateral inhibition disruption. Individual data points not shown due to high number of ROIs.

Finally, we examined how lateral inhibition affected spatial correlations between spectral channels (Figure 5.11). Blocking ACs significantly increased average spatial correlations (control: 0.933±0.105, AC block: 0.971±0.062, U=519,117, p<0.001). Moderate increases in spatial correlation were observed in On (+0.046, U=33,058, p<0.001) and Opponent (+0.045, U=63,239, p<0.001) ROIs, whilst Off ROIs showed minimal change (+0.016, U=22,466, p<0.001). AC block significantly reduced spatially decorrelated RFs in On (U=253, p=0.047) and Opponent (U=274, p=0.010) categories, whilst Off RFs remained non-significant.

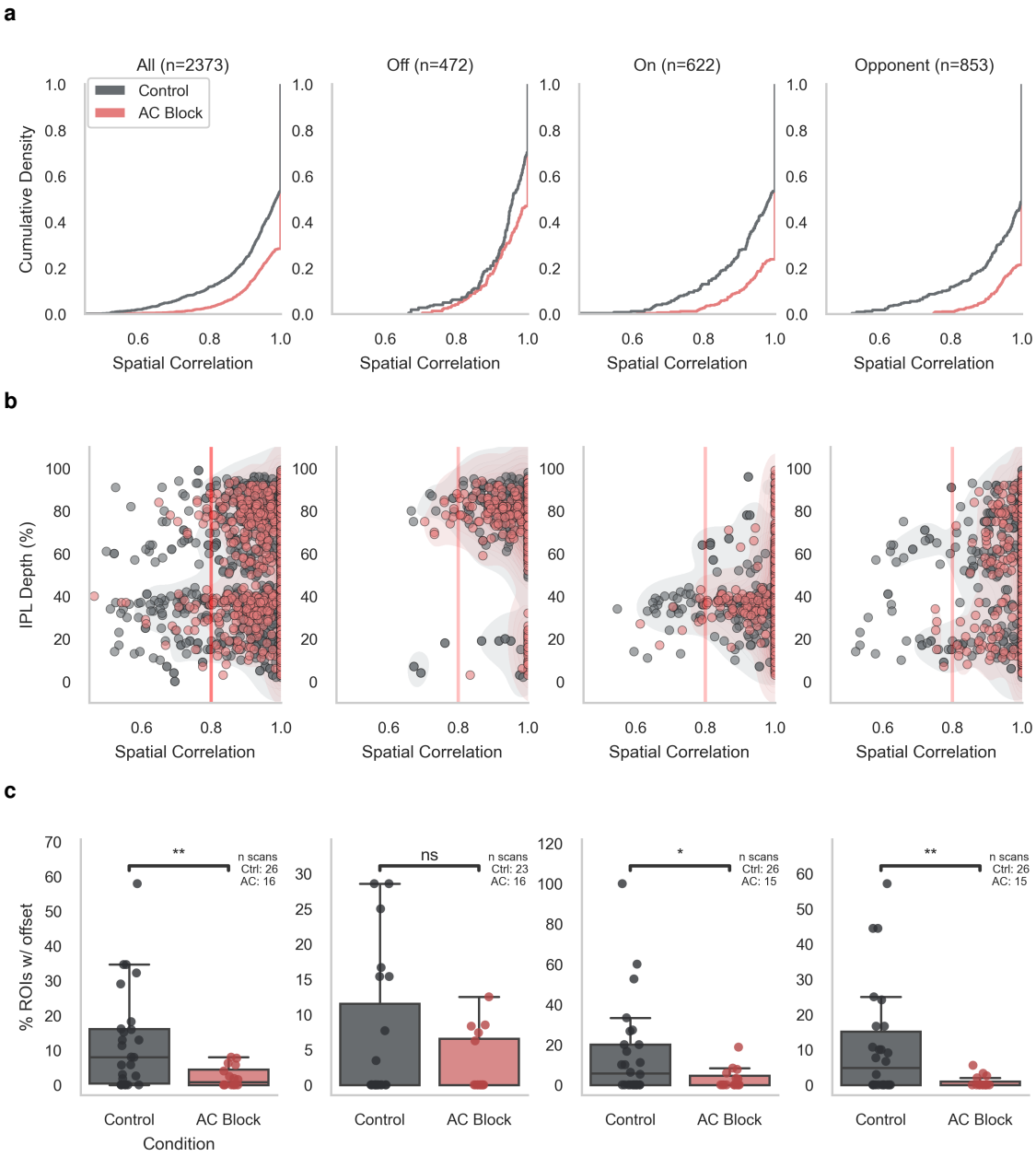

Figure 5.11: Spatial correlation analysis of AC block responses. (a) Cumulative distribution of spatial correlations showing rightward shift following AC block, indicating increased spatial correlations. Threshold analysis (correlation < 0.8) reveals reduced incidence of spatially decorrelated RFs: control 11.7% vs AC block 2.8% (reduction of 8.9 percentage points). **(b)** Kernel density estimation of spatial correlation values demonstrating the distributional changes by integration type. By-category analysis: Off ROIs showed minimal change (control: 0.939±0.075 vs AC block: 0.956±0.065, U=22,466, p<0.001), On ROIs moderate increase (control: 0.929±0.106 vs AC block: 0.975±0.057, U=33,058, p<0.001), Opponent ROIs moderate increase (control: 0.937±0.105 vs AC block: 0.982±0.043, U=63,239, p<0.001). **(c)** Boxplot comparison confirming significant reductions in spatially decorrelated RFs for On (U=253, p=0.047) and Opponent (U=274, p=0.010) categories. IPL stratification analysis revealed significant differences in spatial correlation across IPL depth (Kruskal-Wallis H=55.5, p<0.001), with multivariate analysis confirming independent effects of both category (p<0.001) and IPL depth (p<0.001) on spatial correlation.

5.4 Discussion

5.4.1 Weak classical surrounds persist under ecologically relevant 'white' stimulation

Previous studies in teleosts had difficulty finding strong classical surrounds in bipolar cells (Saito and Kaneko 1983; Kaneko and Tachibana 1981). However, surrounds have also been reported in some BC with the use of large spots or annuli (Shimbo et al. 2000; Toyoda 1973; Saito and Kujiraoka 1982). Moreover, identifying surrounds is a known limitation of RF mapping with binary noise, which may fail to drive weak surrounds effectively (Wienbar and Schwartz 2018), necessitating the use of large pixel sizes. Our use of 10° pixels should have partially mitigated this (Pamplona et al. 2022; Gupta, Młynarski, Symonova, et al. 2022), yet we still observed very weak surrounds contributions. As such, we supplemented previous experiments with 'white' stimulation to maximise bipolar cell activation and bar stimuli to further probe surrounds.

Here we show that larval zebrafish bipolar cells exhibit predominantly weak classical centre-surround organisation under broadband 'white' stimulation, which more closely mimics natural visual conditions and should evoke stronger responses. This confirms and extends previous findings from chapter 4, demonstrating that weak surrounds are a robust feature of zebrafish bipolar cells. Moreover, bar stimuli confirmed the overall weak surrounds, with most cells showing simple responses and minimal antagonism (Figure 5.3). This suggests that weak surrounds are a genuine feature of larval zebrafish bipolar cells.

5.4.2 Cross-channel spatial processing enables non-classical antagonism

However, 'white' stimulation revealed a subset of terminals exhibiting strong non-classical, split-field spatial antagonism. These terminals often displayed orientation selectivity (Figure 5.4), perhaps indicating functional relevance for spatial processing. When comparing their IPL stratification, they resemble opponent terminals observed under standard cycling spectral stimulation (Figure 5.2b, c).

To test whether spatial offsets between spectral channels underlie this phenomenon, we returned to our original tetrachromatic dataset (described in chapter 4) to investigate spatial relationships between spectral channels across the entire population of terminals. This revealed that opponent terminals exhibit significantly lower correlations compared to non-opponent On and Off terminals (Figure 5.6). This relationship was particularly strong between R and UV channels, but could be reliably detected across all channel pairs. Long wavelength channels (R, G) were oriented around -141° whilst short wavelength channels (B, UV) oriented around +60°, yielding 159.8° separation. This fell roughly in line with the 90° bias observed in split-field RFs under 'white' stimulation (Figure 5.2e).

One explanation for this could be chromatic aberration, which could cause systematic spatial offsets between spectral channels. However, chromatic aberration would be expected to affect all terminals equally, whereas we observed a specific relationship

with integration type. The spatial offsets were also not random but exhibited systematic directional biases aligned to retinal axes (Figure 5.7A). Additionally, the presence of these offset opponent terminals was greatly reduced following AC block, suggesting a neuronal mechanism rather than an optical one. Taken together, the characteristics of split-field RFs suggest they are the net result of systematic spatial offsets between spectral channels, rather than traditional concentric surrounds mediated by local inhibitory circuits.

5.4.3 Role of lateral inhibition in spatial organisation

We sought to understand the role of lateral inhibition in spatial tuning of larval zebrafish BC. Lateral inhibition is mediated by HCs in the outer retina and ACs in the inner retina. Here, we injected a drug cocktail to block GABAergic and glycinergic inhibition, thereby disrupting inner retinal lateral inhibition (Wang et al. 2023). If lateral inhibition shapes spatial organisation, we would expect AC block to reduce spatial antagonism thereby increasing the size of RFs. Indeed, we found that AC block significantly increased RF size across nearly all spectral channels and integration types (Figure 5.9). Correspondingly, spatial antagonism was significantly reduced following AC block.

Moreover, temporal properties were altered in a channel- and integration type-dependent manner. The main effect was a reduction in biphasic index, particularly in Off cells and long wavelength channels. Both the increase in RF size and reduction in biphasic index are consistent with a loss of lateral inhibition, which normally sharpens spatial and temporal tuning (Kramer and Davenport 2015; Werblin 1972; Thoreson and Mangel 2012). This then confirms that while the classical surrounds are indeed weak, ACs still play a crucial role in shaping bipolar cell RF properties.

Interestingly, the degree of spatial correlation between spectral channels significantly increased following AC block (Figure 5.11). This effect was most pronounced in On and Opponent ROIs, with Off ROIs showing minimal change. Correspondingly, the proportion of spatially decorrelated RFs significantly decreased in On and Opponent categories, whilst Off RFs remained non-significant. The interpretation of this that AC block reduces the incidence of spatially offset spectral channels by segregating their signals, rather than causing a re-alignment.

5.4.4 Mechanisms for cross-channel spatial antagonism

Accordingly, an explanation for the observed cross-channel spatial antagonism is that lateral inhibition via ACs mediates cross-channel spatial interactions, generating systematic offsets between spectral channels. In other words, ACs serve to intermix spectral channels between neighbouring BCs. Blocking ACs would then homogenise spatial organisation and reducing spatial antagonism. This is consistent with the observed reduction in coefficient of variation following AC block (Figure 5.10), indicating more uniform spectral integration and reduced diversity in spectral channel responses after lateral inhibition disruption.

We can only speculate on the precise circuit mechanisms underlying these effects. How-

ever, we propose two models (Figure 5.12). On the circuit level, either crossover inhibition or feedforward inhibition between sublaminae via one or more AC types could potentially mediate these effects. In crossover inhibition (Figure 5.12a), On ACs inhibit Off BCs and vice versa (Molnar et al. 2009; Werblin 2010). Although this is typically associated with a rectification of the non-linear output at the BC terminal, it could conceivably generate spatial offsets if the AC integrates two distal BC inputs. Feedforward inhibition (Figure 5.12b), where one BC type inhibits another via in AC, could also generate spatial offsets. It would likely be an Off BC inhibiting an On BC, given that the spatial correlation changes were least pronounced in Off ROIs. Both mechanisms could create spatially offset receptive fields across spectral channels, leading to the observed decorrelation and antagonism.

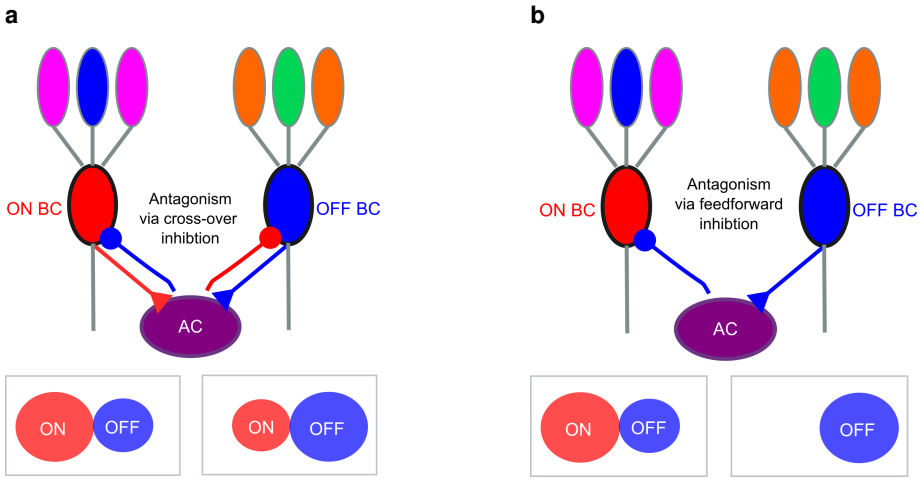

Figure 5.12: Potential mechanisms for cross-channel spatial antagonism. (a) Crossover inhibition model where On amacrine cells inhibit Off bipolar cells and vice versa, creating spatial offsets between spectral channels through their inhibitory connections. **(b)** Feedforward inhibition model where a single amacrine cell type inhibits bipolar cells in both On and Off layers, generating spatial decorrelation through differential spatial sampling. Triangles indicate excitatory synapses and circle indicate inhibitory synapses. The boxes beneath each model illustrates the hypothetical RF profiles resulting from each mechanism as measured from the two contributing bipolar cells.

Alternatively, cone BC with opposing polarities could be electrically coupled via gap junctions, leading to spatial summation in their RF profiles. However, electrical coupling would not explain the dependence on lateral inhibition, as gap junctions are not affected by AC block. Another possibility is that BC expressing both metabotropic and ionotropic glutamate receptors could exhibit complex spatial integration due to differential receptor kinetics and localisation. To our knowledge, there is no evidence for such dual receptor expression, making this less likely.

5.4.5 Ecological relevance of broadband processing

The spatial antagonism that emerges specifically under broadband stimulation may reflect adaptation to natural visual environments, where zebrafish encounter predominantly broadband illumination (Zimmermann et al. 2018). Moreover, the overlap in cone opsin spectra and their opponent tuning driven by outer retina circuits (Yoshimatsu, Bartel, et al. 2021) suggest that zebrafish can exploit this broadband information for complex

visual processing. Recent evidence demonstrates that zebrafish visual centres exploit the 'whiteness' of scenes to encode distance as a function of spectral content (Fornetto, Euler, and Baden 2024), indicating that broadband processing mechanisms have functional significance beyond colour discrimination. Moreover, zebrafish retinal circuits seem particularly well poised to spectrally decompose their visual environment for behaviourally relevant tasks such as prey capture, predator avoidance, and surveying the river bed rather than principally to derive colours (Yoshimatsu, Schröder, et al. 2020; Zimmermann et al. 2018).

The spatially antagonistic terminals may similarly utilise spectral channels as flexible, ancestrally conserved inputs for spatial computation rather than colour processing (Baden 2024a; Yoshimatsu, Bartel, et al. 2021; Baden 2024b). For example, when encountering a vertical edge, long wavelength channels (R, G) with Off encoding may be activated on one side whilst short wavelength channels (B, UV) with On encoding activate on the other (Figure 5.13). The systematic 180° spatial offsets between these channel groups would generate robust orientation-selective responses, effectively encoding edge orientation through cross-channel interactions rather than classical centre-surround mechanisms. In this framework, the colour information is secondary to the spatial computation enabled by the spectral encoding.

We can only speculate on the functional and behavioural implications of these findings. Spatially antagonistic terminals may be involved in detecting oriented edges or patterns in the visual scene. Due to the scale of their receptive fields, they are unlikely to contribute to fine spatial detail necessary for prey capture (Yoshimatsu, Schröder, et al. 2020), but may play a role in broader large scale spatial processing. One such example could be the optokinetic motor response, where zebrafish will reflexively swim in the direction of moving visual patterns to stabilise their position relative to their visual surroundings (Dehmelt et al. 2021). Similarly, they may contribute to the optokinetic response, where zebrafish make reflexive eye movements to track moving stimuli and stabilise images on the retina (Maaswinkel and Li 2003). Further studies are needed to elucidate their precise functional roles and how they integrate into broader visual processing circuits. Nevertheless, these findings highlight a novel mechanism for spatial processing in the zebrafish retina, leveraging broadband spectral inputs to generate non-classical antagonism and orientation selectivity amongst an otherwise spatially simple BC RF population.

5.4.6 Limitations and future directions

There are several limitations to this study that should be acknowledged. The simple stimuli experiments (bar and moving bar stimuli) were intended as qualitative demonstrations to confirm weak surrounds and illustrate orientation selectivity rather than for quantitative analysis, but could benefit from more trials and robust statistical testing. Only a limited number of experiments of this type were conducted (n=3 and n=2, respectively), reflecting technical challenges of performing paired RF mapping and additional stimuli in the same preparation. However, further experiments of this type would help confirm and extend the

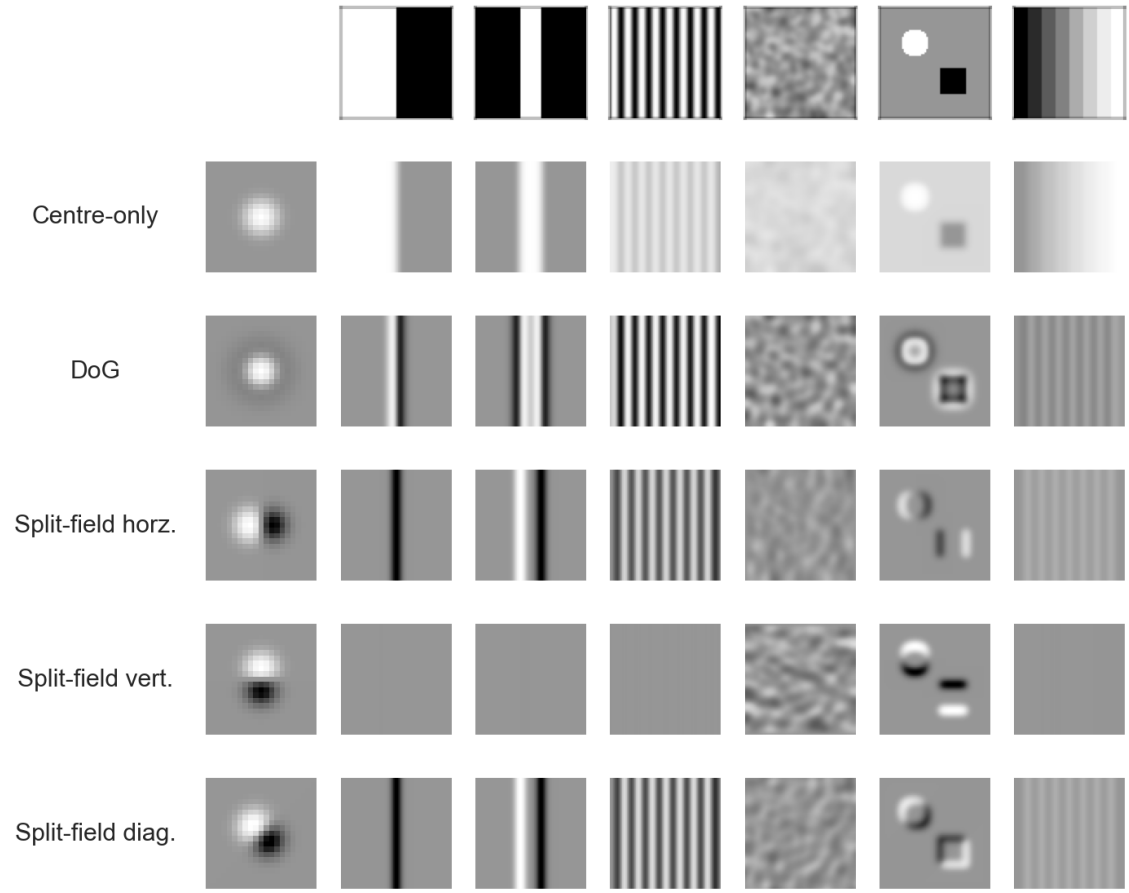

Figure 5.13: Comparison of receptive field types across different stimulation paradigms. Demonstration of how different receptive field organisations respond to various visual stimuli, showing center-only, difference-of-Gaussians (DoG), and split-field configurations across different spatial patterns including edges, gratings, and texture. Each model was convolved with the stimulus to illustrate response profiles, highlighting the encoding properties of each receptive field type. Convolutions are displayed with row-wise normalization to enable comparison across different spatial features within each model type. The centre-only (here shown as an On RF) primarily encodes luminance information linearly, with fine spatial features eroded. The DoG model, representing classical centre-surround organisation (Akram, Garcia, and Puig 2017; Marr, Hildreth, and Brenner 1980), non-linearly encodes contrast transitions such that both positive and negative contrasts are represented, with enhanced sensitivity to edges, gratings, and texture. The split-field models (in horizontal, vertical, and diagonal forms), represent the spatially antagonistic RFs described here. These also encode oriented features non-linearly, with strong responses to edges and orthogonal to the RF orientation. When features align with the RF orientation, responses are diminished due to spatial antagonism.

findings here presented.

In terms of lateral inhibition block we focused on GABAergic and glycinergic pathways, which are the predominant inhibitory mechanisms for sensory processing in the inner retina (Masland 2012a; Werblin 2010). However, a few caveats should be noted. First, while the inhibitory cocktail effectively disrupts AC function and should similarily affect the GABAergic pathway of the HCs, it does not affect the electrical coupling between HCs and BCs nor the feedback between HCs and cones which utilises a non-GABAergic mechanism that is poorly understood (Thoreson and Mangel 2012; Kramer and Davenport 2015). For this reason, we refer to this manipulation as AC block rather than a complete lateral inhibition block.

Future work should investigate the role of GABA and glycine separately, as they may have distinct roles in shaping spatial and spectral processing. For example, GABAergic ACs are often wide-field and may contribute more to global spatial tuning, whereas glycinergic ACs are typically narrow-field and may influence local processing (Masland 2012a). Dissecting their individual contributions could provide deeper insights into the mechanisms underlying spatial antagonism and spectral integration in bipolar cells. One intuition is that glycine mediates the non-classical, highly antagonistic split-field RFs while GABA mediates the weak classical surrounds. However, this remains speculative and further testing is needed. Similarly, selectively blocking AC and HC separately would help clarify their respective roles in shaping bipolar cell receptive fields. This would likely have to be done genetically, as pharmacological tools for selectively blocking HCs without affecting downstream circuits are limited.

Additionally, other neurotransmitters like acetylcholine and dopamine were not addressed. Acetylcholine is typically associated with starburst AC in the mammalian retina(Famiglietti 1983), but homologues have now been identified in zebrafish (Yoshimatsu and Baden 2024; Li, Yu, et al. 2024). The role of dopamine, which is often associated with diurnal regulation and circadian signalling (Moya-Díaz, Simões, and Lagnado 2024), was also not assessed. However, these neurotransmitters are not typically implicated in fast inhibitory processing in the inner retina. Nevertheless, future studies could dissect their roles in visual processing further.

We also did not perform sham injection controls for the AC block experiments. The protocol used here follows a recent study that showed the drug cocktail effectively disrupts AC function without significant off-target effects (Wang et al. 2023). It seems unlikely that the injection procedure itself would specifically alter spatial correlations between spectral channels, particularly in a wavelength-dependent manner.

Finally, we cannot be certain of the exact circuit mechanisms underlying the observed spatial antagonism. The evidence points towards an AC-mediated mechanism, but the precise nature of the interactions remains speculative. Future research using complementary techniques such as electron microscopy to map synaptic connections and electrophysiology to record from specific cell types will be necessary to elucidate the details of circuitry

involved.

5.5 Summary

Here we investigated the spatial organisation of larval zebrafish BC, focusing on confirming the previously observed weak classical surrounds and exploring the mechanisms underlying spatial antagonism in these cells. Using spectrally 'white' stimulation to approximate natural visual conditions, we confirmed that most bipolar cells exhibit weak classical surrounds even under this strong activation. However, a subset of terminals (4.2%) displayed pronounced spatially antagonistic receptive fields with split-field organisation under the 'white' condition, showing two distinct On and Off lobes. Simple bar stimuli confirmed that most cells had simple spatial tuning and weak surrounds, whereas the antagonistic terminals showed minimal response to bars and contrast steps indicating their strong spatial antagonism. However, these split-field terminals often exhibited orientation selectivity, suggesting a functional role in spatial processing.

We hypothesised that this spatial antagonism arises from systematic spatial offsets between spectral channels in opponent BC terminals. Analysis of spatial correlations between spectral channels confirmed that opponent terminals had significantly lower spatial overlap compared to non-opponent On and Off terminals. Moreover, the spatial offsets were not random but exhibited systematic directional biases aligned to retinal axes, with long and short wavelength channels exhibiting a nearly 180° rotation relative to each other. This organisation was abolished following AC block, indicating that lateral inhibition via ACs is essential for maintaining these spatial relationships. We speculate that crossover or feedforward inhibition via ACs could mediate these effects, generating spatial antagonism through cross-channel interactions between spectrally distinct BC pathways.

6 | Summary and conclusions

6.1 Summary

The work here presented aimed to characterise the spatial processing strategies employed by larval zebrafish BCs and establish how tetrachromatic vision influences early retinal computations. We sought to systematically map RF properties across BC populations, investigate the relationship between chromatic and spatial integration, examine IPL organisation principles, and dissect the role of ACs in larval zebrafish BC spatial processing. In doing so, we hoped to gain insight into how aquatic visual systems process spatial information and determine whether zebrafish employ fundamentally different strategies compared to terrestrial vertebrates.

6.1.1 In vivo receptive field mapping

We developed calcium cross-correlation analysis (CCA), a method for mapping spatiotemporal RFs *in vivo* using two-photon calcium imaging. This approach overcomes the traditional requirement for discrete spike events in spike-triggered averaging (Chichilnisky 2001), enabling high-throughput, non-invasive mapping of receptive fields from graded calcium responses. Our tetrachromatic noise stimulation system (Franke, Berens, et al. 2017) combined with shifted-white noise paradigms (Gupta, Młynarski, Symonova, et al. 2022; Pamplona et al. 2022) allowed simultaneous characterisation of spatial and temporal response properties across multiple spectral channels.

CCA proved effective for characterising BC receptive fields with robust signal-to-noise ratios and high reproducibility. Despite inherent limitations including temporal resolution constraints from calcium indicator kinetics and assumptions of linear stimulus-response relationships, CCA provides a powerful foundation for systematic investigation of retinal processing in intact visual systems, enabling population-level analysis of spatiochromatic integration that would be difficult to achieve through traditional approaches.

6.1.2 Weak spatial antagonism with strong spectral diversity

The vast majority of larval zebrafish BCs exhibited weak surrounds, with only a small fraction showing pronounced spatial antagonism. This pattern was consistent across all four spectral channels, indicating that strong centre-surround organisation is not a

dominant feature of zebrafish BC RFs. Functional clustering analysis aimed to align functional diversity with the 21 transcriptomically distinct cone BC types identified in zebrafish (Hellevik et al. 2023), revealing systematic gradients in spectral integration and consistent long- vs. short-wavelength opponency patterns.

Functional BCs types stratified within the IPL according to their encoding polarity and spectral integration properties, consistent with previous reports (Zimmermann et al. 2018; Bartel, Yoshimatsu, et al. 2021), but showed no systematic organisation based on spatial RF properties. Centre-mediated spectral integration and encoding polarity emerged as the primary drivers of diversity, with longer wavelengths exhibiting larger RFs and slower temporal kinetics compared to shorter wavelengths.

6.1.3 Non-classical spatial antagonism through cross-channel interactions

Given the predominantly weak spatial antagonism observed in most zebrafish BCs, we investigated alternative mechanisms using spectrally broadband 'white' noise stimulation. While most BCs continued to exhibit weak surrounds, this approach revealed a distinct subset displaying pronounced spatial antagonism characterised by Gabor-like split-field organisation with discrete On and Off lobes and frequent orientation selectivity.

Analysis of spatial relationships between spectral channels in the tetrachromatic dataset revealed that opponent BCs frequently exhibited pronounced spatial offsets between their long-wavelength (R, G) and short-wavelength (B, UV) channels. These were positioned approximately 180 degrees opposite to one another. However, spatial offsets were not identified in On and Off BCs. Under AC block, these spatial offsets were greatly reduced, implicating inhibitory amacrine cell circuits in establishing this organisation and creating effective spatial antagonism through cross-channel interactions rather than classical centre-surround mechanisms.

6.2 Underwater vision may depend on distinct spatial processing strategies

Our findings provide systematic evidence that larval zebrafish BCs exhibit predominantly weak spatial antagonism, with chromatic processing serving as a primary organising principle. This work also identified a previously uncharacterised form of spatial processing through cross-channel interactions in opponent cells, expanding our understanding of how spatial and chromatic integration may interact in tetrachromatic systems.

The weak spatial antagonism we observed across zebrafish BC populations supports early electrophysiology studies that reported difficulty eliciting surrounds in carp BCs (Saito and Kujiraoka 1982; Saito and Kaneko 1983) or required large stimuli up to several millimetres in diameter to drive the surrounds (Toyoda 1973; Shimbo et al. 2000; Kaneko 1973).

This pattern differs markedly from the well-characterised centre-surround organisation observed in terrestrial vertebrate BCs. These reliably exhibit strong surrounds that are

proportionally balanced with the centre using stimulus sizes of a few hundred microns (Berntson and Taylor 2000; Dacey et al. 2000). Moreover, Strauss et al. 2022 employed a similar reverse-correlation method as used here to map RFs in mouse BCs and reported antagonistic surrounds with comparable strength to the centre in most cells.

6.3 The role of photoreceptor diversity in aquatic species

Together, these findings suggest a genuine difference in spatial processing strategies between aquatic and terrestrial vertebrates, potentially reflecting adaptations to the distinct visual environments they inhabit. This aligns with previous findings that propose zebrafish spectral channels are specialised for different behavioural roles (Zimmermann et al. 2018; Yoshimatsu, Schröder, et al. 2020). Our results suggest that despite their tetrachromatic vision, zebrafish chromatic processing supports information decomposition rather than traditional colour vision.

A recent addition to this line of evidence is the discovery that zebrafish may use their rich cone inputs and their opponencies to infer distance information based on the perceptual whiteness of objects (Fornetto, Euler, and Baden 2024). This mechanism would only function in aquatic environments due to the differential absorption of light underwater. Moreover, zebrafish opsins are known to be ancestrally ancient based on their transcriptomic signature (Baden 2024a; Tommasini et al. 2025). This has led to the suggestion that tetrachromacy evolved for visual roles other than traditional colour vision, and that colour vision as we know it in terrestrial vertebrates is a repurposing of circuits caused by terrestrialisation breaking spectral integration rules that were originally adapted for aquatic vision (Baden 2024b; Baden 2024a).

Similarly, the weak surrounds and chromatic diversity we observed in teleosts may reflect adaptations to the aquatic environment, where the spatial structure of visual scenes differs from terrestrial settings. A recent study of natural scenes from zebrafish habitats showed that these environments contained lower spatial frequencies and lower spatial contrast, but stronger coherent motion when compared to terrestrial scenes (Cai et al. 2023). As such, the need for strong spatial antagonism may be reduced in aquatic environments, where chromatic cues and motion information play more prominent roles in visual processing.

On the other hand, the discovery of spatial offsets between long- and short-wavelength channels in opponent BCs provides a potential mechanism for generating strong spatial antagonism in a functionally distinct channel. These offsets, which create split-field RFs during broadband stimulation and are reduced by amacrine cell block, demonstrate that spatial antagonism can arise through cross-channel interactions. By virtue of having diverse spectral inputs, which can be combined or contrasted across space, zebrafish BCs can potentially achieve spatial processing without relying on classical centre-surround organisation with strong surrounds as seen in terrestrial vertebrates.

6.4 Outlook and future directions

Several questions remain open for future investigation. The functional significance of the weak surrounds observed in most zebrafish BCs is not fully understood. It is possible that these weak surrounds still contribute to spatial processing in ways that are not captured by static measures of antagonism. For example, some mouse RGCs with weak surrounds have been shown to strongly encode motion well outside the classical RF (Riccitelli et al. 2025). It would be interesting to explore whether the broad spatial extents of the zebrafish BC surrounds similarly contribute to motion processing.

The RF mapping and assessment of spatial antagonism should also be extended to RGCs to determine how these properties are transformed downstream. One could also record somatic calcium activity from HC and AC to assess their RF properties and understand how they integrate spatial features. Perhaps RF mapping of photoreceptors themselves is conceivable, at which point one could build a complete picture of spatial processing from the photoreceptors to the RGCs. This should help elucidate how spatial and chromatic information is integrated and processed at different stages of the retinal circuitry.

Similarly, experiments should be conducted at different eccentricities and azimuths of the eye, to determine how spatial processing varies across the visual field. The results here presented were obtained from the central retina. However, zebrafish are known to have regional specialisations in their retina, with different distributions of photoreceptor types and BC types across the retinal surface (Yoshimatsu, Schröder, et al. 2020; Zimmermann et al. 2018). It quite likely that RF properties and spatial processing strategies also vary across the retina to accommodate different visual demands. As such, future studies could map RF properties at different retinal locations to assess how spatial processing differs by region, providing further insight into the functional specialisations of different retinal areas.

The paradigm here used to map BC RFs should also be applied at different stages of development to gain a more complete understanding of the development of spatial processing in zebrafish. It is possible that the weak surrounds here reported are a feature of an immature visual system, and that stronger surrounds may emerge later in development as the retinal circuitry matures. As such, future studies could compare RF properties for example at 5 dpf, 10 dpf, and 15 dpf to track how spatial processing develops over time. Later developmental stages would prove more difficult to image in vivo, but such attempts would be valuable.

Finally, broader comparative studies across different aquatic species should provide further insights into whether the weak surrounds and chromatic diversity observed are genuine features associated with aquatic visual systems or specific adaptations of zebrafish. Aquatic mammals such as whales or seals should be particularly interested in this regard, although the feasibility of studying their retinal circuitry is naturally limited. Semiaquatic species such as frogs or turtles could also provide interesting comparisons. This would help clarify the evolutionary roles of photoreceptor diversity and spatial processing strategies in different visual environments, and shed light on how spatial processing differs between

aquatic and terrestrial vertebrates.

6.5 Concluding remarks

Taken together, our findings suggest that aquatic visual systems may employ fundamentally different strategies for spatial processing compared to terrestrial systems. The weak surrounds here identified are consistent with previous electrophysiological efforts of measuring BC RFs in teleosts. However, we extend these findings by demonstrating these phenomena in vivo and systematically across all cone channels. The chromatic diversity and opponency patterns we observed further highlight the importance of spectral processing in zebrafish vision. This may reflect adaptations to the unique visual demands of aquatic environments, where chromatic cues and motion information are more critical than fine spatial detail. The identification of cross-channel interactions as a mechanism for generating spatial antagonism further highlights the complexity and versatility of retinal processing afforded by its tetrachromatic visual system.

Bibliography

Abu-Siniyeh, Ahmed and Walid Al-Zyoud (Apr. 2020). “Highlights on Selected Microscopy Techniques to Study Zebrafish Developmental Biology”. In: *Laboratory Animal Research* 36.1, p. 12. ISSN: 2233-7660. DOI: 10.1186/s42826-020-00044-2. (Visited on 06/03/2022).

Adolph, A. R. (May 1988). “Center-Surround, Orientation, and Directional Properties of Turtle Retinal Horizontal Cells”. In: *Biological Cybernetics* 58.6, pp. 373–385. ISSN: 1432-0770. DOI: 10.1007/BF00361345. (Visited on 11/05/2024).

Adrian, E. D. and Rachel Matthews (Dec. 1927). “The Action of Light on the Eye”. In: *The Journal of Physiology* 64.3, pp. 279–301. ISSN: 0022-3751. DOI: 10.1113/jphysiol.1927.sp002437. (Visited on 06/11/2025).

Akram, Farhan, Miguel Angel Garcia, and Domenec Puig (Nov. 2017). “Active Contours Driven by Difference of Gaussians”. In: *Scientific Reports* 7.1, p. 14984. ISSN: 2045-2322. DOI: 10.1038/s41598-017-14502-w. (Visited on 05/23/2022).

Angueyra, Juan M et al. (Feb. 2023). “Transcription Factors Underlying Photoreceptor Diversity”. In: *eLife* 12. Ed. by Paola Bovolenta, Marianne E Bronner, and Daisuke Kojima, e81579. ISSN: 2050-084X. DOI: 10.7554/eLife.81579. (Visited on 12/08/2024).

Antinucci, Paride and Robert Hindges (July 2016). “A Crystal-Clear Zebrafish for in Vivo Imaging”. In: *Scientific Reports* 6.1, p. 29490. ISSN: 2045-2322. DOI: 10.1038/srep29490. (Visited on 06/03/2022).

Antinucci, Paride, Oniz Suleyman, et al. (July 2016). “Neural Mechanisms Generating Orientation Selectivity in the Retina”. In: *Current biology: CB* 26.14, pp. 1802–1815. ISSN: 1879-0445. DOI: 10.1016/j.cub.2016.05.035.

Ashmore, J F and D R Copenhagen (1983). “An Analysis of Transmission from Cones to Hyperpolarizing Bipolar Cells in the Retina of the Turtle.” In: *The Journal of Physiology* 340.1, pp. 569–597. ISSN: 1469-7793. DOI: 10.1113/jphysiol.1983.sp014781. (Visited on 08/26/2024).

Baden, T., F. Espotsi, et al. (2011). “Spikes in Retinal Bipolar Cells Phase-Lock to Visual Stimuli with Millisecond Precision”. In: *Current Biology* 21.22, pp. 1859–1869. DOI: 10.1016/j.cub.2011.09.042.

Baden, T. and D. Osorio (2019). “The Retinal Basis of Vertebrate Color Vision”. In: *Annual Review of Vision Science* 5.1, pp. 177–200. DOI: 10.1146/annurev-vision-091718-014926. (Visited on 05/23/2023).

Baden, Tom (Jan. 2024a). “Ancestral Photoreceptor Diversity as the Basis of Visual Behaviour”. In: *Nature Ecology & Evolution*, pp. 1–13. ISSN: 2397-334X. DOI: 10.1038/s41559-023-02291-7. (Visited on 02/19/2024).

– (Jan. 2024b). “From Water to Land: Evolution of Photoreceptor Circuits for Vision in Air”. In: *PLOS Biology* 22.1, e3002422. ISSN: 1545-7885. DOI: 10.1371/journal.pbio.3002422. (Visited on 03/17/2024).

Baden, Tom, Philipp Berens, Matthias Bethge, et al. (Jan. 2013). “Spikes in Mammalian Bipolar Cells Support Temporal Layering of the Inner Retina”. In: *Current Biology* 23.1, pp. 48–52. ISSN: 0960-9822. DOI: 10.1016/j.cub.2012.11.006. (Visited on 11/24/2021).

Baden, Tom, Philipp Berens, Katrin Franke, et al. (Jan. 2016). “The Functional Diversity of Retinal Ganglion Cells in the Mouse”. In: *Nature* 529.7586, pp. 345–350. ISSN: 1476-4687. DOI: 10.1038/nature16468. (Visited on 06/28/2021).

Baden, Tom, Thomas Euler, and Philipp Berens (Jan. 2020). “Understanding the Retinal Basis of Vision across Species.” In: *Nature Reviews Neuroscience* 21.1, pp. 5–20. DOI: 10.1038/s41583-019-0242-1.

Balasubramanian, Vijay and Peter Sterling (2009). “Receptive Fields and Functional Architecture in the Retina”. In: *The Journal of Physiology* 587.12, pp. 2753–2767. DOI: 10.1113/jphysiol.2009.170704. (Visited on 06/04/2022).

Balraj, Annika, Takeshi Yoshimatsu, and Ralph F Nelson (Sept. 2016). “Thyroxin B2 Receptor (Trb2) Overexpression Alters Cone Spectra in Zebrafish.” In: *Investigative Ophthalmology & Visual Science* 57.12, p. 586. ISSN: 1552-5783.

Barlow, H B and W R Levick (1965). “The Mechanism of Directionally Selective Units in Rabbit’s Retina.” In: *The Journal of Physiology* 178.3, pp. 477–504. ISSN: 1469-7793. DOI: 10.1113/jphysiol.1965.sp007638. (Visited on 12/16/2022).

Barlow, H. B. (1953). “Summation and Inhibition in the Frog’s Retina”. In: *The Journal of Physiology* 119.1, pp. 69–88. ISSN: 1469-7793. DOI: 10.1113/jphysiol.1953.sp004829. (Visited on 01/25/2022).

– (1961). “Possible Principles Underlying the Transformations of Sensory Messages”. In: *Sensory Communication*. MIT Press.

Bartel, Philipp, Filip K. Janiak, et al. (Mar. 2021). “Colourfulness as a Possible Measure of Object Proximity in the Larval Zebrafish Brain”. In: *Current Biology* 31.5, R235–R236. ISSN: 0960-9822. DOI: 10.1016/j.cub.2021.01.030. (Visited on 09/26/2025).

Bartel, Philipp, Takeshi Yoshimatsu, et al. (Dec. 2021). “Spectral Inference Reveals Principal Cone-Integration Rules of the Zebrafish Inner Retina”. In: *Current Biology* 31.23, 5214–5226.e4. ISSN: 0960-9822. DOI: 10.1016/j.cub.2021.09.047. (Visited on 06/03/2022).

Behrens, Christian et al. (Nov. 2016). “Connectivity Map of Bipolar Cells and Photoreceptors in the Mouse Retina”. In: *eLife* 5. Ed. by Fred Rieke, e20041. ISSN: 2050-084X. DOI: 10.7554/eLife.20041. (Visited on 08/20/2024).

Berntson, Amy and W Rowland Taylor (May 2000). “Response Characteristics and Receptive Field Widths of On-Bipolar Cells in the Mouse Retina”. In: *The Journal of Physiology*

524.Pt 3, pp. 879–889. ISSN: 0022-3751. DOI: 10.1111/j.1469-7793.2000.00879.x. (Visited on 08/12/2021).

Bilotta, J. and S. Saszik (2001). “The Zebrafish as a Model Visual System”. In: *International Journal of Developmental Neuroscience* 19.7, pp. 621–629. DOI: 10.1016/S0736-5748(01)00050-8.

Bollmann, Johann H. (2019). “The Zebrafish Visual System: From Circuits to Behavior”. In: *Annual Review of Vision Science* 5.1, pp. 269–293. DOI: 10.1146/annurev-vision-091718-014723. (Visited on 06/03/2022).

Borges, S. and M. Wilson (Dec. 1987). “Structure of the Receptive Fields of Bipolar Cells in the Salamander Retina”. In: *Journal of Neurophysiology* 58.6, pp. 1275–1291. ISSN: 0022-3077. DOI: 10.1152/jn.1987.58.6.1275. (Visited on 04/28/2023).

Bowmaker, James K. (May 1998). “Evolution of Colour Vision in Vertebrates”. In: *Eye* 12.3, pp. 541–547. ISSN: 1476-5454. DOI: 10.1038/eye.1998.143. (Visited on 06/02/2022).

Broussard, Gerard Joey et al. (Sept. 2018). “In Vivo Measurement of Afferent Activity with Axon-Specific Calcium Imaging”. In: *Nature Neuroscience* 21.9, pp. 1272–1280. ISSN: 1546-1726. DOI: 10.1038/s41593-018-0211-4. (Visited on 12/08/2024).

Burkhardt, Dwight A., Theodore M. Bartoletti, and Wallace B. Thoreson (May 2011). “Center/Surround Organization of Retinal Bipolar Cells: High Correlation of Fundamental Responses of Center and Surround to Sinusoidal Contrasts”. In: *Visual Neuroscience* 28.3, pp. 183–192. ISSN: 1469-8714, 0952-5238. DOI: 10.1017/S0952523811000071. (Visited on 08/20/2024).

Cai, Lanya T. et al. (July 2023). “Spatiotemporal Visual Statistics of Aquatic Environments in the Natural Habitats of Zebrafish”. In: *Scientific Reports* 13.1, p. 12028. ISSN: 2045-2322. DOI: 10.1038/s41598-023-36099-z. (Visited on 04/03/2025).

Carleton, Karen L. et al. (Apr. 2020). “Seeing the Rainbow: Mechanisms Underlying Spectral Sensitivity in Teleost Fishes”. In: *Journal of Experimental Biology* 223.8, jeb193334. ISSN: 0022-0949. DOI: 10.1242/jeb.193334. (Visited on 07/10/2025).

Chapot, Thomas Euler, and Timm Schubert (Aug. 2017). “How Do Horizontal Cells ’talk’ to Cone Photoreceptors? Different Levels of Complexity at the Cone-Horizontal Cell Synapse”. In: *The Journal of Physiology* 595.16, pp. 5495–5506. ISSN: 1469-7793. DOI: 10.1113/JP274177. (Visited on 08/01/2025).

Chaya, Taro et al. (July 2017). “Versatile Functional Roles of Horizontal Cells in the Retinal Circuit”. In: *Scientific Reports* 7.1, p. 5540. ISSN: 2045-2322. DOI: 10.1038/s41598-017-05543-2. (Visited on 09/13/2021).

Chen, Tsai-Wen et al. (July 2013). “Ultrasensitive Fluorescent Proteins for Imaging Neuronal Activity”. In: *Nature* 499.7458, pp. 295–300. ISSN: 1476-4687. DOI: 10.1038/nature12354. (Visited on 08/15/2021).

Chichilnisky, E. J. (May 2001). “A Simple White Noise Analysis of Neuronal Light Responses”. In: *Network: Computation in Neural Systems* 12.2, p. 199. ISSN: 0954-898X. DOI: 10.1088/0954-898X/12/2/306. (Visited on 11/10/2022).

Choe, Chong Pyo et al. (Sept. 2021). “Transgenic Fluorescent Zebrafish Lines That Have Revolutionized Biomedical Research”. In: *Laboratory Animal Research* 37.1, p. 26. ISSN: 2233-7660. DOI: 10.1186/s42826-021-00103-2. (Visited on 06/24/2025).

Connaughton, V. P. (Jan. 2011). “Bipolar Cells in the Zebrafish Retina”. In: *Visual Neuroscience* 28.1, pp. 77–93. ISSN: 1469-8714, 0952-5238. DOI: 10.1017/S0952523810000295. (Visited on 09/29/2023).

Cook, Jeremy E. and David L. Becker (1995). “Gap Junctions in the Vertebrate Retina”. In: *Microscopy Research and Technique* 31.5, pp. 408–419. ISSN: 1097-0029. DOI: 10.1002/jemt.1070310510. (Visited on 08/03/2025).

Cook, Paul B. and John S. McReynolds (Dec. 1998). “Lateral Inhibition in the Inner Retina Is Important for Spatial Tuning of Ganglion Cells”. In: *Nature Neuroscience* 1.8, pp. 714–719. ISSN: 1546-1726. DOI: 10.1038/3714. (Visited on 08/17/2021).

Cooler, Sam and Gregory W. Schwartz (Jan. 2021). “An Offset ON-OFF Receptive Field Is Created by Gap Junctions between Distinct Types of Retinal Ganglion Cells”. In: *Nature neuroscience* 24.1, pp. 105–115. ISSN: 1097-6256. DOI: 10.1038/s41593-020-00747-8. (Visited on 07/25/2025).

Cousin, Michael A. (2021). “Synaptophysin-Dependent Synaptobrevin-2 Trafficking at the Presynapse-Mechanism and Function”. In: *Journal of Neurochemistry* 159.1, pp. 78–89. ISSN: 1471-4159. DOI: 10.1111/jnc.15499. (Visited on 08/25/2025).

Dacey, Dennis et al. (June 2000). “Center Surround Receptive Field Structure of Cone Bipolar Cells in Primate Retina”. In: *Vision Research* 40.14, pp. 1801–1811. ISSN: 0042-6989. DOI: 10.1016/S0042-6989(00)00039-0. (Visited on 06/03/2022).

Daw, N. W. (Aug. 1968). “Colour-Coded Ganglion Cells in the Goldfish Retina: Extension of Their Receptive Fields by Means of New Stimuli”. In: *The Journal of Physiology* 197.3, pp. 567–592. ISSN: 0022-3751. DOI: 10.1113/jphysiol.1968.sp008575.

Dehmelt, Florian A et al. (June 2021). “Spherical Arena Reveals Optokinetic Response Tuning to Stimulus Location, Size, and Frequency across Entire Visual Field of Larval Zebrafish”. In: *eLife* 10. Ed. by Kristin Tessmar-Raible, Tirin Moore, and Andrew D Straw, e63355. ISSN: 2050-084X. DOI: 10.7554/eLife.63355. (Visited on 08/18/2021).

Deveau, Ciana et al. (June 2020). “Thyroid Hormone Receptor Beta Mutations Alter Photoreceptor Development and Function in Danio Rerio (Zebrafish)”. In: *PLOS Genetics* 16.6, e1008869. ISSN: 1553-7404. DOI: 10.1371/journal.pgen.1008869. (Visited on 12/08/2024).

Dreosti, E., F. Esposti, et al. (2011). “In Vivo Evidence That Retinal Bipolar Cells Generate Spikes Modulated by Light”. In: *Nature Neuroscience* 14.8, pp. 951–952. ISSN: 1546-1726. DOI: 10.1038/nn.2841. (Visited on 08/22/2025).

Dreosti, Elena, Benjamin Odermatt, et al. (Dec. 2009). “A Genetically Encoded Reporter of Synaptic Activity in Vivo”. In: *Nature Methods* 6.12, pp. 883–889. ISSN: 1548-7105. DOI: 10.1038/nmeth.1399. (Visited on 12/08/2024).

Eggers, Erika D. and Peter D. Lukasiewicz (Jan. 2011). “Multiple Pathways of Inhibition Shape Bipolar Cell Responses in the Retina”. In: *Visual Neuroscience* 28.1, pp. 95–

108. ISSN: 0952-5238, 1469-8714. DOI: 10.1017/S0952523810000209. (Visited on 08/17/2021).

Endeman, Duco, Lauw J. Klaassen, and Maarten Kamermans (July 2013). "Action Spectra of Zebrafish Cone Photoreceptors". In: *PLOS ONE* 8.7, e68540. ISSN: 1932-6203. DOI: 10.1371/journal.pone.0068540. (Visited on 11/15/2022).

Enroth-Cugell, Christina and J. G. Robson (1966). "The Contrast Sensitivity of Retinal Ganglion Cells of the Cat". In: *The Journal of Physiology* 187.3, pp. 517–552. ISSN: 1469-7793. DOI: 10.1113/jphysiol.1966.sp008107. (Visited on 11/29/2021).

Euler, Thomas, Susanne E. Hausselt, et al. (Apr. 2009). "Eyecup Scope—Optical Recordings of Light Stimulus-Evoked Fluorescence Signals in the Retina". In: *Pflugers Archiv : European journal of physiology* 457.6, pp. 1393–1414. ISSN: 0031-6768. DOI: 10.1007/s00424-008-0603-5. (Visited on 08/15/2021).

Euler, Thomas, Silke Haverkamp, et al. (Aug. 2014). "Retinal Bipolar Cells: Elementary Building Blocks of Vision". In: *Nature Reviews Neuroscience* 15.8, pp. 507–519. ISSN: 1471-0048. DOI: 10.1038/nrn3783. (Visited on 07/03/2021).

Famiglietti, Edward V. (Jan. 1983). "On and off Pathways through Amacrine Cells in Mammalian Retina: The Synaptic Connections of "Starburst" Amacrine Cells". In: *Vision Research* 23.11, pp. 1265–1279. ISSN: 0042-6989. DOI: 10.1016/0042-6989(83)90102-5. (Visited on 03/21/2024).

– (2025). "Mammalian Retinal Bipolar Cells: Morphological Identification and Systematic Classification in Rabbit Retina With a Comparative Perspective". In: *Journal of Comparative Neurology* 533.2, e70015. ISSN: 1096-9861. DOI: 10.1002/cne.70015. (Visited on 08/04/2025).

Field, Andy (2007). *Discovering Statistics Using SPSS: And Sex, Drugs and Rock'n'roll*. 2. ed., reprinted. ISM, Introducing Statistical Methods. London: SAGE Publ. ISBN: 978-0-7619-4451-5 978-0-7619-4452-2.

Field, Greg D. et al. (Oct. 2010). "Functional Connectivity in the Retina at the Resolution of Photoreceptors". In: *Nature* 467.7316, pp. 673–677. ISSN: 0028-0836. DOI: 10.1038/nature09424. (Visited on 08/25/2022).

Fleisch, V.C. and S.C. Neuhauss (2006). "Visual Behavior in Zebrafish". In: *Zebrafish* 3.2, pp. 191–201. DOI: 10.1089/zeb.2006.3.191.

Forman, C. J. et al. (May 2017). "Openspritzer: An Open Hardware Pressure Ejection System for Reliably Delivering Picolitre Volumes". In: *Scientific Reports* 7.1, p. 2188. ISSN: 2045-2322. DOI: 10.1038/s41598-017-02301-2. (Visited on 08/06/2025).

Fornetto, Chiara, Thomas Euler, and Tom Baden (Nov. 2024). *Vertebrate Vision Is Ancestrally Based on Competing Cone Circuits*. DOI: 10.1101/2024.11.19.624320. (Visited on 03/07/2025).

Franke, Katrin, Philipp Berens, et al. (Feb. 2017). "Inhibition Decorrelates Visual Feature Representations in the Inner Retina". In: *Nature* 542.7642, pp. 439–444. ISSN: 0028-0836. DOI: 10.1038/nature21394. (Visited on 08/15/2021).

Franke, Katrin, André Maia Chagas, et al. (Sept. 2019). "An Arbitrary-Spectrum Spatial Visual Stimulator for Vision Research". In: *eLife* 8. Ed. by Alexander Borst, Joshua I

Gold, and Armin Bahl, e48779. ISSN: 2050-084X. DOI: 10.7554/eLife.48779. (Visited on 06/01/2022).

Freed, Michael A., Robert G. Smith, and Peter Sterling (1992). "Computational Model of the On-Alpha Ganglion Cell Receptive Field Based on Bipolar Cell Circuitry". In: *Proceedings of the National Academy of Sciences of the United States of America* 89.1, pp. 236–240. ISSN: 0027-8424. DOI: 10.1073/pnas.89.1.236. JSTOR: 2358511. (Visited on 06/03/2022).

Gaynes, John A. et al. (Sept. 2022). "Classical Center-Surround Receptive Fields Facilitate Novel Object Detection in Retinal Bipolar Cells". In: *Nature Communications* 13.1, p. 5575. ISSN: 2041-1723. DOI: 10.1038/s41467-022-32761-8. (Visited on 07/14/2025).

Gernandt, Bo and Ragnar Granit (July 1947). "Single Fibre Analysis of Inhibition and the Polarity of the Retinal Elements". In: *Journal of Neurophysiology* 10.4, pp. 295–301. ISSN: 0022-3077. DOI: 10.1152/jn.1947.10.4.295. (Visited on 07/28/2025).

Granit, Ragnar (May 1948). "Neural Organization of the Retinal Elements, as Revealed by Polarization". In: *Journal of Neurophysiology* 11.3, pp. 239–251. ISSN: 0022-3077. DOI: 10.1152/jn.1948.11.3.239. (Visited on 07/28/2025).

Gupta, Divyansh, Wiktor Młynarski, Anton Sumser, et al. (Apr. 2023). "Panoramic Visual Statistics Shape Retina-Wide Organization of Receptive Fields". In: *Nature Neuroscience* 26.4, pp. 606–614. ISSN: 1546-1726. DOI: 10.1038/s41593-023-01280-0. (Visited on 03/28/2024).

Gupta, Divyansh, Wiktor Młynarski, Olga Symonova, et al. (Jan. 2022). *Panoramic Visual Statistics Shape Retina-Wide Organization of Receptive Fields*. Preprint. Neuroscience. DOI: 10.1101/2022.01.11.475815. (Visited on 08/31/2022).

Hare, W A and W G Owen (Feb. 1990). "Spatial Organization of the Bipolar Cell's Receptive Field in the Retina of the Tiger Salamander." In: *The Journal of Physiology* 421.1, pp. 223–245. ISSN: 0022-3751, 1469-7793. DOI: 10.1113/jphysiol.1990.sp017942. (Visited on 07/30/2025).

Hartline, H. K. (Jan. 1938). "The Response of Single Optic Nerve Fibers of the Vertebrate Eye to Illumination of the Retina". In: *American Journal of Physiology-Legacy Content* 121.2, pp. 400–415. ISSN: 0002-9513. DOI: 10.1152/ajplegacy.1938.121.2.400. (Visited on 01/27/2022).

Haug, Marion F. et al. (Mar. 2010). "Visual Acuity in Larval Zebrafish: Behavior and Histology". In: *Frontiers in Zoology* 7.1, p. 8. ISSN: 1742-9994. DOI: 10.1186/1742-9994-7-8. (Visited on 05/24/2022).

Haverkamp, S., U. Grünert, and H. Wässle (2000). "The Cone Pedicle, a Complex Synapse in the Retina". In: *Neuron* 27, pp. 85–95. DOI: 10.1016/S0896-6273(00)00011-8.

Hellevik, Ayana M et al. (Oct. 2023). "Ancient Origin of the Rod Bipolar Cell Pathway in the Vertebrate Retina". In: *bioRxiv*, p. 2023.09.12.557433. DOI: 10.1101/2023.09.12.557433. (Visited on 03/21/2024).

– (June 2024). "Ancient Origin of the Rod Bipolar Cell Pathway in the Vertebrate Retina". In: *Nature Ecology & Evolution* 8.6, pp. 1165–1179. ISSN: 2397-334X. DOI: 10.1038/s41559-024-02404-w. (Visited on 08/01/2025).

Hollbach, Nadine et al. (Mar. 2015). “Photopic and Scotopic Spatiotemporal Tuning of Adult Zebrafish Vision”. In: *Frontiers in Systems Neuroscience* 9. ISSN: 1662-5137. DOI: 10.3389/fnsys.2015.00020. (Visited on 08/16/2025).

Hsiang, Jen-Chun et al. (Mar. 2024). “Distributed Feature Representations of Natural Stimuli across Parallel Retinal Pathways”. In: *Nature Communications* 15.1, p. 1920. ISSN: 2041-1723. DOI: 10.1038/s41467-024-46348-y. (Visited on 03/10/2024).

Hubel, D. H. and T. N. Wiesel (Dec. 1960). “Receptive Fields of Optic Nerve Fibres in the Spider Monkey”. In: *The Journal of Physiology* 154.3, pp. 572–580. ISSN: 0022-3751. (Visited on 04/26/2022).

– (Jan. 1962). “Receptive Fields, Binocular Interaction and Functional Architecture in the Cat’s Visual Cortex”. In: *The Journal of Physiology* 160.1, pp. 106–154.2. ISSN: 0022-3751. (Visited on 04/26/2022).

Hughes, Malcolm C., Alex M. Zimmer, and Steve F. Perry (Mar. 2019). “Role of Internal Convection in Respiratory Gas Transfer and Aerobic Metabolism in Larval Zebrafish (Danio Rerio)”. In: *American Journal of Physiology-Regulatory, Integrative and Comparative Physiology* 316.3, R255–R264. ISSN: 0363-6119. DOI: 10.1152/ajpregu.00315.2018. (Visited on 12/07/2024).

Ul-Hussain, Mahboob et al. (May 2008). “IRES-mediated Translation of the Carboxy-Terminal Domain of the Horizontal Cell Specific Connexin Cx55.5 in Vivo and in Vitro”. In: *BMC Molecular Biology* 9.1, p. 52. ISSN: 1471-2199. DOI: 10.1186/1471-2199-9-52. (Visited on 12/08/2024).

Jacob, E. et al. (Oct. 2002). “Influence of Hypoxia and of Hypoxemia on the Development of Cardiac Activity in Zebrafish Larvae”. In: *American Journal of Physiology-Regulatory, Integrative and Comparative Physiology* 283.4, R911–R917. ISSN: 0363-6119. DOI: 10.1152/ajpregu.00673.2001. (Visited on 12/07/2024).

Janiak, F. K. et al. (Jan. 2022). “Non-Telecentric Two-Photon Microscopy for 3D Random Access Mesoscale Imaging”. In: *Nature Communications* 13.1, p. 544. ISSN: 2041-1723. DOI: 10.1038/s41467-022-28192-0. (Visited on 01/29/2022).

Johnston, Jamie, Huayu Ding, et al. (Nov. 2014). “Rapid Mapping of Visual Receptive Fields by Filtered Back Projection: Application to Multi-Neuronal Electrophysiology and Imaging”. In: *The Journal of Physiology* 592.Pt 22, pp. 4839–4854. ISSN: 0022-3751. DOI: 10.1113/jphysiol.2014.276642. (Visited on 08/04/2025).

Johnston, Jamie, Sofie-Helene Seibel, et al. (June 2019). “A Retinal Circuit Generating a Dynamic Predictive Code for Oriented Features”. In: *Neuron* 102.6, 1211–1222.e3. ISSN: 0896-6273. DOI: 10.1016/j.neuron.2019.04.002. (Visited on 04/15/2025).

Kaneko, A., L.H. Pinto, and M. Tachibana (1989). “Transient Calcium Current of Retinal Bipolar Cells of the Mouse”. In: *The Journal of Physiology* 410.1. DOI: 10.1113/jphysiol.1989.sp017551.

Kaneko, A. and M. Tachibana (Sept. 1981). “Retinal Bipolar Cells with Double Colour-Opponent Receptive Fields”. In: *Nature* 293.5829, pp. 220–222. ISSN: 1476-4687. DOI: 10.1038/293220a0. (Visited on 08/01/2022).

Kaneko, Akimichi (1970). “Physiological and Morphological Identification of Horizontal, Bipolar and Amacrine Cells in Goldfish Retina”. In: *The Journal of Physiology* 207.3, pp. 623–633. ISSN: 1469-7793. DOI: 10.1113/jphysiol.1970.sp009084. (Visited on 10/31/2024).

– (1973). “Receptive Field Organization of Bipolar and Amacrine Cells in the Goldfish Retina”. In: *The Journal of Physiology* 235.1, pp. 133–153. ISSN: 1469-7793. DOI: 10.1113/jphysiol.1973.sp010381. (Visited on 07/31/2025).

Karlsson, Johnny, Jonas von Hofsten, and Per-Erik Olsson (Nov. 2001). “Generating Transparent Zebrafish: A Refined Method to Improve Detection of Gene Expression During Embryonic Development”. In: *Marine Biotechnology* 3.6, pp. 522–527. ISSN: 1436-2228. DOI: 10.1007/s1012601-0053-4. (Visited on 12/06/2024).

Kerschensteiner, Daniel (2022). “Feature Detection by Retinal Ganglion Cells”. In: *Annual Review of Vision Science* 8.1, null. DOI: 10.1146/annurev-vision-100419-112009. (Visited on 04/26/2022).

Kramer, Richard H. and Christopher M. Davenport (Dec. 2015). “Lateral Inhibition in the Vertebrate Retina: The Case of the Missing Neurotransmitter”. In: *PLOS Biology* 13.12, e1002322. ISSN: 1545-7885. DOI: 10.1371/journal.pbio.1002322. (Visited on 08/30/2021).

Kuffler, Stephen W. (1953). *Discharge Patterns and Functional Organization of Mammalian Retina - PubMed*. https://pubmed.ncbi.nlm.nih.gov/13035466/. (Visited on 06/11/2025).

Lamb, T.D. (2013). “Evolution of Phototransduction, Vertebrate Photoreceptors and Retina”. In: *Progress in Retinal and Eye Research* 36, pp. 52–119. DOI: 10.1016/j.preteyeres.2013.06.001.

Lamb, Trevor D., Shaun P. Collin, and Edward N. Pugh (Dec. 2007). “Evolution of the Vertebrate Eye: Opsins, Photoreceptors, Retina and Eye Cup”. In: *Nature Reviews Neuroscience* 8.12, pp. 960–976. DOI: 10.1038/nrn2283.

Leyden, Claire et al. (Mar. 2022). “Efficacy of Tricaine (MS-222) and Hypothermia as Anesthetic Agents for Blocking Sensorimotor Responses in Larval Zebrafish”. In: *Frontiers in Veterinary Science* 9. ISSN: 2297-1769. DOI: 10.3389/fvets.2022.864573. (Visited on 12/06/2024).

Li, Yan, Shuguang Yu, et al. (Feb. 2024). “Defining Morphologically and Genetically Distinct GABAergic/Cholinergic Amacrine Cell Subtypes in the Vertebrate Retina”. In: *PLOS Biology* 22.2, e3002506. ISSN: 1545-7885. DOI: 10.1371/journal.pbio.3002506. (Visited on 08/04/2025).

Li, Yong N., Taro Tsujimura, et al. (2012). “Bipolar Cell–Photoreceptor Connectivity in the Zebrafish (Danio Rerio) Retina”. In: *Journal of Comparative Neurology* 520.16, pp. 3786–3802. ISSN: 1096-9861. DOI: 10.1002/cne.23168. (Visited on 03/21/2024).

Maaswinkel, H. and L. Li (2003). “Spatio-Temporal Frequency Characteristics of the Optomotor Response in Zebrafish”. In: *Vision Reserach* 43.1, pp. 21–30. DOI: 10.1016/S0042-6989(02)00395-4.

MacIver, Malcolm A. et al. (Mar. 2017). “Massive Increase in Visual Range Preceded the Origin of Terrestrial Vertebrates”. In: *Proceedings of the National Academy of Sciences*

114.12. ISSN: 0027-8424, 1091-6490. DOI: 10.1073/pnas.1615563114. (Visited on 08/03/2025).

Macpherson, Neil (May 2020). *Prof Vince Tropepe's Lab Using Zebrafish as a Vertebrate Model for Usher Syndrome-linked Blindness*. (Visited on 07/18/2025).

Magupalli, Venkat Giri et al. (Aug. 2008). "Multiple RIBEYE–RIBEYE Interactions Create a Dynamic Scaffold for the Formation of Synaptic Ribbons". In: *The Journal of Neuroscience* 28.32, pp. 7954–7967. ISSN: 0270-6474, 1529-2401. DOI: 10.1523/JNEUROSCI.1964-08.2008. (Visited on 12/08/2024).

Marr, D., E. Hildreth, and Sydney Brenner (Feb. 1980). "Theory of Edge Detection". In: *Proceedings of the Royal Society of London. Series B. Biological Sciences* 207.1167, pp. 187–217. DOI: 10.1098/rspb.1980.0020. (Visited on 06/03/2022).

Marre, Olivier et al. (July 2015). "High Accuracy Decoding of Dynamical Motion from a Large Retinal Population". In: *PLOS Computational Biology* 11.7, e1004304. ISSN: 1553-7358. DOI: 10.1371/journal.pcbi.1004304. (Visited on 08/23/2024).

Marvin, Jonathan S. et al. (Nov. 2018). "Stability, Affinity, and Chromatic Variants of the Glutamate Sensor iGluSnFR". In: *Nature Methods* 15.11, pp. 936–939. ISSN: 1548-7105. DOI: 10.1038/s41592-018-0171-3. (Visited on 12/08/2024).

Masland, Richard H. (Oct. 2012a). "The Neuronal Organization of the Retina". In: *Neuron* 76.2, pp. 266–280. ISSN: 08966273. DOI: 10.1016/j.neuron.2012.10.002. (Visited on 01/13/2022).

– (Jan. 2012b). "The Tasks of Amacrine Cells". In: *Visual Neuroscience* 29.1, pp. 3–9. ISSN: 1469-8714. DOI: 10.1017/s0952523811000344.

McCauley, David W and Marianne Bronner-Fraser (Apr. 2002). "Conservation of Pax Gene Expression in Ectodermal Placodes of the Lamprey". In: *Gene*. Workshop 'Comparative Developmental Biology', Naples, 17- April 2001 287.1, pp. 129–139. ISSN: 0378-1119. DOI: 10.1016/S0378-1119(01)00894-0. (Visited on 06/30/2025).

Mcilwain, J. T. (Nov. 1964). "RECEPTIVE FIELDS OF OPTIC TRACT AXONS AND LATERAL GENICULATE CELLS: PERIPHERAL EXTENT AND BARBITURATE SENSITIVITY". In: *Journal of Neurophysiology* 27, pp. 1154–1173. ISSN: 0022-3077. DOI: 10.1152/jn.1964.27.6.1154.

Molnar, Alyosha et al. (2009). "Crossover Inhibition in the Retina: Circuitry That Compensates for Nonlinear Rectifying Synaptic Transmission". In: *Journal of Computational Neuroscience* 27.3, pp. 569–590. ISSN: 0929-5313. DOI: 10.1007/s10827-009-0170-6. (Visited on 07/07/2025).

Morgans, Catherine W (2000). "Neurotransmitter Release at Ribbon Synapses in the Retina". In: *Immunology & Cell Biology* 78.4, pp. 442–446. ISSN: 1440-1711. DOI: 10.1046/j.1440-1711.2000.00923.x. (Visited on 08/01/2025).

Morgans, Catherine W. et al. (Nov. 1996). "A SNARE Complex Containing Syntaxin 3 Is Present in Ribbon Synapses of the Retina". In: *Journal of Neuroscience* 16.21, pp. 6713–6721. ISSN: 0270-6474, 1529-2401. DOI: 10.1523/JNEUROSCI.16-21-06713.1996. (Visited on 08/25/2025).

Moya-Díaz, J, P Simões, and L Lagnado (Apr. 2024). “Substance P and Dopamine Form a "Push-Pull" System That Diurnally Regulates Retinal Gain”. In: *Current biology : CB* 34.21. ISSN: 1879-0445. DOI: 10.1016/j.cub.2024.09.048. (Visited on 09/29/2025).

Muto, Akira et al. (Mar. 2011). “Genetic Visualization with an Improved GCaMP Calcium Indicator Reveals Spatiotemporal Activation of the Spinal Motor Neurons in Zebrafish”. In: *Proceedings of the National Academy of Sciences* 108.13, pp. 5425–5430. DOI: 10.1073/pnas.1000887108. (Visited on 06/24/2025).

Naka, K. I. and P. W. Nye (Sept. 1971). “Role of Horizontal Cells in Organization of the Catfish Retinal Receptive Field”. In: *Journal of Neurophysiology* 34.5, pp. 785–801. ISSN: 0022-3077. DOI: 10.1152/jn.1971.34.5.785.

Nakai, J., M. Ohkura, and K. Imoto (2001). “A High Signal-to-Noise Ca2+ Probe Composed of a Single Green Fluorescent Protein”. In: *Nature Biotechnology* 19, pp. 137–241. DOI: 10.1038/84397.

Nelson, Ralph F. et al. (Nov. 2022). “The Developmental Progression of Eight Opsin Spectral Signals Recorded from the Zebrafish Retinal Cone Layer Is Altered by the Timing and Cell Type Expression of Thyroxin Receptor B2 (trB2) Gain-Of-Function Transgenes”. In: *eNeuro* 9.6. ISSN: 2373-2822. DOI: 10.1523/ENEURO.0326-22.2022. (Visited on 12/08/2024).

Nemitz, Lena, Karin Dedek, and Ulrike Janssen-Bienhold (May 2021). “Synaptic Remodeling in the Cone Pathway After Early Postnatal Horizontal Cell Ablation”. In: *Frontiers in Cellular Neuroscience* 15. ISSN: 1662-5102. DOI: 10.3389/fncel.2021.657594. (Visited on 08/01/2025).

Nevala, N. E. and T. Baden (July 2019). “A Low-Cost Hyperspectral Scanner for Natural Imaging and the Study of Animal Colour Vision above and under Water”. In: *Scientific Reports* 9.1, p. 10799. ISSN: 2045-2322. DOI: 10.1038/s41598-019-47220-6. (Visited on 06/30/2025).

Ng, Lily et al. (Jan. 2001). “A Thyroid Hormone Receptor That Is Required for the Development of Green Cone Photoreceptors”. In: *Nature Genetics* 27.1, pp. 94–98. ISSN: 1546-1718. DOI: 10.1038/83829. (Visited on 12/08/2024).

Pamplona, Daniela et al. (May 2022). “Receptive Field Estimation in Large Visual Neuron Assemblies Using a Super-Resolution Approach”. In: *Journal of Neurophysiology* 127.5, pp. 1334–1347. ISSN: 0022-3077. DOI: 10.1152/jn.00076.2021. (Visited on 05/05/2022).

Pan, Z.-H. et al. (2001). “T-Type Ca2+ Channels Mediate Neurotransmitter Release in Retinal Bipolar Cells”. In: *Neuron* 32.11, pp. 89–98. DOI: 10.1016/S0896-6273(01)00454-8.

Pelster, Bernd and Warren W. Burggren (Aug. 1996). “Disruption of Hemoglobin Oxygen Transport Does Not Impact Oxygen-Dependent Physiological Processes in Developing Embryos of Zebra Fish (*Danio Rerio*)”. In: *Circulation Research* 79.2, pp. 358–362. ISSN: 0009-7330, 1524-4571. DOI: 10.1161/01.RES.79.2.358. (Visited on 12/07/2024).

Perkins, Brian D., James M. Fadool, and John E. Dowling (Jan. 2004). “Photoreceptor Structure and Development: Analyses Using GFP Transgenes”. In: *Methods in Cell*

Biology. Vol. 76. The Zebrafish: Cellular and Developmental Biology. Academic Press, pp. 315–331. DOI: 10.1016/S0091-679X(04)76015-X. (Visited on 06/02/2024).

Riccitelli, Serena et al. (Jan. 2025). "Retinal Ganglion Cells Encode the Direction of Motion Outside Their Classical Receptive Field". In: *Proceedings of the National Academy of Sciences of the United States of America* 122.1, e2415223122. ISSN: 1091-6490. DOI: 10.1073/pnas.2415223122.

Richter, A and E J Simon (1975). "Properties of Centre-Hyperpolarizing, Red-Sensitive Bipolar Cells in the Turtle Retina." In: *The Journal of Physiology* 248.2, pp. 317–334. ISSN: 1469-7793. DOI: 10.1113/jphysiol.1975.sp010976. (Visited on 08/26/2024).

Rodieck, R. W. (Dec. 1965). "Quantitative Analysis of Cat Retinal Ganglion Cell Response to Visual Stimuli". In: *Vision Research* 5.12, pp. 583–601. ISSN: 0042-6989. DOI: 10.1016/0042-6989(65)90033-7. (Visited on 01/27/2022).

Roska, Botond and Frank Werblin (Mar. 2001). "Vertical Interactions across Ten Parallel, Stacked Representations in the Mammalian Retina". In: *Nature* 410.6828, pp. 583–587. ISSN: 1476-4687. DOI: 10.1038/35069068. (Visited on 06/26/2025).

Saito and Toru Kujiraoka (1982). "Physiological and Morphological Identification of Two Types of On-Center Bipolar Cells in the Carp Retina". In: *Journal of Comparative Neurology* 205.2, pp. 161–170. ISSN: 1096-9861. DOI: 10.1002/cne.902050207. (Visited on 08/20/2024).

Saito, T and A Kaneko (Apr. 1983). "Ionic Mechanisms Underlying the Responses of Off-Center Bipolar Cells in the Carp Retina. I. Studies on Responses Evoked by Light". In: *The Journal of general physiology* 81.4, pp. 589–601. ISSN: 1540-7748. DOI: 10.1085/jgp.81.4.589. (Visited on 08/20/2024).

Saito, T, H Kondo, and J I Toyoda (Jan. 1979). "Ionic Mechanisms of Two Types of On-Center Bipolar Cells in the Carp Retina. I. The Responses to Central Illumination". In: *The Journal of general physiology* 73.1, pp. 73–90. ISSN: 1540-7748. DOI: 10.1085/jgp.73.1.73. (Visited on 08/20/2024).

Schmitt, E.A. and J.E. Dowling (1999). "Early Retinal Development in the Zebrafish, Danio Rerio: Light and Electron Microscopic Analyses". In: *Journal of Comparative Neurology* 404.4, pp. 515–536. DOI: 10.1002/(SICI)1096-9861(19990222)404:4<515::AID-CNE8>3.0.CO;2-A.

Schmitz, Frank, Andreas Königstorfer, and Thomas C. Südhof (Dec. 2000). "RIBEYE, a Component of Synaptic Ribbons: A Protein's Journey through Evolution Provides Insight into Synaptic Ribbon Function". In: *Neuron* 28.3, pp. 857–872. ISSN: 0896-6273. DOI: 10.1016/S0896-6273(00)00159-8. (Visited on 12/08/2024).

Schreyer, Helene Marianne and Tim Gollisch (May 2021). "Nonlinear Spatial Integration in Retinal Bipolar Cells Shapes the Encoding of Artificial and Natural Stimuli". In: *Neuron* 109.10, 1692–1706.e8. ISSN: 1097-4199. DOI: 10.1016/j.neuron.2021.03.015.

Schroeter, Eric H., Rachel O. L. Wong, and Ronald G. Gregg (Sept. 2006). "In Vivo Development of Retinal ON-bipolar Cell Axonal Terminals Visualized in Nyx::MYFP Transgenic Zebrafish". In: *Visual Neuroscience* 23.5, pp. 833–843. ISSN: 1469-8714, 0952-5238. DOI: 10.1017/S0952523806230219. (Visited on 03/21/2024).

Schwartz, E. A. (1974). “Responses of Bipolar Cells in the Retina of the Turtle”. In: *The Journal of Physiology* 236.1, pp. 211–224. ISSN: 1469-7793. DOI: 10.1113/jphysiol.1974.sp010431. (Visited on 08/26/2024).

Seifert, Marvin et al. (Aug. 2023). “Birds Multiplex Spectral and Temporal Visual Information via Retinal On- and Off-channels”. In: *Nature Communications* 14.1, p. 5308. ISSN: 2041-1723. DOI: 10.1038/s41467-023-41032-z. (Visited on 08/25/2025).

Shimbo, Kiyoshi et al. (July 2000). “Color-Opponent Responses of Small and Giant Bipolar Cells in the Carp Retina”. In: *Visual Neuroscience* 17.4, pp. 609–621. ISSN: 1469-8714, 0952-5238. DOI: 10.1017/S0952523800174103. (Visited on 08/20/2024).

Spira, M.E. and A. Hai (2013). “Multi-Electrode Array Technologies for Neuroscience and Cardiology”. In: *Nature Nanotechnology* 8, pp. 83–94. DOI: 10.1038/nnano.2012.265.

Strauss, Sarah et al. (Sept. 2022). “Center-Surround Interactions Underlie Bipolar Cell Motion Sensitivity in the Mouse Retina”. In: *Nature Communications* 13.1, p. 5574. ISSN: 2041-1723. DOI: 10.1038/s41467-022-32762-7. (Visited on 03/21/2024).

Südhof, T.C. (2012). “Calcium Control of Neurotransmitter Release”. In: *Cold Spring Harbor Perspectives in biology* 4.1, p. 011353. DOI: 10.1101/cshperspect.a011353.

Suzuki, Sachihiro C. et al. (Sept. 2013). “Cone Photoreceptor Types in Zebrafish Are Generated by Symmetric Terminal Divisions of Dedicated Precursors”. In: *Proceedings of the National Academy of Sciences* 110.37, pp. 15109–15114. DOI: 10.1073/pnas.1303551110. (Visited on 12/08/2024).

Swamynathan, Shivalingappa K. et al. (Nov. 2003). “Adaptive Differences in the Structure and Macromolecular Compositions of the Air and Water Corneas of the “Four-eyed” Fish (Anableps Anableps)”. In: *The FASEB Journal* 17.14, pp. 1996–2005. ISSN: 0892-6638, 1530-6860. DOI: 10.1096/fj.03-0122com. (Visited on 08/03/2025).

Swygart, David et al. (Jan. 2024). “A Presynaptic Source Drives Differing Levels of Surround Suppression in Two Mouse Retinal Ganglion Cell Types”. In: *Nature Communications* 15.1, p. 599. ISSN: 2041-1723. DOI: 10.1038/s41467-024-44851-w. (Visited on 08/03/2025).

Takeshita, Daisuke and Tim Gollisch (May 2014). “Nonlinear Spatial Integration in the Receptive Field Surround of Retinal Ganglion Cells”. In: *Journal of Neuroscience* 34.22, pp. 7548–7561. ISSN: 0270-6474, 1529-2401. DOI: 10.1523/JNEUROSCI.0413-14.2014. (Visited on 08/23/2024).

Talbot, S. A. and S. W. Kuffler (Dec. 1952). “A Multibeam Ophthalmoscope for the Study of Retinal Physiology*”. In: *JOSA* 42.12, pp. 931–936. DOI: 10.1364/JOSA.42.000931. (Visited on 06/11/2025).

Thoreson, Wallace B. and Dennis M. Dacey (July 2019). “Diverse Cell Types, Circuits, and Mechanisms for Color Vision in the Vertebrate Retina”. In: *Physiological Reviews* 99.3, pp. 1527–1573. ISSN: 0031-9333. DOI: 10.1152/physrev.00027.2018. (Visited on 06/13/2025).

Thoreson, Wallace B. and Stuart C. Mangel (Sept. 2012). “Lateral Interactions in the Outer Retina”. In: *Progress in Retinal and Eye Research* 31.5, pp. 407–441. ISSN: 1873-1635. DOI: 10.1016/j.preteyeres.2012.04.003.

Tommasini, Dario et al. (May 2025). “Comparative Transcriptomic Insights into the Evolution of Vertebrate Photoreceptor Types”. In: *Current Biology* 35.10, 2228–2239.e4. ISSN: 0960-9822. DOI: 10.1016/j.cub.2025.03.060. (Visited on 09/29/2025).

Toyoda, Jun-Ichi (Feb. 1973). “Membrane Resistance Changes Underlying the Bipolar Cell Response in the Carp Retina”. In: *Vision Research* 13.2, pp. 283–294. ISSN: 0042-6989. DOI: 10.1016/0042-6989(73)90107-7. (Visited on 08/20/2024).

Trenholm, Stuart and Gautam B. Awatramani (1995). “Myriad Roles for Gap Junctions in Retinal Circuits”. In: *Webvision: The Organization of the Retina and Visual System*. Ed. by Helga Kolb et al. Salt Lake City (UT): University of Utah Health Sciences Center. (Visited on 07/07/2025).

Turner, Maxwell H, Gregory W Schwartz, and Fred Rieke (Sept. 2018). “Receptive Field Center-Surround Interactions Mediate Context-Dependent Spatial Contrast Encoding in the Retina”. In: *eLife* 7. Ed. by Andrew J King, e38841. ISSN: 2050-084X. DOI: 10.7554/eLife.38841. (Visited on 01/29/2022).

Valtorta, Flavia et al. (2004). “Synaptophysin: Leading Actor or Walk-on Role in Synaptic Vesicle Exocytosis?” In: *BioEssays* 26.4, pp. 445–453. ISSN: 1521-1878. DOI: 10.1002/bies.20012. (Visited on 08/25/2025).

Vlasits, A.L. et al. (2016). “A Role for Synaptic Input Distribution in a Dendritic Computation of Motion Direction in the Retina”. In: *Neuron* 89.6, pp. 1317–1330. DOI: 10.1016/j.neuron.2016.02.020.

Völgyi, Béla et al. (May 2013). “Gap Junctional Coupling in the Vertebrate Retina: Variations on One Theme?” In: *Progress in Retinal and Eye Research* 34, pp. 1–18. ISSN: 13509462. DOI: 10.1016/j.preteyeres.2012.12.002. (Visited on 08/03/2025).

Wan, Lei, Wolfhard Almers, and Wenbiao Chen (Jan. 2005). “Two Ribeye Genes in Teleosts: The Role of Ribeye in Ribbon Formation and Bipolar Cell Development”. In: *The Journal of Neuroscience* 25.4, pp. 941–949. ISSN: 0270-6474. DOI: 10.1523/JNEUROSCI.4657-04.2005. (Visited on 06/24/2025).

Wang, Xinwei et al. (July 2022). *Amacrine Cells Differentially Balance Zebrafish Colour Circuits in the Central and Peripheral Retina*. DOI: 10.1101/2022.01.22.477338. (Visited on 08/25/2022).

– (Feb. 2023). “Amacrine Cells Differentially Balance Zebrafish Color Circuits in the Central and Peripheral Retina”. In: *Cell Reports* 42.2, p. 112055. ISSN: 22111247. DOI: 10.1016/j.celrep.2023.112055. (Visited on 08/03/2025).

Wässle, H.S. (0). “The Cone Pedicle, the First Synapse in the Retina”. In: *The Neural Basis of Early Vision*.

Werblin, F S and J E Dowling (May 1969). “Organization of the Retina of the Mudpuppy, Necturus Maculosus. II. Intracellular Recording.” In: *Journal of Neurophysiology* 32.3, pp. 339–355. ISSN: 0022-3077. DOI: 10.1152/jn.1969.32.3.339. (Visited on 08/26/2024).

Werblin, Frank S. (Mar. 1972). “Lateral Interactions at Inner Plexiform Layer of Vertebrate Retina: Antagonistic Responses to Change”. In: *Science* 175.4025, pp. 1008–1010. DOI: 10.1126/science.175.4025.1008. (Visited on 11/01/2024).

Werblin, Frank S. (Mar. 2010). “Six Different Roles for Crossover Inhibition in the Retina: Correcting the Nonlinearities of Synaptic Transmission”. In: *Visual neuroscience* 27.1-2, pp. 1–8. ISSN: 0952-5238. DOI: 10.1017/S0952523810000076. (Visited on 07/07/2025).

Westbrook, Aileen M (1994). “A Review of the Neurophysiology of the Turtle Retina: Horizontal and Bipolar Cells”. In: *Clinical and Experimental Optometry* 77.4, pp. 153–166. ISSN: 1444-0938. DOI: 10.1111/j.1444-0938.1994.tb03001.x. (Visited on 08/26/2024).

White, Richard Mark et al. (Feb. 2008). “Transparent Adult Zebrafish as a Tool for In Vivo Transplantation Analysis”. In: *Cell Stem Cell* 2.2, pp. 183–189. ISSN: 1934-5909. DOI: 10.1016/j.stem.2007.11.002. (Visited on 08/06/2025).

Wienbar, Sophia and Gregory W. Schwartz (Nov. 2018). “The Dynamic Receptive Fields of Retinal Ganglion Cells”. In: *Progress in Retinal and Eye Research* 67, pp. 102–117. ISSN: 1350-9462. DOI: 10.1016/j.preteyeres.2018.06.003. (Visited on 01/25/2022).

Wong, Kwoon Y., Alan R. Adolph, and John E. Dowling (Jan. 2005). “Retinal Bipolar Cell Input Mechanisms in Giant Danio. I. Electroretinographic Analysis”. In: *Journal of Neurophysiology* 93.1, pp. 84–93. ISSN: 0022-3077. DOI: 10.1152/jn.00259.2004. (Visited on 07/26/2025).

Wong, Kwoon Y. and John E. Dowling (July 2005). “Retinal Bipolar Cell Input Mechanisms in Giant Danio. III. on-off Bipolar Cells and Their Color-Opponent Mechanisms”. In: *Journal of Neurophysiology* 94.1, pp. 265–272. ISSN: 0022-3077. DOI: 10.1152/jn.00271.2004. (Visited on 07/26/2025).

Yazulla, Stephen (Jan. 1976). “Cone Input to Bipolar Cells in the Turtle Retina”. In: *Vision Research* 16.7, 737–IN3. ISSN: 00426989. DOI: 10.1016/0042-6989(76)90184-X. (Visited on 08/26/2024).

Yoshimatsu, T., C. Schröder, et al. (2020). “Fovea-like Photoreceptor Specializations Underlie Single UV Cone Driven Prey-Capture Behavior in Zebrafish”. In: *Neuron* 107.2, pp. 320–337 6. DOI: 10.1016/j.neuron.2020.04.021.

Yoshimatsu, Takeshi and Tom Baden (Feb. 2024). “New Twists in the Evolution of Retinal Direction Selectivity”. In: *PLOS Biology* 22.2, e3002538. ISSN: 1545-7885. DOI: 10.1371/journal.pbio.3002538. (Visited on 03/17/2024).

Yoshimatsu, Takeshi, Philipp Bartel, et al. (Apr. 2021). *Ancestral Circuits for Vertebrate Colour Vision Emerge at the First Retinal Synapse*. DOI: 10.1101/2020.10.26.356089. (Visited on 07/21/2025).

Zhang, Ai-Jun and Samuel M. Wu (Mar. 2010). “Responses and Receptive Fields of Amacrine Cells and Ganglion Cells in the Salamander Retina”. In: *Vision Research* 50.6, pp. 614–622. ISSN: 0042-6989. DOI: 10.1016/j.visres.2010.01.009. (Visited on 08/23/2024).

Zhang, Yan and Loren L. Looger (Apr. 2024). “Fast and Sensitive GCaMP Calcium Indicators for Neuronal Imaging”. In: *The Journal of Physiology* 602.8, pp. 1595–1604. ISSN: 1469-7793. DOI: 10.1113/JP283832. (Visited on 08/22/2025).

Zhang, Yan, Márton Rózsa, et al. (Mar. 2023). “Fast and Sensitive GCaMP Calcium Indicators for Imaging Neural Populations”. In: *Nature* 615.7954, pp. 884–891. ISSN: 1476-4687. DOI: 10.1038/s41586-023-05828-9. (Visited on 12/08/2024).

Zhang, Yifeng, In-Jung Kim, et al. (Sept. 2012). “The Most Numerous Ganglion Cell Type of the Mouse Retina Is a Selective Feature Detector”. In: *Proceedings of the National Academy of Sciences of the United States of America* 109.36, E2391–E2398. ISSN: 0027-8424. DOI: 10.1073/pnas.1211547109. (Visited on 06/04/2022).

Zhao, Xiao-Feng, Staale Ellingsen, and Anders Fjose (Aug. 2009). “Labelling and Targeted Ablation of Specific Bipolar Cell Types in the Zebrafish Retina”. In: *BMC Neuroscience* 10.1, p. 107. ISSN: 1471-2202. DOI: 10.1186/1471-2202-10-107. (Visited on 03/21/2024).

Zhou, Mingyi et al. (Aug. 2020). “Zebrafish Retinal Ganglion Cells Asymmetrically Encode Spectral and Temporal Information across Visual Space”. In: *Current Biology* 30.15, 2927–2942.e7. ISSN: 09609822. DOI: 10/gmw7zg. (Visited on 09/24/2021).

Zimmermann, Maxime J. Y. et al. (July 2018). “Zebrafish Differentially Process Color across Visual Space to Match Natural Scenes”. In: *Current Biology* 28.13, 2018–2032.e5. ISSN: 0960-9822. DOI: 10.1016/j.cub.2018.04.075. (Visited on 06/11/2021).

A | Appendix

A.1 Additional Calibration Data

Power measurements were taken at different positions to validate the calibration procedures described in the Methods chapter. Figure A.1 shows measurements taken directly in front of the projection screen, providing comparison data for the standard measurement position used during experiments.

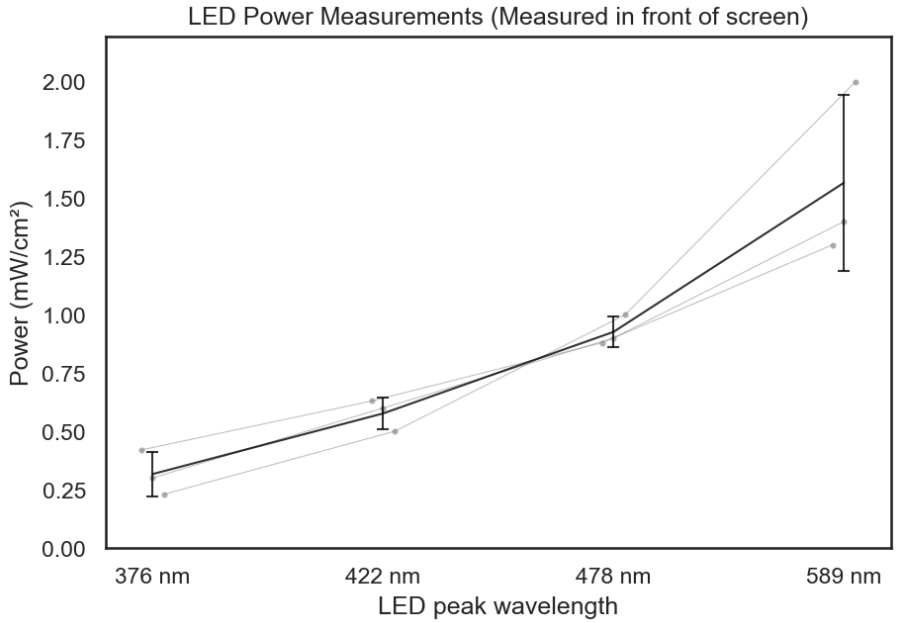

Figure A.1: LED power measurements taken in front of the projection screen. Power output (mW/cm²) measured for each LED wavelength (UV: 376 nm, Blue: 422 nm, Green: 478 nm, Red: 589 nm) with n=3 measurements per wavelength. Error bars represent standard deviation. These measurements were taken at a different position compared to the standard calibration described in the main text, demonstrating spatial variability in power distribution across the projection field. UV LED: 0.32 ± 0.10 mW/cm², B LED: 0.58 ± 0.07 mW/cm², G LED: 0.93 ± 0.06 mW/cm², R LED: 1.57 ± 0.38 mW/cm² (n=3).

A.2 Additional Scan Alignment Data

Additional example showing Y-axis misalignment, underlining the critical importance of precise spatial alignment between the stimulus projection and imaging plane.

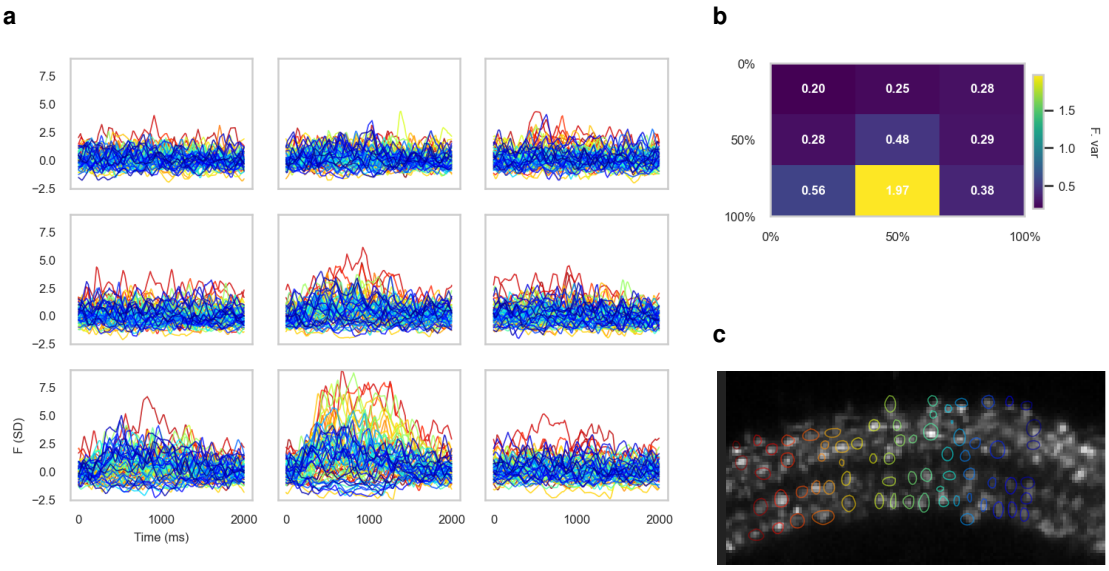

Figure A.2: Effects of Y-axis misalignment on scan plane alignment and receptive field mapping. **(a)** Calcium traces showing degraded response patterns due to vertical spatial offset. **(b)** Spatial heatmap revealing misalignment. Mapping an RF in this configuration would lead to severe edge artefacts and potential masking of surround effects. **(c)** ROI locations demonstrating the vertical displacement between cellular positions and stimulus grid.

A.3 Additional Cross-Correlation Examples

The following figures provide additional examples of cross-correlation analysis applied to bipolar cell terminals with weak signal and no signal.

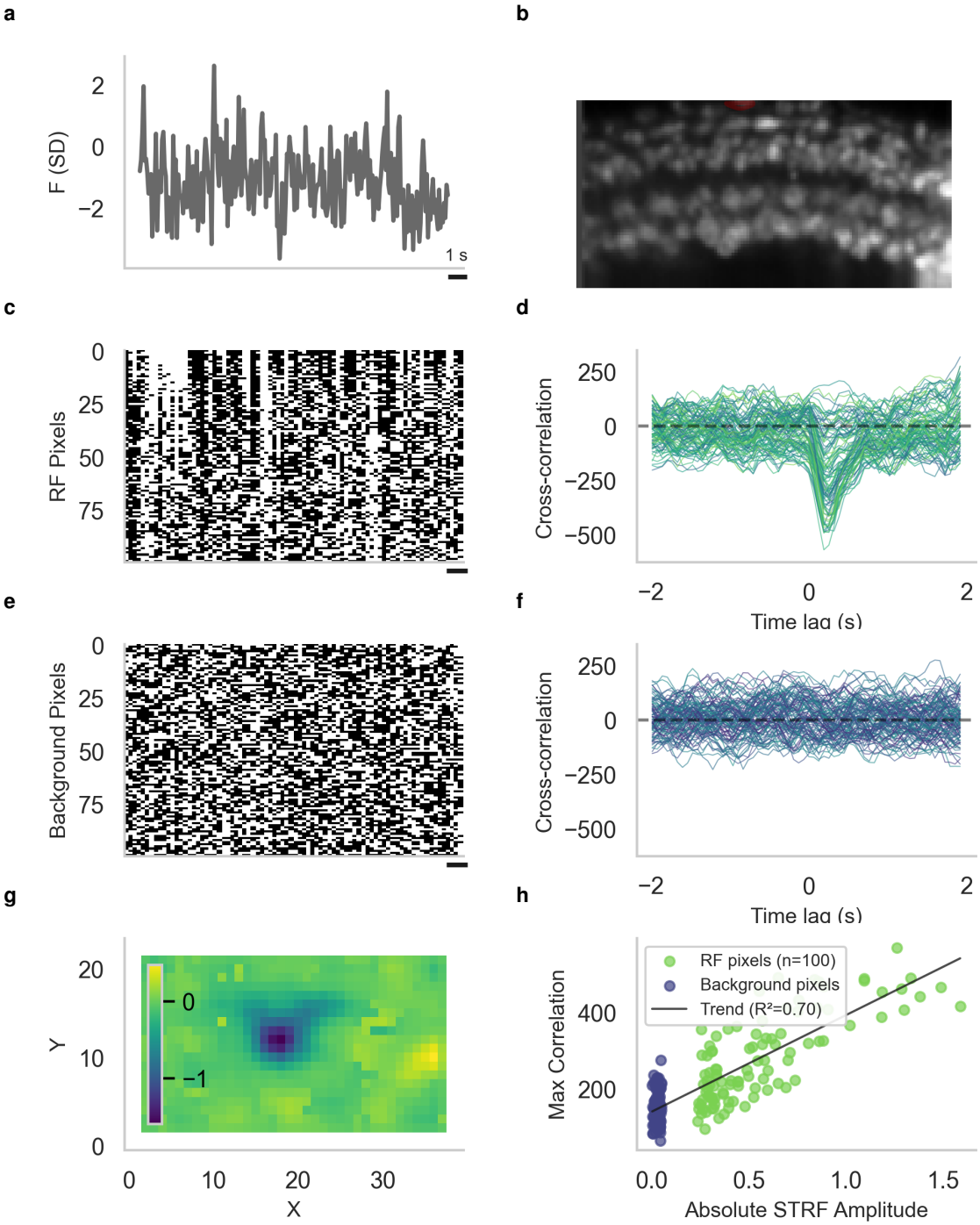

Figure A.3: Cross-correlation analysis of a weakly responding bipolar cell terminal. **(a)** Calcium fluorescence responses (SD) from a bipolar cell terminal exhibiting weak temporal dynamics during spatial binary noise presentation. **(b)** The analysed ROI within the retinal tissue scan plane. **(c)** Stimulus time series extracted for pixels with detectable but low-amplitude STRF responses. **(d)** Cross-correlation functions between ROI fluorescence and centre-driving pixels, showing attenuated correlation profiles compared to strongly responding cells. **(e)** Control stimulus time series from background pixels with minimal STRF amplitudes. **(f)** Cross-correlation functions for background control pixels, demonstrating minimal correlation similar to the weak receptive field signal. **(g)** Spatially-organised STRF map showing reduced spatial organisation and lower amplitude responses. **(h)** Quantitative analysis showing the relationship between STRF amplitude and maximum cross-correlation strength for weakly responding cells, demonstrating the detection limits of the cross-correlation approach.

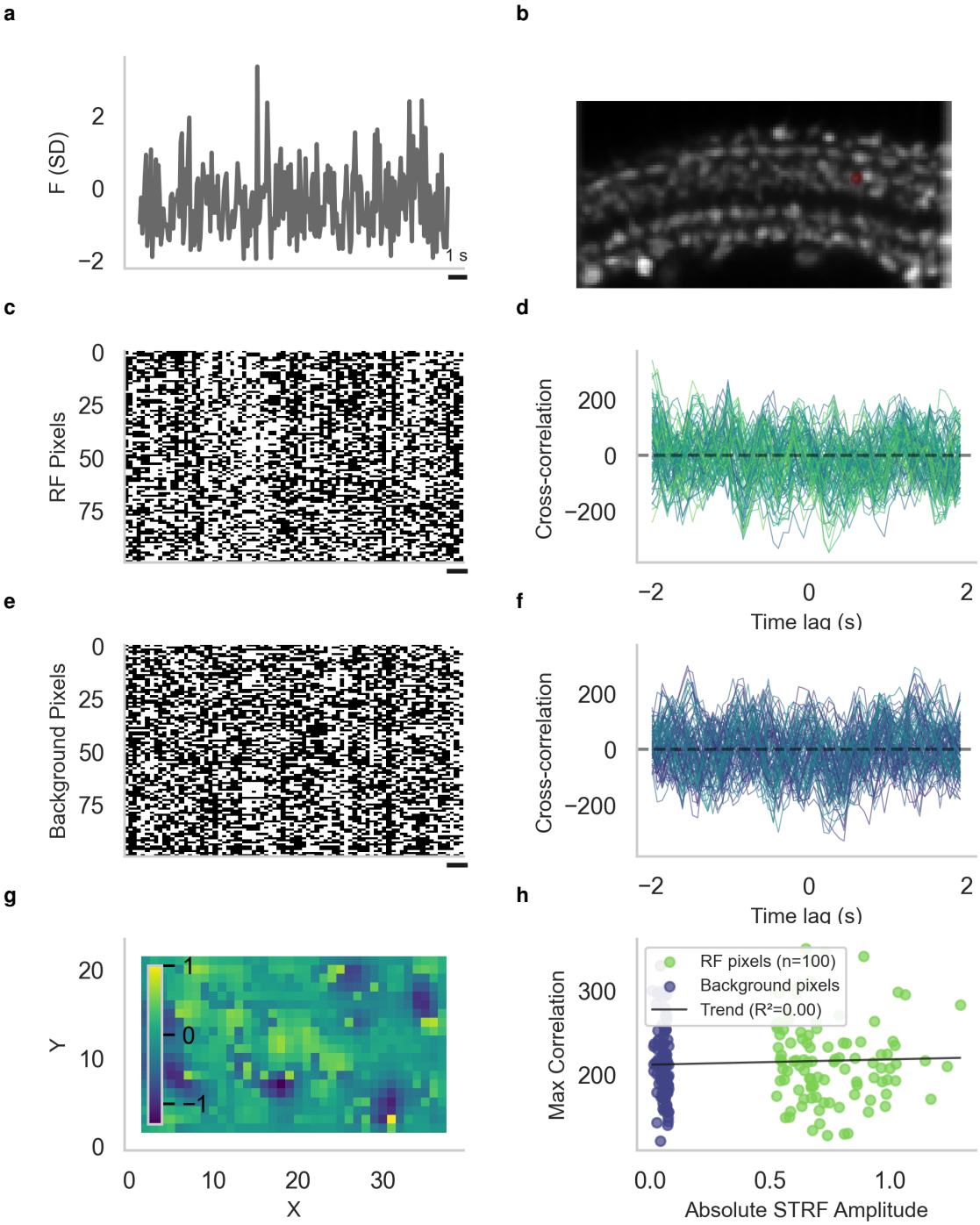

Figure A.4: Cross-correlation analysis demonstrating absence of detectable receptive field structure. **(a)** Calcium fluorescence responses (SD) from a bipolar cell terminal showing minimal temporal dynamics during spatial binary noise presentation. **(b)** The analysed ROI within the retinal tissue scan plane. **(c)** Stimulus time series extracted for pixels with negligible STRF responses, representing noise-level activity. **(d)** Cross-correlation functions between ROI fluorescence and putative centre pixels, showing flat correlation profiles indicative of no receptive field structure. **(e)** Control stimulus time series from background pixels with similar minimal STRF amplitudes. **(f)** Cross-correlation functions for background control pixels, demonstrating correlation levels comparable to the putative receptive field centre, confirming absence of spatial selectivity. **(g)** Spatially-organised STRF map showing absence of coherent spatial structure and uniformly low amplitudes across all pixels. **(h)** Quantitative analysis showing no significant relationship between STRF amplitude and cross-correlation strength, demonstrating the method's ability to distinguish cells without detectable receptive fields.

A.4 Additional Clustering Analysis Data

The complete cluster-feature expression profile showing all 28 features used in the clustering analysis. This extended view provides comprehensive detail of how each cluster expresses spatial and temporal characteristics across all four spectral channels (R, G, B, UV) for seven feature categories.

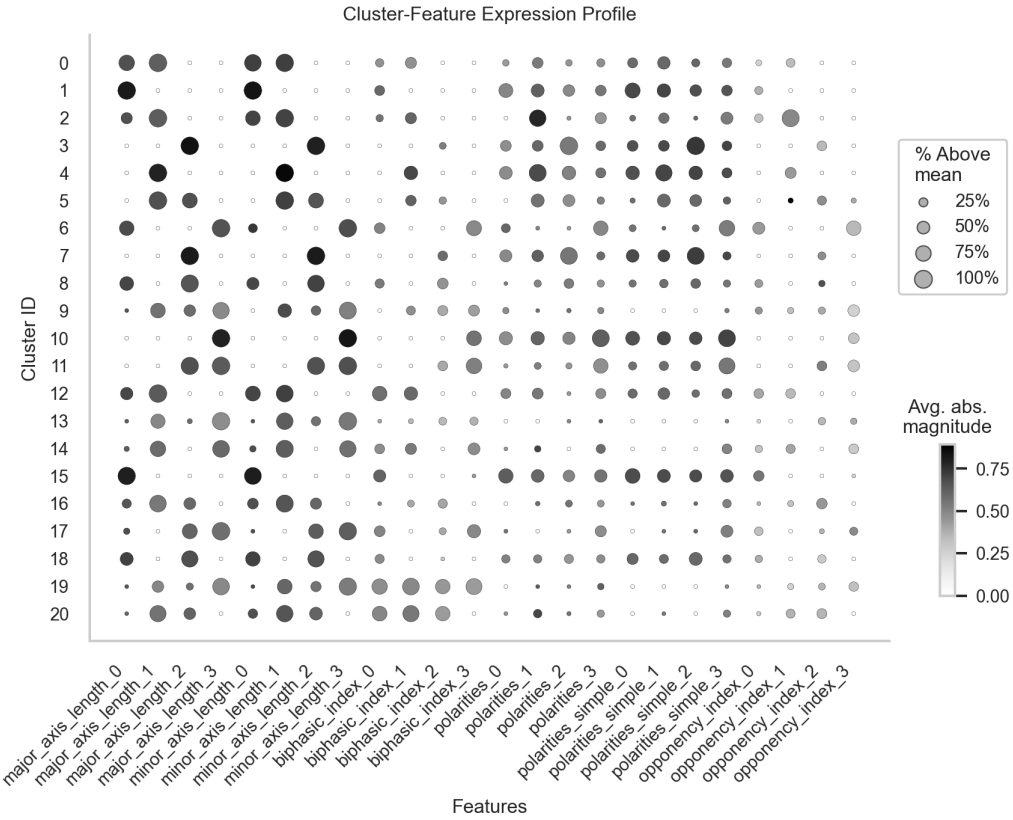

Figure A.5: Complete cluster-feature expression profile for all 28 features. Dot size represents the percentage of cells above threshold for each feature within each cluster, whilst colour intensity indicates the average magnitude among active cells. Features are organised by category: spatial amplitudes, temporal amplitudes, major axis length, minor axis length, biphasic index, spectral centroid, and polarity assignments across R (580 nm), G (478 nm), B (420 nm), and UV (365 nm) channels. This comprehensive view reveals the full feature space used for hierarchical clustering and demonstrates the spectral organisation underlying functional diversity in the bipolar cell population.

A.5 Temporal Properties Statistics

Detailed descriptive statistics for temporal properties showing biphasic index values across spectral channels and encoding polarities. These data support the analysis of temporal complexity differences between On and Off pathways across the tetrachromatic visual system.

Table A.1: Biphasic index descriptive statistics by colour channel and polarity. Values closer to 0 indicate monophasic responses, while values approaching 1 indicate biphasic responses.

Colour Channel	Polarity	n	Mean	SD	Median
R (580 nm)	Off	367	0.172	0.217	0.086
	On	218	0.606	0.306	0.664
G (478 nm)	Off	266	0.223	0.241	0.139
	On	157	0.663	0.281	0.751
B (420 nm)	Off	158	0.145	0.195	0.057
	On	314	0.315	0.289	0.217
UV (365 nm)	Off	86	0.224	0.248	0.120
	On	231	0.561	0.272	0.594

Table A.2: Cluster summary with encoding type, sample size, and silhouette scores. Average silhouette score across all clusters: 0.323. Quality grades assigned using conventional thresholds: Good (>0.5), Fair (0.25-0.5), Poor (<0.25).

Cluster ID	Encoding Type	Sample Size	Silhouette Score	Quality Grade
0	Off	78	0.404	Fair
1	Off	46	0.346	Fair
2	Off	17	0.311	Fair
3	Off	13	0.488	Fair
4	On	15	0.258	Fair
5	Opp	11	0.162	Poor
6	Opp	19	0.332	Fair
7	On	78	0.386	Fair
8	On	29	0.275	Fair
9	Opp	30	0.238	Poor
10	On	46	0.330	Fair
11	On	32	0.475	Fair
12	On	36	0.252	Fair
13	Off	60	0.608	Good
14	Opp	22	0.047	Poor
15	On	53	0.187	Poor
16	Off	58	0.310	Fair
17	On	37	0.087	Poor
18	Off	22	0.337	Fair
19	On	72	0.645	Good
20	On	34	0.448	Fair

A.6 Additional Anatomical Data

Detailed descriptive statistics for inner plexiform layer stratification patterns across spectral channels and encoding types.

Table A.3: IPL stratification by spectral channel and integration type. Note that one ROI can be counted multiple times if its multichromatic RF contains more than one cone channel with detectable activity.

Colour Channel	Type	n	Mean	SD	Median	Q1	Q3
R (580 nm)	Off	266	75.44	20.54	80.00	74.00	87.93
	On	204	37.84	16.48	37.00	31.36	41.00
	Opp	139	50.34	26.58	56.84	21.00	72.00
G (478 nm)	Off	206	76.22	19.60	80.64	75.36	86.93
	On	156	37.84	14.13	37.00	33.00	39.87
	Opp	115	52.20	26.57	58.00	25.00	75.00
B (420 nm)	Off	158	74.28	23.38	80.21	71.25	89.00
	On	245	36.78	17.06	36.49	24.00	45.00
	Opp	118	44.94	25.43	50.63	19.00	63.00
UV (365 nm)	Off	86	70.55	27.56	81.00	66.00	88.00
	On	176	35.50	16.38	37.00	25.00	41.25
	Opp	92	46.13	24.90	55.00	19.00	66.25

Displaced bipolar cell terminals were identified based on whether their stratification depth fell outside the typical On and Off sublamina boundaries.

Table A.4: Percentage of ROIs with response characteristics suggesting displacement from the ON and OFF sublaminae. Separation threshold at 45% IPL depth, anatomically separating the ON and OFF sublaminae. Opponent terminals were excluded, due to their bimodal distribution across both sublaminae.

Wavelength	Off terminals			On terminals		
	Total	Displaced	%	Total	Displaced	%
R (580 nm)	266	23	8.6	204	33	16.2
G (478 nm)	206	18	8.7	156	18	11.5
B (420 nm)	158	18	11.4	245	61	24.9
UV (365 nm)	86	15	17.4	176	37	21.0
Average			**11.5**			**18.4**

The following figure presents the raw dataset showing all measured receptive field properties as a function of IPL depth, stratified by integration category. Spatial properties exhibited minimal depth organisation whilst temporal properties show laminar effects.

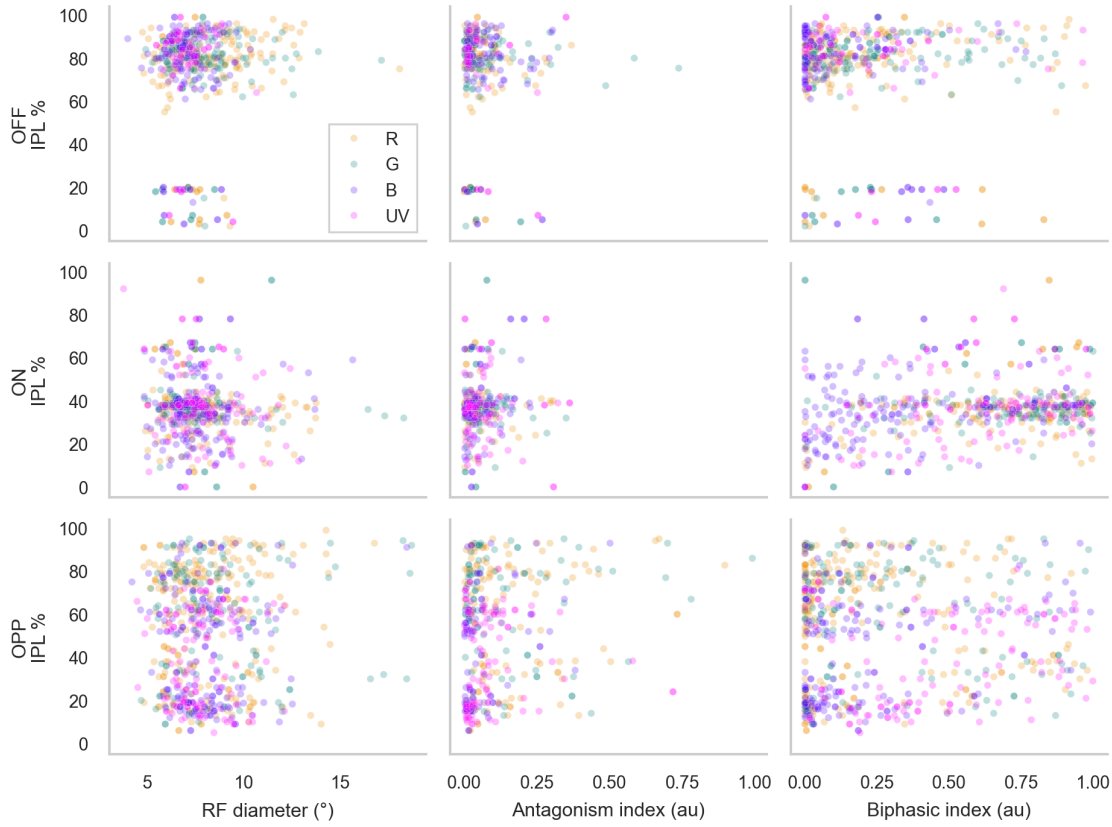

Figure A.6: Complete IPL stratification dataset by integration category. Raw data scatter plots showing all measured receptive field properties (n = 1,800) as a function of IPL depth across integration categories. **Rows:** Integration categories (OFF: n = 799, ON: n = 878, Opponent: n = 124). **Columns:** RF diameter (left), antagonism index (middle), biphasic index (right). Point colours indicate spectral channels (R, G, B, UV). **Comprehensive statistical analysis: RF diameter:** Overall colour channel effect negligible ($H = 4.32$, $p = 0.229$, $\eta^2 = 0.0007$). Category effect small but significant ($H = 23.03$, $p < 0.001$, $\eta^2 = 0.012$). Individual depth correlations mostly negligible: strongest correlations in B channel ($r^2 = 0.017$ overall; ON B channel $r^2 = 0.001$, OFF R channel $r^2 = 0.023$). **Antagonism index:** Overall colour channel effect negligible ($H = 8.11$, $p = 0.044$, $\eta^2 = 0.004$). Category effect small ($H = 27.90$, $p < 0.001$, $\eta^2 = 0.022$). Strongest depth relationships in B channel ON cells ($r^2 = 0.078$) and UV channel ON cells ($r^2 = 0.079$), with Opponent B and UV channels showing modest correlations ($r^2 = 0.049$, $r^2 = 0.039$). **Biphasic index:** Robust laminar organisation with large colour channel effect ($H = 95.95$, $p < 0.001$, $\eta^2 = 0.051$), large category effect ($H = 419.85$, $p < 0.001$, $\eta^2 = 0.229$), and large category-colour interaction ($H = 571.97$, $p < 0.001$, $\eta^2 = 0.309$). Strong polarity-dependent depth correlations: OFF R channel ($r^2 = 0.104$), OFF G channel ($r^2 = 0.049$), ON B channel ($r^2 = 0.141$), ON UV channel ($r^2 = 0.127$). Mixed/Other polarity cells show medium to large negative correlations across R, G, B channels ($r^2 = 0.160$, 0.076, 0.194 respectively). All statistical tests employed non-parametric approaches (Kruskal-Wallis, Spearman correlations) with Cohen's effect size interpretations: negligible ($\eta^2/r^2 < 0.01$), small (0.01-0.06/0.09), medium (0.06-0.14/0.09-0.25), large (> 0.14/0.25).

A.7 Centre-Surround Analysis Statistics

Detailed descriptive statistics for centre-surround organisation metrics across integration categories and spectral channels. Statistical analysis revealed no significant differences across either integration categories or spectral channels, confirming that spatial antagonism is minimal and uniform across functional types.

Table A.5: Descriptive statistics by integration category showing distribution of antagonism metrics across Off, On, and Opponent RFs at the ROI level (N = 800 ROIs, NaN values removed). One-way ANOVA revealed no significant category effect (F = 2.641, p = 0.071921, η^2 = 0.0067).

Category	Count	Mean	Std	Median	Min	Max
Off	294	0.041182	0.047963	0.027193	0.0	0.287227
On	432	0.043283	0.059541	0.020917	0.0	0.343570
Opponent	82	0.057111	0.062063	0.042496	0.0	0.344309
Total	808					

Table A.6: Descriptive statistics by color channel showing distribution of opponency metrics across spectral channels (R, G, B, UV). Analysis conducted on ROI$\times$channel combinations accounting for within-subject dependencies. One-way ANOVA revealed a significant but small color channel effect (F(3,1828) = 6.229, p < 0.001, η^2 = 0.0101). Kruskal-Wallis test confirmed significance (H = 29.911, p < 0.001). Despite statistical significance, the effect size indicates spectral channel accounts for only 1% of variance in antagonism.

Color Channel	Count	Mean	Std	Median	Min	Max
R (580 nm)	601	0.051829	0.104610	0.010927	0.0	0.895830
G (478 nm)	434	0.064736	0.121187	0.022159	0.0	0.990553
B (420 nm)	476	0.037569	0.067246	0.007581	0.0	0.501163
UV (365 nm)	321	0.059087	0.097680	0.020367	0.0	0.717655